Observation of Very-High-Energy Gamma-Rays from Blazars with the MAGIC Telescope

Masaaki Hayashida

München 2008

Observation of Very-High-Energy Gamma-Rays from Blazars with the MAGIC Telescope

Masaaki Hayashida

Dissertation
an der Fakultät für Physik
der Ludwig–Maximilians–Universität
München

vorgelegt von
Masaaki Hayashida
aus Saitama, JAPAN

München, Februar 2008

Erstgutachter: Prof. Dr. Christian Kiesling

Zweitgutachter: Prof. Dr. Masahiro Teshima

Tag der mündlichen Prüfung: 20 März 2008

Abstract

Blazars, a subclass of active galactic nuclei in which the jet is aligned very close to our line of sight, can accelerate charged particles to relativistic energies in the jet. Electromagnetic emission from this class of sources can be observed from radio up to TeV energies. The MAGIC telescope is an Imaging Atmospheric Cherenkov Telescope with a 17-m diameter dish, located on the Canary Island of La Palma, in operation for exploring a new window of very high energy (VHE) γ-ray bands, above 50 GeV.

Searching for new VHE γ-ray blazars, BL Lacertae was observed with the MAGIC telescope in 2005 and 2006. A VHE γ-ray signal was discovered with a 5.1 σ excess in the 2005 data. This discovery established a new class of VHE γ-ray emitters, "low-frequency peaked BL Lac objects". On the other hand, the 2006 data showed no significant excess. This drop in flux followed the observed trend in the optical activity.

The MAGIC telescope continuously observed the bright known blazars Mkn501, 1ES1959+650 and Mkn421. In particular, extensive simultaneous multiwavelength observations with the MAGIC telescope and the X-ray Satellite Suzaku were carried out for Mkn501 in July 2006 and for 1ES1959+650 in May 2006. VHE γ-ray signals from about 100 GeV to a few TeV were clearly detected. For the first time, the VHE γ-ray spectra were simultaneously obtained with the X-ray spectra during their low states of activity. Long term observations of Mkn421 in 2006 showed a strong variability in VHE γ-ray emission.

The spectral energy distributions (SEDs) of these four blazars could be well explained by a homogeneous one-zone synchrotron self-Compton model. This model suggests that the variation of the injected electron population in the jet is responsible for observed variations of the SEDs of the blazars. For all sources, the derived magnetic field strength in the jet and the Doppler beaming factor showed similar values.

A contribution on the hardware sector is also presented in this thesis. For further lowering energy threshold in the MAGIC project, a new type of photosensor, "HPDs with an 18-mm diameter GaAsP photocathode", were developed. A quantum efficiency of the photocathode could reach over 50%. Compared to the PMTs currently used in MAGIC, the new photosensors would improve the overall Cherenkov photon conversion efficiency by a factor of 2. Other performance values including lifetime also fulfilled the requirements of photosensors to be used in the MAGIC telescope.

Zusammenfassung

Blazare, eine Unterklasse von aktiven galaktischen Kernen, deren Jet sehr nahe zur Sichtlinie des Beobachters ausgerichtet ist, können in ihrem Jet geladene Teilchen bis hin zu relativistischen Energien beschleunigen. Von diesen Quellen kann elektromagnetische Strahlung vom Radiobereich bis hin zu TeV Energien beobachtet werden. Das MAGIC Teleskop ist ein abbildendes atmosphärisches Cherenkov Teleskop mit einem Reflektor von 17m Durchmesser, das auf der kanarischen Insel La Palma betrieben wird, um im neu erschlossenen Beobachtungsfenster sehr hoch energetischer (SHE) Gammastrahlen über 50 GeV den Himmel zu erforschen.

Auf der Suche nach neuen SHE gammastrahlenden Blazaren beobachtete das MAGIC Teleskop den Blazar BL Lacertae in den Jahren 2005 und 2006. In den Daten aus 2005 wurde ein Signal mit einer Signifikanz von 5.1 σ gemessen. Mit dieser Entdeckung wurden die "niederfrequent dominanten BL Lac Objekte" als neue Klasse von SHE Gammastrahlungsquellen etabliert. In den Daten aus 2006 wurde kein signifikantes Signal gemessen. Der daraus abgeleitete Flussabfall von BL Lacertae entspricht dem beobachteten Abfall der optischen Aktivität.

Das MAGIC Teleskop beobachtete kontinuierlich die hellen, bereits bekannten Blazare Mkn501, 1ES1959+650 und Mkn421. Insbesondere wurden aufwendige, gleichzeitige Multiwellenlängen-Beobachtungen mit dem MAGIC Teleskop und dem Röntgensatelliten Suzaku für Mkn501 im Juli 2006 und für 1ES1959+650 im Mai 2006 durchgeführt. Signifikante Signale von Gammastrahlen mit Energien zwischen ca. 100 GeV und einigen TeV wurden gemessen. Zum ersten Mal wurden simultan ein SHE Gammastrahlenspektrum und ein Röntgenspektrum dieser Quellen aufgenommen, während sie in einem niedrigen Aktivitätsstadium waren. Langzeitbeobachtungen von Mkn421 zeigten eine starke Variabilitaet im Flussniveau in 2006.

Die spektralen Energieverteilungen (SEVs) dieser vier Blazaren können gut durch ein homogenes Einzonen-Synchrotron-Selbst-Comptonmodell beschrieben werden. Dieses Modell legt nahe, dass die beobachteten Variationen der SEVs dieser Blazare auf Veränderungen des in den Jet injizierten Elektronenspektrums zurückzuführen sind. Für alle Quellen wurden die gleichen Magnetfeldstärken und Dopplerfaktoren im Jet abgeleitet.

Mein Beitrag zur Hardwareentwicklung ist ebenfalls Teil dieser Arbeit. Zum Erreichen einer niedrigeren Schwellenenergie des MAGIC Teleskops wurde ein neuer Typ von Photosensoren "HPDs mit einer 18mm durchmessenden GaAsP Photokathode" entwickelt. Die Quanteneffizienz dieser Photokathoden erreicht 50%. Im Vergleich zu den PMTs, die zur Zeit in MAGIC verwendet werden, würden die HPDs die Photonenkonvertierungseffizienz von Cherenkov Licht verdoppeln. Alle weiteren Parameter, wie z.B. die Lebensdauer, erfüllen die Anforderungen an Photosensoren zum Einsatz in Cherenkov Teleskopen wie MAGIC.

Contents

Introduction - This Thesis

In 1912, high energy charged particles striking the earth from outer space, called "Cosmic Rays", were discovered by Victor Hess. Up to now, cosmic rays have been observed with energies even beyond 10^{20} eV. These highest energy particles cannot be generated in any accelerator on Earth, not even within in our galaxy. It is, however, extremely difficult to identify a distant source as origin of cosmic rays using their arrival direction because charged cosmic rays are deflected by the inter-galactic and galactic magnetic fields before they reach the Earth. So far, not a single source has been proven to be the site of cosmic-ray acceleration. On the other hand, a neutral particle, like a photon, can reach the Earth without deflection by magnetic fields. High energy photons are attributed to high energy charged particles and point to their origin of generation.

"Active galactic nuclei (AGNs)" are considered to be one of the prime candidates for an acceleration site of the highest-energy cosmic rays. AGNs are galaxies in which the galactic core produces more radiation than the entire rest of the galaxy itself. It is believed that, AGNs, like most galaxies, have supermassive black holes (mass in the range of $10^6 - 10^9 M_\odot$) in their cores and the radiated power is produced by mass accretion onto the supermassive black hole. Some AGNs have relativistic outflows (jets), which are considered to be the site of particle acceleration and generate high energy photons. If a relativistic jet is viewed at a small angle relative to its axis the observed emission from the jet is amplified by the relativistic beaming effect. Such sources are called blazars; they are, in fact, the most dominant class of high-energy photon emitters among AGNs in γ-ray astronomy. For example, 3C 279, the first γ-ray blazar discovered with a γ-ray satellite "EGRET", was one of the brightest γ-ray sources in the sky at the time of its discovery in 1991. In 1992, TeV emission was discovered from a blazar, Mkn421, which was established as the first extra-galactic TeV photon emitter. Electromagnetic emission from this class of sources can be observed from radio up to TeV energies. Based on the phenomenological aspects of their emission features, blazars are divided into two classes, **Flat Spectrum Radio Quasars (FSRQs)** and **BL Lacertae Objects (BL Lacs)**. Their spectral energy distributions (SEDs) are characterized by a two-bump structure. Among BL Lacs, where the lower peak is located in the sub-millimeter to optical band, the objects are classified as **"Low-frequency peaked BL Lacs (LBLs)"**, while in **"High-frequency peaked BL Lacs (HBLs)"** the lower peak is located at UV to X-ray energies. However, the physical origin of these sub-classes is still unclear.

The ultimate goal of blazar research is to learn how energy is extracted from the black hole. We are still at a very early stage in this area, trying, at this point, simply to understand how much energy is involved and what is the physical state of the jet. The observed radiation must

be associated with the intrinsic properties of the jet. In particular, due to its fast variability, γ-ray emission may prove to be more directly related to the physics of the central black hole than other low-energy emissions. Therefore, **"How is the γ-ray spectrum produced?"** is therefore one of the most interesting questions in blazar research and it may provide new knowledge about the fundamental physics of blazars. Unfortunately, the number of blazars from which very high energy (VHE: $E > 50$GeV) γ-rays have been detected ("TeV blazar") is too small for investigating the fundamental physics of blazars. In 2004, when I started this work, there were only 7 AGNs confirmed as VHE γ-ray emitters. All but one of them belonged to the class of HBLs. VHE γ-rays had never been detected from either LBLs or FSRQs. Therefore, there was a strong desire to increase the number of TeV blazars.

So far, observed emission from HBLs has been very successfully interpreted in the framework of **Synchrotron Self-Compton (SSC) models**. The lower energy bump is attributed to synchrotron emission by relativistic electrons in the jet, while the higher energy bump originates from inverse Compton (IC) scattering of the synchrotron photons off their own parent electrons. It should be noted that other emission models based on the acceleration of hadrons, with subsequent creation of neutral pions to photons, have also been proposed. Emission in the framework of these "hadronic origin" models would lead to a direct evidence of a cosmic-ray accelerator, but no observational result has confirmed this type of models yet.

Simultaneous multiwavelength observations over a wide energy range are essential for discussing those emission models of TeV blazars, because these often show a strong flux variability down to time scales of a few minutes in the VHE γ-ray band. Especially, a correlation between X-rays and VHE γ-rays is an important feature because of its being well associated with the SSC model. Most of the previous multiwavelength campaigns suffered from the low sensitivity of the participating γ-ray telescopes. Therefore, simultaneous observations were limited to being conducted only during flaring states (i.e., states with high source flux). In addition, the energy region between 30 and 300 GeV was unexplored even though it is an important range for TeV blazar observations, as it is the energy range where blazars are supposed to show their luminosity peaks .

Considering these open issues, I decided to study VHE γ-ray emission from blazars with the MAGIC (Major Atmospheric Gamma-ray Imaging Cherenkov) telescope. The MAGIC telescope is an Imaging Atmospheric Cerenkov Telescope (IACT) with a 17-m diameter dish, located on the Canary Island of La Palma ($28.2°$ N, $17.8°$ W, 2225 m a.s.l.). IACTs are currently the most successful instruments for VHE γ-ray observations thanks to the innovations achieved in the "imaging technique". IACTs record images of γ-ray induced air showers in the atmosphere using their emitted Cherenkov light instead of direct detection of cosmic VHE γ-rays themselves. Nearly all important discoveries of TeV sources including the first one concerning both galactic and extra-galactic objects have been achieved with IACTs.

Thanks to the currently largest mirror dish worldwide, the MAGIC telescope is operating at a γ-ray trigger threshold of ~ 50 GeV and a spectral threshold of $\sim$80 GeV, which are the lowest energy thresholds to be found among current IACTs. The MAGIC telescope allows us to study the VHE γ-ray emission from blazars in the newly opened energy range. IACT observations with a low energy threshold have another advantage for studying VHE γ-rays from blazars. While traveling through the universe, VHE γ-rays from blazars are absorbed by faint diffuse

light, called "Extra-galactic background light (EBL)". The absorption effect decreases as the VHE γ-ray energy becomes lower. The telescope's high sensitivity allows the detection of VHE γ-ray signals with rather short observation times even in low states of source activity. Together with wide energy-range X-ray satellites, these new instruments make it possible to perform multiwavelength observations in a much wider range than ever, also in various states of activities of the observed objects.

In order to further improve the observation performance, the MAGIC project will be upgraded to "MAGIC-II" during the year of 2008 by a second 17-m diameter telescope at 85 m distance from the first one. One of the key tasks within the MAGIC-II project is the development of a new type of photosensor to which I contributed, the **"Hybrid PhotoDetectors (HPD) with an 18-mm diameter GaAsP photocathode"**,for achieving an even lower energy threshold. Currently, photomultiplier tubes (PMTs) are widely used as photosensors for IACTs. Their conversion efficiency from a photon to a photoelectron - the so-called "quantum efficiency (QE)"- is only 20 to 30%. On the other hand, HPDs with a GaAsP photocathode have a QE of $\sim$ 50%. In conventional HPDs, the size of the GaAsP photocathode was too small (< 8 mm) to be used as a pixel element in the MAGIC telescope camera. Therefore, HPDs with a larger GaAsP photocathode size (18 mm) are required and their performance, for a first application in the field as photosensors for IACTs, needs to be verified.

Thus, this thesis has the following key objectives:

- Development of a new type of photosensor, "HPD", with a high quantum efficiency to further lower the energy threshold in IACT observations.

- Search for new TeV blazars to increase the number of sources among all sub-classes of blazars for investigating the fundamental physics of blazars.

- Wide-range simultaneous multiwavelength observations in the X-ray and VHE γ-ray bands in order to obtain wide-range spectral energy distributions in different states for discussing emission models of blazars, especially with a Synchrotron Self-Compton model.

My thesis follows the structure outlined below where I also mention my personal contributions within the overall project.

Physics of AGN observations with VHE γ-ray emission: AGNs are the prime candidate sites for acceleration of the highest-energy cosmic rays. In Chapter 1, the acceleration mechanisms and the emission processes for cosmic high-energy photons in celestial objects are described. The current status of the VHE γ-ray astronomy is briefly reviewed. Chapter 2 present a basic model of AGNs and some detailed information about blazars, including emission models for their spectral energy distributions. The motivation for observation strategies of this thesis is also mentioned.

Imaging Air Cherenkov Telescope, "MAGIC": Chapter 3 briefly describes the physics of air showers and the subsequent production of Cherenkov light, including general descriptions of IACTs. The hardware layout of the MAGIC telescope is presented Chapter 4.

Development of a new type of photosensor, "HPD": The development status of HPDs is reported in Chapter 5. First, their basic performance as photosensors and tests of a circuit to compensate for temperature dependences in their gain characteristic are presented. Results of QE measurements are covered including applications of the wavelength shifter technique for increasing the QE in the UV region. Measurement results of aging properties are also reported. Based on these results, simulation studies are carried out to estimate the HPDs' durability for operation as photosensors in the MAGIC camera.

This task was my personal responsibility and I performed all the measurements and simulation studies as reported in this Chapter. The HPDs were developed together with Hamamatsu Photonics. I was the direct contact for the company at MPI throughout the development.

Analysis methods of the MAGIC telescope: Chapter 6 gives an overview of the standard chain of the MAGIC data analysis. For verification of my analysis in the following sections, the results of Crab Nebula observations are presented as well.

First discovery of VHE γ-ray emission from the LBL object, "BL Lacertae": For the first time, VHE γ-ray emission was discovered from a LBL object, "BL Lacertae". In Chapter 7, the observation results of 2005 and 2006 are reported. A comparison with previous observations in the VHE γ-ray band, a correlation between the optical and the VHE γ-ray emission, and emission models for the observed SED are discussed.

As a Principle Investigator for this source I proposed the related observations and performed the analysis as a main analyzer. The results published were based on my analysis.

Extensive observation of known bright TeV blazars: Observation results and discussions of Mkn501 (Chapter 8) , 1ES1959+650 (Chapter 9) and Mkn421 (Chapter 10) are covered. Wide-range simultaneous multiwavelength (MWL) observations together with the X-ray satellite Suzaku were carried out in 2006 for Mkn501 and 1ES1959+650. In addition, the MAGIC telescope performed long term monitoring observations of these three TeV blazars. Light curves and spectra in both VHE γ-ray and X-ray bands obtained during the MWL campaigns for Mkn501 and 1ES1959+650 are presented in detail. Long term light curves (in 2005 and 2006 for Mkn501 and 1ES1959+650, in 2006 for Mkn421) are also shown. The obtained SEDs are compared to previous measurements and discussed within an SSC model, which can provide the physical parameters in the jet.

I worked for these MWL campaigns as a coordinator on the MAGIC side for both Mkn501 and 1ES1959+650, and proposed the observations with the MAGIC telescope as a Principle Investigator to obtain simultaneous data of VHE γ-ray and X-ray. I analyzed the VHE γ-ray data for Mkn501 taken in 2006, 1ES1959+650 taken in 2005 and 2006, and Mkn421 taken in 2006 as a main analyzer. The results from my analyses were published in a paper and in proceedings as the results of the MAGIC collaboration.

Chapter 11 summarizes the discussions of observed SEDs of four TeV blazars within the SSC model. Concluding remarks and an outlook based on the results of this thesis are given in Chapter 12.

Chapter 1

Very high energy γ-ray astronomy

1.1 Accelerators in Universe

In 1912, energetic charged particles striking the Earth from outer space, called "Cosmic Rays", were discovered by Victor Hess. Up to now, cosmic rays have been observed with energies over 10^{20} eV as shown in Fig. 1.1. The variation of the flux with energy is referred to as the "Energy Spectrum". The slope with respect to energy is described by the spectral index α, $dN/dE \propto E^{-\alpha}$. Remarkably, it appears to be a smooth curve over 10 decades of energy with only a few noticeable structures. There are small, abrupt changes in the local just above 10^{15} eV and again just above 10^{18} eV. They appear as small "kinks" on a power law. Within the Cosmic Ray community, these features are usually referred to as the "knee" and the "ankle", respectively. The spectral index follows $\alpha \sim 2.7$ for energy above about 1 GeV. At an energy just above "knee" the spectral index steepens to $\alpha \sim 3.0$, and at an energy around "ankle" the spectral index gets again harder.

Cosmic-rays with an energy above several 10^{19} eV (above the ankle) are a particularly interesting topic. The highest-energy particles ($> 6 \times 10^{19}$ eV) interact strongly with the ubiquitous cosmic microwave background radiation and lose energy by pion production while propagating through the universe, thus, they can only travel limited distances. This effect is known as "GZK effects" [121, 255]. Due to this effect, the cosmic-ray flux is strongly attenuated above 6×10^{19} eV and the spectrum is expected to have a sharp cut-off around that energy, so-called "GZK cut-off". However, a Japanese group, the AGASA experiment [82], detected 11 events above 10^{20} eV, which indicated that the energy spectrum is likely to extend beyond 10^{20} eV without the GZK-cutoff [232]. In contrast, a U.S. group, the HiRes experiment [4], derived the spectrum which followed with the predicted flux by the GZK effect [1]. A current on-going project, the Pierre Auger experiment [2], which has a much higher sensitivity than both previous ones, has challenged to settle the issue of the highest-energy cosmic rays. In the latest results, the Auger experiment showed the energy spectrum steepening above 4×10^{19} eV [252], the origin of this feature (whether due to the GZK-effect or other effects) is, however, still under discussion [247].
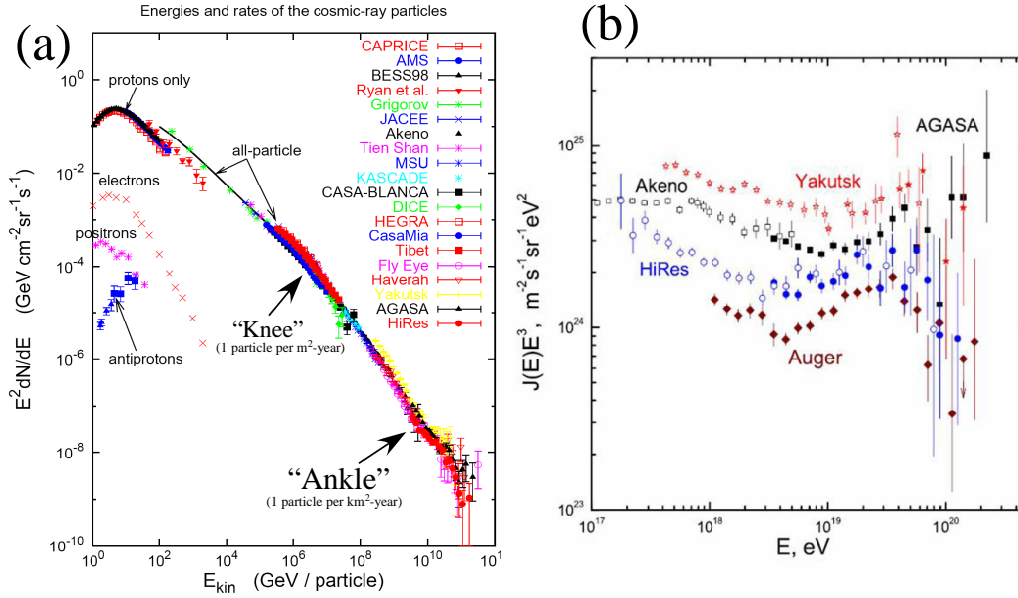
Figure 1.1: **[Left] (a):** Many measurements of the cosmic-ray flux over a wide energy range (taken from [131]). **[Right] (b):** Measured E-cubed energy spectra $E^3 \mathrm{d}N/\mathrm{d}E$ above 10^{17} eV from four experiments [AGASA, Yakutsk, HiRes and Auger] (taken from [237]).

1.1.1 Sources of Cosmic Accelerator

For a long time, people have tried to understand the origin of cosmic rays. In current scenarios, particles with higher energy (up to the "knee" at about 10^{15} eV) are supposed to be accelerated in galactic objects, like supernova remnants (e.g., [48]). The origin of particles with energies between the knee and the ankle is a matter of recent scientific discussions. Some models have suggested that the spectral break at the knee is due to a limitation in the maximum energy of the protons accelerated in the galactic objects (e.g., [244]). Particles with energy above the ankle are thought to be originated from extra-galactic sources (e.g., [228]). However, not a single source, neither galactic nor extra-galactic one, has been proven as the site of a cosmic-ray accelerator, yet.

Fig. 1.2 is the so-called "Hillas-plot", which plots the known cosmic sources where particle acceleration may occur, with their sizes ranging from kilometers to mega-parsec [129]. A general condition that has to be fulfilled is that the cosmic accelerator has to confine the accelerated particle up to the highest energies. Following this argument leads to the expression:

$$E_{\mathrm{max}} \propto ZeBL, \tag{1.1}$$

where Z is the charge of the accelerated particle, B is the magnetic field strength, e is the elementary charge and L is the linear dimension of the source size. The Diagonal lines represent the possible maximum energy to be accelerated under the conditions of magnetic strength and source size. Sites lying below each line are excluded from the candidate sites to produce the

highest-energy particle as indicated in the figure.

Not many types of sources are expected as accelerators of the highest-energy cosmic rays. Active galaxies (AGNs: see detail in Chapter 2), a type of extra-galactic objects, is one of the prime candidate site where protons can be accelerated up to 10^{20} eV. Recently (November 2007), the Auger experiment just published the evidence of correlations between the arrival directions of cosmic rays with energy above 6×10^{19} eV and the positions of AGNs lying within $\sim$75 Mpc. This is the first experimental evidence that indicate AGNs are a likely source of the highest-energy cosmic rays [3].
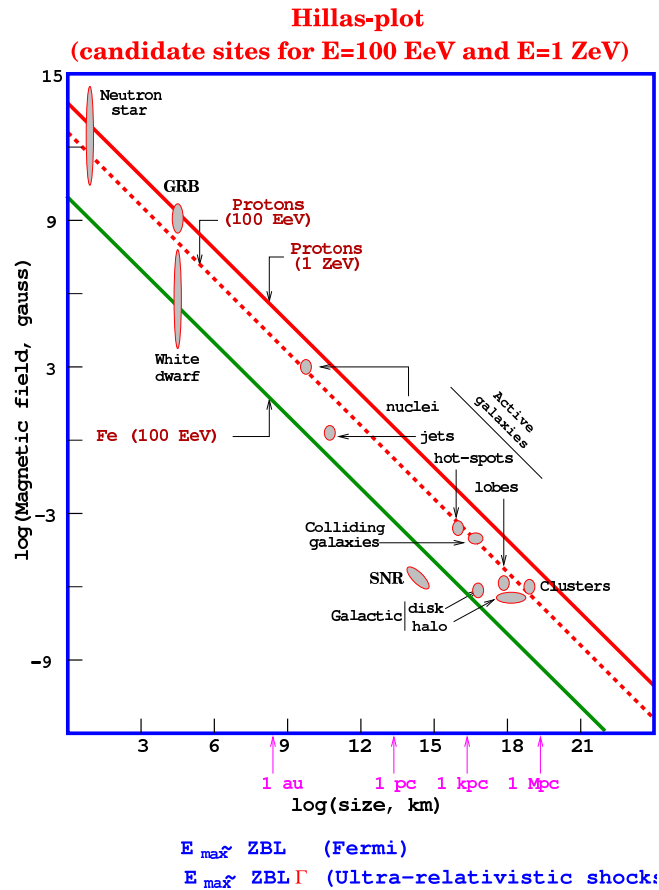
Figure 1.2: Source size (*L*: x-axis) and magnetic filed strength (*B*: y-axis) of possible sites of particles acceleration. Objects below diagonal lines can not accelerate (1) protons to 10^{21} eV (*red solid*), (2) protons to 10^{20} eV (*red dashed*), (3) iron to 10^{20} eV (*green*).

1.1.2 Acceleration mechanisms

A process was originally considered by Fermi [96]. This mechanism is called "Fermi acceleration". In Fermi's original paper, it was assumed that collisions with interstellar clouds would be the main source of energy for the particles. This, however, led to problems for describing measured cosmic-ray spectrum. First, this process is very inefficient[1]. Second the universal spectral index of cosmic rays can not be explained.

To solve these problems, new version of the Fermi acceleration mechanism was invented by several authors (e.g., [55, 61]). This is the acceleration mechanism in the presence of strong shock waves, so-called "Diffusive Shock Acceleration".

The situation is pictured in Fig. 1.3 in the rest frame of the shock, which is treated as a discontinuity. The mean velocities and densities of the scattering centers "upstream" ,"downstream" of the shock are u_1, u_2 and ρ_1, ρ_2 respectively which are taken to be constant throughout the respective region.
The essence of this acceleration process is

- The particle energy can increase at each crossing of the shock wave front.

Here we consider only those particles which have energies high enough for their gyroradii to be much larger than the thickness of the shock front. Such energetic particles hardly notice the shock at all and the velocities of the particles ($v \approx c$) is much more than the velocity of the shock. The energetic particles are consequently able to pass freely between the regions upstream and downstream of the shock.
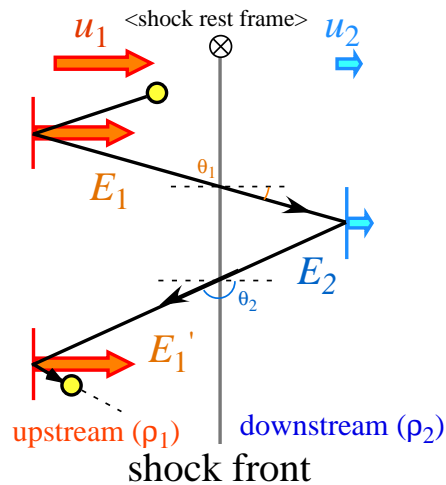
Figure 1.3: Schematic drawing of the first-order Fermi acceleration mechanism. See detailed in text.

---

[1]In this mechanism, the average increase in energy is only second order in (V/c), where V is the velocity of the cloud. The original process is called "second-order Fermi acceleration"

While a particle is in the upstream or downstream region, its energy is constant when viewed in the rest frame of the relevant region. When it crosses from one region to the other, a Lorentz transformation gives its energy in the rest frame of the new region. For a particle with E_1, the energy after a one cycle of passing from upstream to downstream and back to upstream E_1' is given by

$$\frac{E_1'}{E_1} = \frac{E_1'}{E_2}\frac{E_2}{E_1} = \frac{(1 - \frac{u_1 v}{c^2}\cos\theta_2)(1 - \frac{u_2 v}{c^2}\cos\theta_1)}{(1 - \frac{u_2 v}{c^2}\cos\theta_2)(1 - \frac{u_1 v}{c^2}\cos\theta_1)} \tag{1.2}$$

Angles at crossing of the shock are isotropically distributed on either side of the shock front. The distributions of $\cos\theta_1$ and $\cos\theta_2$ for the plane shock front are the projections onto a plane in the range of $0 \leq \cos\theta_1 \leq 1$ and $-1 \leq \cos\theta_2 \leq 0$, so that $\langle\cos\theta_1\rangle = 2/3$ and $\langle\cos\theta_2\rangle = -2/3$ can be derived, respectively. Considering $v \approx c$, Eq. 1.2 becomes:

$$\left\langle\frac{E_1'}{E_1}\right\rangle \approx 1 + \frac{4}{3}\frac{(u_1 - u_2)}{c} \tag{1.3}$$

The energy increase is first order in $(u_1 - u_2)/c$ on average so that this mechanism is called "first-order Fermi acceleration". This is a much more efficient process than the original one.

After k cycles, the energy of the particle E_k can be written using the initial energy of the particle E_0 by

$$\frac{E_k}{E_0} \approx \left(1 + \frac{4}{3}\frac{(u_1 - u_2)}{c}\right)^k \tag{1.4}$$

All of the particles which penetrate into the upstream region return across the shock. For the configuration of the large, plane shock, the rate of particles passing from the upstream to the downstream region is given by the projection of an isotropic particle flux onto the plane shock front,

$$\int_0^1 d\cos\theta \int_0^{2\pi} d\Phi \frac{Nv}{4\pi}\cos\theta = \frac{Nv}{4}, \tag{1.5}$$

where N is the number density of particles undergoing acceleration. On the other hand, in the case for those travelling downstream, some particles can escape by the motion of the downstream. Therefore, the escape probability of particles away from the region can be estimated:

$$P_{\text{esc}} = \frac{\text{Rate of particle loss of downstream region}}{\text{Rate of particles passing from the upstream to the downstream region (Eq. 1.5)}}$$
$$= \frac{Nu_2}{Nv/4} = 4\frac{u_2}{v} \tag{1.6}$$

Therefore, a particle can pass back from downstream and upstream with a probability of $1 - P_{\text{esc}}$. After k cycles, the probability that a particle still remains the acceleration region $S(k)$ is $(1 - P_{\text{esc}})^k = (1 - 4u_2/v)^k$. Using Eq. 1.4, we can eliminate k and then,

$$S(k) \approx \left(\frac{E_k}{E_0}\right)^{(-3u_2/(u_1 - u_2))} \tag{1.7}$$

With this formula, the number of particle with energy between E and $E + \mathrm{d}E$ ($N(E)\mathrm{d}E$) can be written by

$$S(k) \propto \int_{E_k}^{\infty} N(E)\mathrm{d}E \tag{1.8}$$

We can derive the differential energy spectrum as:

$$N(E) \propto E^{-\mu}, \quad \mu = \frac{2u_2 + u_1}{u_1 - u_2} \tag{1.9}$$

A shock can form when $u_1 > a_1$, a_1 is the sound speed in the gas of the upstream. The Mach number of the gas flow is $M = u_1/a_1$. The continuity of mass flow across the shock ($\rho_1 u_1 = \rho_2 u_2$), together with the kinetic theory of gases (the Rankine-Hugoniot conditions), gives (see details in [160])

$$\frac{u_1}{u_2} = \frac{\rho_2}{\rho_1} = \frac{(\gamma + 1)M^2}{(\gamma - 1)M^2 + 2} \tag{1.10}$$

where $\gamma (= c_p/c_v)$ is the ratio of specific heats of the gas. Taking $\gamma = \frac{5}{3}$ for a monatomic or fully ionized gas and $M \gg 1$ for a strong shock, we find $u_1/u_2 = 4$, which leads to a value $\mu = 2$. This mechanism shows excellent physical reasons why power-law energy spectra with a unique spectral index should occur in diverse astrophysical environments. In this simplest version of the theory, the only requirements are the presence of strong shock waves and that the velocity vectors of the high energy particles should be randomized on either side of the shock. It is entirely plausible that there are strong shocks in most sources, e.g., supernova remnants, active galactic nuclei.

However, there is a big problem to identify a source as origin of cosmic rays using the arrival direction of cosmic ray itself because a cosmic ray is deflected by galactic and intergalactic magnetic fields while traveling through the universe[2]. Therefore, it is hard to study cosmic rays with connections of specific targets just from observations of the cosmic rays themselves.

On the other hand, a neutral particle, like photon, can reach the Earth without deflection by magnetic fields. Taking advantage of the information from such energetic **photons**, we can get closer to the "accelerator" sources in the universe.

1.2 High energy photons

If one wants to locate the site of particle acceleration, the best suited neutral "messenger" particle is a high energy photon. While traveling through the universe, the trajectories of photons are not affected by magnetic fields, so they

- point to origin of their generation

---

[2]An arrival direction of the highest energy cosmic rays ($\gtrsim 10^{19}$ eV) is somewhat useful to identify its origin because the highest energy cosmic rays are deflected only by a few degrees [221].

- carry energy information about their generation process

- carry, as mass-less particles, time information

At low energies, photons can be generated also in thermal processes from stars and inter-stellar gas. The thermal continuum radiations are characterized by black-body spectra with temperatures extending up to $\sim 10^6$ K and various line emissions are associated with atoms and molecules in the material at the site. In the hottest objects, like accretion disk surrounding black-hole, thermal radiation can appear as X-rays up to few keV.

On the other hand, most photons in high energy regime ($> \text{GeV}$) are generated in non-thermal processes. The production of high energy photon is associated with phenomena that take place in the astronomical object, resulting in the observed γ-ray flux. The most important processes responsible for producing high energy photons are briefly explained in the following.

Synchrotron radiation

When a relativistic electron is bent in a magnetic field, it emits "synchrotron radiation". In a uniform magnetic field B, a relativistic charged particle moves in a spiral path at a constant pitch angle[3] θ by means of the Lorentz Force. During this motion, the charged particle is accelerated towards the guiding center of its orbit, and it loses energy by electromagnetic radiation (see details in e.g.,[163]).

The average (over an isotropic distribution of pitch angle) energy loss rate due to the synchrotron radiation is

$$-\frac{dE}{dt} = \frac{4}{3}\sigma_T c U_{mag} \gamma^2 \tag{1.11}$$

where $\sigma_T = 6.67 \times 10^{-25} [\text{cm}^{-2}]$ is the Thomson scattering cross section, $U_{mag} = B/8\pi$ is the energy density of the magnetic field and γ is the Lorentz factor of the relativistic particle (electron).

The maximum of the emission spectrum in fact had value $\nu_{max} = 0.29\nu_c$, where ν_c is called "critical frequency ($\nu_c = \frac{3}{4\pi}\frac{eB\sin\theta}{mc}\gamma^2$)". Therefore, the maximum value can be written as

$$\nu_{max} = 1.2 \times 10^6 \left(\frac{B_\perp}{\text{gauss}}\right) \gamma^2 \, [\text{Hz}] \tag{1.12}$$

For example, in the case of AGNs (see details Chapter 2), the synchrotron radiation from relativistic electrons is responsible for the emission between the radio and X-ray bands.

Generally, proton synchrotron radiation is an inefficient process. For the same energy of protons and electrons, $E_p = E_e = E$, the energy loss rate of protons (dE/dt) is $(m_p/m_e)^4 \approx 10^{13}$ times lower than the energy loss rate of electrons. Also, the critical frequency of the synchrotron radiation emitted by a proton is $(m_p/m_e)^3 \approx 6 \times 10^9$ times smaller than the critical frequency of synchrotron radiation emitted by an electron of the same energy. However, under certain conditions (e.g., above 10^{18} eV) the synchrotron cooling time of protons can be comparable or even shorter than other time scales that characterize the acceleration and confinement regions of relativistic protons [24].

---

[3]the angle between the velocity and the magnetic field

(a) in laboratory frame (S)   (b) in rest frame of   (c) in laboratory frame (S)
(before scattering)   electron (S^*)   (after scattering)
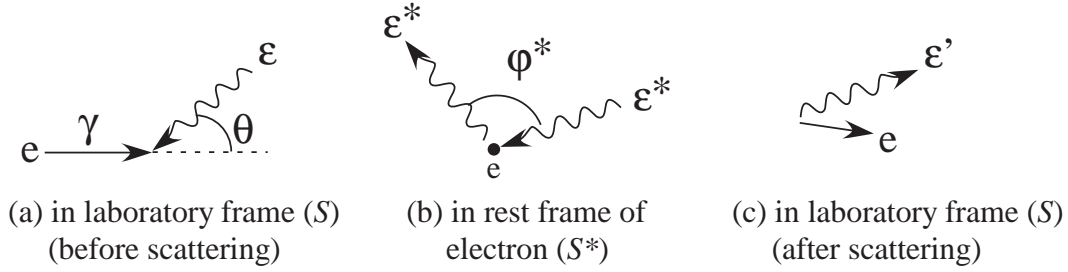
Figure 1.4: The geometry of inverse Compton scattering in the laboratory frame reference S and that in which the electron is rest S^*.

Inverse Compton scattering

High energy electrons may scatter low energy photons to high energy ($e + \epsilon \to \epsilon' + e : \epsilon' > \epsilon$) so that in the Compton interaction the photons now can gain energy. The process is called "inverse Compton (IC) scattering", though it is basically no different from Compton scattering. Many of the most important results can be worked out using simple arguments (see details in e.g.,[65]). Here, we briefly explain some of those arguments.

We consider a collision between a photon of energy ϵ and an electron with Lorentz factor γ (laboratory frame: S). The geometry of the scattering is described in Fig. 1.4. ϵ^*, the photon energy in rest frame of electron S^*, before scatting is

$$\epsilon^* = \gamma\epsilon(1 + \beta\cos\theta), \tag{1.13}$$

where θ is the angle between the incident electron and photon direction in S. If we assume that $\gamma\epsilon \ll mc^2$, then in S^* the energy of the photon remains same after the scattering and the Thomson scattering cross-section can be used. ϵ', the photon energy after scattering in S is described using the scattering angle of photon in rest frame of electron φ^* as

$$\epsilon' = \gamma\epsilon^*(1 + \beta\cos\varphi^*) = \gamma^2\epsilon(1 + \beta\cos\theta)(1 + \beta\cos\varphi^*). \tag{1.14}$$

Therefore, the maximum energy which the photon can acquire is

$$\epsilon'_{\text{max}} \sim 4\gamma^2\epsilon \tag{1.15}$$

corresponding to a head-on collision, and the average energy of the scattering photons is

$$\langle\epsilon'\rangle \sim \frac{4}{3}\gamma^2\epsilon. \tag{1.16}$$

Using the total energy density of the soft photon field U_{rad}, the energy incident on electron per unit time is $c\sigma_T U_{\text{rad}}$, so that the average total energy loss rate of the electron by the inverse-Compton scattering in this Thomson regime, is

$$-\frac{dE}{dt} = \frac{4}{3}\sigma_T c U_{\text{rad}} \gamma^2 \tag{1.17}$$

However, if $\gamma\epsilon$ is getting close to (even higher than) mc^2 ($\gamma\epsilon \gtrsim mc^2$), we must use the proper quantum relativistic cross section for scattering. The relevant total cross section can be derived by the Klein-Nishina formula [163]:

$$
\begin{aligned}
\sigma_{\text{K–N}} &= \frac{3}{8}\sigma_T \frac{1}{x}\left\{\left[1 - \frac{2(x+1)}{x^2}\right]\ln(2x+1) + \frac{1}{2} + \frac{4}{x} - \frac{1}{2(2x+1)^2}\right\} \\
&\rightarrow \frac{3}{8}\sigma_T \frac{1}{x}\left(\ln 2x + \frac{1}{2}\right) \quad \text{(ultrarelativistic limit: } x \gg 1)
\end{aligned}
\tag{1.18}
$$

with $x = \gamma\epsilon/(mc^2)$. Therefore, the cross section decreases roughly as ϵ^{-1} at the highest energy.

This process is particularly important in the production of high energy γ-ray in AGNs because the inverse-Compton scattering by relativistic electrons is able to produce GeV-TeV photons.

High energy protons can also interact with soft photons, but the energy loss rate of the protons by the inverse Compton scattering is suppressed by a factor of $(m_e/m_p)^4 \approx 10^{-13}$ and significantly lower than pair production losses [24].

π^0 decay

The interactions of high energy protons with ambient matter or radiation produce hadronic particles, mostly pions (πs). π^0 and $\pi^\pm$ are produced with the same probability, thus one third of the π-mesons produced are neutral. The π^0 produces two γ-rays,

$$
p + p \rightarrow \pi^0 + X \rightarrow \gamma\gamma + X
\tag{1.19}
$$

where X represents minor secondary particles. The minimum kinetic energy of a proton to produce a π^0 is

$$
E_{\text{th}} = 2m_\pi c^2\left(1 + \frac{m_\pi}{4m_p}\right) \approx 280\,\text{MeV}
\tag{1.20}
$$

where m_π is the mass of a π^0 (134.97 MeV).

The energy of the photons emitted by a π^0 at rest is $E_\gamma = \frac{1}{2}m_\pi c^2 \approx 67.5\,\text{MeV}$. If the π^0 is moving with velocity $v = \beta c$, the energy of the photons in the laboratory frame is:

$$
E_\gamma = \frac{1}{2}m_\pi c^2 \frac{1 + \beta\cos\theta_\gamma}{\sqrt{1 - \beta^2}}
\tag{1.21}
$$

with θ_γ being the angle between the direction of the photon with respect to the original π^0.

At the same time, charged pions are produced in proton-proton collisions. These charged pions subsequently decay into muons and electrons and corresponding (anti-) neutrinos. As an example the production and decay of a positive pion proceeds according to the following reaction chain:

$$
p + p \rightarrow \pi^+ + X \rightarrow \mu^+ + \nu_\mu + X \rightarrow e^+ + \nu_e + \bar{\nu}_\mu + \nu_\mu + X
\tag{1.22}
$$

The ν's spectra would be similar to the γ-ray spectrum from π_0 decay. The ν and γ-ray associated spectra would be the strongest indications of the site of the cosmic-ray (proton) accelerator.

1.3 Instruments for γ-ray observations

The launch of the Energetic Gamma-Ray Experiment Telescope (EGRET) for γ-rays between 20 MeV and 30 GeV on board of the Compton Gamma-Ray Observatory (CGRO) in 1990 opened up the γ-ray sky (see [219] for a review). EGRET discovered 271 sources [124], 101 of which could be associated with already known astronomical objects, while a large number (170) newly discovered and yet unidentified sources remain. A sky map of the EGRET sources can be seen in Fig. 1.5.

Since photon spectra in astronomical objects is associated with the cosmic-ray spectrum, the photon index is expected to be negative and the number of photons significantly decreases in the very high energy γ-ray band ("VHE γ-ray" defined as $E_\gamma > 50\,\text{GeV}$ in this thesis). It is, therefore, not reasonable anymore for satellites to search for the high energy band because of limitations in the instrument size. On the other hand, ground-based Cherenkov telescopes with their huge detection areas are well suited to observe photons in the VHE γ-ray regime. Thanks to the innovation of the "Imaging technique" for the Cherenkov telescopes, "Imaging Atmospheric Cerenkov Telescope (IACT)" are currently the most successful instruments for VHE γ-ray observations. Table 1.1 summarizes principle characteristics of the current operating and two historical IACTs. Until recently, before the "new generation" of IACTs (such as MAGIC, H.E.S.S. and VERITAS) became operative, the energy range from 30 GeV to 300 GeV was unexplored by any instruments.

Figure 1.5: Sky map of the third EGRET catalogue (above 100 MeV)

Table 1.1: Principle characteristics of current operating (and selected historical [last two]) Imaging Atmospheric Cherenkov Telescopes. The energy threshold given is the approximate trigger-level (rather than post-analysis) threshold for observations close to zenith.

Instrument	Lat. (°)	Long. (°)	Alt. (m)	num. Tels.	Tel. Area (m²)	Total A. (m²)	Pixels	FoV (°)	Thresh. (TeV)
MAGIC	29	18	2225	1	236	236	574	3.5	0.05
H.E.S.S. [133]	-23	16	1800	4	107	428	960	5	0.1
VERITAS [168]	32	-111	1275	4	106	424	499	3.5	0.1
CANGAROO-III [180]	-31	137	160	3	57.3	172	427	4	0.3
Whipple [248]	32	-111	2300	1	75	75	379	2.3	0.3
TACTIC [114]	25	78	1300	1	9.5	9.5	349	3.4	1.2
HEGRA [203]	29	18	2200	5	8.5	43	271	4.3	0.5
CAT [49]	42	2	1650	1	17.8	17.8	600	4.8	0.25
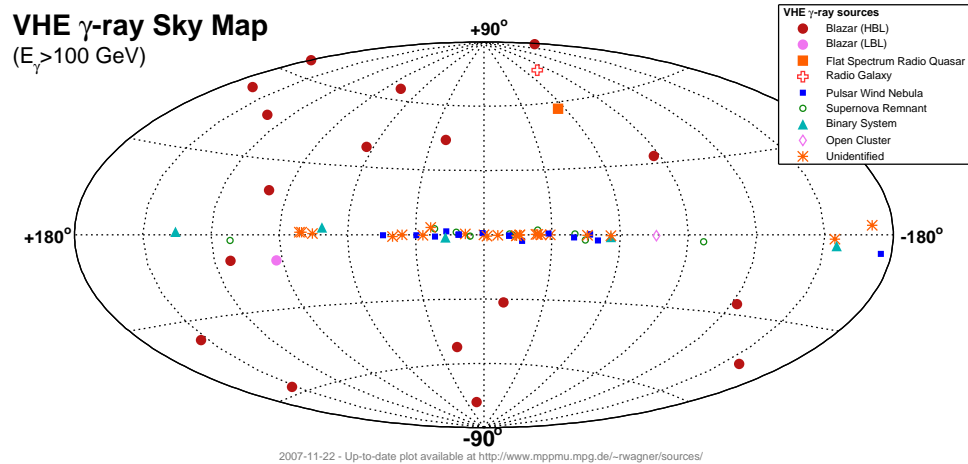
Figure 1.6: VHE γ-ray source sky map (in November 2007) [taken from http://www.mppmu.mpg.de/~rwagner/sources/]

1.4   Sources of VHE γ-rays

The first discovery of VHE γ-ray emission from a celestial object was achieved in 1989 by an IACT, "Whipple" (see Table 1.1), in their observations for the Crab Nebula [249]. The Crab Nebula is the brightest and stable point-like VHE γ-ray source. Therefore it is often referred to as the "standard candle" of VHE γ-ray observations and is commonly used for inter-calibration between different γ-ray instruments. In addition, this source is also useful to check the telescope performances and to verify analysis procedures as this thesis uses in Chapter 6.

In 1992, VHE γ-ray emission was discovered from Mkn421 [204] as the first extra-galactic VHE γ-ray source.

In 2003, just before those "new generation" of IACTs went into operation, only 12 sources were established as VHE γ-ray sources (see Table 1.2). Taking advantage of advanced techniques of the "new generation" of IACTs, we could obtain higher sensitivity and lower energy thresholds in the observations so that the number of VHE γ-ray sources have dramatically increased to 33 in 2005, and to 71 at present (in 2007). A current sky map of known VHE γ-ray sources is shown in Fig. 1.6. In the following, we will briefly highlight the most prominent astronomical sources in the VHE γ-ray band.

Table 1.2: Number of VHE γ-ray sources for each source class in 2003, 2005 and 2007 [132]

Source class	2003	2005	2007
Active galactic nucleus	7	11	19
Supernova remnant	2	3	7
Pulsar wind nebula	1	6	18
Binary system	0	2	4
Diffuse emission	0	2	2
Unidentified source	2	6	21
Total	12	33	71

1.4.1   Extra-galactic sources

Active galactic nucleus (AGN):   Supermassive black holes (SMBHs)[4] seem to in the cores of most galaxies. The fueling of SMBHs by infalling matter produces spectacular activity: In some galaxies, known as "active galactic nuclei (AGNs)", the nucleus produces more radiation than the entire rest of the galaxy. In $\sim$ 10% of all AGNs, the spin of the SMBH induces twisted magnetic field lines as jets at the poles of the rotating source. The jets of AGNs are considered to be one of the prime candidates for the acceleration of the highest energy cosmic rays (with $E > 10^{19}$ eV) (e.g., [228]).

If a relativistic jet is viewed at small angle to its axis the observed emission from the jet is amplified by relativistic beaming and dominates the observed emission. Such sources are called

---

[4]mass in the range $10^6 - 10^9 M_{\odot}$

blazars [240]. Currently (in 2007) 19 AGNs are well-established as VHE γ-ray sources (see Table 1.3). All but one[5] are classified as blazars.

Further explanations about AGNs are given in Chapter 2.

Table 1.3: Summary of the extra galactic VHE γ-ray sources in 2007

Source Name	Redshift	Spectral Index	Type[1]	Discovery (year[2])
M87	0.0044	2.9	FR I	HEGRA (2004) [11]
Mkn 421	0.031	2.2	HBL	Whipple (1992) [204]
Mkn 501	0.034	2.4	HBL	Whipple (1996) [205]
1ES 2344+514	0.044	2.9	HBL	Whipple (1998) [76]
Mkn 180	0.045	3.3	HBL	MAGIC (2006) [32]
1ES 1959+650	0.047	2.4	HBL	Tel. Array (1999) [187]
PKS 0548-322	0.069	n/a	HBL	H.E.S.S. (2007) [227]
BL Lacertae	0.069	3.6	LBL	MAGIC (2007) [37] (Chapter 7)
PKS 2005-489	0.071	4.0	HBL	H.E.S.S. (2005) [13]
PG 1553+113	>0.09	4.0	HBL	H.E.S.S./MAGIC (2006) [17, 38]
PKS 2155-304	0.116	3.3	HBL	Durham Mark 6 (1999) [79]
H 1426+428	0.129	3.3	HBL	Whipple (2002) [135]
1ES 0229+200	0.14	2.5	HBL	H.E.S.S. (2007) [21]
H 2356-309	0.165	3.1	HBL	H.E.S.S. (2006) [18]
1ES 1218+304	0.182	3.0	HBL	MAGIC (2006) [33]
1ES 1101-232	0.186	2.9	HBL	H.E.S.S. (2006) [18]
1ES 0347-121	0.188	3.1	HBL	H.E.S.S. (2007) [22]
1ES 1011+496	0.212	4.0	HBL	MAGIC (2007) [39]
3C279	0.536	4.1	FSRQ	MAGIC (2007) [238]

(1): explanations for the Types can be found in Chapter 2.

(2): the year of the corresponding paper published.

Gamma-ray burst (GRB):   These are the most energetic and violent short term phenomena in the universe. GRBs occur at cosmological distances. The mean distance of these objects has been recently measured to be Redshift (z)=2.8 with at least 7% of the GRBs originating at $z > 5$ [141]. The γ-ray emissions take place with very short time constant (from tens of milliseconds to few hundred seconds) the γ-ray emissions can be stronger (typically, 10^{51} to 10^{54}erg s^{-1}) than any other known γ-ray sources.

There is a currently accepted model that the basic mechanism of GRB emission is an expanding relativistic fireball (e.g., [210]), with the beamed radiation (Doppler beaming factor $\sim$ O(10^2)). In the fireball shock framework, several models have predicted VHE γ-ray emission.

MAGIC has observed some GRBs, including a observation just a few minutes after the emergence [40], but VHE γ-ray emission was not confirmed, yet.

---

[5]One is the FR-I galaxy, M87. But it is thought to be a "mis-aligned blazar".

1.4.2   Galactic sources

Supernova remnants (SNR):   A final stage of stellar evolution is reached when a star runs out of fuel necessary for the fusion reactions that counteract the gravitational pressure. If the star is heavy enough, a collapse of the stellar core is followed by the ejection of the outer shells of the stellar material. While depending on the mass of the remaining object, a neutron star or a black hole is formed, the ejected material forms a nebula, sweeping up interstellar material along its way. This expanding structure is called a "supernova remnant (SNR)".

SNRs have long been a prime candidate for the acceleration of the galactic cosmic-ray protons and nuclei. They have sufficient energy, with about 10% of the kinetic energy of an average supernova explosion are converted into relativistic particles (see e.g., [112]).

Pulsar and Pulsar wind nebula (PWN):   Pulsars are rapidly rotating neutron stars which are produced in a type II supernova explosion [250]. A pulsar wind nebula (PWN) is a nebula powered by the relativistic wind of an energetic pulsar. Young pulsar wind nebulae are often found inside the shells of supernova remnants.

The rotating strong magnetic filed of the neutron star produces strong and variable electric fields [117], where charged particles are accelerated to high energies. Due to the variable electric field, light charged particles (electrons and positrons) emit pulsed synchrotron radiation. Depending on the location of the acceleration region, so-called "polar cap" (e.g., [226]) and "outer gap" (e.g., [80]) models are distinguished. They predict γ-ray emission with a cut-off at a few GeV or a few tens of GeV, respectively.

Almost all pulsars have rotational periods that are steadily increasing with time. This "spin-down" corresponds to a loss of rotational kinetic energy in the range up to 10^{39} erg/s. At some distance from the pulsar, the pressure of the wind in eventually balanced by the external pressure, resulting in a strong stationary shock front, where charged particles can be accelerated to very high energy (see e.g.,[87]).

The prototype pulsar wind nebula is the Crab Nebula, which is the first VHE γ-ray source [249]. At present, PWN have emerged as the largest population of identified galactic VHE γ-ray sources (see Table 1.2).

Binary systems: Very massive stars can accrete matter from stars in orbit around them. They form so-called "binary systems", which can have different characteristics and evolutions depending on the involved objects. X-ray binary systems are composed of a compact object, such as a neutron star or a black hole and a companion star (blue giant or white dwarf or very massive stars but less compact).

In some binary systems, a central black hole produces relativistic jets and a companion is responsible for mass accretions. This class is also called "Microquasar", which comes from the observed morphological and physical similarities with quasars (a class of AGNs). The mass of a microquasar is about seven orders of magnitude lower than that of a quasar. They are interesting because the processes taking place in AGNs can be studied in a shorter time in microquasars, considered from many aspects as their scaled-down versions. Some known microquasars are considered as counterparts of unidentified EGRET sources. Recently, MAGIC and H.E.S.S.

have detected VHE γ-ray emission from a few of them (e.g., [19, 34]). They show variable VHE γ-ray emission, which is not confirmed among any other classes of galactic objects.

Unidentified sources: Most VHE γ-ray sources are predicted to emit X-ray and radio emission under current known models (e.g.,[6]. see also section 1.2), there are, however, some examples of VHE γ-ray sources which do not have a counterpart in lower-energy bands.

The first unidentified VHE γ-ray source is "TeV J2032+4130" [9], which was discovered by the HEGRA CT system. Several more unidentified VHE γ-ray sources were discovered recently during the H.E.S.S. Galactic Plane Survey program [14, 23] (see also Fig. 1.7). In each case, the source spectrum in the VHE γ-ray energy range can be characterized as a power-law with a differential spectral index in the range 2.0 to 2.5. The general characteristics of these sources –spectra, size, and position– are similar to previously identified galactic VHE γ-ray sources. Further multiwavelength study is required to understand the emission mechanisms powering them. A non-detection of longer-wavelength emission for some of these objects may be an indication that a new VHE γ-ray source class exists [14].

Diffuse emission: Particles (particularly protons and nuclei) with above GeV energies can readily propagate very large distances in the interstellar medium without significant energy losses. As a consequence the emission associated with these energy losses is often rather diffuse.

The MILAGRO collaboration have detected TeV emission along the plane with localised enhancements which have been identified as sources [139]. After subtraction of these sources the remaining emission roughly follows the distribution of target material in the galaxy and is identified as diffuse emission.

A localised measurement of diffuse emission has been made in the galactic center by H.E.S.S. [20]. This emission correlates with giant molecular clouds in the galactic center region and suggests an enhanced cosmic-ray spectrum from that region. This enhanced diffuse emission could originate from a succession of SNRs in the galactic center over the past 10^5 years [31].
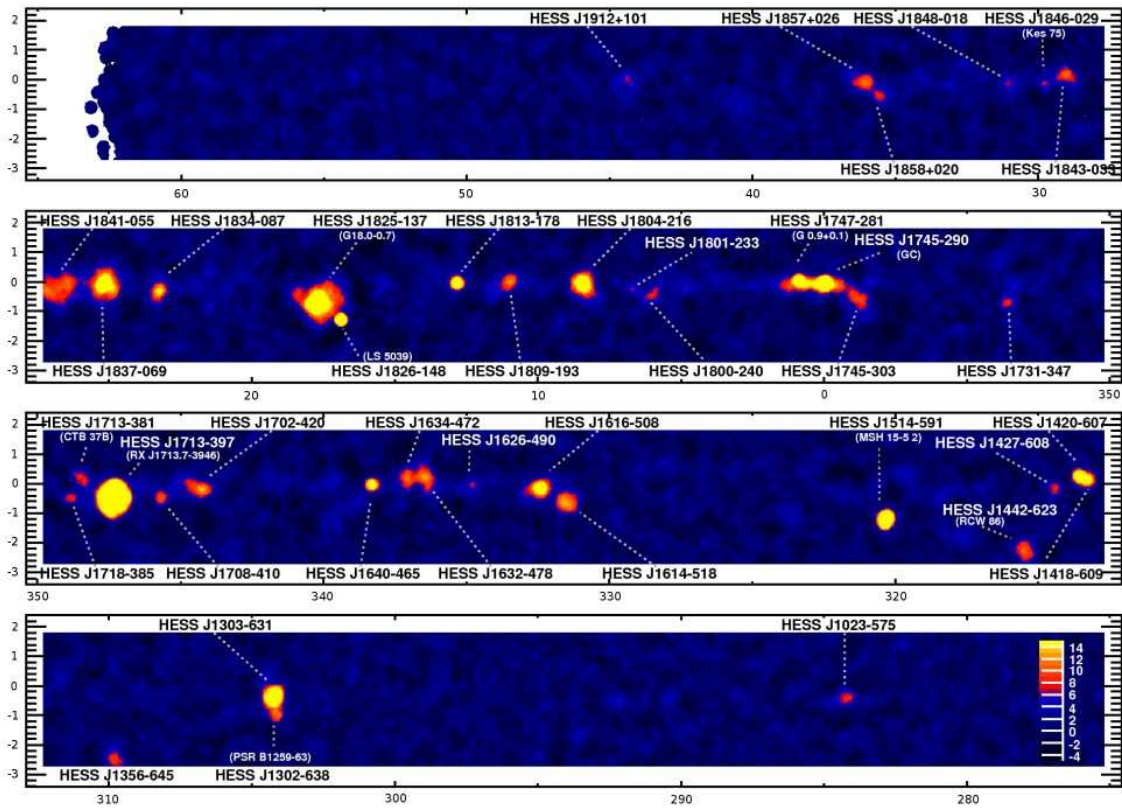
Figure 1.7: VHE γ-ray sky in Milky way (Galactic longitude $l = 60° \sim -85°$) as observed with H.E.S.S. telescope system. (taken from [132])

Chapter 2

Active Galactic Nuclei

A mysterious feature of *Active Galactic Nuclei* (AGN) is their very high luminosity in a very concentrated volume, probably through physical processes other than the nuclear powering the "normal" stars. AGNs are, therefore, special laboratories for extreme physics we would like to understand,

The first class of AGNs, the Seyfert galaxies, was discovered by Seyfert in the 1940s. They appeared to be spiral galaxies, but with a star-like nucleus showing broad and strong emission lines. Quasars, a subclass of AGNs with very high luminosity, were discovered in the early 1960s in radio surveys. The optical counterparts of some of the observed bright radio sources were star-like, and turned out to be the most distant sources among the known celestial objects at that time. The first quasar, 3C273, was detected by Maarten Schmidt in 1962 and is more than 1000 times more luminous than a normal galaxy like our own. Many AGNs have been found since then in a wide range of wavelengths, from radio to γ-ray (see review e.g., [146]). Depending on the observed features, AGNs have been classified into Seyfert galaxies, radio galaxies, quasars, blazars and others (see Table 2.1). Detailed descriptions of classes of AGNs can be found e.g., in [240]. The connection between these subclasses has been thoroughly investigated, but not yet completely understood.

In the "standard model" of AGNs [165], it is generally assumed that the energy source is an accretion of gas onto a super massive black hole ($10^6 - 10^9 M_\odot$) in the central region. A unified scheme has been proposed [240] which attributes the differences in the characteristics of the observed phenomena to the orientation of the source relative to our line of sight. Here I briefly describe this *unified model* of AGNs.

2.1   Unified model

The unified model of AGNs, explaining all the different subclass of AGNs shown in Fig. 2.1, has a spinning super massive black hole (SMBH) as its central power source. The SMBH is surrounded by matter that is accreting on the SMBH at the Schwarzschild radius. For instance, a $10^8 M_\odot$ SMBH would have a Schwarzschild radius of approximately 2 AU (10^{-5} pc). The area surrounding the Schwarzschild radius consists of extremely hot plasma accelerated by the intense
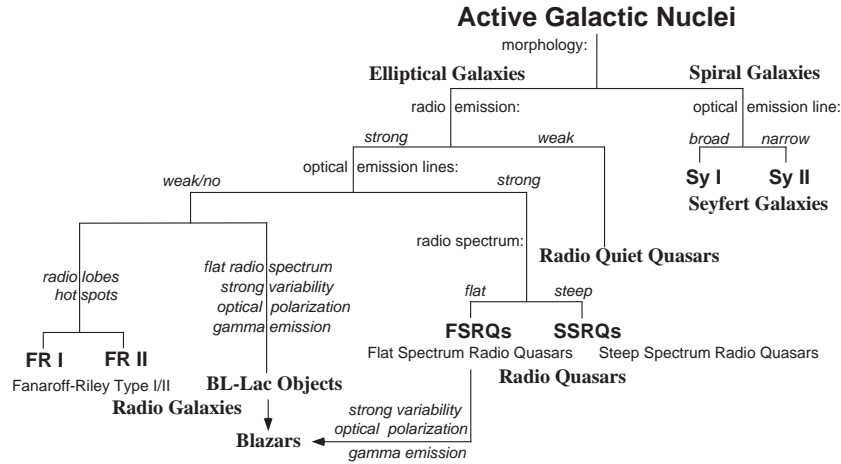
Figure 2.1: Classification of Active Galactic Nuclei (taken from [68])

gravitational field produced by the SMBH. The spin of the black hole induces twisted magnetic field lines as jets at the poles of the rotating source [62]. Particles can be accelerated by strong shock waves in the jets to ultra-relativistic energies.

The accretion disk produces a strong radiation in ultra-violet and optical wavelengths and creates a cloud of highly ionized gas up a radius of to approximately 10^{-2} pc that is the observed as a "broad emission line region (BLR)". This region is surrounded by a molecular torus that effectively shields the central AGN when viewed from the equatorial plane. Clouds of interstellar medium outside the molecular torus and within the polar cones are ionized by the radiation which flows from the central AGN and is not blocked by the torus. These clouds produce the "narrow emission line region (NLR)". Beyond this region, the radio jets may become prominent. The jets may extend up to 1 Mpc for the FR-II type, where lobes form as the jets interact with the inter-galactic material. A schematic drawing of the unified model can be seen in Fig. 2.2.

This model can be used to explain the observed features as being related to the viewing angle. A blazar is a polar view of an AGN. Narrow line radio galaxies and type-II of quasars or Seyfert galaxies are generally equatorial views, and broad line radio galaxies and type-I of quasars or Seyfert galaxies are intermediate views.

Blazars are the most "active" kind of AGNs. Due to the polar view of the jet, the bulk relativistic motion of the emitting plasma causes radiation to be beamed in a forward direction, making the variability appear more rapid and the luminosity appear higher than in the rest frame due to the relativistic beaming effect (e.g., [209, 108]). First, virtually every blazar exhibits superluminal motion of jet in high-resolution radio maps [242]. This motion is easily explained by relativistic bulk motion along the line-of sight. Second, radiation is highly polarized. Indeed, the classical definition of blazars as "optically violently variable AGN" turns out to be consistent with defining them by high polarization. Third, blazars are well matched with radio galaxies, which are known to have jets and are located closer to us in the universe. Their multiwavelength variability and polarization characteristics can be well explained by shocks in an aligned
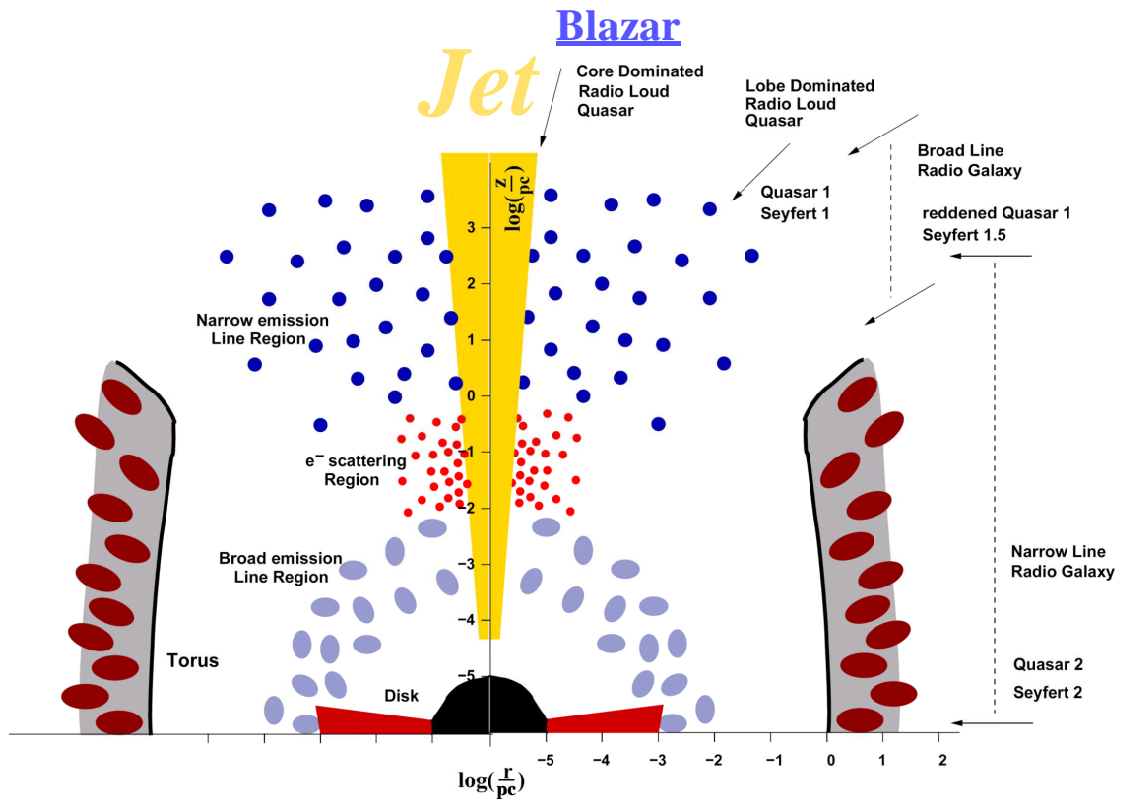
Figure 2.2: Schematic drawing of the unified model of AGNs. The classifications according to the viewing angle along with the different regions around the central black hole are illustrated. Note that the scales are logarithmic (taken from [59]).

relativistic jet.

The extreme characteristics of blazars were also found in high energy γ-ray observation. Blazars are the most dominant class among AGNs detected by EGRET [124]. The quasar 3C279, the first γ-ray blazar discovered by EGRET, was one of the brightest γ-ray sources in the sky at the time of its discovery [123]. In addition, it showed a fast daily variability. Other blazars also have shown similar rapid flaring at high energy γ-ray energies during the EGRET observations.

Moreover, at very high energy (VHE) γ-ray energies observed by ground based Cherenkov telescopes, variability with flux doubling times as short as minutes have been seen in Mkn501 [41] and PKS2155-334 [30].

The ultimate goal of blazar research is to learn how energy is extracted from the black hole. We are still at a very early stage, trying at this point simply to understand how much energy is involved and what is the physical state of the jets. Specifically, we are trying to measure the energy density of particles, magnetic fields, and radiation, as well as the velocity field of the jet. These parameters must be inferred since the observed radiation depends strongly on the intrinsic properties of the jet. In addition, even the most fundamental question –which particle is the origin of the high energy γ-ray emission (leptonic or hadronic)– is still under discussion.

Because the emission regions involved are probably only $10^{-8} - 10^{-5}$ arcsec, direct imaging of these regions is not possible with the current technologies. Instead, we infer the jet structure from variability time scales. The VHE γ-ray emission, which has shown the fastest (observed) variability, is likely to be associated with the physics of the innermost region in the jet.

To summarize, the following important scientific questions about blazars have arisen, which are not completely answered at this point. Therefore, this thesis addresses those questions.

- There are several sub-classes of blazars with distinct spectral characteristics.
  What is the physical origin of this difference? (cf. section 2.2)

- How is the γ-ray spectrum produced? (cf. section 2.3)
  Due to its fast variability, γ-ray emission may represent more fundamental physics - more directly related to the physics of the central black hole - than other low-energy emissions from broad emission line clouds or from an accretion disk.

2.2 Blazar sequence

Blazars can be divided into **Flat Spectrum Radio Quasars (FSRQs)** and **BL Lacertae Objects (BL Lacs)** (see Fig. 2.1). The main difference between the two blazar sub-classes is their emission line. Objects with only weak or complete absence of emission lines (equivalent width $< 5\,\text{Å}$) were classified as BL Lacs whereas FSRQs show significant optical emission lines.

Electromagnetic emission from this class of sources can be observed from radio up to VHE γ-rays, with their spectral energy distributions (SEDs) characterized by a two-bump structure. From the SED shape, BL Lacs are sub-divided into two types. When the lower peak is located in the sub-millimeter to optical band, the objects are classified as **"Low-frequency peaked BL Lacs (LBLs)"**, while in **"High-frequency peaked BL Lacs (HBLs)"** the lower peak is located at UV to X-ray energies [194, 100] (see also Fig. 2.3).

Fig. 2.3 shows the average SEDs (bolometric luminosity vs. emission frequency) of 126 blazar samples in total[1] (of which 33 were detected in γ-ray by EGRET) binned according to radio luminosity, irrespective of the original classification as BL Lac or FSRQ [100]. The resulting SEDs show remarkable features:

- As the bolometric luminosity decreases, the first bump moves its peak to progressively larger energies. It follows the "sequence" FSRQ→LBL→HBL.

- The peak frequency of the γ-ray (the higher energy peak) component correlates positively with the peak frequency of the lower energy one.

- The luminosity ratio of the high to the low frequency components increases with bolometric luminosity.

These features cannot be explained solely by the orientation effect of the jet, as argued in the "unified model" mentioned in the last section.

Based on leptonic origin scenarios for photon spectra (see details in the next section), Ghisellini et al. (2002) [107] found that these features in SEDs translated into an (anti-) correlation between the energy of particles at the spectral peaks and the energy density in radiation (U_r) and magnetic (U_B) fields. Fig. 2.4 shows this correlation plot, which has been recently updated by Celotti and Ghisellini (2007) [78] including newly discovered VHE γ-ray (TeV) sources.

An evolutionary scenario has been proposed to explain a physical connection between different blazar subclasses in terms of reducing the black hole accretion power with time [69, 77]. In that scenario, the decline of accretion power could be due to a combination of a decreasing accretion rate and an increasing black hole mass. In view of limitations to power directly extractable from a rotating black hole, disks with high accretion power can produce the huge thermal and non-thermal output featured by many FSRQs. On the other hand, for lower accretion power, we also expect lower particle densities in the acceleration region and less effectively screened electric fields. Under these conditions, the output luminosity is moderate but electrons can be accelerated to higher energies [77].

In addition, as the accretion power declines with time, gas and dust are getting less available for reprocessing accretion-disk radiation. That radiation leads to the observed strong optical emission lines in the broad emission line region, and to a high energy density of the external soft-photon field in the jet [69]. In fact, many previous studies which applied emission models for the observed SEDs have indicated that the contributions of the external soft-photon to the γ-ray spectra become less along the sequence FSRQ $\rightarrow$ LBL $\rightarrow$ HBL (e.g., [109]).

Therefore, the blazar sequence can be related to the evolutionary sequence FSRQ $\rightarrow$ LBL $\rightarrow$ HBL. Following the scenario outlined by Sanders et al. (1988) [217], the earlier stage of blazar evolution would comprise merging galaxies, infrared luminous galaxies, and radio-quiet quasars.

There are, however, some contradicting arguments specifying that the blazar sequence is merely caused by selection biases of the samples [191]. In fact, BL Lacs with low peak energy of the first bump and low luminosity, which were not found in the original study, have turned

---

[1]these blazars were selected from X-ray of the *Einstein* Slew survey [197], the 1-Jy sample at radio 5 GHz [224] and the 2-Jy sample radio 2.7 GHz [246].
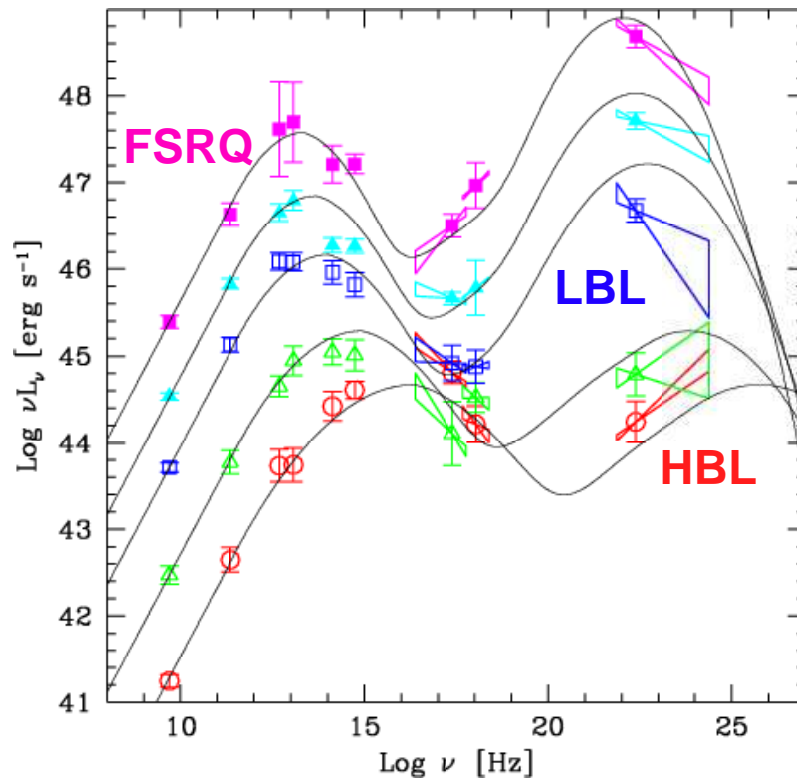
Figure 2.3: The average SED of the blazars studied by Fossati et al (1998) [100], including the average values of the hard X-ray spectra [91]. The data were not taken simultaneously. The lines shown are based on an SSC model (for the model, see section 2.3.1)
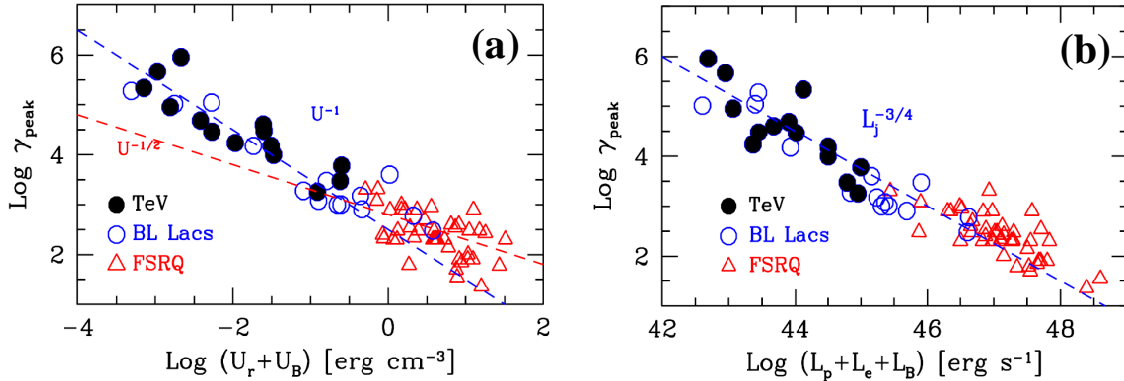
Figure 2.4: (a): The Lorentz factor γ_{peak} of leptons responsible for the emission peaks as a function of the comoving energy density $U\,(=U_r+U_B)$. The dashed lines corresponding to $\gamma_{\mathrm{peak}} \propto U^{-1}$ and $\gamma_{\mathrm{peak}} \propto U^{-1/2}$ are to guide the eye, and not a formal fit. (b): Dependence of γ_{peak} on the total jet power L_j, which is the sum of powers of proton (L_p), lepton (L_e) and magnetic field (L_B). Again, the dashed line $\gamma_{\mathrm{peak}} \propto L_j^{-3/4}$ is to guide the eye, and not a formal fit.

up in some results of recent deep-survey observations in the radio and X-ray bands [183, 192, 193]. However, a candidate for a FSRQ which has as high luminosity as other FSRQs, and is comparable in peak energy of the first bump to HBLs, has not been found yet. Observations with VHE γ-rays for all types of blazars are therefore especially interesting for this topic.

2.3 Emission models

In general, two types of emission models have been considered for blazars. One is based on the acceleration of electrons, the so-called "leptonic origin scenario" (see e.g., [110, 220]), the other is originated from emission by the acceleration of hadrons (protons), the so-called "hadronic origin scenario" (see e.g., [169, 181]).

At present, the measured SEDs of blazars can be successfully explained by the leptonic origin scenarios"(e.g., [109, 78]). If the observed VHE γ-rays are found to be originating from the hadronic scenarios, that result would be a proof of the source of cosmic rays. However, it is still difficult to disentangle the hadronic VHE γ-ray component from the leptonic one produced by inverse-Compton scattering using current available observation data. No observational result has confirmed the hadronic origin scenario, yet. In this section, the two emission origin scenarios are briefly described.

2.3.1 Leptonic origin scenarios

In leptonic origin scenarios, the lower-energy bump in the SED is most likely produced by synchrotron radiation of relativistic electrons in a magnetic field, while inverse-Compton (IC) scat-

tering by the same electrons is believed to be responsible for the high-energy bump in the γ-ray spectrum.

Synchrotron radiation spectrum

For the synchrotron spectrum by isotropic distribution of electrons in a homogeneous, randomly oriented magnetic field B, the emissivity j_ν as a function of frequency ν can be defined using the electron distribution $N(\gamma)$, where γ is the Lorentz factor of the electrons [140]

$$j_\nu = c_2 B \int_{\gamma_{\min}}^{\gamma_{\max}} \mathrm{d}\gamma N(\gamma) F\left(\frac{\nu}{c_1 B \gamma^2}\right). \tag{2.1}$$

$F(x)$ is the function

$$F(x) \equiv x \int_x^\infty K_{5/3}(\xi)\mathrm{d}\xi, \tag{2.2}$$

where $K_{5/3}$ is modified Bessel function of order $5/3$, and here

$$c_1 = \frac{3e}{4\pi m_e c}, \quad c_2 = \frac{\sqrt{3}e^3}{4\pi m_e c}, \quad c_3 = \frac{\sqrt{3}e^3}{8\pi m_e^2 c} \tag{2.3}$$

are defined as constants with mass of the electron m and electric charge of the electron e.

Absorption of the generated synchrotron radiation can occur at a sufficiently low frequency because the brightness temperature of the radiation may approach the kinetic temperature of the radiation in such a frequency range. This is known as *synchrotron self-absorption*. The absorption coefficient is [140]:

$$\alpha_\nu = -c_3 B \frac{1}{\nu^2} \int_{\gamma_{\min}}^{\gamma_{\max}} \mathrm{d}\gamma \gamma^2 \frac{\partial}{\partial \gamma}\left[\frac{N(\gamma)}{\gamma^2}\right] F\left(\frac{\nu}{c_1 B \gamma^2}\right). \tag{2.4}$$

Finally, the overall synchrotron emission spectrum can be represented by the radiative transfer equation using a length of the emission region l

$$I_\nu = \frac{j_\nu}{\alpha_\nu}(1 - e^{-\alpha_\nu l}). \tag{2.5}$$

When the electron distribution can be denoted by a power-law $N(\gamma) = K\gamma^{-n}\mathrm{d}\gamma$, the synchrotron emission spectrum can be expressed by (see e.g., [163])

$$I_\nu \propto \begin{cases} \nu^{-(n-1)/2} & \alpha_\nu l \ll 1. \\ \nu^{5/2} & \alpha_\nu l \gg 1. \end{cases} \tag{2.6}$$

Inverse Compton spectrum

For calculating the inverse Compton (IC) spectrum, we employ the formula derived by Jone (1968) [142]. It is accurate in all soft (target) photon energy ranges (i.e., both the Thomson and Klein-Nishina regimes) as long as the photon and electron distributions are isotropic, and the electrons are ultrarelativistic ($\gamma \gg 1$). The electron energy is denoted by $\gamma m_e c^2$, the soft photon energy by $\epsilon_0 m_e c^2$, and the scattered high energy photon by $\epsilon m_e c^2$. The differential photon production rate $q(\epsilon)$ (number of photons of energy ϵ produced per energy interval per unit volume per unit time) will be a convolution over the electron and soft photon distributions,

$$q(\epsilon) = \int d\epsilon_0 n(\epsilon_0) \int d\gamma N(\gamma) C(\epsilon, \gamma, \epsilon_0), \qquad (2.7)$$

where $n(\epsilon_0)$ is the number density of soft photons per energy interval and $N(\gamma)$ is the electron distribution. The Compton kernel $C(\epsilon, \gamma, \epsilon_0)$ given by Jones (1968) [142] is

$$C(\epsilon, \gamma, \epsilon_0) = \frac{2\pi r_e^2 c}{\gamma \epsilon_0} \left[2\kappa \ln \kappa + (1 + 2\kappa)(1 - \kappa) + \frac{(4\epsilon_0 \gamma \kappa)^2}{2(1 + 4\epsilon_0 \gamma \kappa)}(1 - \kappa) \right], \qquad (2.8)$$

where

$$\kappa = \frac{\epsilon}{4\epsilon_0 \gamma (\gamma - \epsilon)}. \qquad (2.9)$$

For given ϵ_0 and γ, the allowed kinematic energy range for ϵ is

$$\epsilon_0 \leq \epsilon < \gamma \frac{4\epsilon_0 \gamma}{1 + 4\epsilon_0 \gamma}. \qquad (2.10)$$

For a power-law ($N(\gamma) = K\gamma^{-n} d\gamma$) electron spectrum, $dN/d\epsilon$, the resulting γ-ray spectrum in the non-relativistic regime ($a = 4\epsilon\epsilon_0 \ll 1$) has a power-law form with a photon index $\alpha = (n+1)/2$ [112]. In the ultrarelativistic ($a \gg 1$) regime the γ-ray spectrum is noticeably steeper, $dN/d\epsilon \propto \epsilon^{-\alpha}(\ln a + \text{const})$ with $\alpha = (n+1)$ [65]. Several useful analytical approximations for the γ-ray spectra over a broad energy interval, including these two regimes and the Klein-Nishina transition region ($a \sim 1$), can also be found in [25, 84].

Depending on the target photons for IC scattering, the model can be divided into two types: (1) The target photon is the synchrotron photon produced by the same electron population (**Synchrotron self-Compton (SSC)** scattering), (2) The target photon is an external photon either from the broad-line emission region or from the accretion disc[2] (**External inverse Compton (EC)** scattering).

The observed correlations of the X-ray and VHE γ-ray fluxes during large flares of VHE γ-ray emitting blazars [171, 231, 155] provide experimental evidence for the SSC mechanism. The SSC model is widely accepted for describing VHE γ-ray emission of HBL objects. One the

---

[2]Generally, the average energies of the external photons as measured in the local stationary frame can be ~ 10 eV (UV region) for the photons from the broad-line emission region, or ~ 0.4 eV (near-infrared region) for the photons from the accretion disc [220].

other hand, an EC component is generally required to explain high-luminous γ-ray emission in LBLs and FSRQs.

In this thesis, we discuss observed SEDs including VHE γ-ray emission by means of the SSC model. The concept of the model is described in the following. The model codes were developed by Tavacchio et al. [234, 235].

Synchrotron self-Compton model

One of the simplest models, the one-zone homogeneous SSC model, assumes that the soft photons of IC scattering are the synchrotron photons in the same emission region within the jet. The emission region has a characteristic size R, moving at relativistic speed $\beta = v/c$. Both relativistic electrons and photons are isotropic in the source frame. The observed radiation is strongly affected by relativistic beaming effects. The key parameter is the Doppler beaming factor $\delta = [\Gamma(1 - \beta\cos\theta)]^{-1}$, where Γ is the bulk Lorentz factor of the emission region in the jet and θ is the angle between the line of sight and the direction of the relativistic jet. When the observer lies with the angle of $\theta \sim 1/\Gamma$, then $\delta \sim \Gamma$. Since θ is sufficiently small for blazars, $\theta \sim 1/\Gamma$ is assumed throughout this thesis.

The observed spectral shape requires that the relativistic electron spectrum steepens at high energies. This behavior is approximated with a broken power-law with indices n_1 and n_2, below and above the "break" energy $\gamma_b m_e c^2$, respectively. This particular form for the electron spectrum has been assumed on a phenomenological basis in order to describe the curved shape of the SED. In some other models, the electron energy distribution function is determined from a kinetic equation (e.g., [109, 147]). In that case, assuming the standard hypothesis of a power-law injection and subsequent cooling and escape in a homogenous region, the electron spectrum can be characterized by a broken-power law but a spectral change of $\Delta n(= n_1 - n_2) = 1$ is expected by synchrotron or inverse Compton cooling effects. On the other hand, for some blazars the spectral changes in their observed SEDs appears to be larger than $\Delta n = 1$. This might suggest a more complex situation [60, 234]. Throughout the works in this thesis we use the Hubble constant $H_0 = 70$ km/s/Mpc, $\Omega_\Lambda = 0.70$, $\Omega_M = 0.30$ for the calculation of source luminosity distance.

With these approximations, we can completely specify the model using the following parameters:

- the emission region size: R [cm]

- the minimum Lorentz factor of the electrons: γ_{min}

- the Lorentz factor of the electrons at the break: γ_b

- the maximums Lorentz factor of the electrons: γ_{max}

- electron spectral slope before the break: n_1

- electron spectral slope after the break: n_2

- normalization factor of the electron density: K [cm^{-3}]

- the magnetic field intensity: B [G]

- the Doppler beaming factor: δ

The model is not sensitive to the exact value of $\gamma_{\min}$, here we assume $\gamma_{\min} = 1$ in this thesis, and then the model has 8 free parameters.

The available data on the SED can be used to derive 7 "observable" quantities which are of particular relevance for the above model:

- Photon index of synchrotron radiation before the break: α_1

- Photon index of synchrotron radiation after the break: α_2

- The frequency of the synchrotron at peak: $\nu_{s,b}$

- The frequency of the synchrotron at high-energy cut off: $\nu_{s,\max}$

- The frequency of IC peak: ν_c.

- The total measured energy flux for the synchrotron component: l_s

- The total measured energy flux for the IC component: l_c

As shown in Fig. 2.5, the synchrotron frequencies from a single electron of Lorentz factor γ_b at break energy or $\gamma_{\max}$ at maximum energy can be characterized by [147]

$$\nu_{s,b/\max} = 1.2 \times 10^6 B \gamma_{b/\max}^2 \frac{\delta}{1+z}. \tag{2.11}$$

The peak value of the observed SSC energy in the Klein-Nishina regime is

$$h\nu_c = C\gamma_b m_e c^2 \frac{\delta}{1+z}, \tag{2.12}$$

where $C < 1$ is a constant representing the uncertainty of the Klein-Nishina effect.
The third relation is obtained from the ratio of the synchrotron luminosity to the Compton luminosity (see [144]):

$$u_B = \frac{d_L^2}{R^2 c \delta^4} \frac{l_s^2}{l_c}, \tag{2.13}$$

where d_L^2 is the luminosity distance and u_B is the energy density of magnetic field ($u_B = B^2/8\pi$). We recall that the one-zone homogeneous model is self-absorbed at radio frequencies and cannot explain the radio emission, which implies further contributions from the outer regions of the jet.

One more observable quantity can be provided by the minimum timescale of variation, t_{var}, which can be directly connected to the source dimension, R, through the causality relation $R \lesssim ct_{\text{var}}\delta$.

In most cases, these "observable" quantities are rather uncertain because it is not easy to complete such a broad-band SED by observational data which are ideally taken at the same

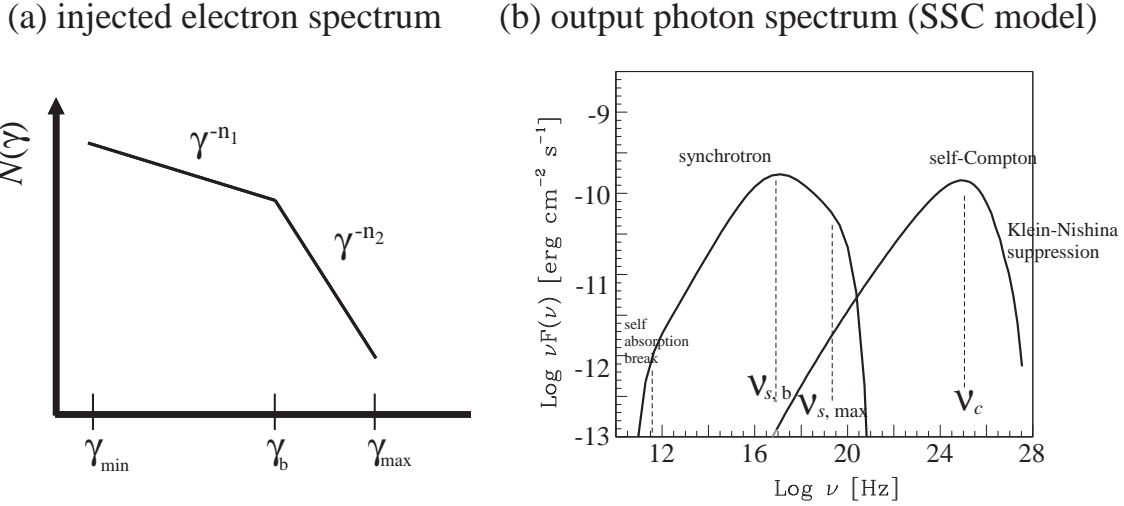(a) injected electron spectrum   (b) output photon spectrum (SSC model)

Figure 2.5: An example of the SSC model. (a): an injected electron spectrum with a simple broken power-law. (b) an output photon spectrum based on the one-zone SSC model using the electron spectrum with a broken power-law distribution. Characteristic features (spectral peaks/breaks) are indicated in the plot. This spectrum was produced using following values. $R = 2 \times 10^{15}$ [cm], $n_1 = 2$, $n_2 = 3.6$, $\gamma_{min} = 1$, $\gamma_b = 5 \times 10^4$, $\gamma_{max} = 2 \times 10^6$, $B = 0.3$ [G], $K = 5 \times 10^4$ [cm^{-3}], $\delta = 20$, $z = 0.034$.

epoch. In practice, they are often inferred from observations obtained at different epochs and with incomplete frequency coverage. It is also possible, by means of hypotheses based on physics processes, to constrain allowed ranges of the SSC parameters by analytical formula (e.g., [234, 54]).

In Fig. 2.6, we demonstrate behaviors of the output photon spectrum from the one-zone SSC model (hereafter, called "SSC spectrum") using the codes developed by Tavecchio et al. [234, 235]. First, we set a "reference" SSC spectrum with nominal values (see e.g., [166, 235] and also Chapter 11) at: $R = 2 \times 10^{15}$ [cm], $n_1 = 2$, $n_2 = 3.6$, $\gamma_{min} = 1$, $\gamma_b = 5 \times 10^4$, $\gamma_{max} = 2 \times 10^6$, $B = 0.3$ [G], $K = 5 \times 10^4$ [cm^{-3}], $\delta = 20$ and $d_L = 147.6$ [Mpc] $(z = 0.034)$. Next, we changed each parameter of (a) γ_b, (b) B, (c) K, (d) δ separately with five steps to demonstrate how each parameter contributes to the evolution of the SSC spectrum. As one can see in Fig. 2.6, the SSC spectrum showed some characteristic changes depending on the parameters. Briefly, as each parameter value increases; (a) The peak positions of both components move towards higher energies (cf. Eq. 2.11 and 2.12). Low energy bands (ratio to optical bands) below the synchrotron peak remain unchanged. (b) The overall flux in SED increases. The flux of the synchrotron component increases more than the other because the magnetic field is directly related to the synchrotron radiation process. In addition, the synchrotron peak is slightly shifting to higher energy (cf. Eq. 2.1 and 2.11). (c) The overall flux in SED increases. The IC component changes more because not only the electron density but also the soft-photon density for the IC scattering increases (roughly, $l_s \propto K$, $l_c \propto K^2$). (d) The relativistic beaming effect contributes equally to

both components because it is independent from radiation processes.

Comparing the observed source SEDs taken in different states of source activity, we can specify the contribution of each parameter to the spectral evolution, which could represent the physical conditions in the jet.

There are other types of SSC models. For example, some models are developed using parameters with time dependence (e.g., [173, 153]). These models can be used to describe flare states which show a fast variability. There are also two-zone models, which assume e.g., a fast jet spine and a slower surrounding sheath (e.g., [111]). Such models can explain more complex structures in SEDs and wider varieties of correlations between different energy bands.

Finally, Fig. 2.7 shows some previous studies of leptonic models which were applied to observational data. (a) Mkn 501 using a one-zone SSC model [235]. (b) BL Lacertae using SSC and EC models [167]. As can be seen in (b), when both soft-photon populations (synchrotron and external photons) contribute to the IC emission (SSC+EC), the overall IC component may have a double local-peak structure.
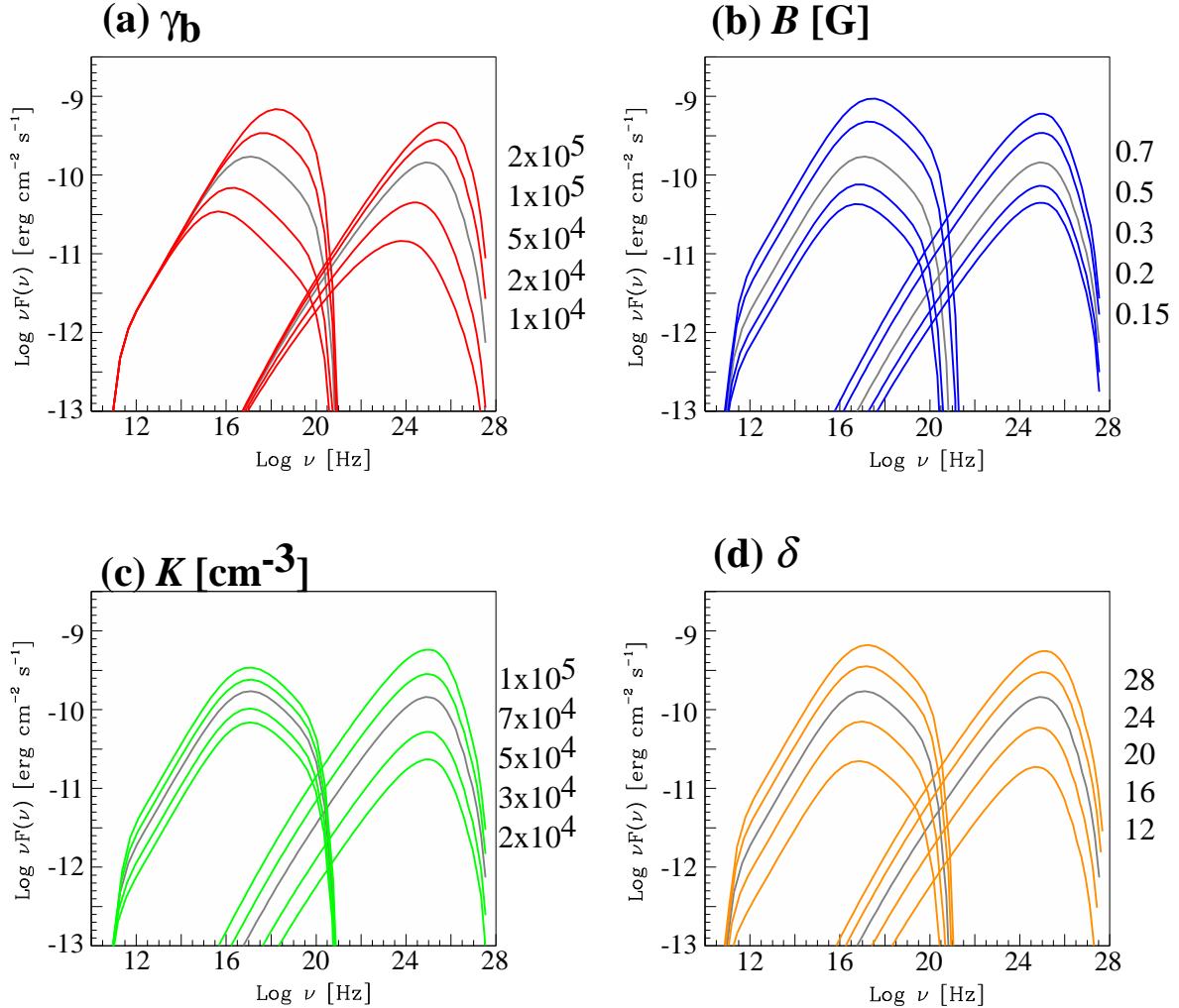
Figure 2.6: Overall photon spectra by the SSC model as functions of the input parameters. A reference spectrum, denoted by a grey curve in all plots, was produced with $R = 2 \times 10^{15}$ [cm], $n_1 = 2$, $n_2 = 3.6$, $\gamma_{min} = 1$, $\gamma_b = 5 \times 10^4$, $\gamma_{max} = 2 \times 10^6$, $B = 0.3$ [G], $K = 5 \times 10^4$ [cm^{-3}], $\delta = 20$, $z = 0.034$. In each plot, a parameter was changed in five steps. The values used are indicated on the right side of each plot. (a) electron Lorentz factor at peak energy γ_b ($1 \times 10^4 \rightarrow 2 \times 10^5$). (b) magnetic field strength B [G] ($0.15 \rightarrow 0.7$). (c) electron density parameter K [cm^{-3}] ($2 \times 10^4 \rightarrow 1 \times 10^5$). (d) Doppler beaming factor δ ($12 \rightarrow 28$).
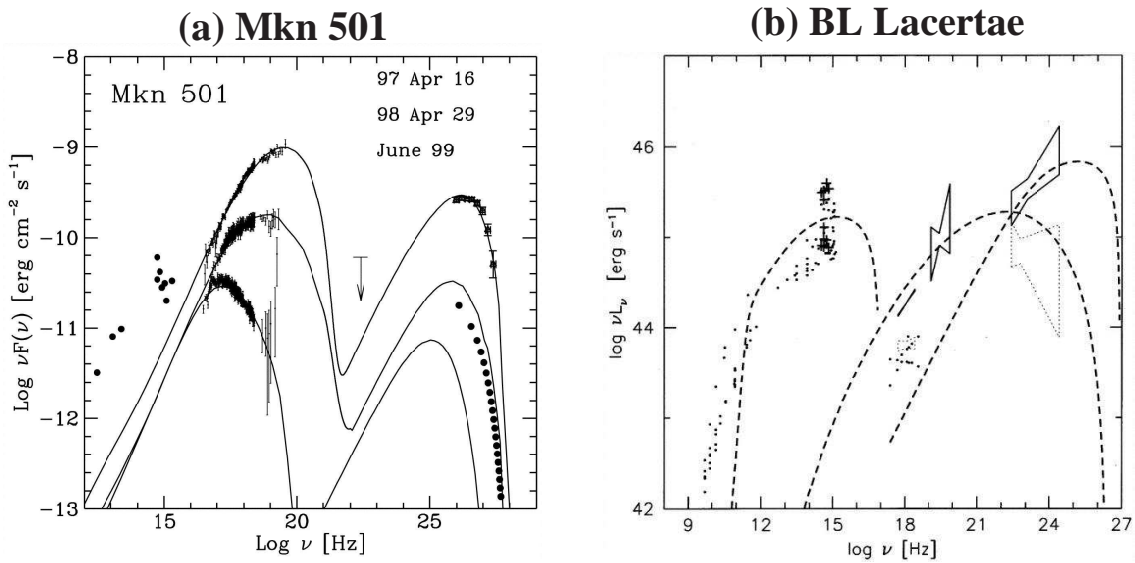
(a) Mkn 501

(b) BL Lacertae

Figure 2.7: Leptonic origin models with observed SEDs. (a) Overall SED of Mkn 501 of April 16, 1997, April 29, 1998, and June 1999. The solid line is the spectrum calculated with the homogeneous SSC model (taken from [235]). For all states: $R = 1.9 \times 10^{15}$ [cm], $n_1 = 1.5$, $\gamma_{\min} = 1$, $\gamma_{\max} = 1 \times 10^7$, $B = 0.32$ [G], $\delta = 10$. For each state: (1997 April 16/ 1998 April 29/ June 1999) $n_2 = 3/3.3/4.3$, $\gamma_b = 7 \times 10^5/3 \times 10^5/1.06 \times 10^5$, $K = 1 \times 10^3/3 \times 10^2/3.5 \times 10^2$ [cm^{-3}]. (b) Overall SED of BL Lacertae in July 1997 (taken from [167]). The dashed lines show the theoretical model, which includes three components: the synchrotron component dominating in the radio-to-UV range, the synchrotron self-Compton (SSC) component in the X-ray range, and the external Compton (EC) component dominating in the MeV-GeV range.

2.3.2   Hadronic origin scenarios

The hadronic models assume that a high energy protonic component contributes to the high-energy bump, while the low-energy bump is explained by synchrotron radiation of co-accelerated electrons. The energy of relativistic protons can be converted into high energy radiation via the following processes: (1) direct synchrotron radiation of protons, (2) photomeson production ($p+\gamma \rightarrow p+k\pi$), and (3) nuclear collisions ($p+p \rightarrow \pi+X$). The first two processes are known to be very inefficient, and they can become important in AGN jets only for proton energies $\geq 10^8 - 10^{10}$ GeV. Only for such high energies can the time scales of the proton energy losses become comparable to or shorter than the propagation time scale of the AGN jets. Energy losses of such energetic protons are dominated by photomeson production, and this process was used for explaining γ-ray production in blazars by the so-called the proton-induced cascade model [170].

In that model, the radiation target for photomeson production is dominated by near/mid-infrared radiation. In blazars, such radiation is provided by hot dust at distances of $\sim 1-10$ pc from the central sources and/or by synchrotron radiation due to relativistic electrons in the jet. The main outputs of the photomeson process are pions. The pions take about 1/3 of the protons' energy and convert it to photons, neutrinos, and through muons, to electrons and positrons. The photons injected by neutral pions are immediately absorbed by soft photons in the pair production process. Most of this radiation is so energetic that it produces two more generations of photons and pairs. The final output of this synchrotron-supported pair cascade is the high energy component, enclosed within or cut off at energies above which photons are absorbed by a $\gamma\gamma$-pair production process. This maximum energy can be ~ 30 GeV in FSRQs, as determined by external UV radiation, and ~ 1 TeV in BL Lac objects, as determined by infrared radiation of dust [202].

Much less extreme proton energies are required in models based on the assumption that the proton energy losses are dominated by collisions with the ambient gas. The final output of these collisions is the same as in the photomeson process, i.e., relativistic electrons/positrons, photons and neutrinos. The process can be efficient only if the column density of the target is $n_H \geq 10^{26}$ cm^{-2}. Bednarek (1993) [53] proposed as a target the funnels formed around the black hole by a geometrically thick disk, while Dar and Laor (1997) [86] suggested interactions of jet with cloud and/or stellar winds. The disadvantage of such models is that relativistic protons, before colliding with the nuclei, may easily suffer deflections by magnetic fields; this generally results in a lack of collimation of the radiation.

In the case the γ-ray radiation is of hadronic origin, one also expects to detect VHE neutrinos, but at least km-square sized detectors are needed, like "ICE CUBE" project [201]. The detection of neutrinos would clearly favour this model. One of the biggest problems of the hadronic models is that the acceleration and cool-down processes involved are rather slow, while flux variations in AGNs have been observed during very short time spans (typically, from a few minutes to a day [41, 30]).

2.4   Gamma-ray absorption by Extra-galactic background light

It is well known that the universe is filled by the "Cosmic microwave background radiation (CMB)". Additionally, the universe is filled by diffuse light, which is called "Extra-galactic background light (EBL)". It is the integrated photon flux from all extra-galactic sources, including those which are not detected individually. Assuming that the universe should appear homogeneous and isotropic to a typical observer ("Cosmological principle"), the EBL is expected to have a uniform mean level on large angular scales over the sky.

When traversing cosmic distances, the high-energy photons can be absorbed by the EBL via process of $\gamma + \gamma \rightarrow e^+ + e^-$ (photon-photon pair production). It is, therefore, important to take into account this effect for measured spectra in the VHE γ-ray band in order to study intrinsic source spectra.

The photon-photon pair production has a kinematic threshold given by

$$E\epsilon(1-\cos\theta) \geq 2(m_e c^2)^2 \tag{2.14}$$

where E and ϵ are the high and low energies of the two photons, and θ is the collision angle. Following [118, 241], the total cross section $\sigma_{\gamma\gamma}$ is

$$\sigma_{\gamma\gamma} = \frac{3}{8}\sigma_T s(q), \tag{2.15}$$

$$s(q) = q\left[\left(1+q-\frac{q^2}{2}\right)\ln\frac{1+\sqrt{1-q}}{1-\sqrt{1+q}} - (1+q)\sqrt{1-q}\right], \tag{2.16}$$

$$q = \frac{(m_e c^2)^2}{E\epsilon}\frac{2}{1-\cos\theta} \tag{2.17}$$

where σ_T is the Thomson cross section. The function $s(q)$, shown in Fig. 2.8, reaches its maximum at $q = 0.508$. For a *head-on* collision ($\theta = \pi$) the peak of the interaction cross section of a γ-ray of energy $E \sim 1$ TeV corresponds to pair production with a soft photon energy $\epsilon \sim 0.5$ eV. Therefore, the wavelength (λ) of the soft photon at the peak cross section can be written as

$$\lambda = 2.41\mu\text{m}\frac{E}{\text{TeV}} \tag{2.18}$$

It is necessary to calculate the absorption probability of the high energy photon per unit path length $d\tau_{\gamma\gamma}/dl$, where $\tau_{\gamma\gamma}$ is the absorption "optical depth" for photons of energy E traversing an isotropic diffuse radiation with spectral density $dn(\epsilon)/d\epsilon$. With an integration over θ, the absorption probability is given by

$$\frac{d\tau_{\gamma\gamma}}{dl} = \frac{3}{8}\sigma_T\int_{\frac{(m_e c^2)^2}{E}}^{\infty}d\epsilon\frac{dn(\epsilon)}{d\epsilon}F\left(\frac{(m_e c^2)^2}{E\epsilon}\right), \tag{2.19}$$
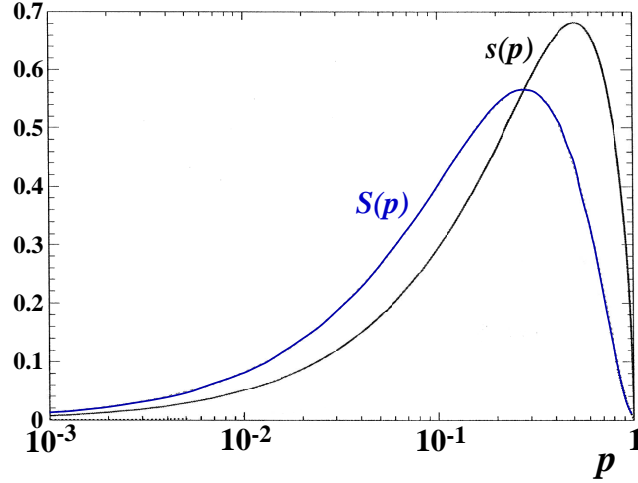
$$S(g) = 2g^2\int_g^1 s(x)x^{-3}dx \tag{2.20}$$

Figure 2.8: The behavior of the functions $s(p)$, $S(p)$ (see text) which peak at $p = 0.508$, 0.28, respectively.

where $s(x)$ is from Eq. 2.16. The attenuation of the high energy γ-rays by *isotropic* background photons peaks at $g = 0.28$ of $S(g)$ (shown in Fig. 2.8), corresponding to $E\epsilon = 3.57(m_e c^2)^2$. This gives a characteristic energy of the soft photon $\epsilon \sim 0.9\,\mathrm{eV}$ for the most effective attenuation of a 1 TeV γ-ray, and the corresponding wavelength is

$$\lambda = 1.33\mu\mathrm{m}\frac{E}{\mathrm{TeV}} \tag{2.21}$$

This energy is almost a factor of two higher than for a head-on collision given in Eq. 2.18.

The lowest energy of a soft photon for interaction with a hard photon of energy E is determined by the threshold for pair production in a head-on collision,

$$\lambda = 4.75\mu\mathrm{m}\frac{E}{\mathrm{TeV}} \tag{2.22}$$

For a γ-ray of energy E, which travels cosmological distances from a source at redshift z, we can generalize Eq. 2.20 to obtain the optical depth [222, 241],

$$\tau_{\gamma\gamma}(E,z) = \frac{3}{8}\sigma_\mathrm{T}\frac{c}{H_0}\int_0^z \sqrt{(1+z)}\mathrm{d}z \int_{\frac{(m_e c^2)^2}{E(1+z)^2}}^\infty \mathrm{d}\epsilon \frac{\mathrm{d}n(\epsilon)}{\mathrm{d}\epsilon}F\left(\frac{(m_e c^2)^2}{E\epsilon(1+z)^2}\right) \tag{2.23}$$

where H_0 is the Hubble constant and $\mathrm{d}n(\epsilon)/\mathrm{d}\epsilon$ is the present-day ($z = 0$) spectral EBL density. Fig. 2.9-(b) shows $\tau_{\gamma\gamma}(E,z)$ for $z = 0.031$, 0.034, 0.047, 0.069[3]. Using those values of $\tau_{\gamma\gamma}(E,z)$, an intrinsic source spectrum $\Phi_\mathrm{intrinsic}(E)$, which is corrected for the absorption by EBL, can be estimated from the measured spectrum $\Phi_\mathrm{measured}(E)$ by,

$$\Phi_\mathrm{intrinsic}(E) = \Phi_\mathrm{measured}(E) \cdot \exp(\tau_{\gamma\gamma}(E,z)) \tag{2.24}$$

---

[3]these values corresponds AGN sources of Mkn421 ($z = 0.031$), Mkn501 ($z = 0.034$), 1ES1959+650 ($z = 0.047$), BL Lacertae ($z = 0.069$), which are observation targets in this thesis
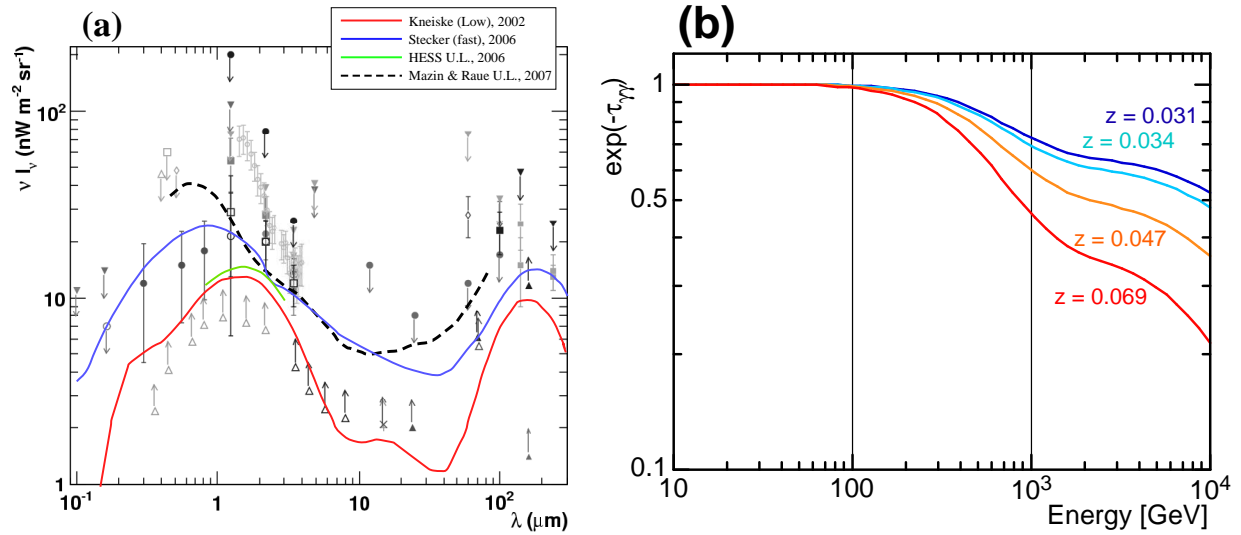
Figure 2.9: **(a)** Various models and upper limits of EBL for z=0, and measurements at various wavelengths. Each upper triangle represents the value from the galaxy count at each wavelength. Red line is based on "low-IR" model of Kneiske et al. (2004) [148]. Blue is taken from "fast evolution" model of Stecker et al. [223]. Other two lines are Upper limit from [18] (*green*) and [174] (*blackdashed*). **(b)** attenuation coefficient $\exp(-\tau_{\gamma\gamma})$ in the case of z=0.031, 0.034, 0.047, 0.069 using the EBL spectrum shown in red line in (a).

According to Eq. 2.21 and 2.22, a VHE γ-ray photon is sensitive for absorption in the optical-infrared range of EBL rather than CMB[4]. Current measurements and some models of EBL at present-day ($z = 0$) in this wavelength range are shown in Fig. 2.9-(a). Two of its main contributions are the (redshifted) relic emission of galaxies and star-forming systems (peak at $\lambda \sim 1-2\,\mu$m) and the light absorbed and re-emitted by dust (peak at $\lambda \sim 100-200\,\mu$m) (see [158, 143] for reviews). The EBL has a strong connection to galaxy evolution in universe.

However, direct measurements of the present EBL spectrum suffer from large uncertainties, as they are dominated by large foregrounds of galactic and zodiacal light. In turn, attempts to model the EBL spectrum (e.g., [148, 223]) are challenged by the need for strong assumptions on cosmology, star formation rate, the distribution of matter in universe; additionally, a good understanding of the light recycling history is required. On the other hand, we can constraint the EBL flux in the optical-infrared region by means of measured the VHE γ-ray spectra of distant AGNs. Recent studies [15, 174] have suggested that the EBL flux at this wavelength range is lower than what previous models predicted and is close to the lower limit, which was derived by direct measurements of galaxy counting. Throughout this thesis, we use the EBL model suggested by Kneiske et al. (2004) [148] as "low-IR" model (the red line in Fig. 2.9-(a)) because this model show similar fluxes to the upper limit by H.E.S.S. [15] around the peak at $\lambda \sim 1-2\,\mu$m.

---

[4]a 100 TeV photon begins to feel the presence of the CMB

As one can see in Fig. 2.9-(b), the effect of absorption decreases as the energy becomes lower. Therefore, observations for blazars with low energy thresholds in the VHE γ-ray band are of great advantage:

- detect γ-rays from distant sources, which increases the number of extra-galactic VHE γ-ray sources. The distant sources can provide us with crucial information about the EBL spectrum.

- study intrinsic fluxes of extra-galactic sources avoiding possible errors by the absorption correction. Due to the ambiguity of the EBL flux, larger systematic uncertainties remain in the corrected VHE γ-ray spectra in higher energies.

The distance where $\tau_{\gamma\gamma}(E,z) = 1$ at a given energy is known as the "γ-ray horizon". This represents an observable distance with a given energy photon. Fig. 2.10 show the "γ-ray horizon" provided by two different EBL models. In general, when lowering γ-ray energy, the corresponding z-value at $\tau_{\gamma\gamma}(E,z) = 1$ becomes higher. This means that the universe is getting more transparent for the VHE γ-ray observations with a lower energy threshold so that we can penetrate deeper into the universe, and hence are able to study early stages of the universe.
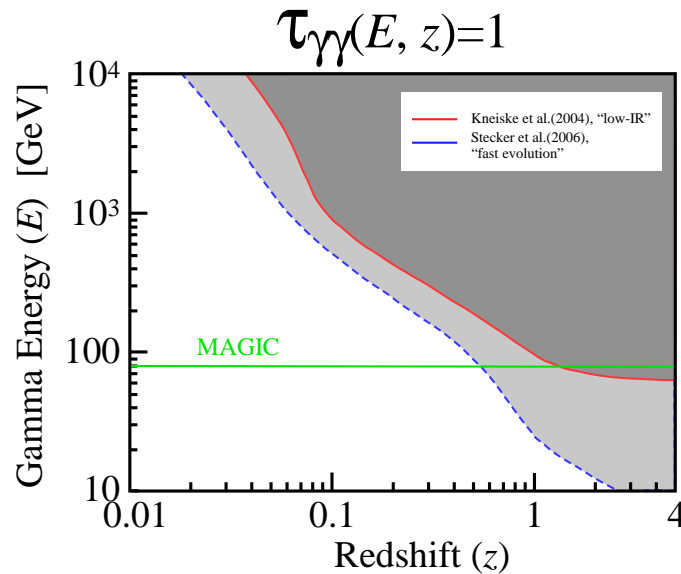

Figure 2.10: Gamma-ray horizon. The lines denote the optical depth $\tau_{\gamma\gamma}(E,z) = 1$ as a function of the γ-ray energy and the redshift for the EBL models of "fast evolution" model in Stecker et al. (2006) [223] (*blue dashed curve*) and the "low-IR" model in Kneiske et al. (2004) [148] (*red solid curve*). The areas to the right and above these curves with dark colors correspond to the region where the universe is optically thick for γ-rays. The horizontal green line indicates the current analysis threshold of the MAGIC telescope (at 80 GeV).

2.5   Motivation for this Thesis

To investigate the fundamental physics of blazars, especially for systematic studies such as the "blazar sequence" (see section 2.2), we need a fair amount of source samples. However, the number of blazars from which VHE γ-rays have been detected ("TeV blazar") is still very small. In 2004, when I started this work, there were **only 7 AGNs** confirmed as VHE γ-ray emitters (see Table 1.2). All of them belonged to the HBL class (except for one, FR-II, M87). None of the TeV sources were found among either LBLs or FSRQs. Therefore, there was a strong desire to increase the source number of TeV blazars.

Searching for new TeV blazars, we designed an observation strategy based on the TeV-source candidate list proposed by Costamante and Ghilleine (2002) [85] (hereafter CG02).

2.5.1   Search for AGNs as new TeV blazars

Target selections

CG02 selected TeV candidates for BL Lac objects among a total number of 246 different AGNs. A main criterion was the existence of both high-energy electrons and sufficient soft photons to enable TeV emission. Thus, the objects were required to show sufficient radio, optical and X-ray fluxes. The selection results can be seen in Fig. 2.11. Finally, they selected 33 objects and calculated the integral fluxes of those objects above 40 GeV, 300 GeV and 1 TeV, using a simple one-zone homogenous leptonic origin model.

The information about the predicted fluxes provided in the CG02 list was used to select the best targets for searching new VHE γ-ray emitters with the MAGIC telescope. For a more realistic feasibility study, we estimated the flux above 80 GeV, which roughly corresponds the MAGIC analysis threshold, using the following formula based on fluxes above 40 GeV as predicted by CG02:

$$F(\geq 80\text{GeV}) = F(\geq 40\text{GeV}) \times \left(\frac{80}{40}\right)^{(-n+1)} \tag{2.25}$$

This method assumes that the photon index of differential spectrum (n) of the potential source is similar to that of the Crab Nebula ($n = 2.6$) because the maximum value of the observed SSC energy (at column 4 in table 2.1 estimated by using Eq.(8) in [147]) is sufficiently higher than the MAGIC threshold of 80 GeV.

In the end, we found that two sources, BL Lacertae ($z = 0.069$) and PG 1553+113 ($z > 0.09$), which showed higher predicted fluxes than the flux sensitivity of the MAGIC observation for 15 hours ($5.8 \times 10^{-11} \text{cm}^{-2}\text{s}^{-1}$). BL Lacertae emerged as the best candidate for a TeV blazar in our observations. In addition, the following results from previous observations supported our selection based on the CG02 list.

- The object with the highest flux prediction among the candidates in their list, 2005-489, had already been detected by H.E.S.S.[5] [16] at that time.

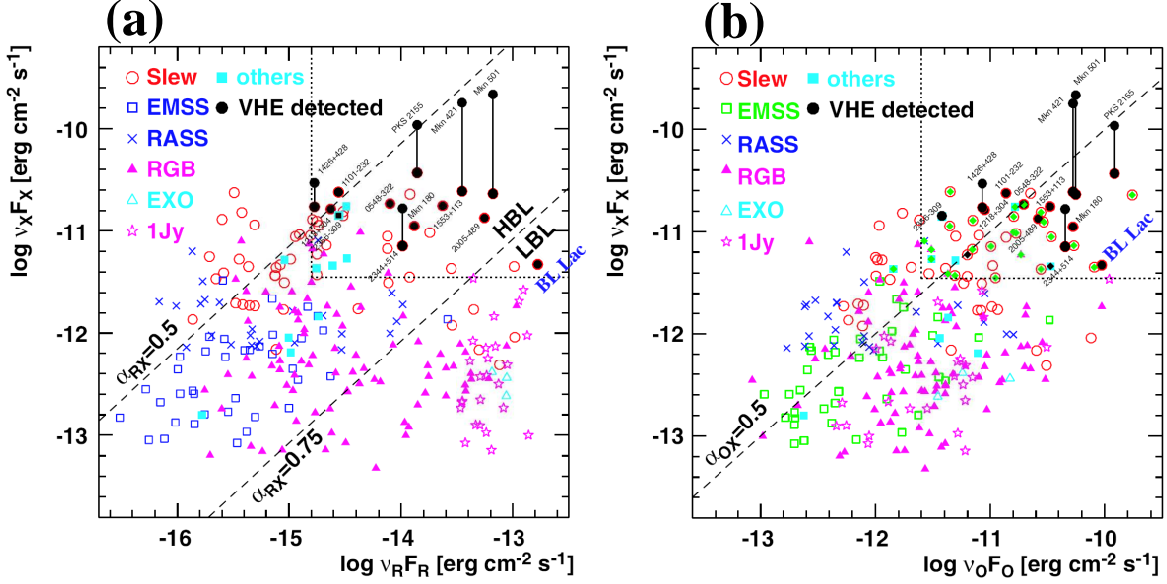[5]This source was one of the first discovered AGNs during the H.E.S.S. observations.

Figure 2.11: BL Lac objects collected by Costamante and Ghilleine (2002) [85]. **(a)**: Radio (5 GHz) and X-ray (1 keV) plane, **(b)**: Optical (550 nm) and X-ray plane. All objects to the right and above both dotted rectangles have been considered to be good candidates for TeV emitters (The plot is updated from the original one with some newly discovered TeV emitters).

Table 2.1: Measured X-ray flux at 1 keV ($F_{1\,\mathrm{keV}}$), predicted integral flux at energies above 40 GeV ($F_{\geq 40\mathrm{GeV}}$, from [85]) and 80 GeV ($F_{\geq 80\mathrm{GeV}}$, from Eq. 2.25) and maximum energy of IC emission ($E_{\mathrm{SSC\,max}}$). The VHE γ-ray fluxes are given in units of $10^{-11}\,\mathrm{cm}^{-2}\,\mathrm{s}^{-1}$.

Source	$F_{1\,\mathrm{keV}}$ [μJy]	$F_{\geq 40\mathrm{GeV}}$	$F_{\geq 80\mathrm{GeV}}$	$E_{\mathrm{SSC\,max}}$ [GeV]
BL Lacertae	1.91	42.8	14.1	442
PG 1553+113	6.54	22.3	7.4	186

- BL Lacertae was observed with the Whipple 10 m telescope for 39.1 hours in 1995. The derived upper limit for the flux above 350 GeV was at 3.8% of the Crab flux [136]. HEGRA found an upper limit above 1.1 TeV at 28% of Crab flux with 26.7 hours observation time [12]. These values are compatible with the flux predicted by CG02. (1.7% Crab flux at 300 GeV and no γ-ray are expected at 1 TeV.)

- MAGIC had observed the fourth-best candidate in the list, 3C66A, for about 20 hours during the commissioning phase in 2004, but did not succeed in detecting VHE γ-ray emission. This result was consistent with the flux predicted by CG02. Accordingly, we can estimate a minimum observation time of ≥ 40 hours.

Concluding that these two objects were the most promising sources for the detection of VHE γ-ray emission with the MAGIC telescope, 20 hours of ON-source observation were proposed in 2005[6].

BL Lacertae is classified as an LBL. Before this thesis, VHE γ-ray emission had not been detected from any objects belonging to this class. Therefore, to search for a VHE γ-ray signal from BL Lacertae is particularly important not only for increasing the number of VHE γ-ray sources, but also for establishing a new class of objects as a source of VHE γ-rays.

I had taken a responsibility for this challenge as a Principle Investigator for the observations. The observations and results of this project are reported in Chapter 7 of this thesis[7].

2.5.2 Simultaneous multiwavelength observations

For discussing emission models of TeV blazars, it is necessary to obtain the SED of the source in a wide energy range. In addition, blazars often show a strong flux variability down to time scales of a few minutes for the highest energy range [103, 41]. Hence, simultaneous multiwavelength (MWL) observations over a wide energy range are essential for studying the physics of TeV blazars.

Correlation between X-ray and VHE γ-ray: In TeV blazars, the correlation between X-ray and GeV-TeV γ-ray fluxes is important because it has been well interpreted by SSC emission models. In these models, emissions in these energy bands are associated with relativistic electrons with comparable energies in the jet.

As an example, the multiwavelength campaign on Mkn421 in 1994 with the ASCA satellite and the Whipple telescope [231] showed significant variability in both X-rays and TeV γ rays with a good correlation. The observed SED can be well explained by the SSC model. On the other hand, during the multiwavelength observation on 1ES 1959+650 in 2002 [156], a TeV γ-ray flare without any X-ray counterparts was observed. This so-called "orphan" flare cannot be explained with conventional one-zone SSC models and suggests to consider new emission models.

---

[6]In total, about 1000 hours per year are available for the MAGIC observations.

[7]the other candidate shown in 2.1, PG 1553+113, was also successfully established as a new TeV blazar. The results were reported in [35]

Previous simultaneous multiwavelength campaigns: Most of the previous multiwavelength campaigns suffered from low sensitivity of the participating γ-ray telescopes. Therefore, the simultaneous observations were limited to being conducted only during flaring states. The study of the sources in low states of activity may reveal new emission components that are masked during flaring states [15]. The connection between high and low states may provide physical information about the jet activity. The old telescopes were unable to measure data below 300 GeV. As discussed in section 2.3.1, it is important to obtain SED information around the IC peak. In some special cases, the peak may occur around several hundreds of GeV during strong flare states. It is, however, widely estimated that in most HBLs the peak is located around several tens of GeV. To access these IC peaks, observations with lower thresholds are necessary.

MAGIC, which has the lowest energy threshold among the current Imaging Atmospheric Cherenkov Telescopes, can access the energy range below 100 GeV. In addition, the high sensitivity allows the detection of GeV-TeV γ-ray signals with observation times shorter than ever even in the quiescent state. Together with wide energy-range X-ray satellites, these new instruments make it possible to perform multiwavelength observations in a much wider range.

Source selections: We selected Mkn501 ($z = 0.034$) and 1ES1959+650 ($z = 0.047$) as targets for the MWL campaigns. They were sources already established as TeV blazars before I started this work[8]. They show rather high fluxes even in their quiet states ($\sim 10\%$ Crab flux, while many of them have only several % Crab flux), which is enough for MAGIC to detect significant VHE γ-ray signals within a few hours. It is an important estimation for obtaining real (quasi-)simulation data with X-ray and VHE γ-ray, because long time overlaps cannot be achieved with X-ray Satellite observations (several hours at most) due to the different operational modes between ground-based telescopes and satellites. These sources are located rather close to us among the TeV blazars. It is an advantage to study intrinsic source spectral features in the VHE γ-ray band because flux uncertainties, possibly incurred by the correction of EBL absorption, can be suppressed (cf. section 2.4).

We organized extensive MWL campaigns for these two sources with an X-ray Satellite, Suzaku, in 2006. The observations and results are reported in Chapter 8 of this thesis (for Mkn501) and Chapter 9 (for 1ES1959+650).

In addition to these intensive MWL observations, we also planned long term observations ("monitoring") for 1ES1959+650 and Mkn421 ($z = 0.031$). Mkn421 is the first-established and brightest of all TeV blazars. We also report parts of these observations in Chapter 9 (for 1ES1959+650 in 2005) and in Chapter 10 (Mkn421 in 2006).

The X-ray Satellite, Suzaku: Suzaku [179] is an X-ray satellite with four X-ray Imaging Spectrometers (XIS) and a separate Hard X-ray Detector (HXD). The XIS are sensitive in the 0.3-10 keV band with two types of CCDs composed of front-illuminated CCDs (for XIS0, 2 and 3) and a back-illuminated type (XIS1). XIS1 is particularly sensitive below 2 keV. The HXD is a non-imaging instrument, sensitive in the 10-600 keV band, composed by a Si-PIN photo-diodes detector (probing the 10-60 keV band) and a GSO scintillator detector (sensitive above 30 keV).

---

[8]i.e. they were two sources among 7 established TeV AGNs at that time.

Thanks to the good noise shielding, the HXD is the most sensitive detector in the 10-60 keV range among the currently available X-ray satellites. Therefore, Suzaku seems to be the best X-ray satellite to cover the wide-range SED for blazar studies.

Chapter 3

Air showers

Once high energy cosmic γ-rays enter the atmosphere of the Earth, they start to interact with particles in the atmosphere and produce large cascades with a huge number of secondary particles ($e^{\pm}, \gamma$), called "Extensive Air Showers (EAS)". The γ-rays generate air showers via the electromagnetic interaction ("Electromagnetic cascade"). The energetic secondary charged particles emit Cherenkov radiation. An Imaging Atmospheric Cherenkov Telescope (IACT) detects the Cherenkov light as a signal to observe the primary γ-ray flux. Cosmic rays of charged particles (protons, helium nuclei.. etc.) also induce Cherenkov light from their air showers. These showers are developed by the strong interaction ("Hadronic cascade") and become backgrounds for the γ-ray observations with the IACT. These two kinds of air showers have different features due to the differences of the interactions inside the showers. Taking advantage of such differences between these two classes of showers, IACTs discriminate most of the hadronic showers as background events. This chapter briefly summarizes the physics of air shower and describes the subsequent production of Cherenkov light including General descriptions about IACTs,

3.1 The atmosphere

The relation between altitude and atmospheric vertical "depth" X_v measured[1] in [g/cm^2] is shown in Fig. 3.1.

X_v is related to the density profile of the atmosphere by

$$X_v = \int_h^\infty \rho(h')\mathrm{d}h',\tag{3.1}$$

where $\rho(h)$ is the density of the atmosphere at altitude h. So far an isothermal atmosphere, the Eq. 3.1 can be described by means of a constant scale height, h_0 as [104]

$$X_v = X_g \exp\left(-\frac{h}{h_0}\right)\tag{3.2}$$

---

[1]It is useful to use the "length" X in [g/cm^2] to discuss particle interactions. In this scale, e.g., the ionization loss is almost constant with respect to the length, regardless of the medium.

where $X_g \cong 1030$ g/cm^2.

In reality the temperature and hence the scale height decrease with increasing altitude until the tropopause (12-16 km). At sea level $h_0 \cong 8.4$ km, and for $X_v < 200$ g/cm^2 the scale height is $h_0 \cong 6.4$ km.

In general, the relation between h and distance up the trajectory (l) is (for $l/R_\oplus \ll 1$)

$$h \cong l \cos\theta + \frac{1}{2}\frac{l^2}{R_\oplus}\sin^2\theta \tag{3.3}$$

for zenith angle θ where $R_\oplus$ is the radius of the Earth.
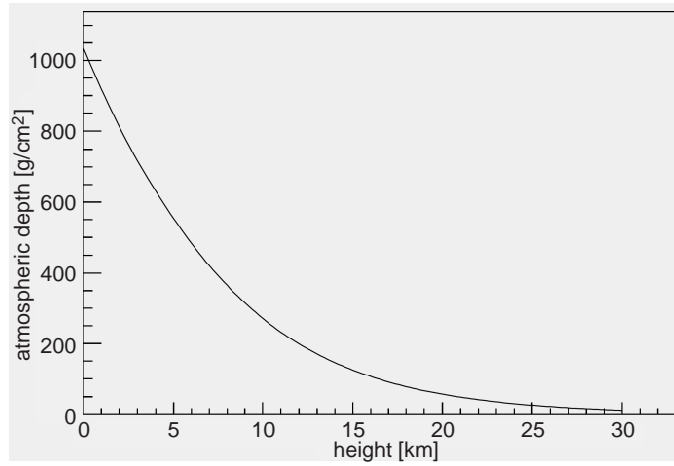
Figure 3.1: Relation between the height in atmosphere and the atmospheric depth.

3.2 Electromagnetic Cascade

The basic high energy processes making up an electromagnetic cascade are bremsstrahlung and pair production.

Bremsstrahlung: Bremsstrahlung is the radiation associated with the acceleration of electrons in the electrostatic fields of ions and the nuclei of atoms. The energy loss per length X (in [g/cm^2]) of a charged particle in the relativistic regime due to Bremsstrahlung can be described by (see e.g., [97])

$$-\frac{\mathrm{d}E}{\mathrm{d}X} = 4\alpha N_A \frac{Z^2}{A}z^2 r_e^2 \left(\frac{m_e}{m}\right)^2 E \ln\left(\frac{183}{Z^{1/3}}\right) \tag{3.4}$$

where α is the fine-structure constant, N_A is the Avogadro number, ρ, A and Z are the average density, atomic mass and charge of the medium, m_e is the electron mass, r_e is the classical electron radius and z, m and E are the incoming particle charge, mass and energy, respectively. The energy loss is inversely proportional to m^2. Therefore bremsstrahlung is an important process for light
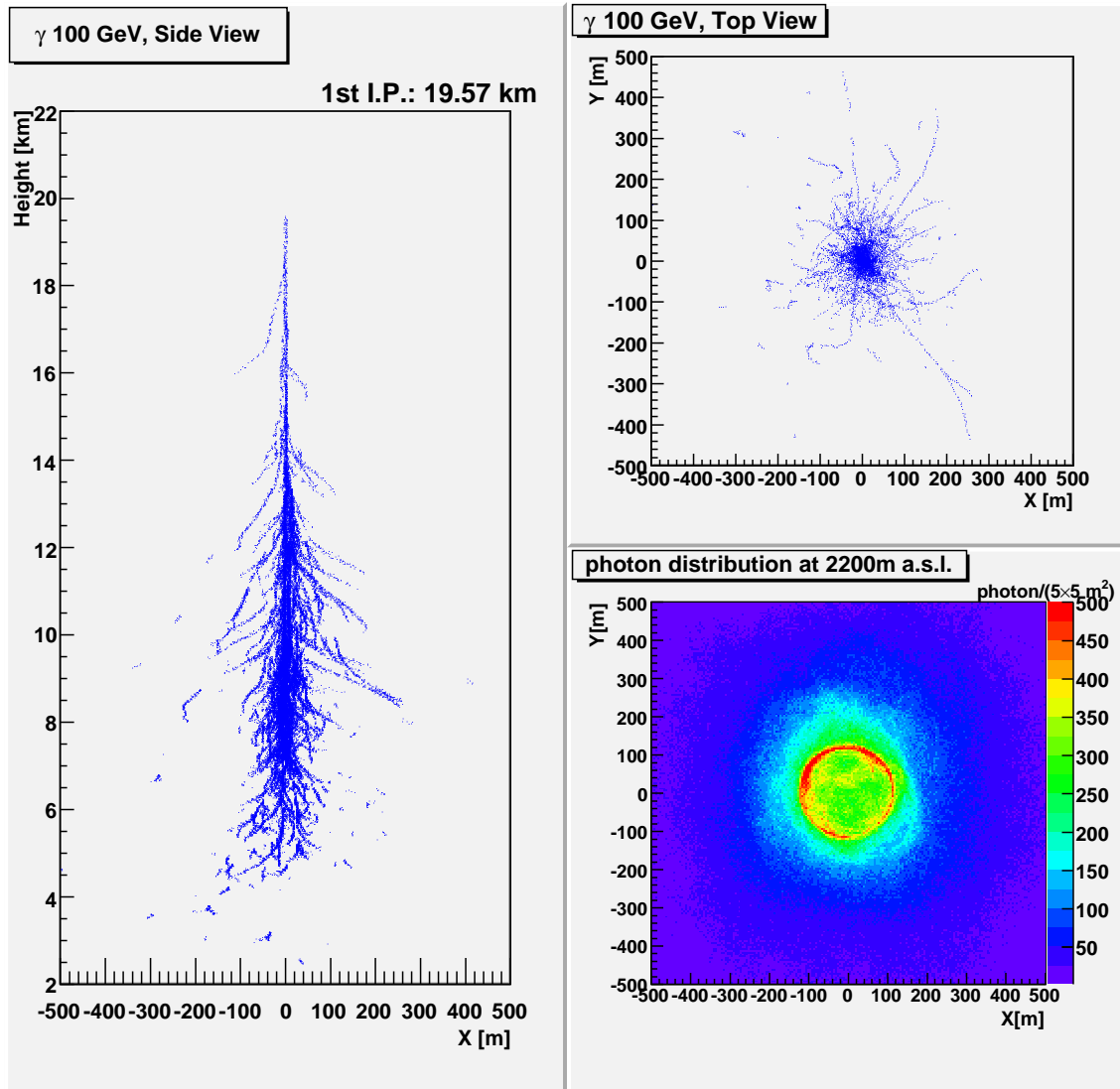
Figure 3.2: Simulated air shower induced by a 100 GeV γ-ray with a zenith angle of $0°$. The shower development is illustrated with particle tracks ($e^{\pm}$ (*blue*), $\mu^{\pm}$ (*red, pink*), hadrons (e.g., $p, \pi^0, \pi^{\pm}$) (*green*)) which contribute to the Cherenkov photon productions. **[Left]:** Side view. The first interaction point of the primary particle is also denoted on the top of the panel. **[Top right]:** Top view. **[Bottom right]:** Cherenkov photon distribution at 2200 m a.s.l.. The scale corresponds to the number of photons in each $25\,\text{m}^2$ area.
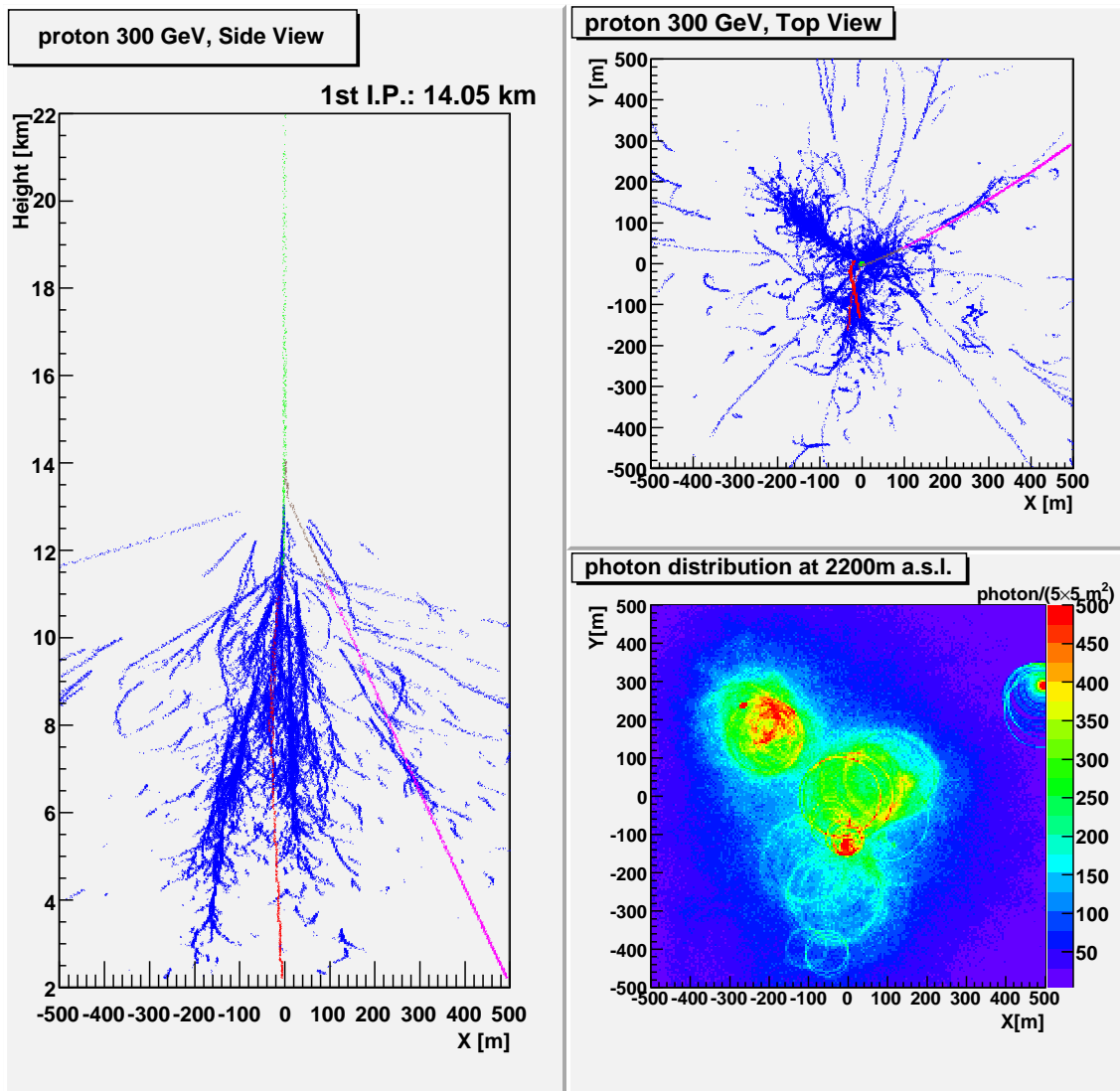
Figure 3.3: Simulated air shower induced by a 300 GeV proton with a zenith angle of $0°$.

charged particles, e.g. electrons and positrons. Here, we can define a radiation length X_0, over which the electron loses a fraction ($1-1/e$) of its initial energy on average by bremsstrahlung.

$$\frac{\mathrm{d}E}{\mathrm{d}X} = -\frac{E}{X_0} \quad \text{with} \quad X_0^{-1} = 4\alpha N_A \frac{Z^2}{A} z^2 r_e^2 \ln\left(\frac{183}{Z^{1/3}}\right) \tag{3.5}$$

The radiation length X_0 for electrons in air is 36.7 g/cm^2, corresponding to ≈ 300 m for standard pressure at sea level [253] .

Pair production: In this process, an electron-positron pair is produced by the interaction of a high energy photon with a virtual photon (γ^*) emitted in the strong electrostatic field of nuclei ($\gamma + \gamma^* \to e^+ + e^-$). The cross section of the pair production σ_p with a high energy photon ($h\nu \gg mc^2$) can be written [128]

$$\sigma_p \approx \frac{Z^2}{137} r_e^2 \left(\frac{28}{9}\log\frac{183}{Z^{1/3}} - \frac{2}{27}\right) \quad [\text{cm}^2] \tag{3.6}$$

The mean free path of pair production X_p can be written using the radiation length X_0 approximately:

$$X_p = \left(\frac{N_A}{A}\cdot\sigma_p\right)^{-1} \approx \frac{9}{7}X_0 \quad (47.2\,\text{g/cm}^2 \text{ in air}). \tag{3.7}$$

Since both characteristic lengths of bremsstrahlung and pair production can be expressed by X_0, the shower development can be discussed using the "length" of medium by scale of X_0.

The energy loss by ionization loss over 1 radiation length ($1X_0$) is defined as "critical energy" for electrons. The critical energy in the atmosphere is 83 MeV. Once an electron reaches the critical energy, in effect, it stop producing secondary photons by bremsstrahlung in the atmosphere for the cascade. It loses its energy by ionization loss.

Primary cosmic γ-rays first interact with nuclei at a height between 15 to 25 km above sea level and induce electron-positron pairs by the pair production process. Subsequently, the electrons and positrons emit γ-rays via bremsstrahlung, and then these γ-rays again produce electron-position pairs. Air showers induced by γ-rays continue to develop through these electromagnetic cascade as long as the secondary particles have energies above the critical energy. Once the particles fall below the critical energy, ionization, excitation and Compton scattering dominate the energy loss and, finally, the cascade shower stops.

The shower development is strongly collimated towards the direction of the incident γ-ray. The total number of electrons and positrons above the critical energy E_c can be approximated by [214]

$$N_e(t,E) = \frac{0.31}{\sqrt{\ln E/E_c}} \exp\left[t\left(1 - \frac{3}{2}\ln s\right)\right] \tag{3.8}$$

$$s(t,E) = \frac{3t}{t + 2\ln(E/E_c)} \tag{3.9}$$

where E is energy of the primary γ-ray, t is the depth of atmosphere scaled with respect to the radiation length ($t = X/X_0$, $X_0 = 36.7\,\mathrm{g/cm^2}$), and s is called "shower age". The shower age can be clarified by

$$\frac{\mathrm{d}N_e(t,E)}{\mathrm{d}s} = N_e(t,E) \cdot \frac{3\ln(E/E_c)(s - 3\ln s - 1)}{(3-s)^2} \tag{3.10}$$

As one can see in this equation, in the range of $0 < s < 1$, the number of electrons and positrons (N_e) increases as s increases ($dN_e/ds > 0$), which means the shower is still developing. At $s = 1$ ($dN_e/ds = 0$), N_e becomes maximum and, hence, the number of secondary particles reaches a maximum in the shower development ("shower maximum"). When $s > 1$, the shower is fading out as N_e decreases ($dN_e/ds < 0$). The shower maximum depends only weakly on the energy of the primary γ-ray ($t_{\max} = \ln(E/E_c)$).
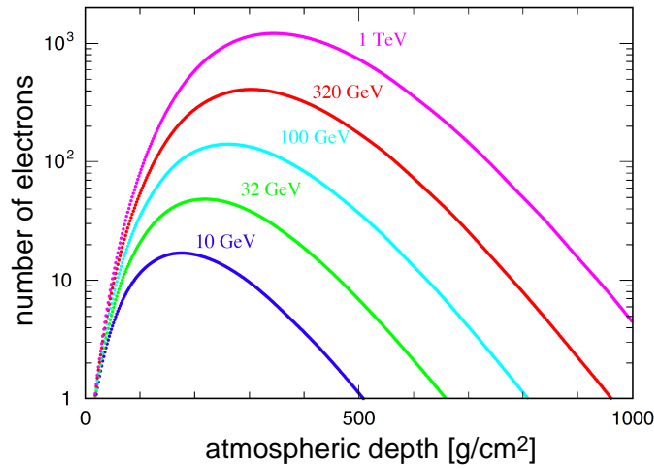
Figure 3.4: The total number of electrons above E_c in an electromagnetic cascade as a function of the atmospheric depth (see Eq. 3.8). Various curves correspond to different primary γ-ray energies and numbers in the figure represent the energies of the primary γ-ray.

Multiple Coulomb scattering is a main process for determining the lateral size in an electromagnetic cascade. The average scattering angle θ of multiple Coulomb scattering is described using depth scaled by radiation length $t = x/X_0$ [185]:

$$\langle \theta^2 \rangle \approx \left(\frac{E_s}{E}\right)^2 t : \qquad E_s = \sqrt{\frac{4\pi}{\alpha}} \cdot m_e c^2 = 21\,\mathrm{MeV} \tag{3.11}$$

The characteristic size of the lateral spread in a shower ("Moliére radius": r_0) is

$$r_0 = \frac{E_s}{E_c} X_0 \approx 9.3\,\mathrm{g/cm^2}, \tag{3.12}$$

which is 78 m at sea level.

The lateral distribution of electrons and positrons can be parameterized by the Nishimura-Kamata-Greisen (NKG) formula [186, 120], which describes the density of electrons and positron as a function of the distance r from the shower axis:

$$\rho_e(r,t,E) = \frac{\Gamma(4.5-s)}{2\pi\Gamma(s)\Gamma(4.5-2s)} \frac{N_e(t,E)}{r_0^2} \left(\frac{r}{r_0}\right)^{s-2} \left(1+\frac{r}{r_0}\right)^{s-4.5} \tag{3.13}$$

where Γ is the Gamma function. This formula is valid strictly only in the range of $1.0 < s < 1.4$. However, this formula can provide information of the lateral distribution immediately and be useful for the air shower simulation.

3.3 Hadronic Cascade

A hadronic shower is produced by the interaction of a hadronic cosmic-ray particle with an atmospheric nucleus governed by the strong interaction. As the result of the interaction, pions $(\pi^\pm, \pi^0)$ represent about 90 % of the secondary particles, and the rest is accounted for by kaons $(K^\pm)$ and light baryons $(p, \bar{p}, n, \bar{n})$.

The Propagation of particle through the atmosphere is described by transport or cascade equations that depend on the properties of the particles and their interactions and on the structure of the atmosphere. Taking into account all types of hadrons which can be produced when an energetic hadron of any flavor interacts, a set of coupled transport equations is needed to describe hadron fluxes in the atmosphere in full detail. In matrix notation one has [104]

$$\frac{\mathrm{d}N_i(E,X)}{\mathrm{d}X} = -\left(\frac{1}{\lambda_i} + \frac{1}{d_i}\right) N_i(E,X) + \sum_j \int \frac{F_{ji}(E_i,E_j)}{E_i} \frac{N_j(E_j)}{\lambda_j} \mathrm{d}E_j, \tag{3.14}$$

Here $N_i(E,X)\mathrm{d}E$ is the flux for particles of type i at depth X in the atmosphere with energies in the interval E to $E+\mathrm{d}E$. The probability that a type i particle interacts in traversing an infinitesimal element of the atmosphere is $\mathrm{d}X/\lambda_i(E)$, where $\lambda_i(E)$ is an interaction length of type i particles in air. The interaction length λ_i in air is defined as [104]

$$\lambda_i = \frac{Am_p}{\sigma_i^{\mathrm{air}}}. \tag{3.15}$$

For the calculation of a hadronic cascade in air we can take the target nucleus to be an average "air" nucleus with $A \approx 14.5$ and omit the target designation from the notation. Hadron-nucleus cross sections have been measured up to several hundred GeV in accelerator experiments and have been studies by several groups (e.g., [254]). The resulting values of hadron interaction lengths in air are summarized as follows [104],

- $\lambda_p^{\mathrm{air}}(100\,\mathrm{GeV}) = 86\,\mathrm{g/cm^2}$

- $\lambda_\pi^{\mathrm{air}}(100\,\mathrm{GeV}) = 116\,\mathrm{g/cm^2}$

- $\lambda_K^{\mathrm{air}}(100\,\mathrm{GeV}) = 138\,\mathrm{g/cm^2}$

Table 3.1: Main decay channels of pions and kaons.

particle	Average lifetime	ϵ (GeV)	decay channel	branch ratio
$\pi^{\pm}$	2.6×10^{-8} s	115	$\pi^{\pm} \rightarrow \mu^{\pm} + \nu_{\mu}(\bar{\nu}_{\mu})$	100%
π^0	8.3×10^{-17} s	3.5×10^{10}	$\pi^0 \rightarrow \gamma + \gamma$	98.8%
$K^{\pm}$	1.2×10^{-8} s	850	$K^{\pm} \rightarrow \mu^{\pm} + \nu_{\mu}(\bar{\nu}_{\mu})$	63.5%
			$K^{\pm} \rightarrow \pi^{\pm} + \pi^0$	21.2%

The function $F_{ji}(E_i, E_j)$ is the probability density (integrated over transverse momentum) for an incident particle (type j) of energy E_j to collide with an air nucleus and produce an out going particle (type i) with energy E_i. In general, it is defined as [104]

$$F_{ac}(E_c, E_a) \equiv E_c \frac{\mathrm{d}n_c(E_c, E_a)}{\mathrm{d}E_c}, \tag{3.16}$$

where $\mathrm{d}n_c$ is the number of particles of type c produced on average in the energy bin $\mathrm{d}E_c$ around E_c per collision of an incident particle of type a.

Finally d_i is the decay length (in g/cm^2) for particles of type i with energy E and can be written with h_0 evaluated at the appropriate atmospheric depth X_v, mass m_i and average lifetime τ_i of type i particles [104],

$$\frac{1}{d_i} = \frac{m_i c^2 h_0}{E c \tau_i X_v} \equiv \frac{\epsilon_i}{E X_v}. \tag{3.17}$$

Here, we call ϵ_i "decay constant", $\epsilon_i = \frac{m_i c^2 h_0}{c \tau_i}$.

Decay or interaction dominates depending on whether $1/\lambda_i$ or $1/d_i$ is larger in Eq. 3.14. This in turn depends on the relative size of ϵ and E for each particle. In Table 3.1, the main decay channels of pions and kaons are summarized, using the high altitude value of $h_0 \cong 6.4$ km for ϵ.

For instance, since the π^0 has only a short lifetime (hence, large decay constant), it decays to γs as soon as it is created by the interaction, and then these γ-rays induce electromagnetic cascades. As the probability for the production of $\pi^{\pm}$ and π^0 is similar, about 30% of the energy of each interaction can be transferred to electromagnetic cascades via π^0 decay.

Muons can reach the ground because of their relatively long lifetime ($\tau \sim 2.2 \times 10^6$ s) and small cross section to other particles. But if it decays, it can induce an electromagnetic cascade through the decay channel of $\mu \rightarrow e + \bar{\nu}_{\mu}\nu_e$. Neutrinos which are created by the decay reach the ground without any interactions.

In a given interaction, a primary particle spends $\sim 40\%$ of its energy for the production of secondary particles and keeps the rest of 60% energy for the next interaction. In this way, a hadronic cascade is generated.

The lateral spread of hadronic shower is mainly caused by the transverse momentum which is given to the secondaries in the hadronic interaction. The mean transverse momentum is almost independent of the primary particle energy and is about 0.3 GeV/c. Consequently, a hadronic shower usually shows broader shape than a pure electromagnetic shower.

3.4 Cherenkov Radiation

A charged particle passing through matter loses energy due to Coulomb interaction with the electrons of the matter. In general this energy is absorbed in the vicinity of the particle track. However if the particle velocity is faster than the local group velocity of light, part of the energy is emitted as radiation and can propagate through the matter in case of materials of high optical transmissivity. This radiation is called Cherenkov light and was discovered by P.A. Cherenkov in 1934 [81]. The theoretical explanation was given by Frank and Tamm in 1937 [101]

The minimum velocity required for the emission of Cherenkov light with a refractive index n.

$$v > \frac{c}{n} \qquad (3.18)$$

where v is the velocity of the charged particle, c is the speed of light in vacuum.

The emission of Cherenkov light is described by the superposition of spherical waves using Huygens' principle (see Fig. 3.5). Under the assumption that a spherical wave emerges from each point of the particle track, constructive interference only takes place for $v > c/n$. The resulting cone-shaped wave-front is similar to the shock wave produced by an airplane flying at supersonic speed. The Cherenkov angle θ_c can be deduced from geometrical considerations only with $\beta = v/c$ (see Fig. 3.5-b):

$$\cos\theta_c = \frac{1}{\beta \cdot n} \qquad (3.19)$$
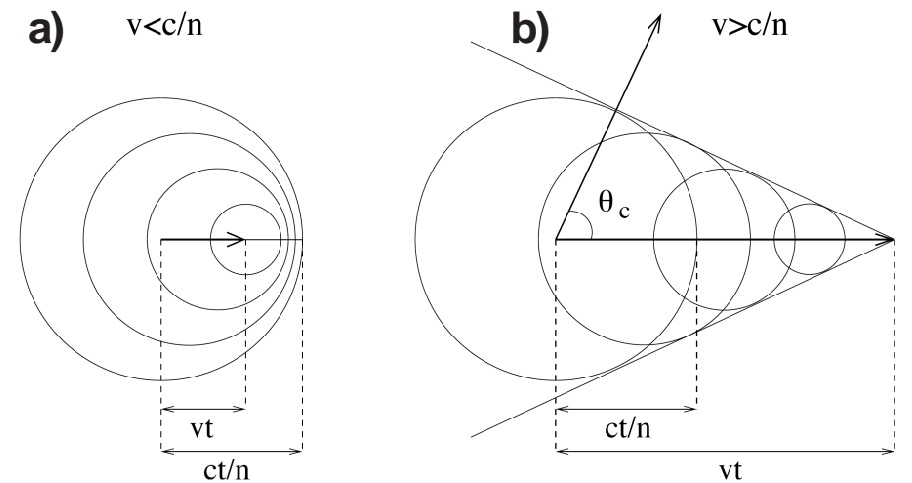
Figure 3.5: Propagation of Cherenkov light in a medium with refractive index n, derived from Huygens' principle. Constructive interference of the spherical waves is achieved for particle velocities $v > c/n$. The resulting cone-shaped wave-front propagates at an angle $\cos\theta_c = 1/(\beta n)$ relative to the particle track.

From Eq. 3.18, the Cherenkov light can be only generated by a particle with sufficiently high energy ($E > E_{th}$):

$$E_{th} = \frac{m_0 c^2}{\sqrt{1 - 1/n^2}} \tag{3.20}$$

where m_0 is the rest mass of the charged particle.

3.4.1 Cherenkov radiation in air shower

As the refractive index depends on the density of the medium, it changes with the atmospheric altitude. Therefore, the Cherenkov emission angle and the energy threshold for Cherenkov productions take different values along the path of the shower.

From Eq. 3.2, the refractive index of the air $n(h)$ be written can as a function of height h:

$$n(h) = 1 + \eta = 1 + \eta_0 \cdot \exp\left(-\frac{h}{h_0}\right) \tag{3.21}$$

Smaller variations of refractive index due to other factors, such as the air temperature or the wavelength of the radiation, can be neglected.

Given the fact that $\eta \ll 1$, the energy threshold of Eq. 3.20 can be written

$$E_{th} \approx \frac{m_0 c^2}{\sqrt{2\eta}} \tag{3.22}$$

As an example, at 20 km a.s.l., which is the average height of the first interaction of the primary particles, E_{th} for electrons, muons and protons are 67 MeV, 14 GeV and 120 GeV, respectively. At see level (0 m a.s.l), E_{th} are 22 MeV, 4.6 GeV and 40 GeV, respectively. As expected, the threshold energy for Cherenkov light decreases as the particles penetrate further through the atmosphere. In addition, the intensity of Cherenkov radiation depends upon the development of the electromagnetic cascade through the atmosphere. For instance, according to Fig. 3.1 and 3.4, the shower maximum for a 320 GeV γ-ray occurs at an atmospheric depth of about 300 g/cm^2, corresponding to about a height of 10 km a.s.l.

Since the charged particles in an EAS can be treated as ultra-relativistic ($\beta \sim 1$), the Cherenkov angle (see Eq. 3.19) can be expressed approximated by η:

$$\theta_c = \cos^{-1}(1/n) \approx \sqrt{2\eta} \tag{3.23}$$

The Cherenkov angle at 2200m a.s.l. (where the MAGIC telescope is located) is $1.2°$.

3.4.2 Cherenkov photon yield

The loss of energy E per unit path length h by a particle of charge e to Cherenkov radiation of wavelength between λ and $\lambda + d\lambda$ is [101]:

$$\frac{dE}{dh} = 4\pi^2 e^2 \int \left(1 - \frac{1}{\beta^2 n^2}\right) \frac{d\lambda}{\lambda^3} \tag{3.24}$$

Therefore the energy loss by Cherenkov radiation dE between λ_1 and λ_2 per atmospheric depth X_v can be written with $1 - 1/n^2 \approx 2\eta$ and $dX_v = -\rho dh$ as:

$$\frac{dE}{dX_v} = \frac{dE}{dh}\frac{dh}{dX_v} = 8\pi^2 c^2 \frac{\eta}{\rho} \int_{\lambda_2}^{\lambda_1} \frac{1}{\lambda^3} d\lambda = 4\pi^2 e^2 \frac{\eta}{\rho} \left(\frac{1}{\lambda_1^2} - \frac{1}{\lambda_2^2}\right) \tag{3.25}$$

One can see from Eq. 3.25 that most of the Cherenkov light is generated with lower wavelength due to the $1/\lambda^2$ dependence. Then, the number of produced Cherenkov photons N_{ph} per atmospheric depth can be estimated as:

$$\frac{dN_{ph}}{dX_v} = \int_{\lambda_2}^{\lambda_1} \frac{1}{\hbar\omega}\frac{d^2 E}{dX_v d\lambda} d\lambda = 4\pi\alpha \frac{\eta}{\rho} \left(\frac{1}{\lambda_1} - \frac{1}{\lambda_2}\right) \tag{3.26}$$

Here, $\alpha = e^2/\hbar c = 1/137$ is the fine structure constant. Since η is proportional to the air density ρ, the amount of energy (the number of photons) per radiation length is constant. In the atmosphere, the wavelength of the Cherenkov radiation is longer than 180 nm because such a wavelength can not satisfy the condition of Eq. 3.18. In addition, photons with wavelength below 300 nm are strongly absorbed by the air (see the next section) before they reach the ground. Using the numbers $\lambda_1 = 300$ nm and $\lambda_2 = 600$ nm (sensitivity limit of PMTs, see section 4.3), $dN_{ph}/dX_v = 336 (\mathrm{g/cm^2})^{-1}$. Each electron therefore emits $\sim 10^4$ Cherenkov photons between 300 nm and 600 nm per radiation length in the atmosphere (cf. $X_0 = 36.7\,\mathrm{g/cm^2}$).

3.4.3 Attenuation of photons in atmosphere

Several processes contribute to the absorption of Cherenkov photons before they reach the ground.

- Rayleigh scattering
  This is the process light scattering on polarizable particles with sizes much smaller than the photon wavelengths. The reduction dI of the photon intensity I per path length dx can be derived from the Rayleigh scattering equation and is approximately [67]

$$\frac{dI}{dx} = -I \cdot \frac{32\pi^3}{3N\lambda^4}(n-1)^2 \tag{3.27}$$

  where N is density of scattering particle, n is refractive index and λ is the Cherenkov photon wavelength. The strong dependence of Rayleigh scattering on the photon wavelength (λ^{-4}) mainly affects the short wavelength range of the Cherenkov photon spectrum. For atmospheric heights between 3 and 15 km (with perfect weather conditions), Rayleigh scattering is the dominant process for Cherenkov light attenuation.

- Mie scattering
  This scattering is caused by relatively large particles called "aerosols", e.g., specks of dust. The relative contribution to the light attenuation above 2000 m height is small, but poor atmospheric conditions (e.g. increased dust, moisture) can make Mie scattering the dominant process. The spectral dependence of the cross section is $\sigma_{\mathrm{mie}} \propto \lambda^{-a}$ with $1 < a < 1.5$.

- Ozone absorption ($O_3 + \gamma \rightarrow O_2 + O$)
  Ozone (O_3) is a particle widely spread between 10 and 40 km a.s.l. and strongly absorbs photons with the wavelengths less than 300 nm. Due to this effect, Cherenkov photons in the UV range ($\lesssim$ 300 nm) can be detected at the ground only when they are generated from particles at short distance to the ground.

Fig. 3.6 show the final spectra of Cherenkov photon at 2200 m a.s.l. reaching the MAGIC telescope with two different incident zenith angles (0° and 60°).
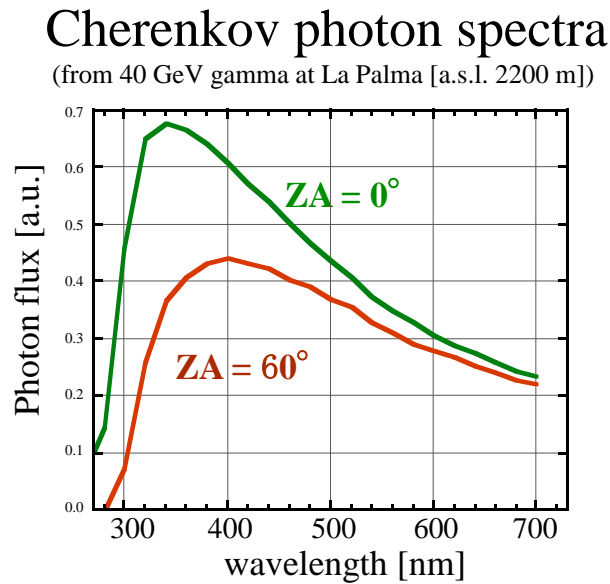
Figure 3.6: Cherenkov photon spectra at 2200 m a.s.l. from a shower induced by a 40 GeV γ-ray. The photon spectrum from a γ-ray incident at zenith angle (ZA) of 0° is represented as the green line, and at 60° as the orange.

3.5 Distinction between γ- and hadron-induced air showers

The previous sections described the basic properties of γ- and proton induced air showers. Fig. 3.2 and 3.3 show a γ- and a proton-induced air shower generated by Monte Carlo simulation. The shower features from charged particles above the energy threshold for Cherenkov light production are represented by a top view and a side view. The photon distributions ("light-pool") at 2200 m a.s.l. can also be seen. Due to the different processes involved, the geometry of both types of air is quite different and it is then possible to distinguish in an air shower by Cherenkov photons. In this section, the main differences between the two types of showers are summarized.

- The interaction length of hadronic particles in air is about 2 times longer than that of photons. Proton showers are therefore more extended then γ-ray showers.

- The secondary particles, which are produced in hadronic interactions, have a mean transverse momentum of about 0.3 GeV/c. The lateral distribution of proton showers is therefore broader.

- Proton showers are subject to larger fluctuations in the shower development due to the larger interaction length of the hadronic particles, the larger transverse momentum of the secondary particles and the variety and number of secondary particles.

- Decaying neutral pions might initiate electromagnetic sub-showers at larger transverse distances and angles from the shower axis. The electromagnetic component of proton-induced air showers contains only a fraction of the primary energy. The overall amount of Cherenkov light produced within proton showers is therefore generally smaller compared to γ-induced air showers of the same energy.

- For point-like sources all γ-rays reaching the earth have the same incident direction. This property is also inherent in the produced air showers. Charged particles, in contrast, are isotropically distributed because they are randomly deflected by galactic and intergalactic magnetic fields while traveling through the universe.

- Pions and kaons can also emit the Cherenkov light. However, these particles usually generate the Cherenkov light only at high altitude due to their short lifetimes and high-energy thresholds for the production of Cherenkov light (see Eq. 3.20). Their contribution to the overall amount of Cherenkov light in the shower is therefore small at the ground level. On the other hand, decay muons can reach the ground without interaction and emit significant amount of the Cherenkov light which is observable at the ground.

High-energy protons are only one part of the cosmic ray spectrum ($\sim$ 54% above 100 GeV). The cosmic rays also contain heavier nuclei (mainly He with $\sim$ 23%) up to iron. There is also a small contribution from electrons ($\sim$ 0.2%). In a simplified picture, air showers produced by heavy nuclei can be regarded as a superposition of several (according to the number of nucleons A) proton showers of reduced energy E/A. The dominant part of the hadronic background can be treated like proton showers.

Electron-induced air showers have indistinguishable shapes from γ-ray showers. But like the hadronic part of the cosmic ray, the electrons are isotropically distributed due to the deflection by galactic and intergalactic magnetic fields while traveling through the universe and only add to the isotropic background. Due to the very steep electron spectrum (spectral index -3.2 [5]), electrons become more abundant as the energy decreases. At about 30 GeV, it is estimated to be about 2% of the flux of hadronic particles.

3.6   Imaging Atmospheric Cherenkov Telescope

Imaging Atmospheric Cherenkov Telescopes (IACTs) are currently the most efficient ground-based experiments for the detection of cosmic γ-rays. As any other optical or radio telescopes, an IACT consists of three basic elements: a mechanical tracking system, which counteracts the Earth's rotation to track an astrophysical object in the sky, a collecting surface, which gathers the incident electromagnetic radiation and focuses it, and a receiver element, which converts the collected light in a recordable image of the observed field of view (FOV). A peculiar feature of Cherenkov telescopes is that they do not detect directly the photon (γ-ray) flux, but instead detect the Cherenkov light which is produced in the air shower induced by the primary photon. A mirror surface collects a fraction of the Cherenkov light pool, and at the focal plane a set of light detectors converts the incident Cherenkov photons into electric pulses which together form an image of the EAS. The very fast ($\sim$ ns) response of the light detectors chosen for IACTs is another important characteristic of these telescopes and is the key for efficient background rejection.

The image formed in the camera of photosensors is a geometrical projection of the air shower as can be seen schematically in Fig. 3.7. Cherenkov photons emitted at different heights reach the telescope mirror dish with different angles and will therefore be focused on different positions in the camera of the telescope. As a consequence, the image contains information of the longitudinal development of the EAS, i.e., the number of particles emitting Cherenkov light as a function of the height in the atmosphere. Light coming from the upper part of the shower, where the secondary particles are more energetic, has smaller Cherenkov angles and is mapped onto a region close to the camera center. Light emitted from the last stages of the showers, from less energetic secondary charged particles, has a larger Cherenkov angle and is therefore mapped further away from the camera center.

The Cherenkov technique takes advantage of the shower development information in the image of the telescope camera. It is therefore possible to take a 'picture' of air showers resolved in space (and time). This information can then be used to distinguish the origin of the air shower (hadronic or γ-ray) using the different spatial development of γ- and hadron-induced air showers. The parameterization of such images is called "Imaging Technique", which dramatically improves the γ/hadron separation power (see also section 6.6.1 for the image parameters) and makes IACTs the most successful instrument for cosmic very high energy γ-ray observations. For the large showers (i.e., induced by very energetic particles) or for showers with high impact parameters, due to the directionality of the Cherenkov radiation, Cherenkov photons from parts of the EAS may not reach the reflector of the telescope and, therefore, may not be fully contained in the recorded image.

The measurement of the Cherenkov light provides a good indicator of the energy absorbed in the atmosphere, which is in fact acting as a calorimeter. Therefore, the total amount of light contained in the image is regarded as one of the main estimators of the energy of the primary particle. In addition, orientation and shape of the image also provide information on the incoming direction of the primary particle.

Two main parameters characterize an IACT: its sensitivity, i.e., the minimum detectable γ-ray flux in a given number of observation hours (traditionally, defined by a 5 σ excess for 50 hours
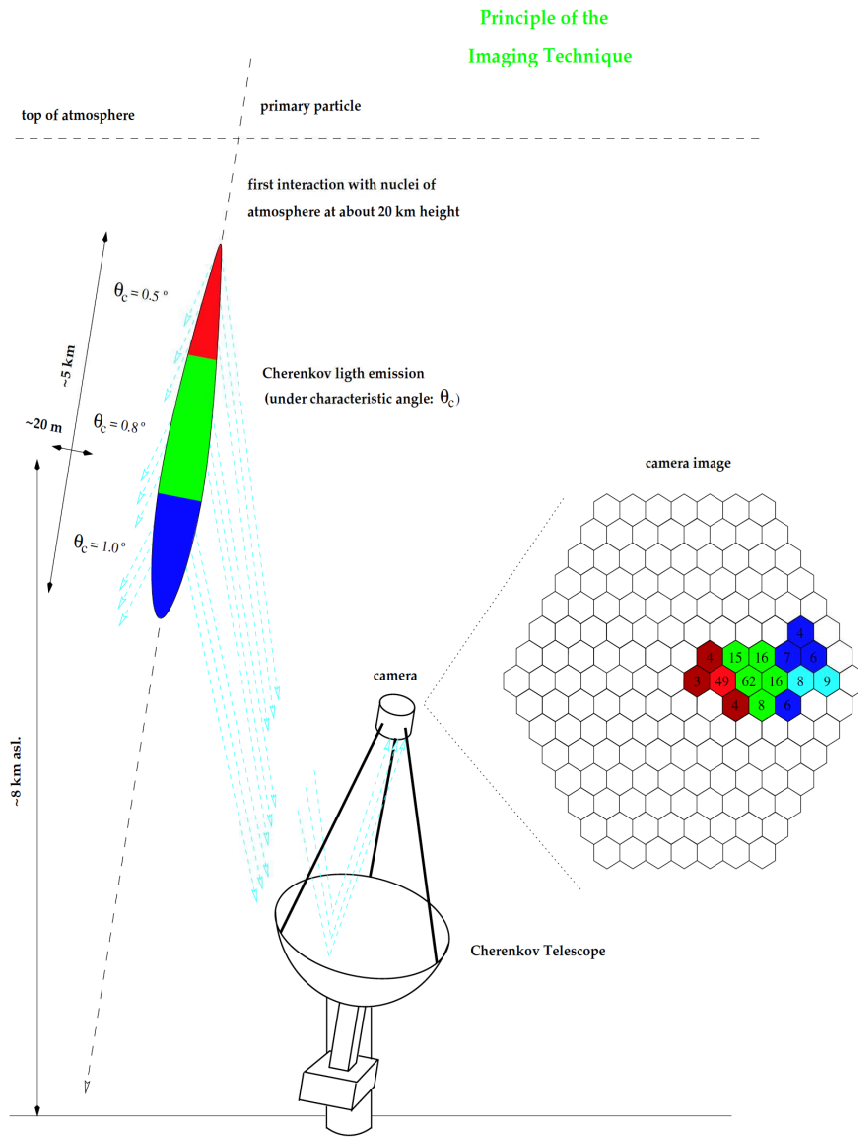
Figure 3.7: Basic principle of the Imaging Technique (see text). The stated dimensions are typical for vertical γ-ray showers of 1 TeV primary energy (taken from [198]).

of observation time), and its energy threshold.

The Cherenkov photons generated in an air shower spread in a large pool on the ground at the observation level. Fig. 3.8 shows the lateral distribution of Cherenkov photons from a 100 GeV γ-induced air shower. The Cherenkov photons are mainly found inside an area of $\sim$120 m radius (see also Fig. 3.2). IACTs can detect EAS from γ-rays over a large range of impact parameters at least until 120 m. This provides IACTs with huge collection areas (of the order of $10^5 \mathrm{m}^2$). Such huge collection areas of the IACTs turn into high sensitivities in comparison with γ-ray detectors mounted on satellites, whose dimensions are clearly limited by space-launching requirements to $\lesssim 1\mathrm{m}^2$. It should be noted that the Cherenkov photons from hadron-induced air showers distribute more widely than those from γ-induced shower as one can see by the comparison between the bottom-right panels in Fig. 3.2 and 3.3. Therefore, the IACTs can detect hadron-induced air showers with even larger impact parameters than those of γ-induced showers.

The energy thresholds E_{th} of IACTs can be defined in a variety of ways, for instance, by the peak the γ-ray energy distribution among the triggered events. As discussed above, the shower image becomes smaller as in size the primary energy deceases. Fig. 3.9 shows how the photon density at an observation site at 2 km a.s.l. diminishes as the energy of the EAS precursor particle drops. going below 10 Cherenkov photons per m^2 for γ-rays of less them 100 GeV.

The triggered events are limited by the number of detected Cherenkov photons per image and require a sufficient signal-to-noise ratio in the instrument. The E_{th} can be described by (see e.g., [189]):

$$E_{\mathrm{th}} \propto \sqrt{\frac{B\Omega t}{\epsilon A}} \tag{3.28}$$

where B is the night sky background (NSB) photon flux, Ω is the solid angle subtended by a pixel (photosensor) of the camera, t is the integration time of the signals, A is the collection area of the mirror(s), and ϵ is the light collection efficiency (i.e. the mirror reflectivity and the fraction of light collected by the photosensors in camera). From Eq. 3.28, it is clear that one can lower the energy threshold of a Cherenkov telescope by reducing the noise contribution from the NSB by working at a dark site or by minimizing the field of view of a pixel and the integration time, or by increasing the amount of Cherenkov signal collected by maximizing the mirror size or the photon collection efficiency of the photosensor. Since the Cherenkov light in EAS has a finite temporal and angular spread, there are limitations to improving the energy threshold by reducing the field of view of a pixel. The most straightforward way to lower the energy threshold is to use larger mirrors or photosensors with higher quantum efficiency. The MAGIC telescope tried to combine both advantages, i.e. large mirror and high quantum efficiency photosensors.
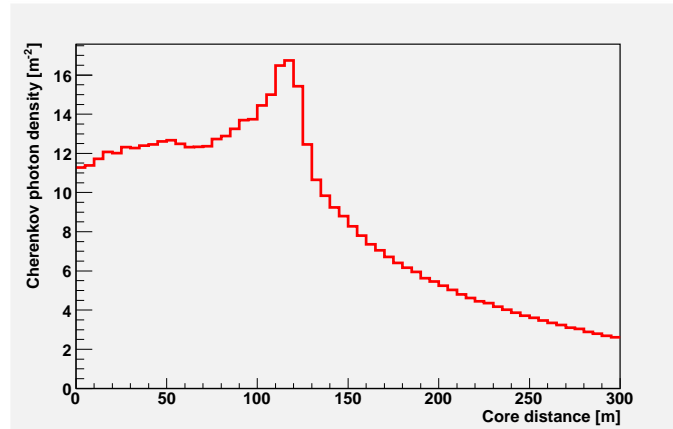
Figure 3.8: Lateral distribution of Cherenkov photons generated by a 100 GeV γ-induced air shower.
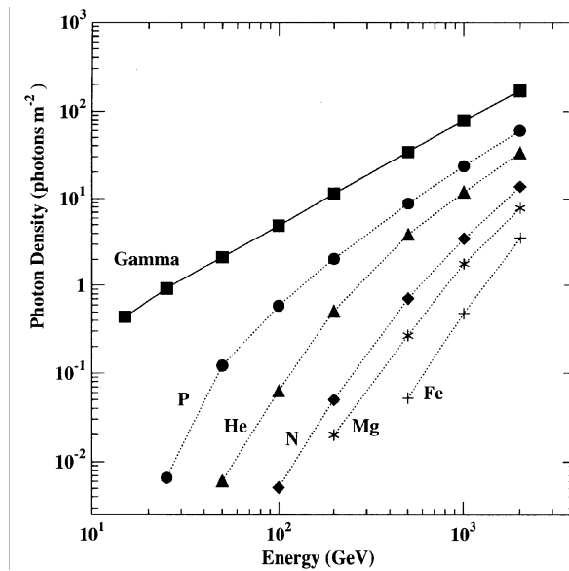

Figure 3.9: Cherenkov photon density at 2 km height above sea level for different types of incident primary particles as a function of their energy. The figure is taken from [189].

Chapter 4

The MAGIC telescope

To achieve an energy threshold lower than in any other previous IACT for the investigation of the unexplored energy region between 30 an 300 GeV, the MAGIC telescope was designed to have 17-m diameter tessellated mirror, making it the currently largest IACT in worldwide. Following the design study in 1998 [50], the production of the telescope components and civil works started in 2001. After a commissioning phase, which commenced in mid 2003, regular scientific observations have been carried out since the fall of 2004.

The MAGIC telescope is located at $28°.45'$ N, $17°.53'$ W and is hosted by the Instituto de Astrofísica de Canarias (IAC) at the Observatorio del Roque de los Muchachos (ORM) on the Canary Island of La Palma at 2245 m above sea level. The ORM is considered to be one of the best observatory sites in the Northern hemisphere [175, 162]. Moreover, due to its relatively high altitude and the, consequently, lower absorption of Cherenkov light, the ORM is excellently suited for the detection of shower images from lower energy γ-rays.

The key components of the MAGIC telescope are described in the following section.

4.1   Telescope Mechanics and the drive system

The MAGIC telescope has a 17m-diameter parabolic mirror dish with a focal length of 17 m. The dish is supported by a lightweight space frame structure with carbon fiber reinforced plastic tubes. The total weight of the mechanical structure including mirrors and the PMT camera could be restricted to only 64 tons. This lightweight telescope design in an Altitude-Azimuth mount together with powerful servomotors enables the MAGIC telescope to be repositioned to an arbitrary sky position within about 30 seconds. This fast movement is a crucial feature for the observation of GRBs.

The tracking system of the telescope is described in detail in [72]. The pointing direction of the telescope is measured using shaft encoders with a resolution of 14 bit, corresponding to a telescope positioning accuracy of about 2'. Due to telescope structure deformations, however, small deviations of the actual telescope pointing from the nominal position may occur. These pointing deviations can be monitored and corrected by using the MAGIC starfield monitor [212]: A video camera is attached to the center of the mirror dish of the MAGIC telescope. It compares
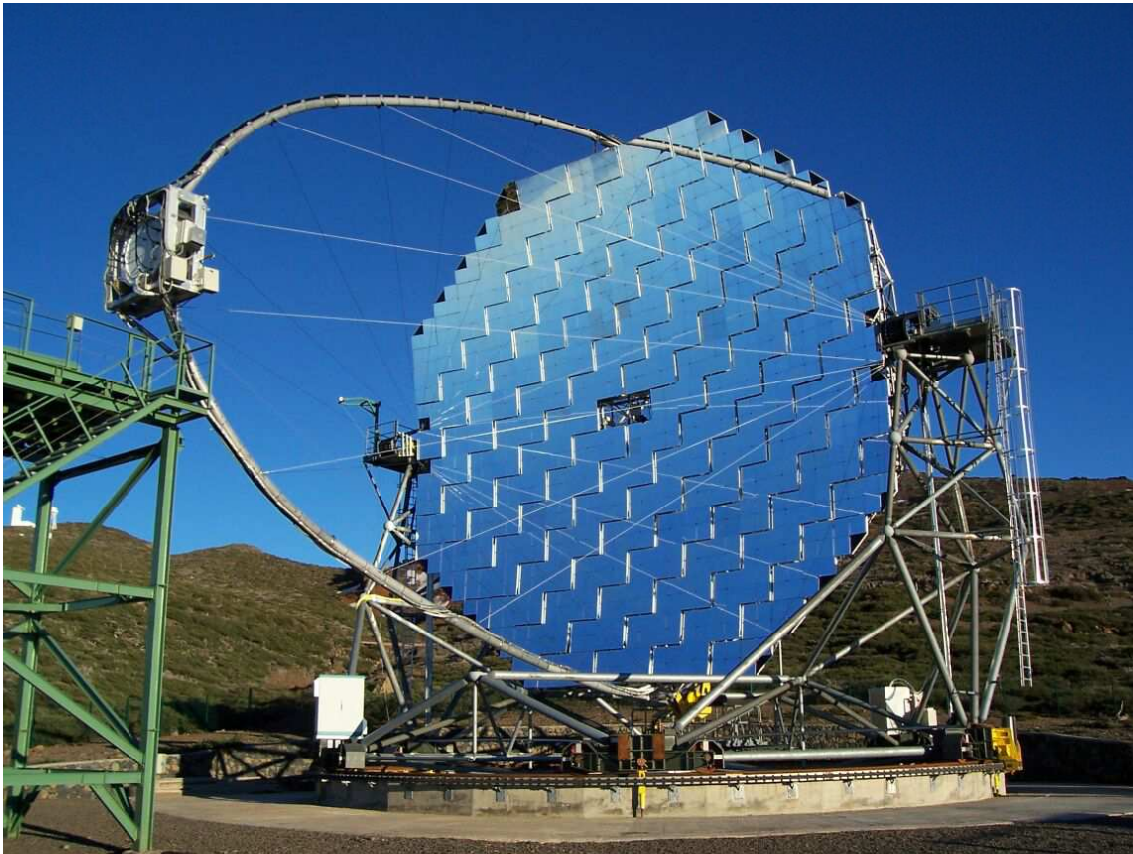
Figure 4.1: The MAGIC telescope.

monitor LEDs mounted on the PMT-camera frame and stars with known positions from the celestial background.

4.2   The reflector mirror system

The 17 m diameter tessellated reflector is composed of 964 mirror element of 49.5×49.5 cm^2 area each. These are grouped in 4-element panels (3-element panels at the rim of the dish) and have a total of 236 m^2 reflector area. In order to minimize the time spread of the Cherenkov flash at the camera plane for short signal integration time, a parabolic shape was adapted for the overall curvature. The focal length to diameter ratio, f/D, is approximately 1. The curvature of the individual mirror elements is spherical, and their focal length increases gradually from 17 m to 18 m when moving from the center of the dish to the rim. Each mirror panel is equipped with an internal heating system to prevent dew and ice formation. A thin layer of quartz protects the mirror surface from aging. The mirror surface reflectivity is ~ 85 % in the wavelength range of 350 - 650 nm.

The camera allows the optical system to be focused to infinity, and to a height of 10 km, at which the shower maximum of a typical extended air shower is expected. The initial calibration of the telescope focusing is achieved by using an artificial source situated at a distance of 920 m. During normal operation, the mirror is focused to a distance of 10 km.

In order to compensate for the small deformations of the mirror dish under gravitational load when varying the elevation angle during tracking, the individual mirror panels can be automatically adjusted with a technique called "Active Mirror Control" so as to guarantee optimal focusing of the mirror system. The position of panels is set such that the light emitted by the lasers situated in the center of each four-mirror panel is correctly focused in the camera plane.

4.3   Camera

4.3.1   The camera layout

The layout of the camera is schematically shown in Fig. 4.2. Due to the optimization of telescope performance and cost, the hexagonal detecting area was divided into two regions: an inner part, segmented in 396 finer hexagonal pixels of $0.1°$ angular diameter (~ 30 mm diameter at the camera plane), which covers the field of view (FOV) of up to $2.1°$ ($2.3°$) diameter for the short (long) hexagonal camera axis, and an outer part with 180 larger hexagonal pixels of $0.2°$ angular diameter ($\sim$60 mm diameter at the camera plane), to cover the FOV of up to $3.5°$ ($3.8°$) diameter for the short (long) hexagonal camera axis.

The MAGIC camera configuration with the finer inner pixels allows a good sampling of the small images that are produced by low energy γ-rays. Although the tails of the high energy shower images will be mapped into the outer region equipped with large pixels, the quality of the image of the higher energy showers is not substantially deteriorated, as the geometrical size of the shower image is also larger.

Another crucial element forming the layout of the MAGIC telescope camera is a plate of light guides of "Winston Cone" shape in front of the photodetector pixel matrix. Basically, a Winston Cone is composed of parabolic curves which provide important benefits: a nearly 100 % effective camera area by minimizing the dead space between photosensors, and the rejection of a large fraction of the background light coming from outside the mirror area with large incident angles. The Winston Cones are made of plastic material covered with aluminized Mylar foils with ~ 90 % reflectivity.

All these elements are installed in the "camera housing" as shown in Fig. 4.3. A Plexiglas window on the front side of the camera protects the elements from adverse weather condition.

4.3.2　The camera photosensors

The main requirements for the photosensors used for the camera of the MAGIC telescope are summarized in this section.

- Diameter of the photosensor smaller than 30/60 mm to achieve a FOV of $0.1°/0.2°$ with one sensor (for the inner/outer parts).

- Sufficient gain to amplify the faint Cherenkov light, but not too high in order to avoid an instability of the gain due to the large current from the starlight and the light of the night sky. An optimal value for the gain is around 2×10^4.

- Fast response with a pulse of a few ns FWHM is important to reduce the contamination of the light of the night sky by means of a short integration time. It also allows an efficient coincidence trigger design for the detection of γ-ray signals.

- Wide dynamic range from a few photoelectrons (p.e.) up to 5×10^3 p.e. to detect the largest expected signals ($\sim 5 \times 10^3$ p.e. per pixel for a ~ 10 TeV γ-induced shower).

- Sufficient quantum efficiency (QE) in the range of the wavelength of the Cherenkov light spectrum at the ground (mainly between 300 to 600 nm) to also access low energy γ-ray events ($\lesssim 100$ GeV).

Photomultiplier tubes (PMTs) as widely used also in other IACTs satisfy these requirements and were therefore selected as photosensors for the MAGIC camera. It should be noted that for the sake of high QE (~ 50 %), the MAGIC collaboration also has considered and developed a new type of photosensor, namely the "Hybrid Photo detector (HPD)" (see details in Chapter 5).

Two types of PMTs are used for the MAGIC camera. They were constructed by the English company Electron Tubes: ET9916A with 25 mm diameter in photocathode for the inner pixels, and ET9917A with 38 mm diameter for the outer pixels. These PMTs have two characteristic features recommending them for application in the camera of the MAGIC telescope: a hemispherical-shaped photocathode and an only 6-stage dynode system in a circular-focused configuration. The hemispherical photocathode can reduce time jitter as the produced photoelectrons travel roughly the same distance between the photocathode and the first dynode. A 6-stage
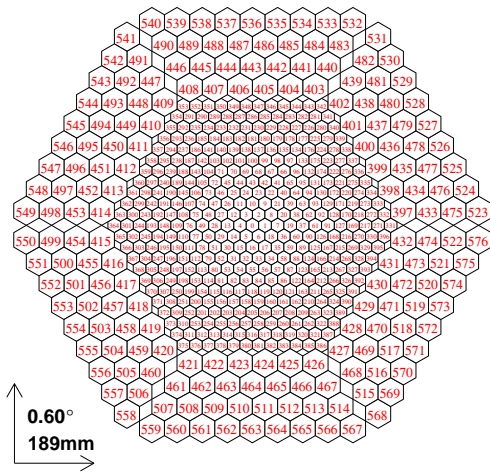
Figure 4.2: Schematic drawing of the MAGIC camera geometry

Figure 4.3: Photograph of the MAGIC camera. The silver colored element is a plate of Winston Cones. The PMTs are equipped behind the plate.

Figure 4.4: Photograph of PMTs for the inner pixels (ET-9116A). The left one is a bared tube and the right one is a tube with additional milky lacquer (see text).
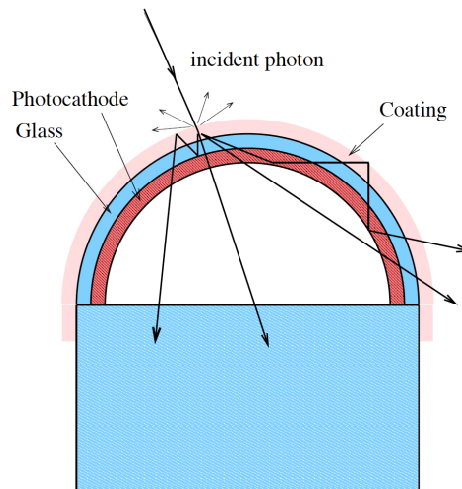

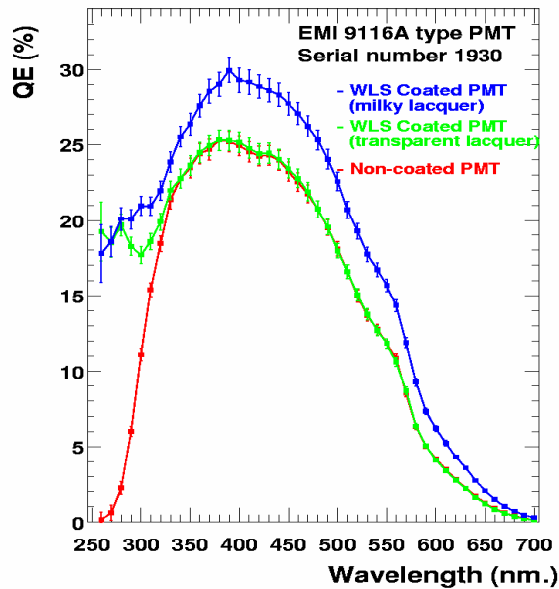Figure 4.5: Scattered photon trajectories by the coating in a hemispherical window PMT

Figure 4.6: Quantum efficiency of a PMT for the inner part of camera with different coatings.

dynode structure was chosen to obtain the relatively low gain (2×10^4) but still keep an equivalent collection efficiency and amplification at the first dynode compared to other typical PMTs with 10 or 12-stage dynode structure.

As one can see in Fig. 4.4, the photocathode glass of all PMTs is covered with a special "milky" coating which contains a wavelength shifter (WLS). Fig. 4.6 shows the QE of this type of PMT (ET9916A) in three different conditions: bare tube (red), transparent coating with WLS (green) and the milky coating with WLS (blue). One can see the enhancement of the QE only below 300 nm with the transparent WLS coating, while the QE is also enhanced in all wavelengths using the milky coating. The peak of QE reaches about 30% with the milky coating. The enhancement below 300 nm is due to the wavelength shifter (1.4 p-Terphenyl) while enhancement in other wavelength is supposed to be caused by scattering photon back towards the photocathode due to the "opaque" milky lacquer: As shown in Fig. 4.5, the photons may be scattered such that their paths inside the photocathode are extended and some of them can be trapped between the coating and the photocathode. A longer path of the photon inside the photocathode enhances the probability of being captured and emitting a photoelectron. In addition, taking advantage of the hemispherical shape of the photocathode, some photons can be deflected such that their trajectories cross the photocathode twice, thus having a second chance of being converted in case they did not interact at first instance. With this special milky coating, we were able to improve the photo collection efficiency relatively by about 20 % compared to that of uncoated PMTs.
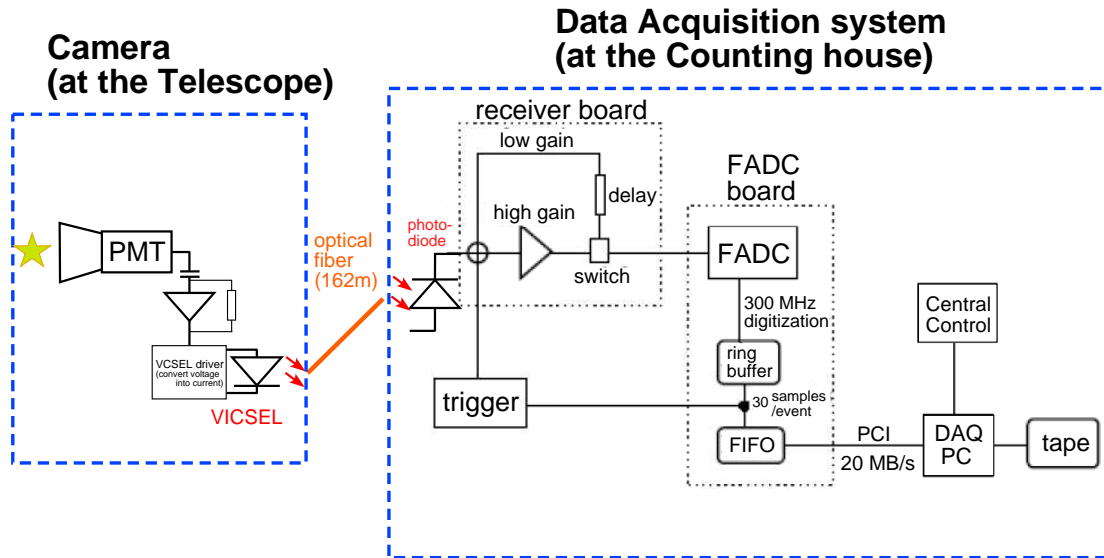
Figure 4.7: MAGIC hardware readout chain. The PMT signals are reconverted into optical pulses, transferred to the counting house, and fed into the trigger and DAQ systems.

4.4   The readout chain

In this section, the readout chain of the MAGIC telescope system is described. The readout chain is illustrated schematically in Fig. 4.7. The chain can be divided into the following three parts: (1) an analog optical transmission system, which is used to transfer the signal detected by the PMTs to the "counting house", where the components of data acquisition hardware are installed, (2) a trigger system, which has logics to detect interesting events, (3) an FADC system, which is used to digitize and record the data of the Cherenkov photon signals. These three parts are described in more detailed in following sections.

4.4.1   Analog optical transmission system

Since the analog output pulses of the PMTs should be transmitted with little distortion over a distance of ~150 m, to where readout electronics are installed ("counting house"), optical fibers were selected as signal transmitters instead of conventional coaxial cables. This system has several advantages, e.g., dispersion and attenuation of the signal are negligible, there is no crosstalk and no noise pick-up, and they have a very limited weight.

   After amplification, the electrical PMT signal enters a transmitter board, still on the camera, where it is transformed into an optical signal pulse by means of a Vertical Cavity Surface Emitting Laser (VCSEL). The output of the VCSEL is coupled to an optical fiber, which runs from the camera to the counting house with a length of 162 m. After transforming the light back into an electrical signal, the signal has a FWHM of about 2.2 ns, a rise time of about 1 ns and a fall time of about 1 ns.

4.4.2   Trigger system

Only the signals from the innermost 325 pixels of the camera are used for the trigger. As shown in Fig. 4.8, the trigger pixels are grouped in 19 overlapping macro cells of 36 pixels each. The decisions of the trigger system are segmented in several levels. The MAGIC trigger system currently consists of two levels:

Level 0: It consists of fast discriminators, which are adjustable and mainly reject signals from the light of the night sky fluctuations. The analog signal of a camera pixel is discriminated by a comparator that gives a logic output signal of approximately 6 ns duration as soon as the amplitude of the input signal exceeds a defined threshold. The effective trigger window is 5 ns. The discriminator thresholds are set to individual pixels by an 8-bit DAC which is controlled by a PC. The trigger rates of individual pixels are monitored by 100 MHz scalars and are used to dynamically adjust the discriminator thresholds pixel by pixel if the rate of the pixel exceeds a certain level. With this "individual pixel rate control" system, bright stars (typically, brighter than 4 magnitude) in the trigger area are effectively taken out of the trigger. The digital signals have individual computer-adjustable time delays to match the intrinsic time-offsets between the different readout channels from the camera.

Level 1 This level applies a simple N-next-neighbor logic during a few ns in one of the 19 hexagonal macro cells of 36 pixels (see Fig. 4.8). The multiplicity requirement of the cluster of next neighbors can be set by a PC during telescope operation. In standard operations, a 4-fold coincidence is required.

The thresholds are adjusted such that data are generally taken at a rate of 250 Hz.
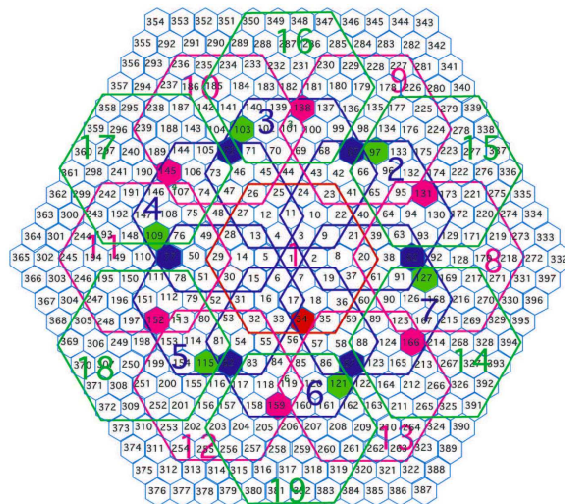
Figure 4.8: Schematics of the trigger: There are 19 overlapping trigger cells of 36 pixels each, corresponding to a total of 325 pixels in the trigger. The location of these 325 trigger channels is indicated (only the inner part of the camera pixels in which the trigger system is equipped is described).

4.4.3 The FADC system

Upon arrival of a trigger (level-1), the continuously digitizing FADC system writes out 30 time slices to a FIFO (first in, first out) buffer. Since the digitization speed is limited to 300 MSamples/s, the analog signals must be stretched in the receiver board to > 6 ns FWHM, so that at least 4 points can be measured for each pulse in order to reconstruct the pulse shape. To provide a dynamic range of $> 10^3$ with an 8-bit digitization system, a two-gain charge extraction is implemented to yield a "high-gain" and "low-gain" signals (cf. Fig. 4.7). In the high-gain readout circuit, the signal is amplified by a factor of 10. In the low-gain readout circuit, the signal is not amplified but delayed by 50 ns (15 FADC-time slices). If the high-gain signal exceeds 250 FADC counts, a switch for the low-gain readout is actuated and the low-gain signal is also recorded 15 FADC-time slices after the high-gain signal due to the delay circuit. Since a typical width of each digitized signal of 4-6 samples, the high- and low-gain signals do not interfere with each other.

4.5 Calibration system

In order to obtain calibration constants for converting an FADC charge to the physical quantity of photoelectrons, and an FADC timing into an absolute signal timing, an optical calibration system providing independent calibration methods has been installed. It consists of differently colored ultra-fast LEDs (370 nm, 460 nm and 520 nm). A box of the calibration system including these LEDs is mounted in the middle of the mirror dish and the LEDs illuminate the camera homogeneously. The light intensity is variable in the range of 4 to 700 photoelectrons per inner pixel. This enables to check the linearity of the readout chain and to calibrate the whole dynamic range. By triggering the MAGIC data acquisition system, calibration events are recorded in dedicated calibration runs as well as interleaved calibration events during regular data taking so as to trace PMT and VCSEL gain variations over time.

4.6 Monte Carlo simulation

The IACT method does not experimentally offer the possibility to evaluate the γ/hadron separation cut efficiency and the energy estimation by means of test beams of VHE γ-rays of known energy. Therefore, the operation of IACTs requires a detailed Monte Carlo (MC) simulation of γ-ray and hadron-induced air showers, as well as of the detector response. In the air shower simulation, the tracks and interactions of each particle are simulated to describe the development of electromagnetic and hadronic showers in the atmosphere. In the detector simulation, responses for the Cherenkov photons which are generated in the shower simulation are simulated in each hardware component of the telescope system. In this section, the details of the MC simulation for the MAGIC experiment are presented.

4.6.1 Air shower simulation

The development of γ- and hadron-initiated air showers is simulated with CORSIKA 6.019 (COsmic Ray SImulations for KAscade, [126]) with some custom options for the MAGIC telescope. CORSIKA simulates air showers based on interactions and decay processes of hadrons, muons, electrons and photons. Each particle in the showers is characterized by its energy, position, moving direction and arrival time. CORSIKA is divided into four sections for the simulation.

- Tracking of each particle: It takes into account the effect of ionization loss, multiple-scattering, geomagnetic effect, and decay processes for each particle.

- Hadronic interactions based on the model of "VENUS" [207] for particles with > 80 GeV

- Hadronic interactions based on the model of "GHEISHA" [98] for particles with < 80 GeV

- Interaction processes of electrons, positrons and photons (electromagnetic interactions) with EGS4 [73]

Several models are available for the simulation of the particle interactions in CORSIKA. In the MC simulation for the MAGIC experiment, above-mentioned models are used. The routines treating the Cherenkov radiation in CORSIKA have been supplied by the HEGRA Collaboration [172] (see also [126]).

In addition, the following custom options are implemented for the MAGIC experiment:

- Wavelength information of the Cherenkov photons: This is important for wavelength dependent detector response (see section 4.3).

- Information of the parent particle of the Cherenkov photon: With this information we can distinguish the original particle of each Cherenkov photon.

A brief summary of the parameters for the generation of MC samples can be seen in Table 4.1.

Table 4.1: Parameters for the generation of the MC samples.

Primary particle	γ-ray	proton
Energy range	10 GeV - 30 TeV	30 GeV - 30 TeV
Spectrum slop	$E^{-2.6}$	$E^{-2.75}$
Impact parameter range	0 - 300m	0 - 400m
Zenith angle	$0° - 45°$	$0° - 30°$
Azimuth angle	$0°$ and $90°$	

Due to historical reasons, attenuation effects of the Cherenkov photons in the atmosphere in the CORSIKA program are applied in a separate step after the air shower generation. Using the US standard atmosphere [149], Rayleigh scattering, Mie scattering and absorption by Ozone are taken into account to calculate the attenuation of light in the atmosphere (cf. section 3.4.3). The effects due to Mie scattering and the absorption by Ozone are estimated by means of the Elterman model [92].

4.6.2 Detector simulation

The detector simulation is subdivided into two steps:

Ray tracing

The rays of the Cherenkov photons are traced throughout the atmosphere until they reach the camera plane. To obtain their locations and arrival times in the camera plane, the real mirror dish structure of 956 tiles is simulated using the curvature radius and the center position for each mirror. In addition, the photon is smeared in position by the Point Spread Function (PSF) with a 2-D Gaussian shape ($\sigma = 5\,\mathrm{mm} \sim 0.017°$).

Camera and electronics

In the second step, the program simulates the behaviour of the MAGIC camera in a detailed way, taking care of the following specific effects:

- pixelization according to the camera geometry.

- adding the light of the night sky in Poisson distribution with a mean value of 0.13 photo-electrons per one inner pixel per ns.

- efficiencies for photon (photoelectron) detection in the various components in the camera

  - transmittance of the Plexiglas: 92%
  - photon collection efficiency of the light guide (Winston Cone): 94% max. (with photon incident angle dependence)
  - QE of the PMT: 30% max. (with wavelength dependence, see Fig. 4.6)
  - collection efficiency at the first dynode of the PMT: 90%

- generation of the analog pulse, including realistic pulse shape information and a single photoelectron response of the PMTs.

- trigger logic: Level 0 (discriminator), Level 1 (4-Next-neighbor logic). See details in section 4.4.2.

- electronic noise: Gaussian shape noise is generated both in the trigger logic and in the FADC based on measurement results for the readout circuits.

- digitization with a 300 MHz FADC using the actual signal shape for the single photoelectron response.

Furthermore, the overall light collection efficiency and PSF of the telescope has been tuned at the camera simulation level, using data from a comparison of the intensities of observed and simulated ring images of single muon events at low impact parameters [115] (see also section 6.3).

4.7 Observation mode and types of data runs

4.7.1 Observation mode

Two distinct observation modes have been used for the data taking with the MAGIC telescope. The advantages and disadvantages of each observation mode are briefly discussed.

ON/OFF observation mode

The telescope tracks a target source at the camera center during "ON" observation. This mode requires additional, so-called "OFF" observations, for estimating the background. During OFF observations the telescope should take data pointing to a region in which no γ-ray source candidates are expected. The OFF position ideally should have the same conditions as the ON position regarding the background light, the atmospheric conditions and the zenith angle range.

Wobble observation mode

This mode allows for simultaneous recording of ON and OFF data at different places in the camera [99]: The source position is displaced at a fixed distance off (0.4° for the MAGIC observations) the camera center. In total, 3 OFF regions are available: One position opposite to the source position (so-called "anti-source position") and two positions displaced by $\pm 90°$ from the source position. To avoid systematic errors due to the selected source position in the camera, source and background positions are regularly swapped (normally two positions; hence the name "wobble mode") every 20 min in our observations. In general, wobble observations guarantee a good match of ON and OFF data. An additional benefit of this mode is the best possible coverage in time for observations because dedicated OFF data do not need to be taken. A disadvantage of the wobble mode is that the off-center observations of the source have a somewhat lower efficiency than the normal "ON" observations, in which the source is located at the camera center. In addition, if strong inhomogeneities exist in the pixel responses of the camera, large systematic errors can occur due to the mismatch between data for the source position and data for background positions.

The data in this thesis were taken with the ON/OFF mode during the observations in 2005. The data in 2006 were taken with the wobble observation mode. The selected mode is specified for each observation in Chapter 7-10, where the details of the observation are reported.

4.7.2 Types of data runs

During normal data taking with MAGIC telescope, three different kinds of runs are performed.

- Data runs: The telescope tracks a position in the sky and an event is generated when a trigger occurs. Additional calibration events (see section 4.5) are interleaved (50 Hz) with the cosmic events.

- Calibration runs: The calibration box emits light pulses and an event is recorded after a synchronized trigger signal is sent to the DAQ. At least one dedicated calibration run using UV light has to be taken before the observation of each of the scheduled sources every night.

- Pedestal runs: Information of the light of the night sky background and other sources of noise is taken during a so-called pedestal run. The trigger is activated randomly, 1000 events are recorded with a trigger rate of 500 Hz. These data allow determining the baseline of the signal and its fluctuations for observations. At least one pedestal run is taken right before a group of calibration runs.

4.8 MAGIC-II

The MAGIC project is currently being upgraded to "MAGIC-II" by the construction of a twin telescope with advanced photosensors and readout electronics. MAGIC-II, the two-telescope system, is designed to achieve an improved sensitivity in the stereoscopic/coincidence operation mode and to simultaneously lower the energy threshold compared to the current MAGIC. In stereo observation mode, i.e. simultaneously observing air showers with both telescopes, the shower reconstruction and background rejection power are significantly improved. This results in a better angular and energy resolution and a reduced analysis energy threshold. The overall sensitivity is expected to increase by a factor of 2 to 3 (see Fig. 4.11). Following the results of a dedicated MC study showing moderate dependence of the sensitivity on the distance of the two telescopes, the second MAGIC telescope has been installed at a distance of 85 m from the first telescope.

In order to minimize the time and the resources required for design and production, the second MAGIC telescope is in most fundamental parameters a clone of the first telescope. Nevertheless, several improvements have been introduced in the second telescope.

- Larger mirror elements have been developed ($1\,m^2$) to reduce cost and installation efforts.

- Newly developed readout system features, i.e. the new 2GSamples/s digitization and acquisition system based on a low power analog sampler (Domino Ring Sampler) [206].

- A new modular design was adapted for the camera with a uniform pixel size in a round configuration. In the first phase, the camera will be equipped with PMTs of increased QE, while the modular camera design allows upgrades with high QE hybrid photo detectors (HPDs).

This thesis contributed to the development of the new design for the MAGIC-II camera; here we focus on a more detailed discussion on about the camera design.
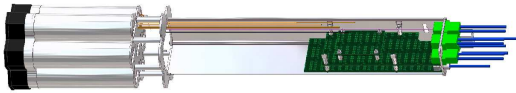
Figure 4.9: The 3-D drawing of one cluster of the MAGIC-II camera.
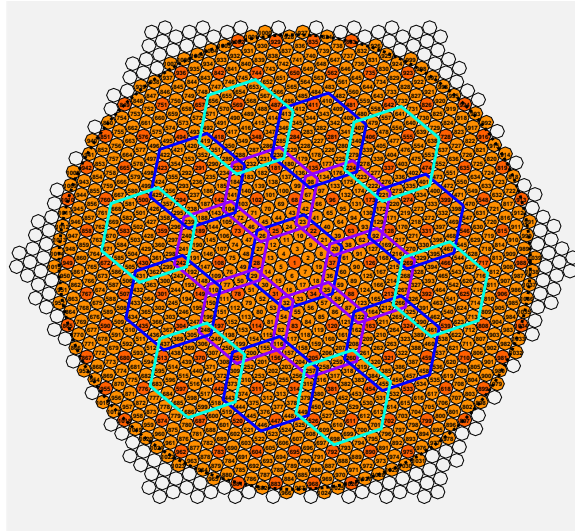
Figure 4.10: Schematics of the MAGIC-II camera. Only the colored pixels in a round configuration will be equipped with PMTs. The hexagonal shapes indicate the trigger region.

The camera for the second telescope

A cluster modular design has been chosen for the camera of the second telescope. Seven pixels grouped in a hexagonal configuration form one cluster, which can easily be removed and replaced (see Fig. 4.9). More important, it allows partial or full upgrade with improved photosensors. The new camera will be uniformly equipped with 1039 identical 0.1° FOV pixels in a round configuration. The schematics of the camera can be seen in Fig. 4.10. As indicated in the figure, the trigger area will be increased by 72% (compared to the first telescope camera), corresponding to the area of 2.5° diameter FOV.

In the first phase PMTs with increased QE will be used. The Hamamatsu R10408 6-stage PMTs with a hemispherical photocathode typically reach a peak QE of 34%. The PMTs have been tested for a low afterpulsing rate (typically 0.3% at a 4-photoelectron level), fast signal response ($\sim$ 1ns FWHM) and acceptable aging properties (Gain drops by 50% after $\sim$ 50000 hours of operation in the MAGIC camera) [138].

In the second phase, it is planned to replace the inner camera region with HPDs [125, 215] produced by the company Hamamatsu Photonics. These advanced photosensors feature peak QE values of 50% and will thus significantly increase the sensitivity for low energy showers. The flexible cluster design allows field tests of this new technology within the MAGIC-II camera without major interference with the rest of the camera. Once tests are successfully completed the whole central region of the camera will be equipped with HPDs. The details of the development of the HPDs are described in the next Chapter.
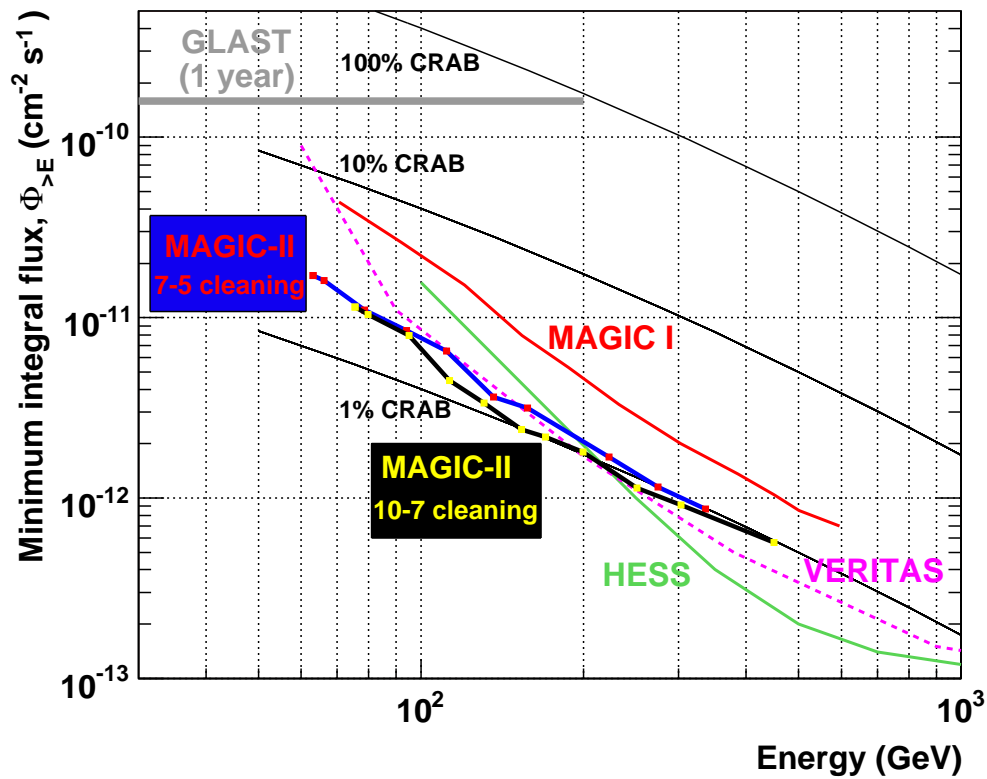
Figure 4.11: Sensitivity (required flux for 5σ detection with 50h observation) curves of several IACTs, including MAGIC-I (red) and MAGIC-II (blue and black). The difference between two lines for MAGIC-II is the analysis method (different image cleaning levels, see details in [74]). The 10% and 100% flux level of the Crab Nebula are also shown for comparison.

Figure 4.12: In the foreground the second MAGIC telescope. The structure is already fully installed. In the background the first MAGIC telescope which has been in scientific operation since summer 2004.

Chapter 5

High Quantum Efficiency Hybrid Photo Detectors

5.1 Introduction

Currently, photomultipliers (PMTs) are widely used as photosensors for IACTs because their performances make them well suited for this purpose (cf. section 4.3). For example, briefly, Cherenkov light flashes from γ-ray air showers have time spreads of 2-3 ns. Fast signal response is required for a short signal integration time to reduce light of the night sky (LONS) contribution. In addition, the total gain needs to amount to at least several tens of thousands to make detection of the faint Cherenkov light possible. On the other hand, in the photocathode of conventional PMTs the conversion efficiency from a photon (Cherenkov light) to a photoelectron - the so-called "quantum efficiency (QE)"- is only 20 to 30%. Therefore, an increase in the QE of a photosensor can provide effects equivalent to an increase of the mirror diameter of the telescope. It allows us to access a lower energy threshold in observations with IACTs.

In order to improve the observation performance, the MAGIC project will be upgraded to "MAGIC-II" by building a second 17-m diameter telescope at 85 m distance from the first tele-scope. One of the key tasks in the MAGIC-II project was the development of high QE Hybrid PhotoDetectors (HPDs) with a GaAsP photocathode [177, 164, 70] as an alternative type of photosensors to PMTs. For a high QE photocathode, Negative Electron Affinity (NEA) photo-cathodes are regarded as the preferred candidates. Especially, a NEA GaAsP type photocathode is a prime candidate to be used for photosensors in IACT because of its high blue sensitivity.

In conventional HPDs, the size of the GaAsP photocathode was too small (< 8 mm) to be used as a pixel element in the MAGIC telescope camera (the necessary pixel size being 30 mm). Recently, together with Hamamatsu Photonics, we succeeded in producing HPDs with a GaAsP photocathode with a 18-mm diameter. By using non-imaging light concentrators like, for exam-ple, Winston cones, one can efficiently compress the light flux from the required 30-mm pixel input size to the 18-mm size of the above-mentioned HPDs.

In this chapter, the development of these HPDs is reported in detail. I was responsible for this task and performed the measurements and simulation studies specified below.

5.2   Working principle

An HPD consists of a photocathode and of an Avalanche Diode (AD) serving as an anode. When applying a tension of several kV to the photocathode, the photoelectrons are accelerated in a high electric field and impinge onto the AD producing around 1000 electron hole pairs. This is the so-called electron bombardment amplification. The electrons subsequently induce avalanches in the active volume of the AD and provide an additional gain of $\sim$30-50 when a bias voltage of a few hundred volts is applied.
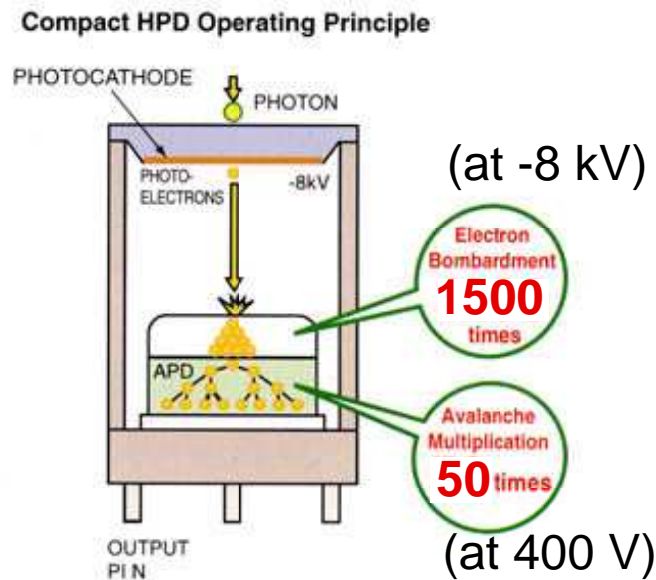
Figure 5.1: Schematic drawing of the HPD.

5.3   18-mm GaAsP photocathode HPD; R9792U-40

We developed a new type of HPD with an 18-mm diameter GaAsP photocathode for the MAGIC-II project together with Hamamatsu Photonics. This type of HPD was named "**R9792U-40**". A 3-mm diameter AD is equipped as an anode. Fig. 5.2 shows a dimensional outline of R9792U-40. A photo image with 7 tubes can be seen in Fig. 5.3. There are two cables for a high voltage to the photocathode and for a ground line. The bias voltage is applied via pins at the backside of the tube. Fig. 5.4 shows the internal divider circuit for the high voltage. An additional resistor with 50G Ω is installed to prevent possible accidental strong light. When such strong light hits the photocathode, a large number of photoelectrons are produced and lead to a high current. At the same time, a voltage drop occurs at the 50G Ω resistor and the photocathode ceases to receive a sufficiently high voltage for inducing photoelectrons toward the AD.
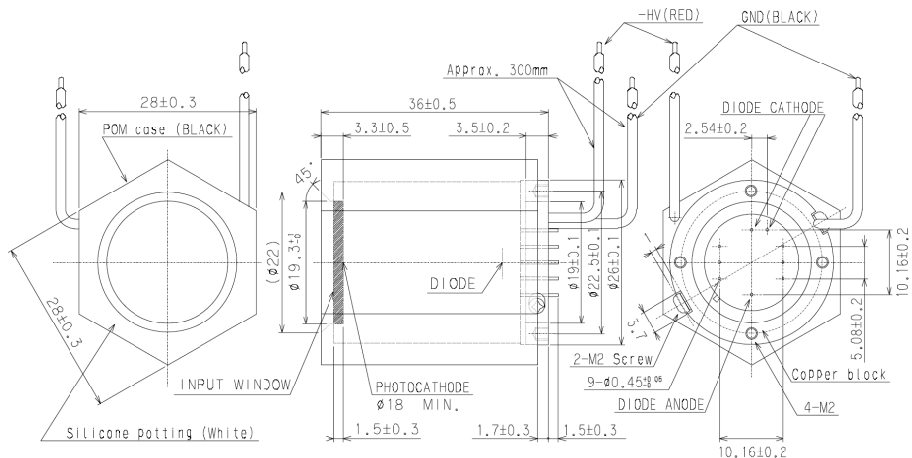
Figure 5.2: R9792U-40 Dimensional Outline.
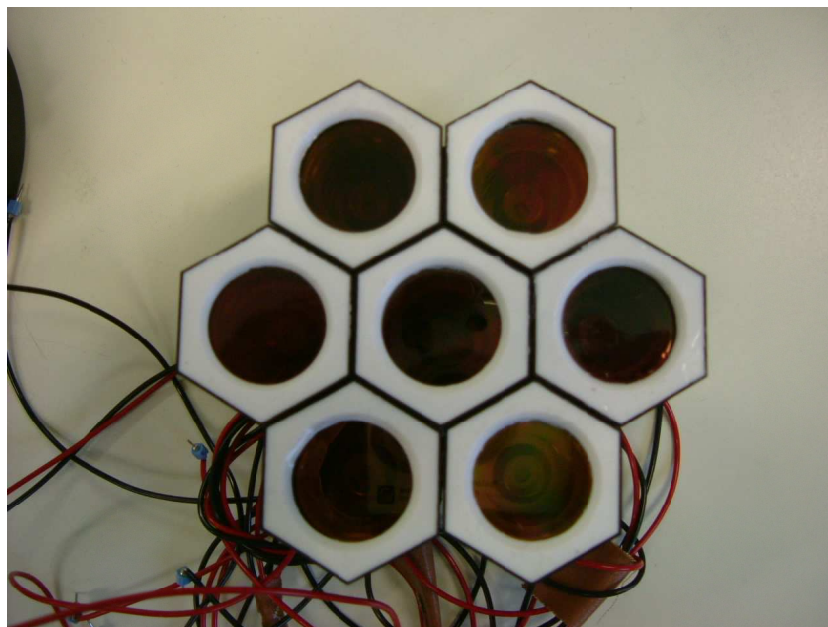
Figure 5.3: Photo image with 7 HPDs of R9792U-40.

5.4   Measurement set-up

A configuration of the measurement set-up can be found in Fig. 5.6. HPD measurements were performed under darkness inside a light-shielded box. The voltages for the photocathode and the AD were supplied separately using two high-voltage modules from outside during the measurements.

The gain measurements (section 5.5) were carried out with DC light. A red-LED was used (peak wavelength $\sim$ 640 nm) as a light source. The current was measured with an electrometer (6517A, Keitley).

In the measurements from section 5.6 to 5.9, pulsed light was used as a light source and the laser diode (PDL 800B, PicoQuant GmbH) as a pulse generator. Its wavelength was 393 nm and the time width was several tens of ps (FWHM). A 2 GHz high-speed amplifier with 40 dB (HSA-Y-2-40, FEMTO) was used to amplify HPD output signals. The signal was acquired by a 1.5-GHz bandwidth digital oscilloscope (LC684DXL, LeCroy) with 8 GSamples/s.

In these measurements, the circuit of "High Speed Light Detection Mode" as shown in Fig. 5.5 was composed for the signal readout.
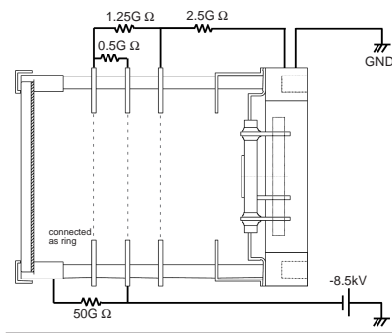
Figure 5.4: Schematics of internal divider circuit for high voltage.
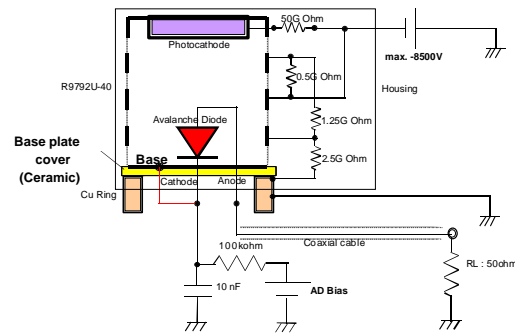
Figure 5.5: Circuit diagram for pulsed signal measurements (High Speed Light Detection mode).
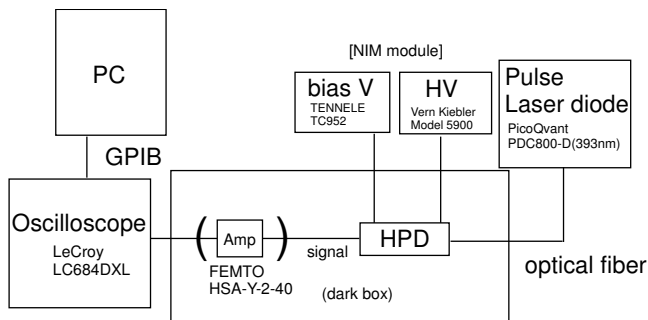
Figure 5.6: Diagram of a measurement set-up and its photo image.

5.5 Gain

Electron bombardment gains and avalanche gains of ADs were measured for the latest three tubes (serial# ZJ2051, ZJ2052 and ZJ2055). Results of the measurements are shown in Fig. 5.7. In the range of a few kV the bombardment gain was rising slowly due to the energy loss in the passive layer at the AD entrance window. Above 4 kV, the gain showed a linear relation with the photocathode voltage. The gain slope should follow a ~ 3.6V/gain, which corresponds to the energy necessary for creating an electron-hole pair in silicon. The gain reached about 600 at -5.0 kV and about 1500 at -8.0 kV. All three tubes showed almost identical gain characteristics with the function of the photocathode voltage.

Up to 100 V of the AD bias voltage, the output current remained constant; hence there was no avalanche gain (gain=1) in this range. It increased sharply, however, at several 100 V. An avalanche gain of 50 could be obtained around 350 to 450 V of the bias voltage. Unlike the bombardment gain, individual tubes showed different characteristic curves for the avalanche gain with respect to the applied AD bias voltage. Therefore, it is necessary to tune the applied bias voltage according to the gain characteristic of each tube for achieving equivalent avalanche gains from different tubes. Breakdowns of ADs occur around 400 to 500 V.

Finally, the overall gain could be achieved e.g., in tube ZJ2052 about 75000 at -8.0 kV of the photocathode at 450 V for the AD bias voltage.
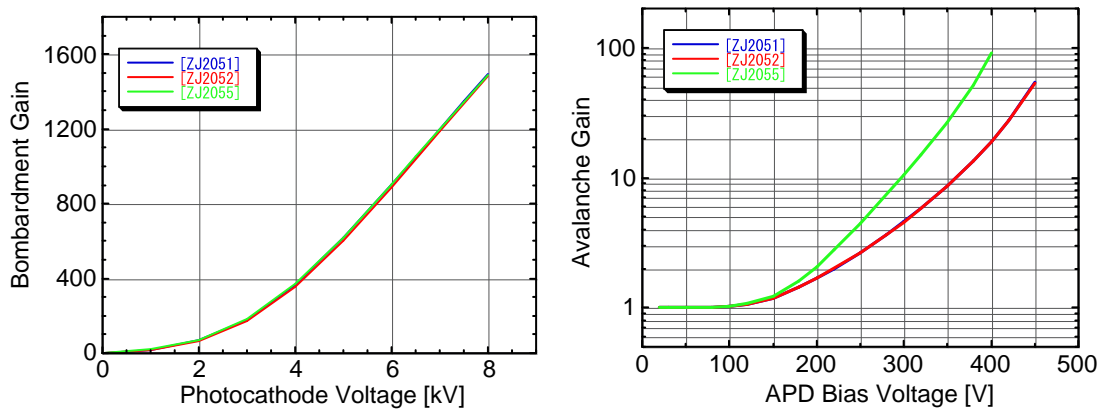
Figure 5.7: Gain measurements for three HPD tubes (serial# ZJ2051, ZJ2052 and ZJ2055). **[Left]** Bombardment Gain. **[Right]** Avalanche Gain.

5.6 Temperature dependence of an AD and the compensation circuit

Generally, an AD shows strong temperature dependence in their performance. The temperature dependence of the avalanche gain and the leakage current are shown in Fig. 5.8 with four different AD bias voltages. In every voltage, we can see about -2%/°C dependence in the gain. This gain
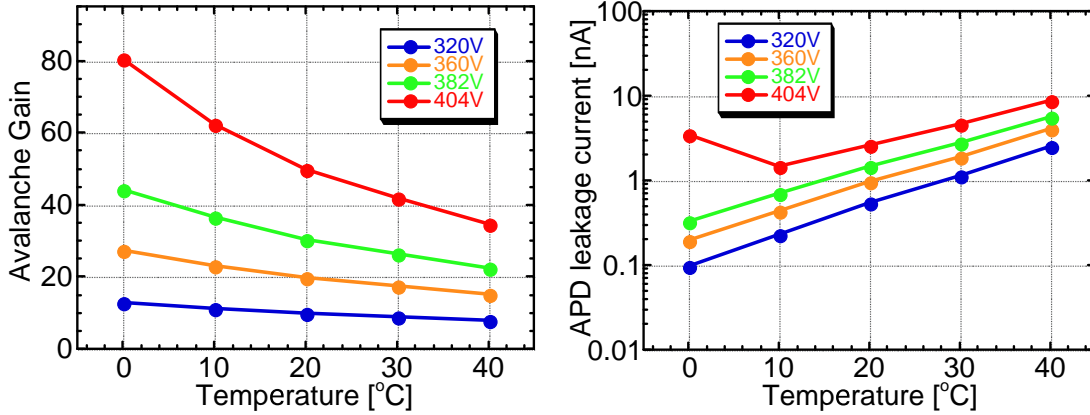
Figure 5.8: Results of the measurements of AD performances of a HPD (serial# MHP0080) with different temperatures (0 to 40 °C) with several fixed voltages. **[Left]** AD avalanche gain. **[Right]** AD leakage current. [The data were provided by Hamamatsu Photonics]

dependence is one order of magnitude larger than that of PMTs. Our telescope is operated in the field. Although a cooling system is installed in the camera to control the temperature, such strong gain dependence can cause instability of the telescope system and needs to be compensated. The leakage current increases by a factor of 2 with every 8°C increase of temperature. This suggests the main component of the leakage current caused by thermal noises. The high leakage current at a high bias voltage and a low temperature could be due to the tunneling effect. However, we have an additional constant DC current of a few μA due to the light of night sky (LONS) during the operation in the MAGIC camera. The leakage current is two orders of magnitude smaller than the contribution of the LONS and, therefore, can be neglected.

In order to reduce the temperature dependence we have considered installing a "temperature compensation circuit" to our HPD system in the MAGIC camera. Fig. 5.9 shows an example of the circuit, which consists of a "thermistor" (103AT-2, Ishizuka Electronic Corporation), three resistors and a DC/DC converter (APD 5P501201, Systems Development & Solutions) for the AD bias voltage. "Thermistor" is the generic name given to thermally sensitive resistors. The resistance value can be described with a function of temperature as follows:

$$R = R_{25} \cdot \exp\left(B\left(\frac{1}{T} - \frac{1}{273+25} \right) \right) \tag{5.1}$$

(R: resistance of the thermistor. R_{25}: resistance of the thermistor at 25°C. T: Temperature [K]. B: "B value [K]", which is a constant and depends on the material of the thermistor.) "103AT-2, Ishizuka Electronic Corporation", which was selected for our circuit, has R_{25} of 10kΩ and B value of 3976 K with a high accuracy: the tolerance of R_{25} and B is $\pm 0.5\%$.

We checked the performance of this circuit with a HPD (serial# ZJ2052) in a temperature regulated chamber. To make sure that the temperature in the chamber was well stabilized and there was no hysteresis, we measured it twice, i.e. first the temperature was raised from 20°C to 40 °C and then lowered to 20°C. The high voltage of the photocathode was fixed at -8 kV in order

to provide a consistently high value of Bombardment gain[1]. The avalanche gain at each point was calculated from the pulse area corresponding to the peak position of a single photoelectron (see Fig. 5.11).

Fig. 5.10 shows the results of the measurements. With this circuit, the temperature dependence was suppressed at the level of $\sim$0.3% / 1°C from 25°C to 35°C, which is the same level as that of PMTs. It should be noted that we selected a combination of resistors which leads to a local peak of the gain around 30°C in our measurements. That position can be easily shifted by changing the resistors of the circuit. In addition, together with a dynamical adjustment of the AD bias voltage by software, we can expect a more stable gain control system.
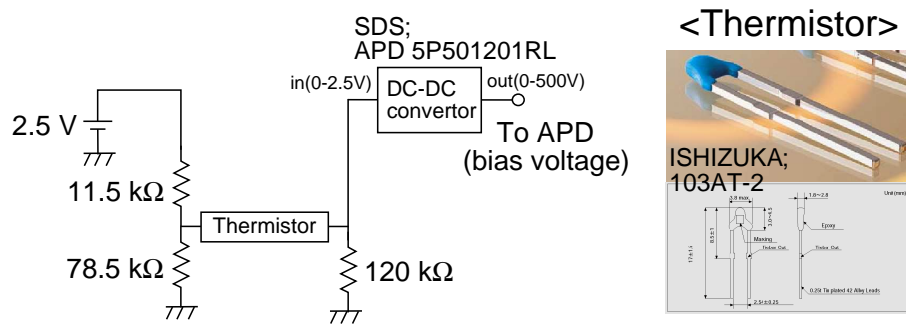
Figure 5.9: Schematic drawing of the temperature compensation circuit.
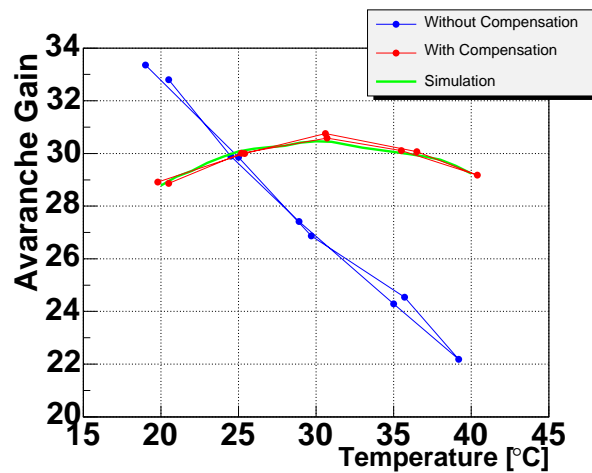
Figure 5.10: Results of the measurements of the AD avalanche gain with the temperature compensation circuit (HPD serial# ZJ2052). Points denote the avalanche gain at each temperature; without a compensation circuit (*blue*), with the compensation circuit *(red)*, simulation results of temperature compensation with this circuit (*green*). Two lines in blue and red represent measurements in the phases of increasing and lowering temperature.

---

[1]It has been confirmed that the Bombardment gain has no temperature dependence.

5.7   Time response

Fig. 5.11 shows the output signal with -8.0 kV (gain ∼1500) for the photocathode and an AD bias voltage of 450 V (gain ∼ 50). The intensity of input light corresponded to a single photoelectron (p.e.). The output signal was recorded with 2.1 ns of FWHM, 0.8 ns of Rise time and 2.5 ns of Fall time.

5.8   Amplitude resolution

As one can see in Fig. 5.11, multi-photoelectron peaks were well resolved at low light intensity. These peaks correspond to pedestal, 1 p.e., 2 p.e., 3 p.e. and 4 p.e. (from left to right). The HPDs show a much better signal resolution than that of PMTs, in which only the single p.e. peak can be resolved. The signal resolution is attributed to gain of the first stage. The HPDs have it at ∼1500 by the electron bombardment while normal PMTs have only about 10 at their 1st dynode.
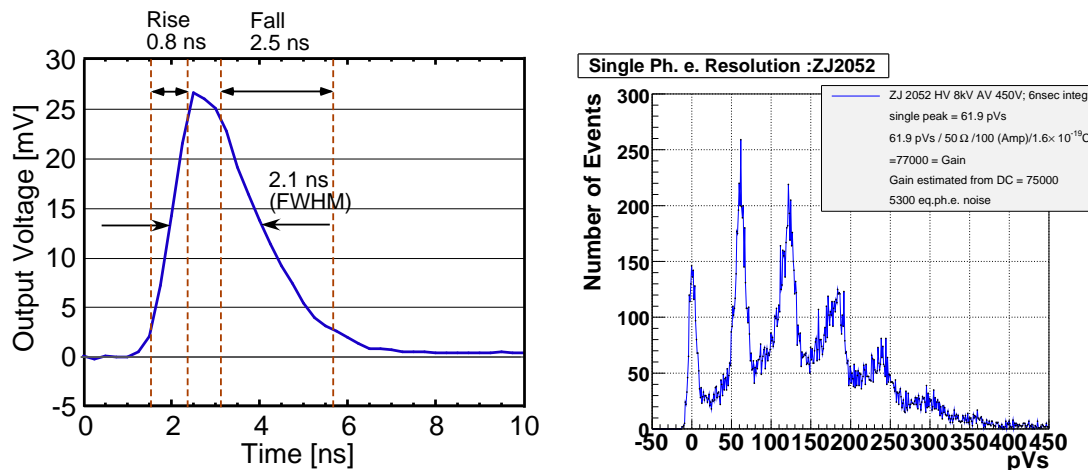
Figure 5.11: Signal measurements of HPD (serial# ZJ2052) at 8 kV for photocathode and 450 V for the APD bias voltage. **[Left]** Output signal shape. **[Right]** Signal amplitude resolution

5.9   Dynamic range

The dynamic range was measured by output-signal areas in the range of input pulse signals of up to ∼10000 p.e. as shown in Fig. 5.12. The amplifier was not used to avoid a saturation effect. For the small signal range (up to 4 p.e.), the signal linearity was estimated from a measurement result of the signal amplitude resolution (see section 5.8 and Fig. 5.11).

In the small signal range, multi-photoelectron peaks appear at regular intervals within a 1% error. The output signal area keeps a linear relation to the input pulse signal up to ∼5000 p.e. and begins to deviate by 5% at ∼7000 p.e..
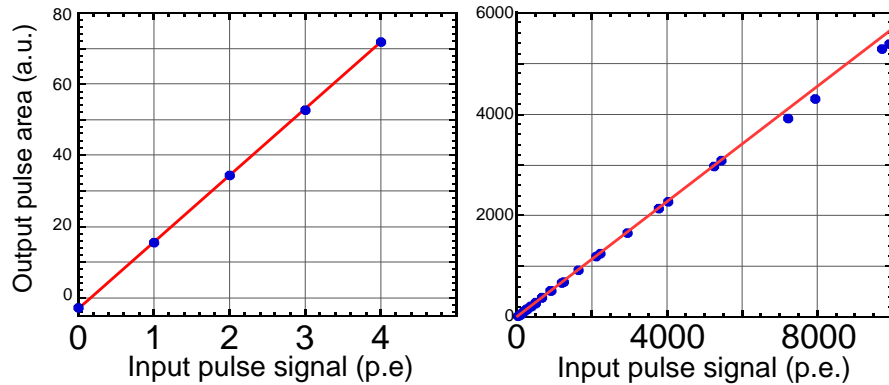
Figure 5.12: Dynamic range measured by comparing output signal areas with input pulse signals of up to 10 000 p.e.. **[Left]** Small signal region. **[Right]** Entire region.

5.10 Uniformity of the GaAsP photocathode

The uniformity of the GaAsP photocathode was measured with a light of 0.1-mm spot size by 0.1-mm scan pitch on the photocathode at Hamamatsu Photonics. The scans were done with respect to X-axis and Y-axis. The output current was measured at the anode (AD). During the measurement, -8kV for photocathode and 300 V for bias voltage for the AD were applied.

Fig. 5.13 shows the relative output current as a result of the uniformity measurement. The relative output current was defined with respect to the maximum current recorded during each scan. The result showed that the photocathode had a high sensitivity over 18mm in a diameter in both axes. An 18-mm effective area in the diameter of a photocathode was confirmed. The fluctuation of the photocathode sensitivity was no more than 15% at peak to peak value in both scans.
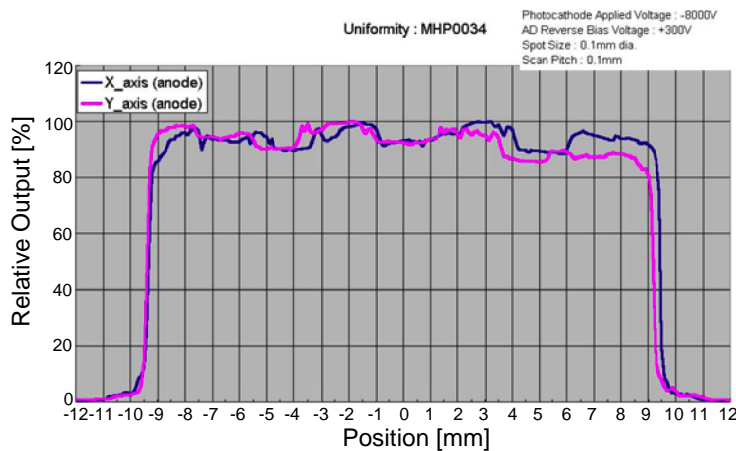
Figure 5.13: Results of the measurements for GaAsP photocathode uniformity (serial# MHP0034). The plot displays the relative output current during the measurements in each axis of the scan.

5.11   Quantum efficiency

We measured the QE in a range from 290 to 750 nm at 10 nm intervals using a spectrometer. Two light sources were installed in the spectrometer. One was a deuterium lamp for up to 400 nm and the other was a halogen lamp for above 400 nm.

The output current of the HPD was measured with a picoammeter Keitley-485 by shorting the AD anode with the cathode, and by applying -800 V to the photocathode. A calibrated pin-photodiode (S6337-01, Hamamatsu Photonics, calibration accuracy 2%) was used to obtain the absolute value of light intensity.

Fig. 5.14 shows a representative result of the measured QE of a HPD photocathode (serial# MHP0125) as well as the QE of the PMT used in the telescope of MAGIC-I [196] as a function of wavelength. The peak value reached 54% at around 500 nm.

In Fig. 5.15 one can see the distribution of the QE at 500 nm among recent 80 HPDs. Over 50 % of QE were obtained on average.

5.11.1   Wavelength Shifter application

Application of the Wavelength Shifting (WLS) technique can provide an increase in sensitivity in the UV region [70], where Cherenkov photons from air showers are more abundant. Tests of the WLS technique for our HPDs were carried out with a mixture of 0.03 g POPOP, 0.03 g Butyl-PBD and 1.5 g Paraloid B72 dissolved in 20 ml of Toluene. This solution was dripped onto the entrance window of the HPD, thus a thin and transparent layer was obtained. In Fig. 5.14 the resulting QE spectra with and without application of the WLS are also shown. The enhancement became obvious below 360 nm. However, a small drop in sensitivity occurred at around 380 nm because of the absorption by the shifter film.

5.11.2   Quality Improvements

Photon collection efficiency

In order to quantify the anticipated improvement when using HPDs for the MAGIC telescope, overall Cherenkov photon conversion efficiency was estimated by folding the QE and the Cherenkov photon spectrum from γ-ray showers simulated by *CORSIKA* 6.023. Table 5.1 shows the improvement of efficiency by using HPDs for four Cherenkov spectral types based on different zenith angles of the shower incident angle. The peak position of the Cherenkov spectrum shifts towards longer wavelengths at higher zenith angles because the shorter wavelengths are absorbed and scattered stronger by the atmosphere. The obtained values are normalized ones with respect to that of the currently used PMTs. This calculation includes differences (1) in the collection efficiency of light guides due to the difference in size (94% for PMT, 87% for HPD) and (2) in the first anode (dynode) collection efficiency (90% for PMT, 100% for HPD). The results show that the total photon conversion efficiency can be improved by about a factor of 2 compared to the PMTs. At higher zenith angles, the improvement can be even higher due to the red-extended
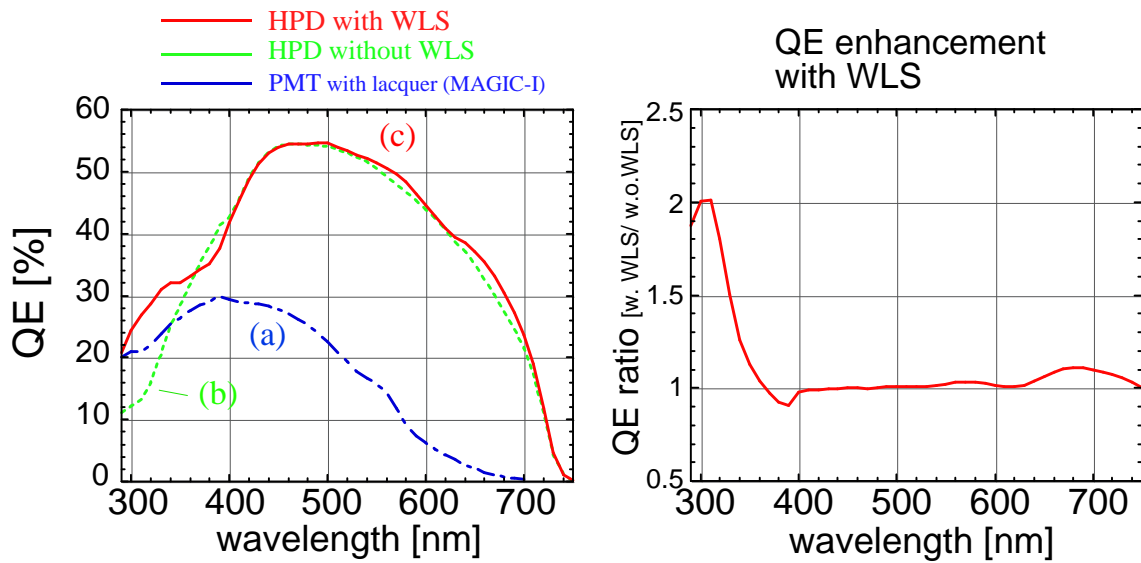
Figure 5.14: Results of the QE measurements. **[Left]** Measured QE spectra (HPD: serial# MHP0125). PMT ET-9116A with milky lacquer used in MAGIC-I [196] *(blue-(a))*, non-coated HPD *(green-(b))*, HPD with WLS *(red-(c))*. **[Right]** Enhancement ratio by WLS as a function of wavelength.
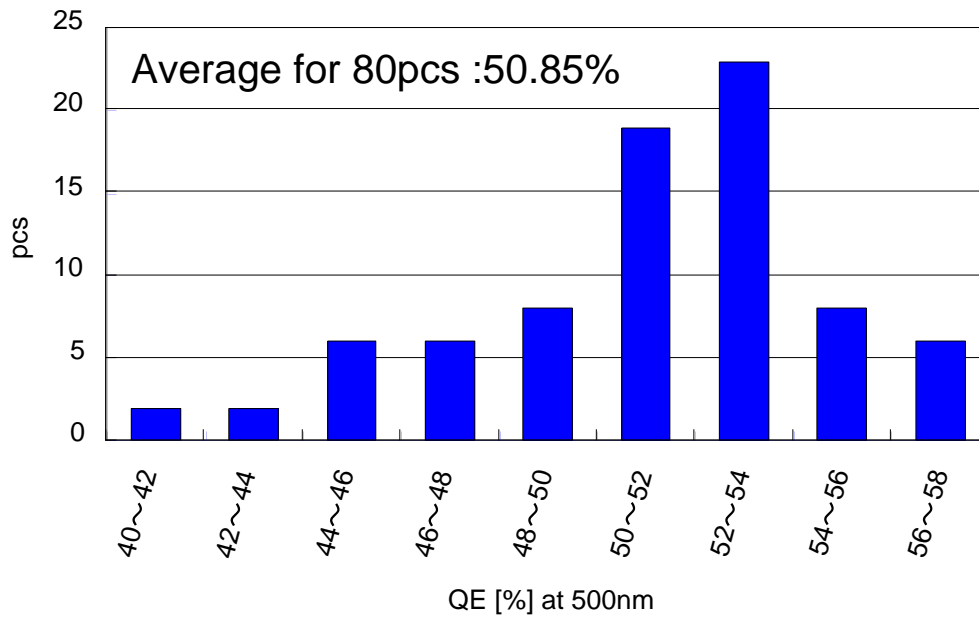

Figure 5.15: Distribution of QE at 500 nm among recent 80 tubes.

Table 5.1: Improvement of overall Cherenkov photon conversion efficiency when using a GaAsP HPD compared relative to PMT (PMT = 1).

Zenith Angle for spectral type	0°	25°	45°	60°
Non-coated	1.90	1.92	2.00	2.14
with WLS	1.99	2.00	2.07	2.17

sensitivity of the HPD. Depending on the observation zenith angle the WLS can provide an additional improvement of 3-9%.

Signal to Noise Ratio

Since the telescope is operated in the field, LONS should be taken into account for background light as "Night Sky Background (NSB)". Here, we used a measured LONS spectrum (see Fig. 5.21 [56]) to estimate the NSB rate with HPD based on the current measured value in the MAGIC telescope with PMT (0.13 p.e./pixels/ns).

- Cherenkov spectral type (two types):

    - primary energy of γ-ray: 40 GeV

    - shower inclination angle (zenith angle [ZA]): (a) 0°, (b) 60°

- the signal intensity: in the case of 10 p.e. for PMT

- QE curve: PMT (currently used in MAGIC), HPD (with WLS, in Fig. 5.14)

- Integration time: (a) 20 ns, (b) 5ns.

10 p.e. is one of the minimum requirements to be recognized as "signal" after background subtraction (see section 6.4 for "Image cleaning"). Since we are interested in lower energy events (hence, lower intense shower image), such a "low signal" condition was selected. Two integration time conditions were also considered: 20 ns and 5 ns, corresponding to the integration times for FADCs with 300MSample/s, and 2GSample/s[2], respectively. Here, we defined the Signal to Noise ratio as $S/\sqrt{(S+N)}$, in which S was the signal intensity and N was the estimated intensity of the NSB with a defined integration time.

The results can be seen in Table 5.2 and Fig. 5.16

---

[2]2GSample/s FADCs have been used in the current MAGIC system since February 2007 and will be used for the second telescope as well.

Table 5.2: Comparison of the Signal to Noise ratio.

Integration time	detector	Sp. type	Signal [p.e.]	Noise [p.e.]	Significance
20ns (300 MSample/s)	PMT		10	2.60	2.82
	HPD	ZA= 0°	21.1	9.02	3.84
	HPD	ZA= 60°	23.3	9.02	4.10
5ns (2 GSample/s)	PMT		10	0.65	3.06
	HPD	ZA= 0°	21.1	2.25	4.37
	HPD	ZA= 60°	23.3	2.25	4.61
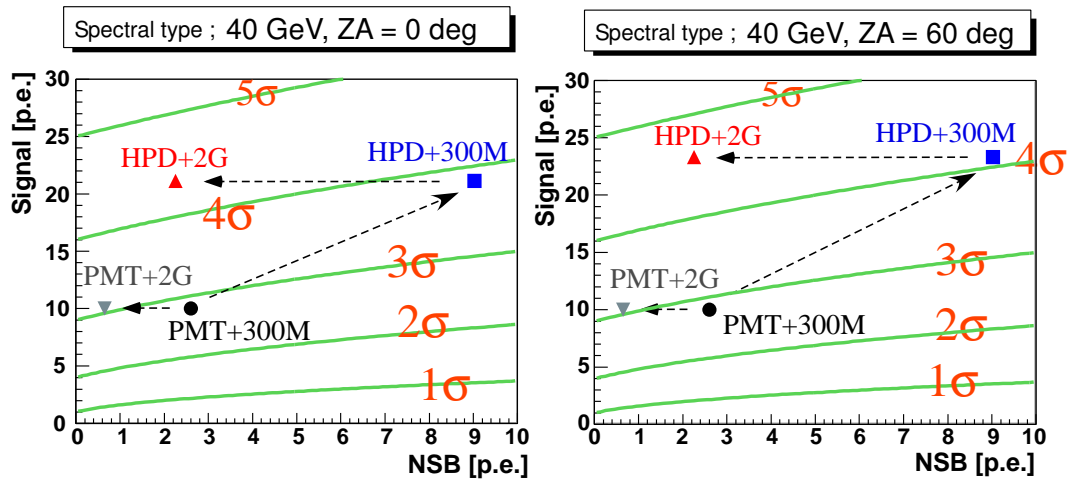
Figure 5.16: Signal to Noise ratios in different conditions. The condition of each point (the type of detectors and sampling frequency of the FADCs) is denoted in the plot. The green lines represent contours of the Signal to Noise ratio between 1 to 5 in the NSB-signal space.

5.12   Lifetime of the HPD with a GaAsP photocathode

Since photosensors of IACTs are constantly exposed to LONS during operation, their photocathodes are required to maintain their sensitivity over several years of operation. However, the type of photosensors with a GaAsP photocathode has never been used under such conditions before. Measurements were carried out in order to understand the aging properties of the HPD. Here we define the lifetime as the period after which the sensitivity degrades by 20 % from the initial value.

5.12.1   Measurements

The photocathode aging tests were performed with 5 tubes in total. 4 tubes [tube serial# MHP51, 55, 67, 133] were measured at Hamamatsu Photonics and 1 tube [MHP100] at MPI. High voltage for the photocathode and bias voltage of AD were constantly being applied throughout the measurements. The high voltage value was set to be -8 kV for all tubes, while the bias voltages were adjusted for total gain to be ∼50000 at Hamamatsu, and ∼45000 at MPI for each tube. A halogen lamp (IWASAKI) without any filters was used as a light source and its intensity was monitored by a pin-photodiode during the measurements to ensure stability of the light source. The measurements were conducted under two different conditions of light intensity at Hamamatsu. For one tube [MHP51], the intensity was adjusted for an initial output current of the AD at 10 μA (with gain of 50000), which corresponds to an intensity about 3 times higher than that of typical NSB conditions at La Palma (∼72pA at photocathode. The calculation was based on the measured LONS spectrum Fig. 5.21 [56]). An initial output current of 50 μA (with gain of 50000), corresponding to about 14 NSB level, was set for another 3 tubes [MHP55,67,133]. In the MPI measurement for one tube [MHP100], the initial output current was 100 μA (with gain of 45000), corresponding to about 31 NSB. The output current of the AD was recorded for several thousand hours while the photocathode was constantly exposed to light. The total exposure times were 5000h [MHP51], 2000h [MHP55], 2000h [MHP63], 4500h [MHP133] and 350h [MHP100] (This difference is due to the measurement setupĄfs availability at individual times.). In addition, gains (both of bombardment and avalanche), AD leakage current and QE were measured each 600h, 1000h and 2000h of the exposure time for MHP55, and, in addition, the photocathode uniformity after an exposure of 4500h for MHP133 was also measured.

5.12.2   Results

The results of the AD output currents for each tube during the aging measurement are shown in Fig. 5.17 and summarized in Table 5.3. For comparison, all results are plotted in one figure with a scaled exposure time by the same NSB intensity in Fig. 5.18. All but one tube [MHP51, 55, 67, 133] reached 80% in their output current after more than 10000 hours of the scaled exposure time. Given the fact that the estimation of the total operation time of IACTs is about 1000 hours in 1 year, we expect the HPDs to have lifetimes of more than 10 years of operation with the MAGIC telescope under the nominal NSB conditions at La Palma. The total charge on the photocathode during a lifetime is estimated to be about 3.85 mC on an average of 4 tubes. It corresponds to

about 190 C in AD output with a gain of 50000. The remaining one tube [MHP100] did not degrade enough for us to derive a lifetime value, but we can see a similar tendency as in the other tubes in the output current curve in Fig. 5.18.

Fig. 5.19 shows results of gains, AD leakage current and QE at each intermediate step (at 0, 600, 1000 and 2000 hours of exposure) of the measurements for MHP55. Degradation could be seen in the bombardment gain and the QE, while the avalanche gain kept the same amplification as the initial value. From our results, one can realize that the drop of the AD output current after long exposure to light is caused by not only the degradation of the QE (photocathode) but also of the bombardment gain. The decrease of the bombardment gain can be compensated by (1) an increase in the voltage applied to the photocathode or (2) an increase in the avalanche gain. With option (2), the signal amplitude resolution will become worse due to the lower amplification at the first stage. This is, however, not a serious effect for photosensors of IACTs because they are not used in photon-counting mode, and a slightly worse resolution will not impair the telescope performance.

The QE finally reached a level of about 80 % of the initial value after 2000 hours of exposure time (Fig. 5.19-d), while the output current dropped to as low as 68 % of the initial value. Therefore, we can expect a longer lifetime if we estimate the lifetime only from QE degradation (= lifetime of the photocathode). For the MHP55 tube, for example, lifetime estimated by QE only, corresponds to 30000 hours of the scaled exposure time to 1 NSB level, while lifetime estimated by the overall output current corresponds to 11000 hours. This issue shall be investigated more profoundly. In this thesis, conservatively, we regard the "lifetime estimated by the overall output current" as "lifetime" of the HPD tubes.

The photocathode uniformity at the end of the measurement for MHP133 is also shown in Fig. 5.19-e. Interestingly, the degradation of the QE showed a dependence on the position on the photocathode. A huge drop could be seen at the central part of photocathode. One can assume that the degradation of the QE is related to the "Ion feed back effect". The "Ion feed back effect" causes molecules on the surface of the AD to be ionized by the impingement of photoelectrons with a certain probability. Due to the mechanical structure and the electric field inside the tube, one can expect that such ions would likely hit the central area of the photocathode and damage it.

AD leakage current was also measured as one can see in Fig. 5.19-(b). It was increasing as the exposure time became longer. However, the absolute value (~ 10 nA) is still negligible compared to the estimated NSB contribution ($\sim$ a few μA).
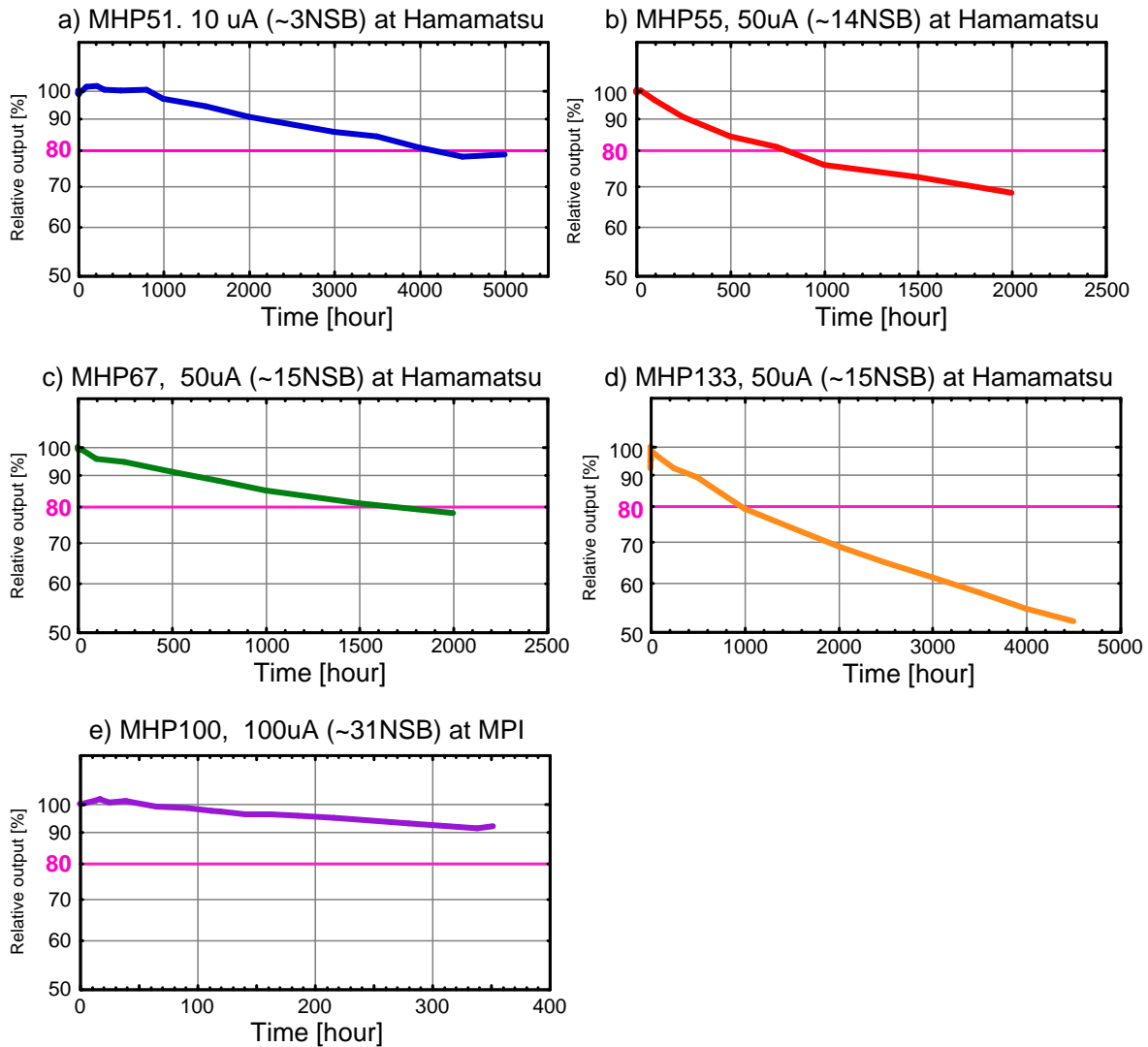
Figure 5.17: Measured AD output current relative to the initial values of 5 tubes during the aging measurements. On top of each plot, serial number of the tube, initial AD output current and the corresponding NSB intensity, measurement place (Hamamatsu or MPI) are denoted. The curves describe the variations in relative value of the AD output current of each tube as a function of exposure time (X-axis) to the light. The scale of the X-axis differs plot to plot. The horizontal pink lines denote the "lifetime" of our definition. The Y-axis is described in log scale and the minimum value is 50% in each plot.
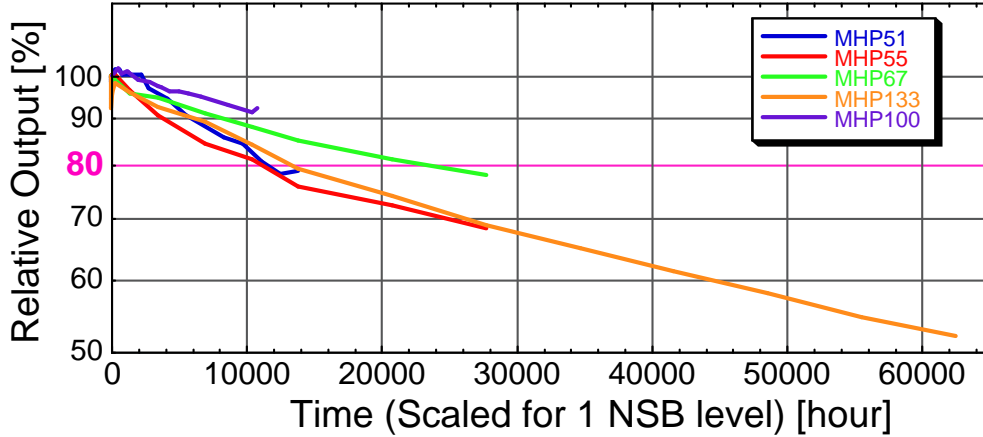
Figure 5.18: Comparison of the aging measurements for 5 tubes. The exposure time (X-axis) is scaled by the light intensity of the NSB contribution at La Palma with the MAGIC telescope. The horizontal pink lines denote the "lifetime" of our definition. The Y-axis is described in log scale and the minimum value is 50%.

Table 5.3: Summary of the results of the aging measurements. First four tubes were measured at Hamamatsu. The last one was measured at MPI. Description of columns: (1) Serial number of the HPD. (2) Initial value of the output current of anode signal. (3) Total gain applied during the measurement. (4) Total exposure time to the light. (5) Final output current relative to the initial value. (6) Corresponding NSB level of the input light intensity used for the measurement (1 NSB = 72 pA at photocathode). (7) Estimated lifetime from the measurement result with respect to the background light intesisty of the 1 NSB level. (8) Estimated total charge at the photocathode during the lifetime.

(1)	(2)	(3)	(4)	(5)	(6)	(7)	(8)
HPD serial#	initial output	gain	total exposure	final output	NSB level	lifetime (with 1 NSB)	total PhC charge during the lifetime
MHP51	10 μA	50000	5000 h	78.8%	2.8	11500 h	3.0 mC
MHP55	50 μA	50000	2000 h	68.1%	13.9	11000 h	2.9 mC
MHP67	50 μA	50000	2000 h	78.0%	13.9	23000 h	6.0 mC
MHP133	50 μA	50000	4500 h	52.0%	13.9	13500 h	3.5 mC
MHP100	100 μA	45000	350 h	92.0%	30.9	n/a	n/a
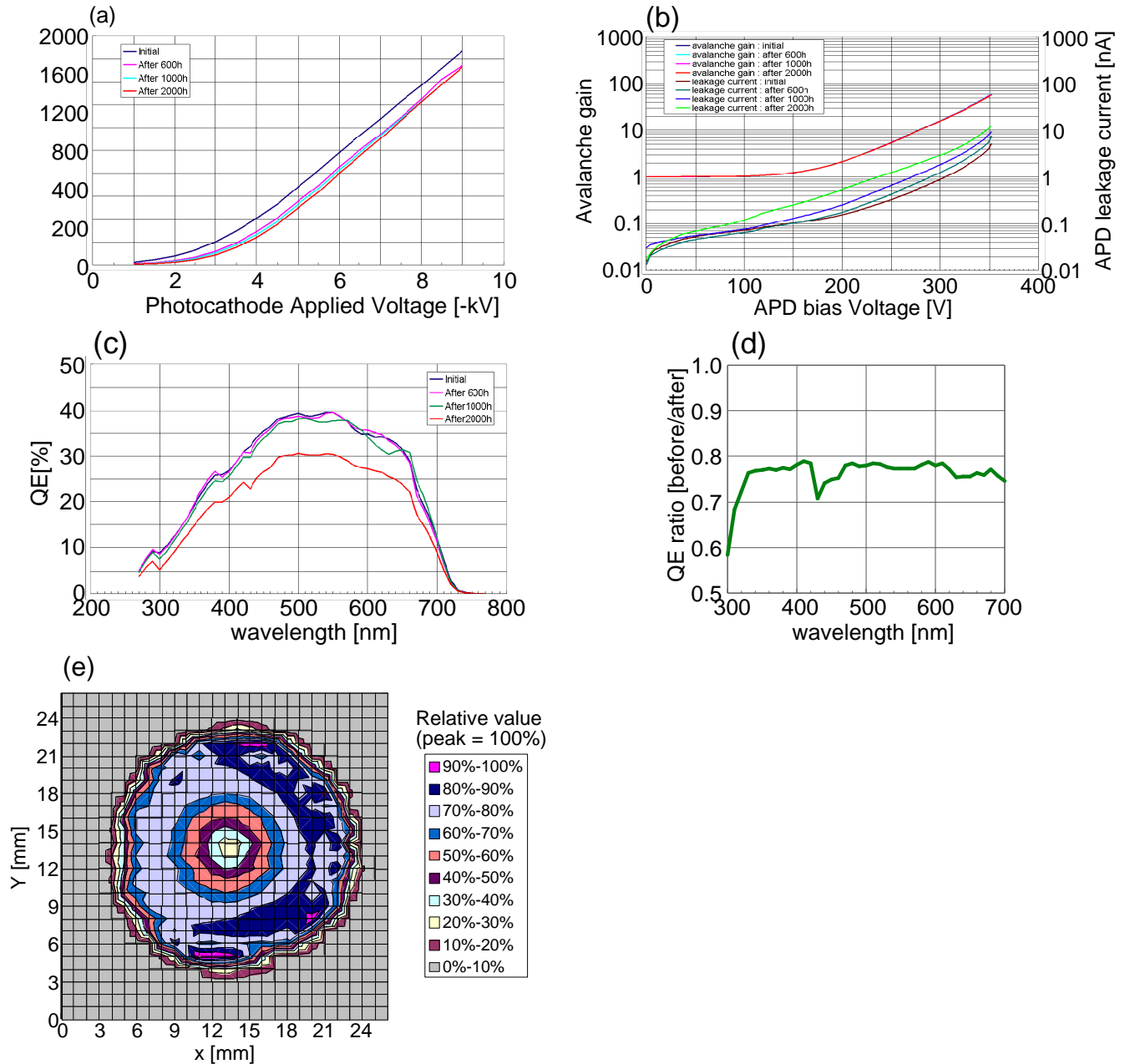
Figure 5.19:　Variation of the HPD performance [MHP55. MHP133 only for (e)] during the aging measurements. (a): Bombardment gain (initial, 600h, 1000h, 2000h). (b): Avalanche gain and APD leakage current (initial, 600h, 1000h, 2000h). (c) QE (initial, 600h, 1000h, 2000h), (d) Ratio of QE between before measurement and after 2000h. (e) Photocathode uniformity.

5.12.3 Simulation with starlight for realistic conditions

In order to confirm the durability of HPDs with a GaAsP photocathode under the realistic conditions of background light, a simulation with starlight and LONS was performed with an imaging camera composed of about 500 HPD tubes. Stars were selected using the "Hipparcos Catalogue" in sky fields around 10 typical observation targets as listed in Table 5.4. Only stars brighter than 11 magnitudes were used because stars with less intensity than that magnitude contribute less to the background light than diffuse NSB. As mentioned before, we assumed 1000 hours of observation time per year; thus, 100-hour observations could be allocated for each source in this simulation. The telescope motion for tracking the object was also considered. Since the telescope was installed with Alt-Az mount a star position on the camera is following a rotation curve as described in Fig. 5.20. We also assumed that the telescope tracked each source up to each maximum zenith angle defined in the Table 5.4. Intensities of starlight were simulated with the following parameters.

- Black-body type spectral shape

- Spectral type (e.g., O5, B4 ...) was used for specifying the temperature of the black-body radiation spectrum.

- Apparent visible magnitude and wavelength. The absolute flux from a star of apparent visual magnitude $m_V = 0.00$ at 550 nm : 3.64×10^{-9} $[\mathrm{J \cdot s^{-1} m^{-2} nm^{-1}}]$ [188].

- Absorption in atmosphere by Rayleigh, Mie scattering and absorption by Ozone. They are estimated using *CORSIKA* code (cf. section 4.6.1)

- Efficiency of the detector responses: mirror reflectivity, transmittance of Plexiglas, photo collection efficiency of light guides and QE of HPD are included.

An example of the simulated starlight can be seen in Fig. 5.20-(b). This is the result of a star "ζ-Tauri", whose spectral type is "B4"; apparent visible magnitude is "3.02" and location is $1.13°$ off the Crab Nebula. In the figure, the starlight of (1) the original spectrum (black-body with given spectral type and apparent visible magnitude), (2) the spectrum at 2200 a.s.l. (after attenuations by the atmosphere) and (3) the final spectrum (including until QE of HPD) with the star location at the zenith angle of $15°$ in the sky are drawn. The final intensity corresponds to 176 p.e. ns^{-1} with $239 \, \mathrm{m}^2$ mirror.

Fig. 5.22~5.24 shows full simulation results using 10 nominal targets in Table 5.4. The distribution of the total charge of pixels, relative sensitivity and the charge distribution on the camera plane are described. The relative sensitivity is calculated on the basis of the result of our aging measurements (3.85 mC in the photocathode for 20% degradation). In the plot of the camera plane, (c), one-bin size corresponds to $0.1 \, \mathrm{deg} \times 0.1 \, \mathrm{deg}$ area, which is almost equivalent to the area size for one pixel of the camera. After one-year of operation (Fig. 5.22) none of the tubes reaches its lifetime. Two peaks are evident in the charge distribution on the camera plane. They are caused by the light of ζ-Tauri, which is the brightest star in the simulation. After 5 years of operation (Fig. 5.23) , a few pixels will be dead. We can easily exchange a few dead
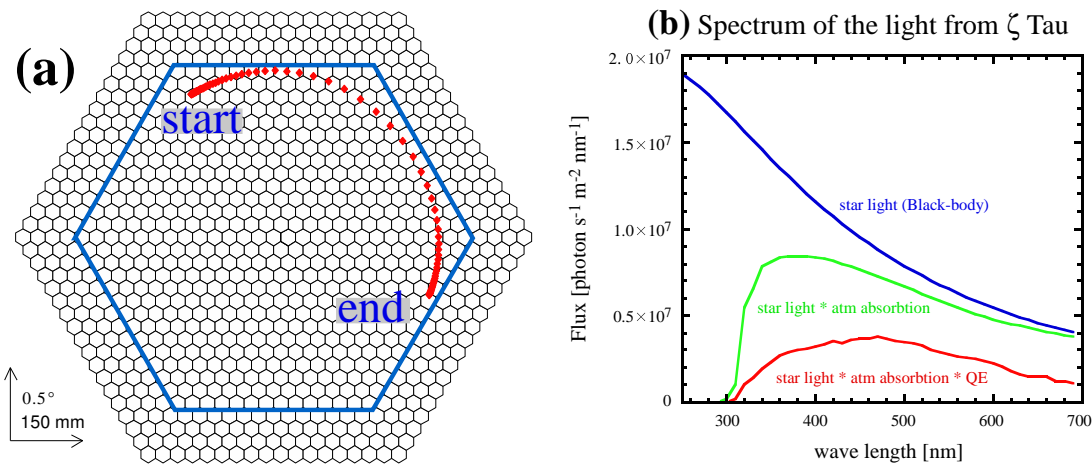
Figure 5.20: An example of starlight simulation with ζ-Tauri. (a) Star position on the camera during tracking the object (until ZA = 45°). Dots are plotted with a 4-min interval. (b): starlight spectrum: original starlight with black-body radiation (Spectral Type B4 ~ 17500 K) (*blue*), after attenuation by the atmosphere (*green*), final spectrum at the camera (*red*).

pixels for new ones. Even after 10 years of operation (Fig. 5.24) , only a small number of tubes lose their sensitivity. Many may still possess more than 80% of their initial sensitivity.

As a result, only bright stars like ζ-Tauri will damage the HPDs in addition to LONS. In fact, the expected number of such stars (brighter than 3.5 magnitude) in the field of view of the HPD camera ($\sim$5 deg^2) is only 0.034. The results of this simulation indicate that the HPD camera can keep its quality over 10 years with only a small number of replacements of the dead tubes damaged by intense light from bright stars.

Table 5.4: Objects selected in the star simulation.

Object name	Num. of star < 11 mag	Brightest star [mag]	Max.ZA [deg]
Crab	22	3.02	45
3C66A	21	6.74	30
Mkn421	24	7.01	30
1H1426	17	6.38	30
Mkn501	16	7.26	30
1ES1959	18	5.23	45
BL Lacertae	24	7.01	30
1ES2344	34	6.41	30
Galactic Center	25	4.84	70
Cas A	27	4.90	40
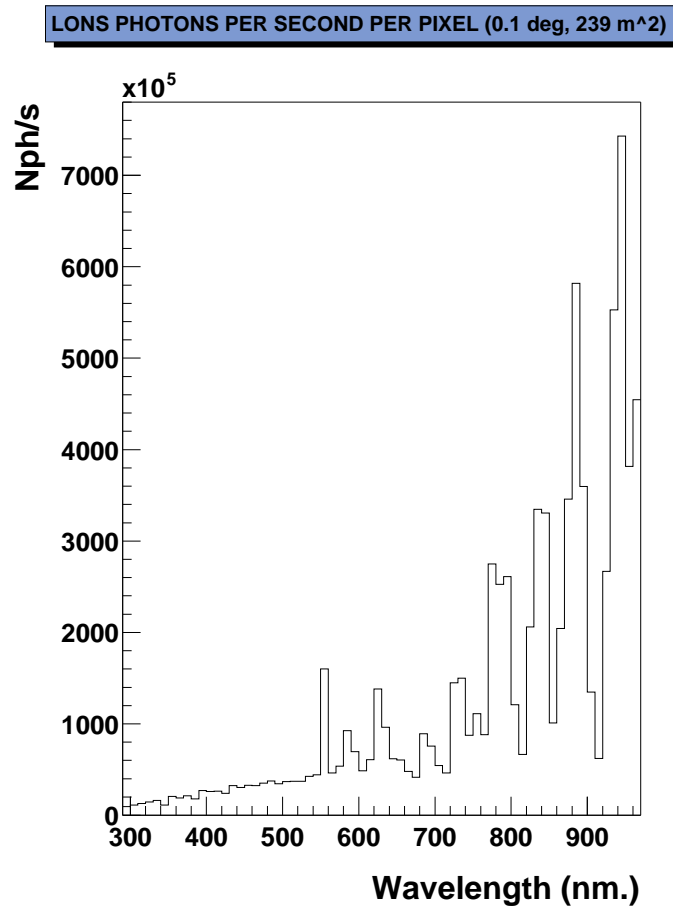
Figure 5.21: Spectrum of light of the night sky. The scale is converted to per pixel size of the MAGIC telescope camera with 239 m² mirror
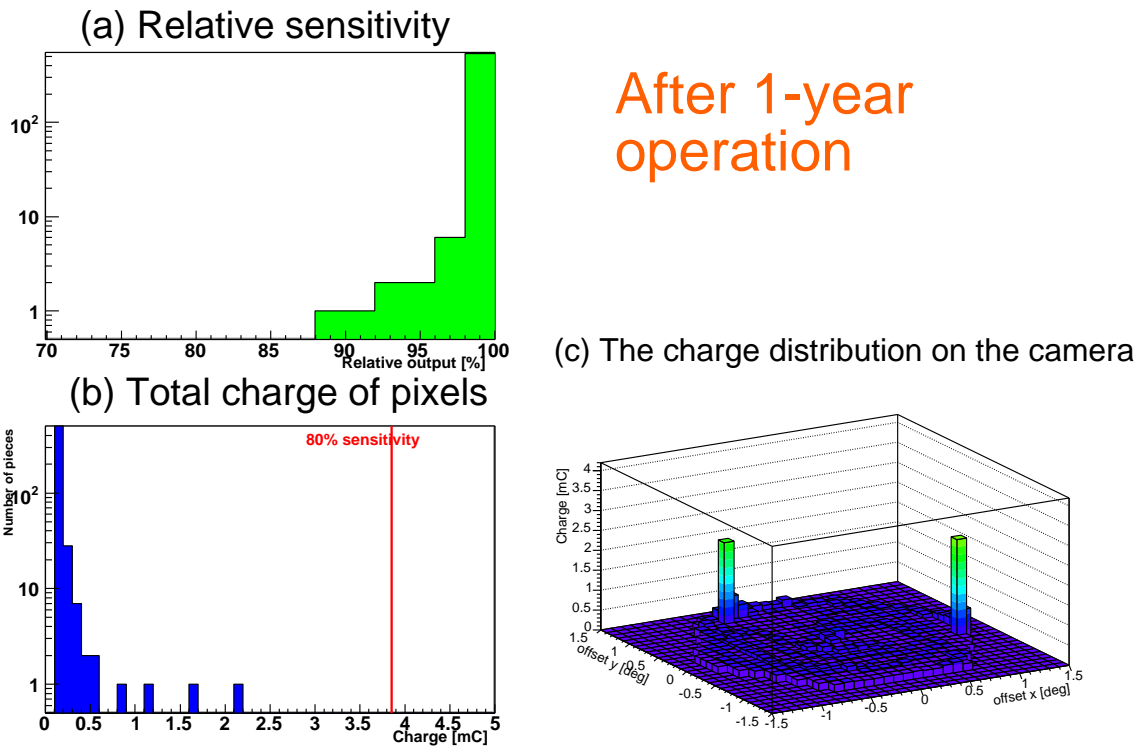
Figure 5.22: Results of the starlight and NSB simulation after 1 year of operation. (a) histogram of relative sensitivity of each pixel. (b) histogram of the total charge of each pixel. The red line indicates the corresponding total charge at lifetime. (c) charge distribution on the camera plane.

(a) Relative sensitivity

After 5-year operation

(b) Total charge of pixels

(c) The charge distribution on the camera
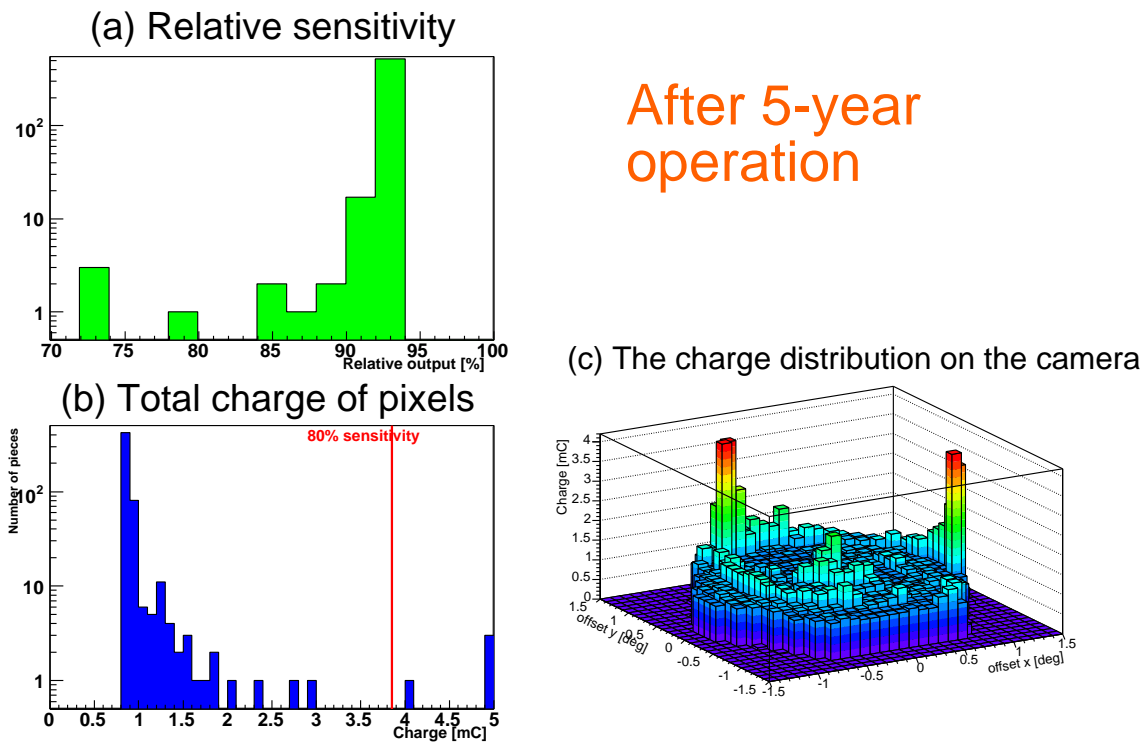
Figure 5.23: Results of the starlight and NSB simulation after 5years of operation.

(a) Relative sensitivity

After 10-year operation

(b) Total charge of pixels

(c) The charge distribution on the camera
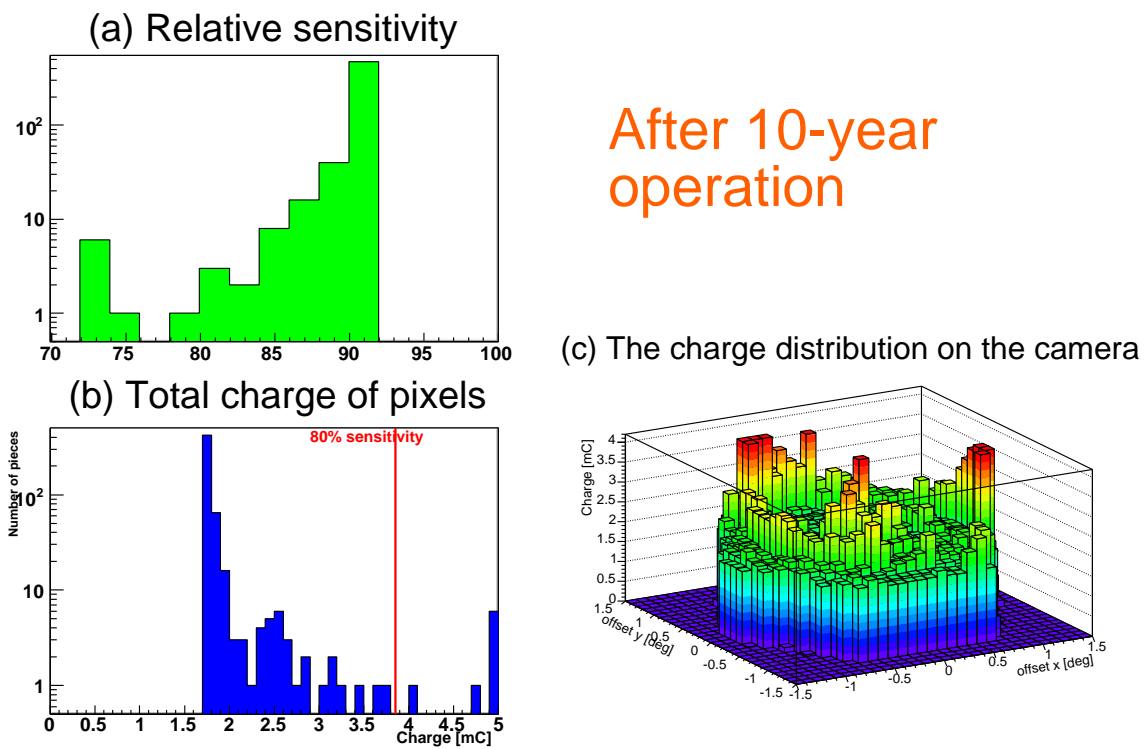
Figure 5.24: Results of the starlight and NSB simulation after 10 years of operation.

5.13   Test operation

A test operation of HPDs has been planned in the second MAGIC telescope camera. At the first stage, PMTs will be used as photosensors in the camera of the second telescope. To facilitate an upgrade to HPDs, the camera is designed with cluster modules in order to have compatibility between PMTs and HPDs. Each cluster consists of 7 pixels. The cluster modules allow us to exchange the photosensors easily. We are considering three steps for installing the HPDs in the MAGIC camera as shown in Fig. 5.25. In the first step, (a) 6 clusters (42 HPDs in total) will be installed outside the effective camera area of PMTs. (There are some free spaces at the edge of the camera due to its geometry). During this stage, we will try to define and solve all problems that might possibly occur in when using HPDs as photosensors in the MAGIC camera. In the second step, (b) we plan to arrange 19 clusters (133 pixels) for both HPDs and PMTs symmetrically with respect to the camera center. Observations will be conducted with this configuration to detect cosmic γ-ray events (e.g., from the Crab Nebula) for comparing HPD and PMT performance. Finally, (c) upon successfully completing these tests, the whole central region of the camera with 61 clusters (427 pixels) will be equipped with HPDs instead of PMTs.
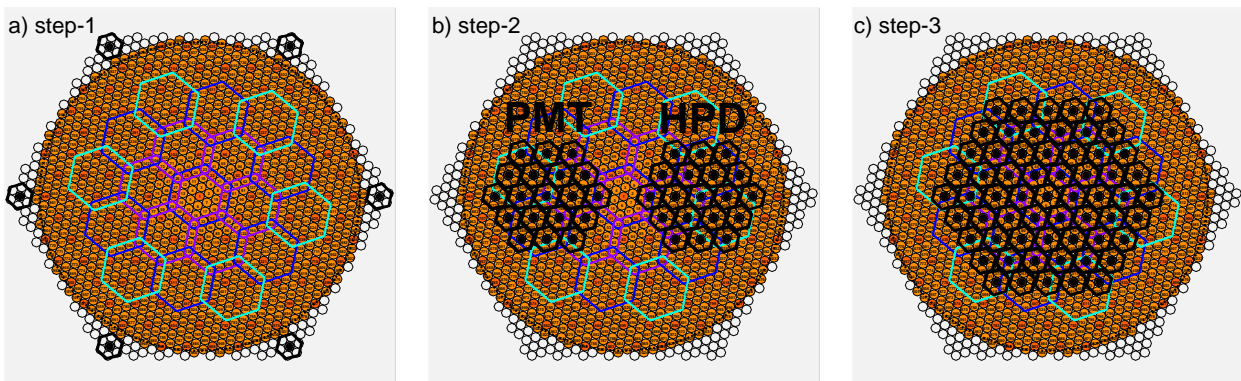
Figure 5.25: Planned HPD arrangements in each step (left to right) for the field test in the camera of the second MAGIC telescope. A black hexagon represents one HPD cluster. The brown colored area represents the effective camera area.

5.14   Summary

In order to obtain lower energy threshold in the MAGIC project, we developed a new type of HPD with an 18-mm diameter GaAsP photocathode together with Hamamatsu Photonics as one of the key tasks within the MAGIC-II project.

A total gain of several tens of thousands could be achieved in nominal operation voltages. The avalanche gain showed a strong temperature dependence ($\sim$2% / 1°C). However, installing a "temperature compensation circuit" based on a "thermistor" to the HPD system, we could reduce the dependence to $\sim$0.3% / 1°C.

The tube showed a fast response to light. An output signal was recorded with 2.1 ns of FWHM. Clear peaks up to 4 p.e. could be resolved in the signal amplitude resolution. The output signal area kept its linearity up to $\sim$ 5000 p.e. of the input light intensity.

An 18-mm effective area in the diameter of the photocathode was confirmed with a 15% fluctuation at peak to peak. The peak of the QE spectrum reached 54% around 500 nm and the tests of the WLS technique demonstrated an increase of sensitivity in the UV region and provided an additional improvement of 3-9% for total Cherenkov light. Compared to the currently used PMTs in MAGIC-I, the overall Cherenkov photon conversion efficiency would be improved by a factor of 2. This can be seen as equivalent to increasing the mirror diameter from 17 m to 24 m.

Aging test measurements showed that the GaAsP photocathode can be expected to have a lifetime of more than 10000 hours for the MAGIC telescope operation. Realistic simulation studies of background light including starlight based on real starfields showed that only bright stars would damage HPD pixels. The expected number of such bright stars (brighter than 3.5 magnitude) in the field of view of the HPD camera ($\sim$5 deg^2) is only 0.034. Therefore, the results of our simulation indicate that the HPD camera can maintain its quality over 10 years with only a small number of replacements of dead tubes damaged by intense light from bright stars.

The new type of HPD with an 18 mm GaAsP photocathode is ready to be used in IACTs with low threshold settings. After some field tests planed in 2008, we intend to upgrade the camera of the second MAGIC telescope from PMTs to HPDs.

Chapter 6

Analysis methods for the MAGIC telescope observation

In this chapter, the standard chain of the MAGIC data analysis is described. The software package is called the standard MAGIC Analysis and Reconstruction Software (named "**MARS**").

6.1 Charge and arrival time reconstruction

6.1.1 Signal extraction

The MAGIC telescope uses a 300 MHz FADC system to sample air shower signals. Charge and time information of the signal is extracted with the aim of minimizing the effect of the night sky background (NSB). For that purpose, a "*digital filter*" signal extractor, defined as the standard signal extractor in MARS, is applied. In the *digital filter*, the signal is calculated as the weighted sum of n consecutive FADC slices, i.e. the number of slices to be summed up into a tuneable parameter of the extractor. Since the pulse shape is dominated by the electronic pulse shaper, a numerical fit is possible. The weights are determined by taking into account the expected pulse shape known from the pulse shaper and from MC γ simulations. A more detailed description of the extraction method is given in [42].

6.1.2 Pedestal evaluation and subtraction

Shower signals always comprise the contamination by NSB and some accidental light (e.g. artificial light from a bypassing car, stray light). Since the output pulse signal of the PMT is AC-coupled, the NSB does not change the pedestal level of the FADC. Instead, the NSB intensity can be estimated by fluctuation of the pedestal because the fluctuation is proportional to the square root of the NSB photoelectron rate. It should be noted that noise from readout systems can also contaminate the FADC signal. In our system, however, the NSB is usually a dominant component for the pedestal fluctuation.
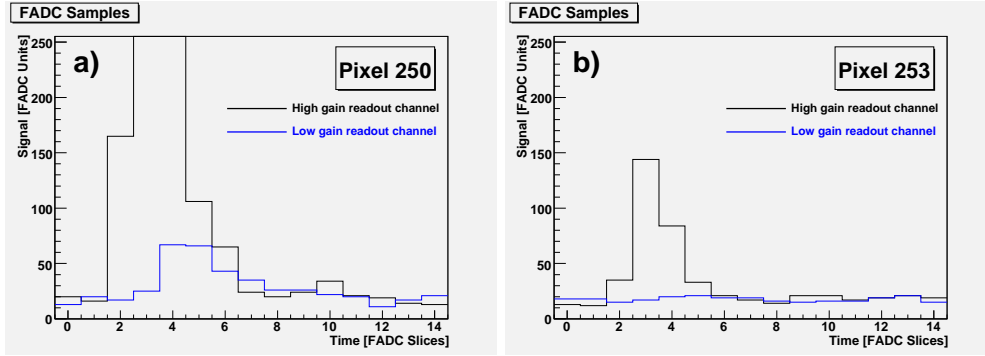
Figure 6.1: FADC signals. The signal in the high gain readout channel is drawn as a black line. The low gain readout signal is in blue. **[Left](a);** The signal in the high gain readout channel was saturated. The signal of the low gain readout channel was used. **[Right](b);** No signal was seen in the low gain readout channel, so the FADC slices in this channel are used for the evaluation of the pedestal and the pedestal fluctuation.

The pedestal and the pedestal fluctuation in the MAGIC data analysis are evaluated in two different ways: (1) By estimating from a dedicated pedestal run in which no cosmic signals are expected to be caught by the random trigger. (2) By using the region of the last 15 slices. This region is allocated to the low gain readout channel. However, if no saturation occurs in the high gain channel (as happens for most of the events), the low-gain pulse cannot be seen there. Consequently, in that case there is no signal contribution in this region (see Fig. 6.1). During observations, the average mean pedestal for each pixel was dynamically evaluated from 2000 measurements each.

6.2   Calibration

The integrated charge of the extracted signal is given in units of FADC counts. In addition to the relative calibration of the pixels for obtaining a uniform response for a given input light, an absolute calibration is needed to compute the conversion factors from FADC counts into the number of photoelectrons (p.e.) arriving at the first dynode of the PMTs. Dedicated calibration runs are used and the conversion factor is calculated with the "F-Factor" method. In this method, assuming a Poissonian variance of the number of photoelectron arriving at the first dynode of the PMTs, a uniform photoelectron detection efficiency, and a constant excess noise introduced by the gain fluctuations, the mean number of p.e. $\langle n \rangle_{\text{p.e.}}$ reaching the first dynode is given by [178]

$$\langle n \rangle_{\text{p.e.}} = F^2 \frac{(\langle Q \rangle - \langle P \rangle)^2}{\sigma_Q^2 - \sigma_P^2} \tag{6.1}$$

with the mean charge of the distribution $\langle Q \rangle$, its standard deviation σ_Q^2, the pedestal $\langle P \rangle$ and the error σ_P^2 introduced by NSB fluctuation, electronic noise and extractor uncertainties (all in FADC

units). The excess noise factor F is defined as

$$F = \sqrt{1 + \frac{\sigma_G^2}{\langle G \rangle^2}} \qquad (6.2)$$

This factor originates in the statistical fluctuations in the amplification of the electrons in the PMT dynode system. $\langle G \rangle^2$ and σ_G^2 can be measured in the laboratory by using the single photo-electron response of the PMTs. Based on the measurements of PMTs of the MAGIC telescope, this value is adapted at 1.15 [105].

Then, the conversion factor from FADC counts to p.e. for each pixel is directly obtained from:

$$Conv_{\text{FADC}\rightarrow\text{p.e.}} = \frac{\langle n \rangle_{\text{p.e.}}}{\langle Q \rangle - \langle P \rangle} = F^2 \frac{(\langle Q \rangle - \langle P \rangle)}{\sigma_Q^2 - \sigma_P^2} \qquad (6.3)$$

Bad pixel treatment: Typically about 4% of the pixels cannot be correctly calibrated because of hardware problems or contamination by the strong light from bright stars. These pixels are tagged as "bad" pixels and have to be specially treated for the analysis because their information is wrong and can distort the images. The criteria for the identification of bad pixels are: (a) pixels with no PMT existing (a central pixel, blind pixels), (b) pixels showing large fluctuations in the extracted signal or too low values of the fluctuations, (c) pixels with a large deviation of the pedestal RMS with respect to the mean value for the entire camera, or (d) pixels illuminated by very bright stars, which results in an increase of both the pedestal fluctuation and the DC values. Instead of excluding those bad pixels from analysis, their signals are replaced by an average value of the signal in the closest pixels.

6.3 Muon ring analysis

The optical point spread function (PSF) and relative overall light collection efficiency of the MAGIC telescope can be monitored using isolated muons hitting the reflector [115]. The geometry and the energy of the muons are reconstructed from the measured ring images and compared with Monte Carlo (MC) predictions. The amount of Cherenkov light produced by muons can be modeled with small systematic uncertainties. Muon ring images are recorded during normal observations with a rate of about 1 Hz. A continuous calibration can therefore be performed with no need for dedicated calibration runs. These monitoring results are available in every observation. The PSF calculated from Muon rings agrees well with the one measured from star images. So far, the PSF showed some small changes caused by degradations (possible damage due to heavy snow or simple aging effects) or by improvements (intensive works for adjustment of the mirror alignment or upgrading of the active mirror control system). The parameters of the MC simulation samples are adjusted based on these results. In the MAGIC data center, several types of MC samples which were generated with different values of PSF are available. The best matched type of MC samples among them can be selected according to the telescope conditions in each observation period.
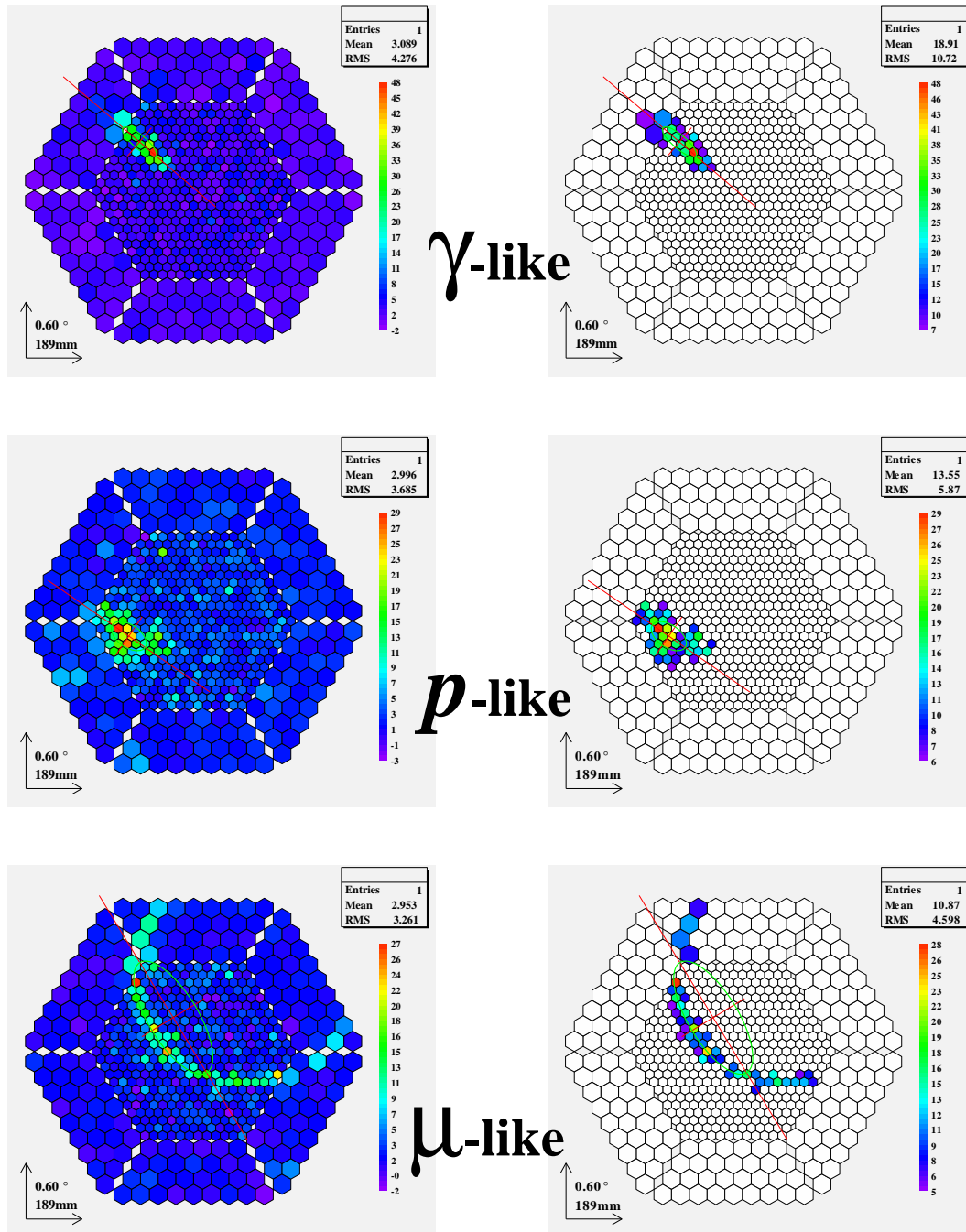
Figure 6.2: Measured shower images on the MAGIC camera. [Left]: calibrated images (before image cleaning). [Right]: cleaned images (after image cleaning). The color bars are defined by a relative scale in each event. *(from Top to Bottom)* γ-like, hadron-like, μ-like shower images.

6.4   Image cleaning

In obtained camera images, many pixels contain only fluctuations of the light of the night sky (LONS). Those pixels have to be rejected for the reconstruction of an air shower image. It is essential for parameterizations of the image to employ only the signal content of the pixels. This procedure is called **image cleaning**. It is achieved by applying a two-stage tail cut procedure. The first iteration keeps those pixels with a charge amplitude larger than the first tail cut. These pixels are called **core pixels**. In the second iteration, neighbors of core pixels are rescued if they pass the second tail cut. These pixels remain as **boundary pixels**. As an example, Fig. 6.2 demonstrates the calibrated images (before image cleaning) and cleaned images (after image cleaning) of air showers by γ-ray, hadron and muon candidates.

The tail cut levels are defined in the absolute p.e. scale. As a standard value, 7 p.e. for the core pixels and 5 p.e. for the boundary pixels are defined. These values were used in most of the analyses in this thesis. The combination of 10/5 p.e. (for core/boundary) is also used as a conventional standard value.

Another, advanced, method uses arrival time information of the light in the pixels in addition to the amplitude information. The method is based on the idea that a shower image of Cherenkov photons from γ-ray should spread within a few ns while the NSB can reach the camera randomly. This method with an extra coincidence requirement allows us to lower the tail cut levels of the signal amplitude. It results in retrieving some faint images, which originate from low-energy primary particles. Detailed information on the algorithm of this method can be found in [190, 43]. In this advanced method, 6 p.e. for the core and 4 p.e. for boundary, and the coincidence of arrival time within 1 FADC slice (= 3.3 nsec) are required. This option was used in the analysis for the 2006 data of Mkn501 observations in Chapter 8.

6.5   Data Quality Checks

To be suitable for analysis, data runs have to pass a quality check. The event rate is the most useful indicator for weather conditions and possible problems in the hardware or the software. Ideally, it needs to be stable over the whole observation time within statistical fluctuations (apart from a small dependence on the zenith angle). Bad atmospheric conditions can be detected by low rates. Technical problems normally result in unstable rates. Extraordinarily high rates indicate software instabilities or some accidental strong light, like a car flash.

6.6   Gamma/hadron separation

In measurements with IACTs, the number of hadron (background) events in the recorded data is typically about 1000 times or more higher than that of γ-ray events. Efficient methods for separating "γ-ray like" events from the dominant "hadron-like" events are therefore urgently needed. As described in detail in section 3.5, γ-ray induced showers and hadron-induced shower have a number of different features. One of the most efficient methods to characterize these

is the parameterization of the image on the camera. By means of these image parameters, the "Random Forest method" is adapted for the γ/hadron separation as a standard method in the MAGIC analysis program. In this section, the details of image parameters and the "Random Forest method" are described.

6.6.1   Shower Image parameters

After image cleaning, the shower image on the camera is represented as the number of photoelectrons for each pixel. For further analysis (γ/hadron separation and energy reconstruction) it is useful to characterize the image by simple parameters. A possible set of parameters are the 2nd and 3rd moments of the shower image, which were first proposed by Hillas [130].

Fig. 6.3 shows the definitions of the image parameters. There are two kinds of parameters: one is the so-called "image shape parameters" and the other is "source dependent parameters".

Image shape parameters: These parameters describe the shape of the shower image on the camera, They can therefore be defined independently from the reference position of the shower image.

SIZE: Total number of photoelectrons in the shower image.

LENGTH: The RMS spread of light along the major axis of the shower images, which is a measure of the longitudinal development of the air shower.

WIDTH: The RMS spread of light along the minor axis of the shower images, which is a measure of the lateral spread of the air shower.

M3LONG: The third moment along the ellipse major axis, which indicates the shower direction.

CONC(N): Fraction of photoelectrons contained in the N brightest pixels, which represents the compactness of the shower image.

LEAKAGE: Fraction of photoelectrons contained in the outermost ring of pixels of the camera.

Source dependent parameters: These parameters depend on a reference point in the camera, which is normally the γ-ray source position. The parameters are calculated with respect to the defined reference points of the events.

DIST: Distance from the center of gravity of the shower image to a reference point.

ALPHA (α): Angle between the shower image major axis and the line connecting the image center of gravity with the camera center.

DELTA (δ): Angle between the shower axis and the x-axis of the camera.

Fig. 6.4 and 6.5 compares distributions of shower image parameters of MC γ samples and OFF data (= hadrons) samples. Fig. 6.4 represents the low SIZE range (150 p.e. < SIZE < 250 p.e.), corresponding to a peak γ-ray energy of about 120 GeV with a spectral photon index of -2.6 (see Fig. 6.6). Fig. 6.4 shows the higher SIZE range (SIZE > 350 p.e.), corresponding to a peak γ-ray energy of about 250 GeV.

While in the high SIZE events the differences in the distributions of the parameters are significant (see Fig. 6.5), they shrink in the low SIZE region (see Fig. 6.4) when approaching the threshold because the image parameters are influenced by the fluctuations of the shower development and Cherenkov photon statistics. In addition, in the low SIZE region, the following contributions become larger than in the high SIZE events. (1): Muons with large impact parameters produce image shapes similar to γ-ray shower images in that SIZE range. (2): Shower branches produced by π^0 (electromagnetic components) in a hadron-induced shower become more dominant. The distinction between hadron-induced showers and γ-induced showers becomes less significant. (3): Fraction of electrons in cosmic-rays becomes larger because cosmic-ray electrons have softer spectrum index (-3.2 [5]) than that of the cosmic-ray protons. An air shower induced by an electron shows features (only electromagnetic cascade) identical to that of a γ-induced shower, so that it is impossible to distinguishes between them by means of the shower image shape on the camera.
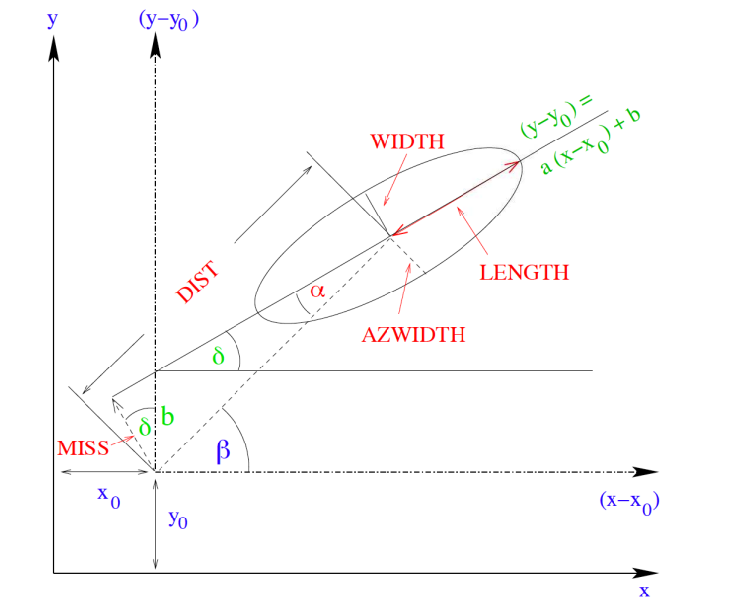
Figure 6.3: Definition of the shower image parameters. (x, y) are coordinates in the original camera system. (x_0, y_0) is a reference point, for example the source position or the center of the camera.
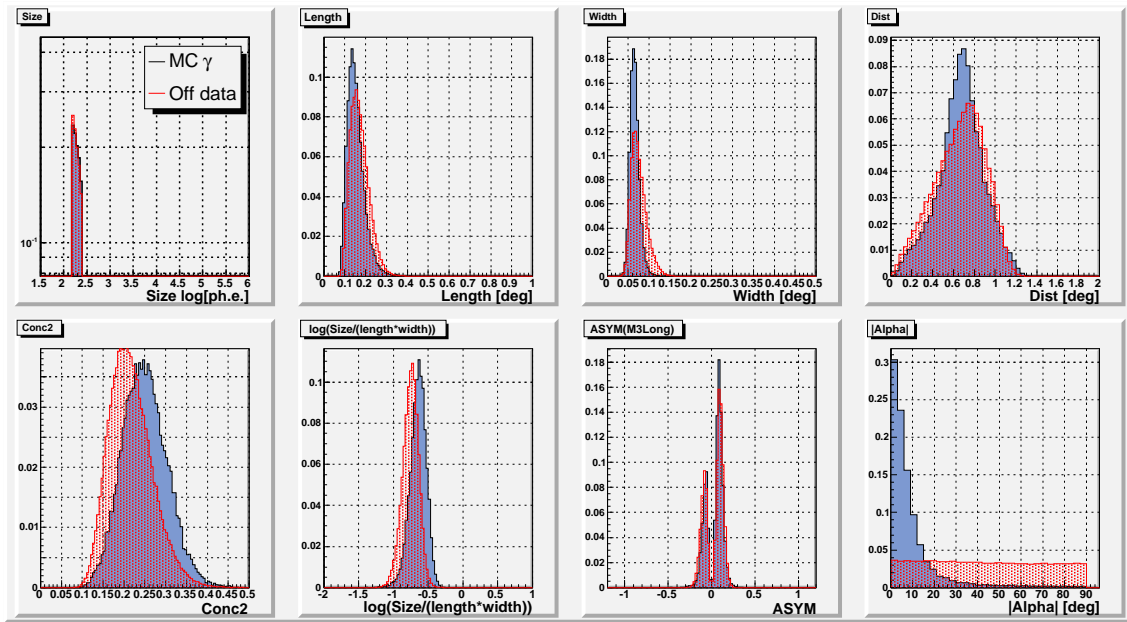
Figure 6.4: Distributions of the shower image parameters in MC γ *(blue)* and OFF data *(red)*. The SIZE range is between 150 and 250 p.e.. The area of each distribution is normalized to 1 with respect to the total number of events.
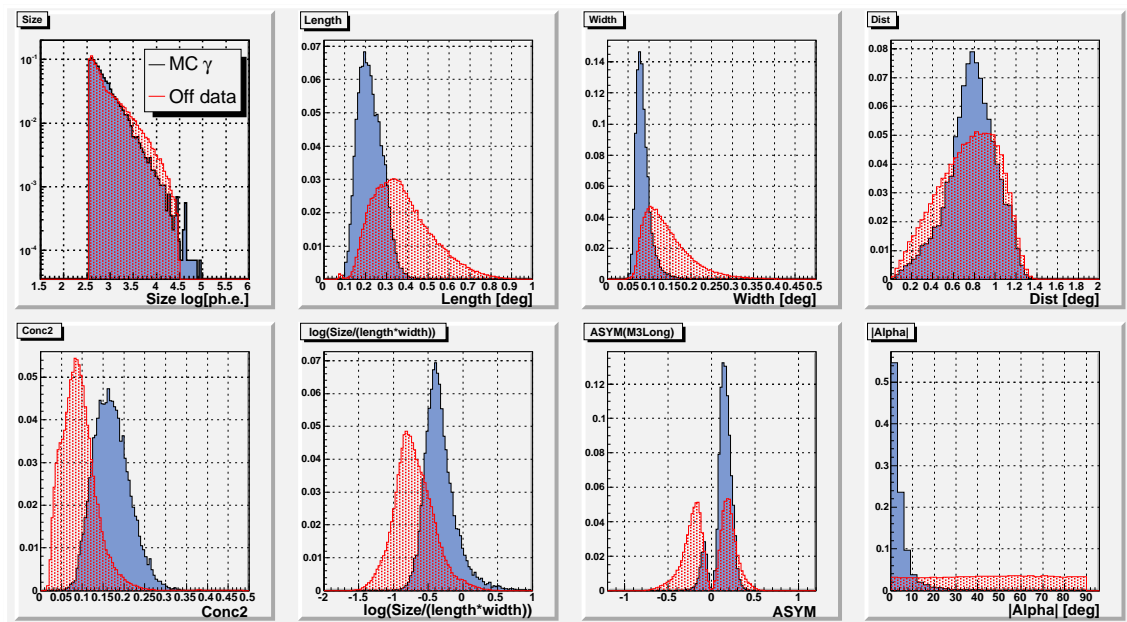
Figure 6.5: Distributions of the shower image parameters in MC γ *(blue)* and OFF data *(red)*. The SIZE range is above 350 p.e.. The area of each distribution is normalized to 1 with respect to the total number of events.
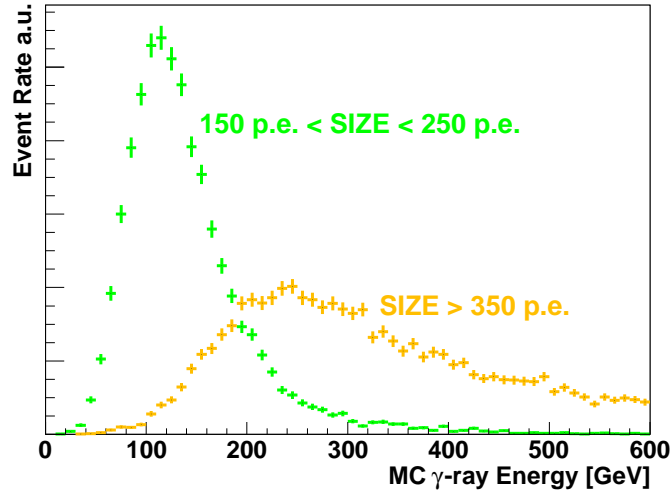
Figure 6.6: Energy distribution of MC *gamma*-rays with a spectral photon index of -2.6, using events with 150 p.e. < SIZE < 250 p.e. (*green*), using events with SIZE > 350 p.e. (*orange*).

6.6.2 Random Forest Method

In order to reject most hadronic background events while still conserving the majority of the γ-candidates, a multi-tree classification method called "Random Forest (RF)" method [71, 66] was used for the γ/hadron separation.

The Random Forest method is based on a collection of decision trees, built up with some elements of random choices. Like many other classification and regression methods, a Random Forest is constructed on the basis of training samples suitable for the application.

As training samples, we use MC simulated γ-ray samples for γ events, while real data are used for the hadron samples. On the other hand, it is usually advisable not to use MC hadrons, since hadronic showers are difficult to simulate very precisely (unlike γ showers, which have a pure electromagnetic cascade). OFF data, which do not contain any γ candidate events, are used for hadron samples, if available. It is also possible to use observational data with a small contamination of γ-rays (< 1%) for the hadron training sample, because this level of the γ-ray contamination does not affect the results. Usually, observational data contains much less than 1 % of gamma-ray events. (e.g. even in the data taken for the Crab Nebula, which is one of the brightest TeV sources, the fraction of γ-ray events in the observational data are less than 1%). Therefore, in most cases we do not need to take additional OFF data for the hadron training samples.

Each event is characterized by image parameters, which are used as input parameters for the RF method. From the training samples, a binary decision tree can be constructed, subdividing the parameter space first in two parts depending on one of the parameters, and subsequently repeating the process again and again for each part.

To understand the classification process, a completely grown tree may serve as a starting point
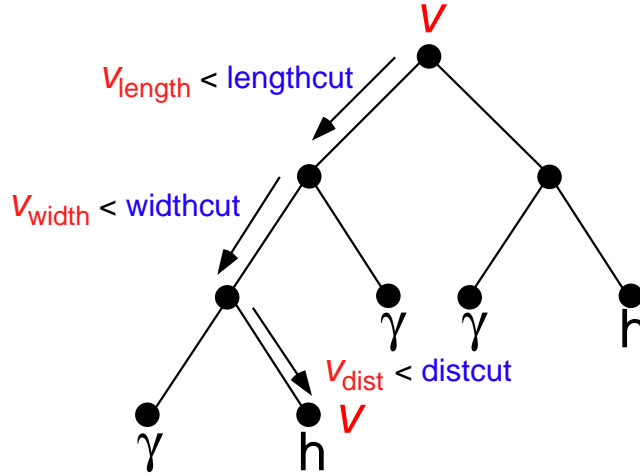
Figure 6.7: Sketch of a tree structure for the classification of an event v with the components v_{length}, v_{width}, v_{dist}. One can follow the decision path through the tree as it leads to classification of the events as hadrons.

(see Fig. 6.7). The task is to classify an event characterized by a vector v in the image parameter space. v is fed into the decision tree; at the first (highest level) node there is a split in a certain image parameter (e.g. 'length'). Depending on the component (image parameter) 'length' in v, the event v proceeds to the left node ($v_{\text{length}} < length\ cut$) or to the right node ($v_{\text{length}} > length\ cut$) at the next lower level. This node again splits in some other (or by chance the same) component, and the process continues. The result is that v follows a track through the tree determined by the numerical values of its components and the split values of the tree nodes, until it will end up in a terminal node. This terminal node assigns a class label l to v, which can now be denoted as $l_i(v)$, where i is the tree number. The vector v will be classified by all trees. Due to the randomization involved, different trees will often give different results, hence the name 'Random Forest'. From these results, a mean classification is calculated:

$$h(v) = \frac{\sum_{i=1}^{n_{\text{tree}}} l_i(v)}{n_{\text{tree}}} \tag{6.4}$$

This mean classification is called "HADRONNESS", and is used as the only test statistic (split-parameter) in the γ/hadron separation.

The splitting process is somewhat randomized by a feature called random split selection. The parameter candidates for a split are chosen randomly from the total number of available parameters. Among the candidates, the parameter and corresponding cut value to be used for splitting are chosen by the minimal Gini index. In the case of two classes, the Gini index Q_{Gini} can be referred to as a binomial variance of the sample scaled to the interval [0, 1]. The Gini index can be expressed in terms of the node class populations N_γ, N_h and the total node population N:

$$Q_{Gini} = \frac{4}{N} \sigma_{binomial} = 4 \frac{N_\gamma}{N} \frac{N_h}{N} = 4 \frac{N_\gamma (N - N_\gamma)}{N^2} \quad \in \quad [0, 1] \tag{6.5}$$
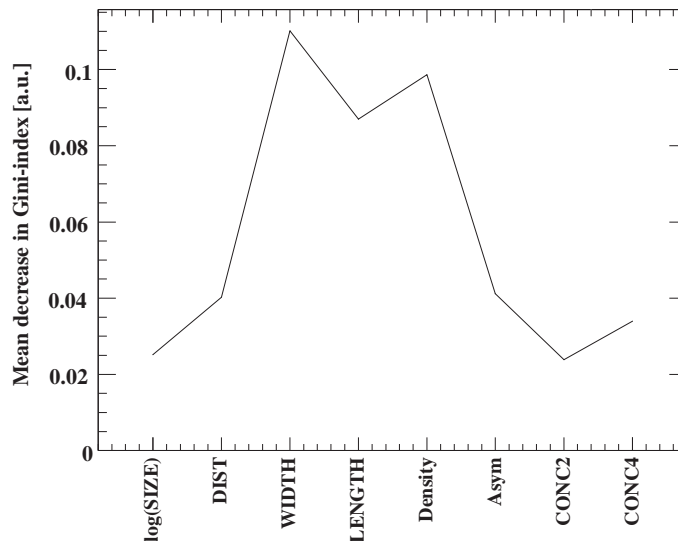
Figure 6.8: Importance of RF input parameters measured by the mean decrease in Gini-index. "Density" is defined as log(SIZE/(WIDTH×LENGTH)), "Asym" is M3LONG×(sign of DELTA). The most important parameters are related to WIDTH and LENGTH.

Choosing the smallest Q_{Gini} corresponds to minimizing the variance of the population of γs and hadrons, and naturally purifies the sample. Minimization of the Gini index provides both the choice of the image parameter and the split value to be used. The RF method for the MAGIC experiments is discussed in more detail in [44].

The relative discrimination power of the individual parameters can be characterized by the decrease of the Gini index (Fig. 6.8). As expected from the properties of electromagnetic and hadronic air showers, WIDTH and LENGTH are the key parameters for discrimination ("Density" is a combination of WIDTH and LENGTH). Prior to the training, the SIZE distributions of the two training data samples are adjusted to be equal, such that the SIZE parameter does not contribute to the γ/hadron separation but is only used for scaling the other parameters. It should be noted that the combination of input parameters in Fig. 6.8 is used for the "ALPHA analysis (cf. section 6.7.1)". In the "DISP analysis (cf. section 6.7.2)", the source dependent parameters (DIST and ASYM in Fig. 6.8) should not be used as RF input parameters so that γ/hadron separations can be applied independently from the arrival direction of the γ-ray events.

Fig. 6.9 shows the distribution of the HADRONNESS as a function of the SIZE parameter for two test samples of MC γs and OFF data [hadrons]. HADRONNESS assigns to each event a number between 0 and 1, which specifies the event to be more γ-ray like (close to "0") or more hadron-like (close to "1"). One can see that γs and hadrons are well distinguishable with respect to the HADRONNESS parameter. However, in small SIZE values (log(SIZE) $\lesssim$ 2.5), the separation of the HADRONNESS distribution is less clear. This is due to the differences of image parameter distributions between γ and hadron becoming less significant in low SIZE events, as discussed in section 6.6.1 (see also Fig. 6.4 and 6.5). Therefore, the power of γ/hadron

separation is relatively poor for events with such a low SIZE.
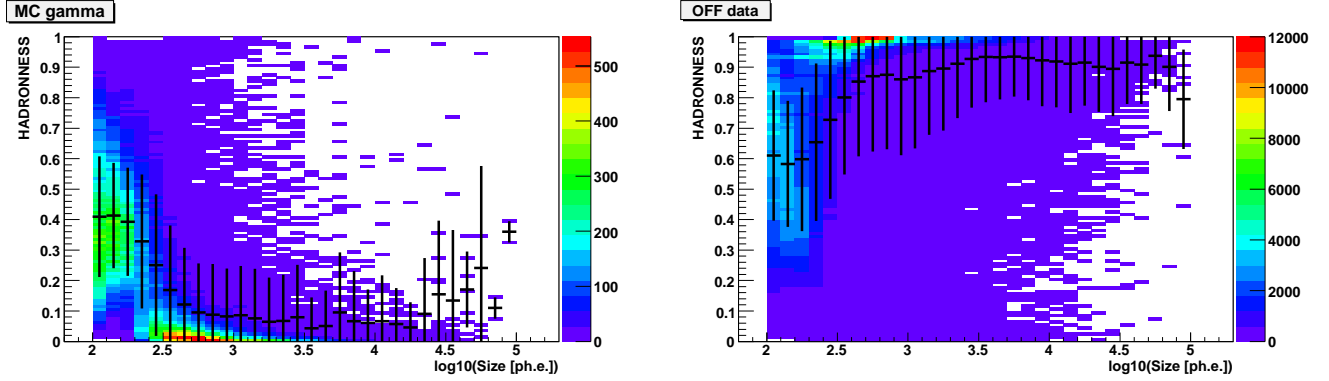
Figure 6.9: Distribution of HADRONNESS as a function of the SIZE parameter in a MC γ sample [**left panel**] and in an OFF data (hadron) sample [**right panel**]. In each bin, a horizontal black line denotes the average value of the HADRONNESS and a vertical line represents the RMS of the HADRONNESS distribution.

6.7 Gamma-ray signal extraction

After γ/hadron separation, the data contain the events of γ-ray candidates N_{ON} as well as a number of remaining background events with γ like image parameters N_{OFF}. The number of these background events is estimated by using independent OFF samples and applying the same cuts as for γ/hadron separation in HADRONNESS. The OFF samples should be obtained from observations of a region in the sky that presumably contains no γ-ray source under the same observational conditions (same LONS, zenith angle range and telescope conditions) as ON observations. The number of real γ-ray from the source N_γ is given as the excess of the ON samples over the scaled number of background:

$$N_\gamma = N_{\mathrm{ON}} - \alpha N_{OFF} \tag{6.6}$$

where α is the normalization factor between the ON samples and the OFF samples. This method relies on the assumption that the systematic differences of the ON and OFF samples are small compared to the statistical fluctuation of the samples.

The significance of the excess of the real γ-ray signal from the source is given in equation (17) of Li and Ma [161]:

$$S = \sqrt{2} \left(N_{\mathrm{ON}} \ln \left[\frac{1+\Gamma}{\Gamma} \left(\frac{N_{\mathrm{ON}}}{N_{\mathrm{ON}} + N_{\mathrm{OFF}}^{\mathrm{eff}}} \right) \right] + N_{\mathrm{OFF}}^{\mathrm{eff}} \ln \left[(1+\Gamma) \left(\frac{N_{\mathrm{OFF}}^{\mathrm{eff}}}{N_{\mathrm{ON}} + N_{\mathrm{OFF}}^{\mathrm{eff}}} \right) \right] \right)^{1/2} \tag{6.7}$$

where Γ and $N_{\mathrm{OFF}}^{\mathrm{eff}}$ are effectives values proposed by [195] aiming at taking the error of number

of the background events (ΔN_{OFF}) into account. They are derived as follows:

$$\Gamma \cdot N_{\text{OFF}}^{\text{eff}} = \alpha \cdot N_{\text{OFF}} \tag{6.8}$$

$$\Gamma \cdot \sqrt{N_{\text{OFF}}^{\text{eff}}} = \alpha \cdot \Delta N_{\text{OFF}} \tag{6.9}$$

Therefore, the variables $N_{\text{OFF}}^{\text{eff}}$ and Γ are given by the following expressions:

$$N_{\text{OFF}}^{\text{eff}} = \left(\frac{N_{\text{OFF}}}{\Delta N_{\text{OFF}}} \right)^2 \quad \text{and} \quad \Gamma = \alpha \frac{(\Delta N_{\text{OFF}})^2}{N_{\text{OFF}}} \tag{6.10}$$

Note that in the case of estimating ΔN_{OFF} by a Poisson distribution, thus, $\Delta N_{\text{OFF}} = \sqrt{N_{\text{OFF}}}$, then $N_{\text{OFF}}^{\text{eff}} = N_{\text{OFF}}$ and $\Gamma = \alpha$.

In the following, two analysis methods are developed for evaluating the γ-ray signal: the ALPHA analysis and the DISP (θ^2) analysis. In this thesis, the ALPHA analysis was used for the data taken by the ON/OFF observation mode while the DISP analysis was used for the data taken by the Wobble observation mode.

6.7.1 ALPHA analysis

One way to determine the normalization constant between ON and OFF samples is by means of the distribution of the image orientation angle "ALPHA". As shown in the bottom right panel of Fig. 6.4 and 6.5, any γ-ray signal should appear as an excess at small ALPHA values, whereas for background showers the ALPHA parameter is distributed uniformly in first order between $0°$ and $90°$. In our analysis, the following cuts based on the DIST parameter are applied before the final signal evaluation

- DIST$> 0.3°$, DIST$< 1.05 + 0.4(\log_{10}(SIZE) - 3)$, DIST$> 1.2°$

Events with large DIST values are affected by selection biases due to the limited trigger area (the radius$\sim 1°$) in the camera (the radius$\sim 1.75°$), which may lead to some deviations from the flat shape in the ALPHA distribution for the background events. Studies with MC γ samples indicate that most triggered γ-ray events are mostly triggered "ring" area inside the camera. These cuts, therefore, eliminate only a small amount of γ-ray events. Most of the eliminated events have large impact parameters ($\gtrsim 120$ m[1]), which contribute less to the γ-ray signal excess because of their small and faint images.

Fig. 6.10 shows an example of the ALPHA distribution of ON and OFF data taken for the Crab Nebula with ON-OFF observation mode at a zenith angle of $< 30°$. In this plot, a lower SIZE cut of 350 p.e. was applied. Effective observation time of ON data is 0.77 hours and additional dedicated OFF observation samples were used for the background estimation. Based on MC γ-samples, one can expect that there is only a negligible number of γ-ray events with ALPHA values above $20°$ for the images above 350 p.e.. The ON and OFF distributions have been normalized in the region $20° < $ ALPHA $< 80°$. In order to estimate the error of the number

---

[1]i.e. outside the main area of the Cherenkov light pool generated by a γ-ray induced shower.

of background events, a fit to the OFF data distribution from $0° < \text{ALPHA} < 80°$ by a second order polynomial without linear terms is used instead of the number of background events. It is an advantage to improve the statistical precision of the background events. For this procedure, one needs to assume that background events have the same characteristics over the ALPHA range. Since background events are isotropically distributed in ALPHA, it is true the ALPHA parameter is independent from the characteristics of the hadronic (background) air showers. This method is valid as far as the ALPHA distribution of background events can be fitted well by this function.

Cut optimizations

In order to maximize the significance of the signal excess for demonstrations, optimal values of cuts in SIZE, ALPHA and HADRONNESS are checked using other data samples ("reference data") than analyzed data ("main data"). The reference data should contain γ-ray signals, thus Crab Nebula data samples which were taken under similar conditions to the main data are normally used for this purpose. The optimum values of the parameters are determined with the following strategies.

SIZE: As shown in Fig. 6.9, γ/hadron separation power becomes poor for low SIZE events (SIZE $\lesssim 300$ p.e.). Hence, the significance of the excess decreases if we include such low SIZE events. At the same time, due to the negative photon index of the spectrum, the number of γ-ray events increases as the energy goes down. Consequently, the selection of events with the lower SIZE cut of 350 p.e. can maximize the significance of the signal excess.

ALPHA: The width of the ALPHA distribution for γ-ray depends on the SIZE parameter. A fit to the ALPHA distribution with a Gaussian centered at zero degree yields a sigma in the range from $\sim 2°$ (for SIZE > 1000 p.e.) to larger than $10°$ (for SIZE > 100 p.e.). Usually, to achieve the highest significance, the cut in ALPHA could be adjusted to be a factor of about 1.8 larger than the sigma of the γ-ray ALPHA distribution. In $3°$ binning, $9°$ is applied as the final ALPHA cut for SIZE > 350 p.e..

HADRONNESS: In each source analysis the optimal value can change because different train samples are used in the RF method both for the γ sample (according to the observed zenith angle range and the PSF of that observation period) and for the hadron sample (As discussed in the RF section, a part of observational data themselves are used.). Exactly the same procedures as employed in the RF method (using the same train samples) are applied to assign HADRONNESS for both reference and main data. The optimal HADRONEESS value is then found in the reference data with 0.01 binning. Usually, the optimum value can be seen at between 0.05 and 0.15 for SIZE>350 p.e..

Finally, the selection condition of ALPHA $< 9°$ for events with SIZE > 350 p.e. yields an excess of 222.1 ± 17.7 γ-ray candidate events of the ON data over 68.9 ± 4.6 normalized background events, corresponding to a significance of 16.0 σ as shown in Fig. 6.10.
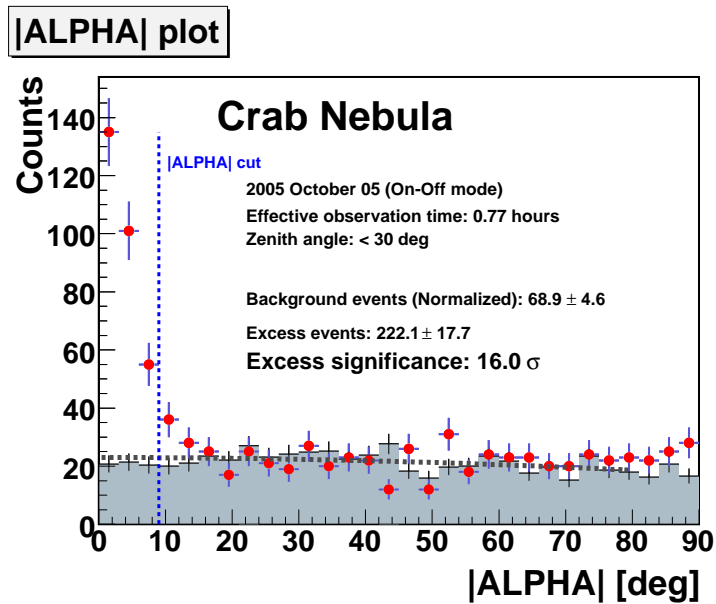
Figure 6.10: ALPHA plot of Crab Nebula observations taken with On-Off mode in October 2005. The filled circles represent the ON-data. The light crosses correspond to the normalized OFF-data. In each data point, a horizontal bar denotes a bin size and a vertical bar denotes 1σ uncertainty. A dotted curve describes a second order polynomial fit to the distribution of the OFF-data. The vertical line indicates the ALPHA selection condition ($< 9°$), which yielded a total excess of 222 events at a significance level of 16.0 σ.

6.7.2   DISP Analysis

The "DISP" method reconstructs the arrival direction of the primary γ-rays on an event-by-event basis using the information of the shower image shape. The source position is assumed to be on the major axis of the shower image in the camera, at a certain distance (DISP) from the image center of gravity (COG). As the basic idea the "ellipticity" of the shower images (defined as the ratio WIDTH/LENGTH) is used to infer the position of the source of individual showers [99]. The idea behind this is that shower images which are closer to the source position in the camera are more roundish, whereas showers which are further away from the source position are more elliptical. In the analysis of data taken by the MAGIC telescope, the following parameterization is used to describe the "DISP" parameter:

$$DISP = A(\text{SIZE}) + B(\text{SIZE}) \cdot \frac{\text{WIDTH}}{\text{LENGTH} + \eta(\text{SIZE}) \times \text{LEAKAGE2}} \tag{6.11}$$

This parameterization includes a second order polynomial dependence of the A, B and η parameters on the logarithm of the total image SIZE. LEAKAGE2 is a parameter which represents the ratio between the charge content in the TWO outermost camera pixel rings. Optimal values for the DISP parameter function (A, B, η) can be determined from MC γ events. A detailed discussion of this parameterization can be found in [90].

The DISP calculation of Eq. 6.11 can provide two possible source positions along the shower major axis. As the image in the camera can also record the information of the shower development in the atmosphere, photons from the upper part of the shower create a narrower section of the image with a high photon density (head), while photons from the lower part of the shower normally generate a much more widely spread image end (tail). Therefore, information of the asymmetries in the charge distribution of the image can indicate that "head"-"tail" direction. In the analysis of this thesis, the "M3LONG" parameter is used for this purpose.

Using the DISP parameters, one can define the parameter which describes the angular distance between the source position in the sky and the reconstructed arrival position of the air shower as "θ". Fig. 6.11 shows an example of the θ^2 distribution of ON and OFF taken for the Crab Nebula in wobble mode for 3.3 hours at a zenith angle of $< 30°$. In order to maximize the significance of the excess, only the events with SIZE > 350 p.e. are used for this figure. For the data with wobble observation mode, the normalization factor is set to be $1/3$, because 3 OFF regions are extracted for the OFF data samples.

The width of the θ^2 distribution represents the PSF of the telescope and corresponds to $\sigma_{\text{PSF}}^2 \sim (0.1°)^2$. As mentioned in the previous section, the optimized value for extracting the signal can be a factor of 1.8 larger than the sigma. We therefore select the value of $0.03[\text{deg}^2] (\sim (0.1 \times 1.8)^2)$ in θ^2 for the final cut.

The selection condition of $\theta^2 < 0.03$ deg^2 yields an excess of 896 ± 36.3 γ-ray candidate events of the ON data over 316 ± 10.3 normalized background events, corresponding to a significance 30.7 σ as shown in Fig. 6.11.

Finally, it should be noted that, in the flux calculation (section 6.9), looser cuts are applied to keep low energy γ-ray events and a sufficiently high γ-cut efficiency. The lower value of the SIZE
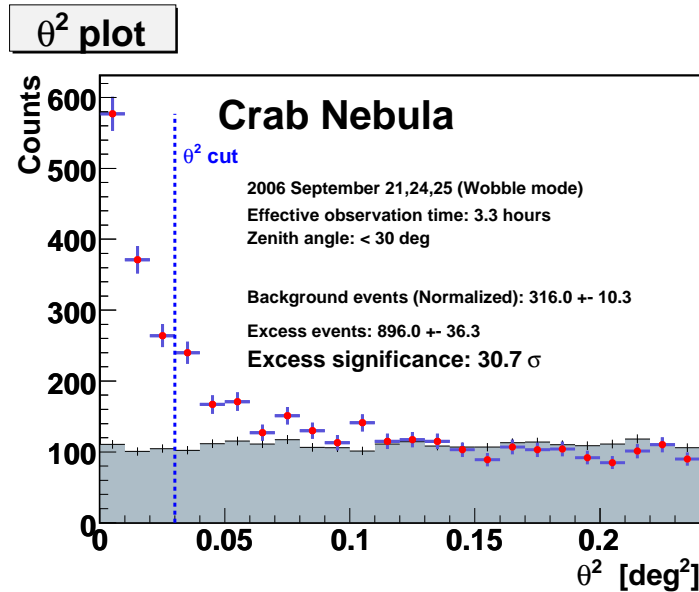
Figure 6.11: θ^2 distribution of Crab Nebula observations in September 2006 taken with Wobble mode. The filled circles represent ON-data. The light crosses correspond to normalized OFF-data. In each data point, a horizontal bar denotes a bin size and a vertical bar denotes 1σ uncertainty. The vertical blue line indicates the θ^2 selection condition (<0.03 deg^2), which yielded a total excess of 869 events at a significance level of 30.7 σ.

cut is selected to be between 100 and 200 p.e.. The values of ALPHA/θ^2 and HADRONNESS cuts are determined by γ-cut efficiencies for each energy bin. The cut efficiencies are estimated using MC γ-ray samples.

6.8   Energy reconstruction

The energy of the γ-ray events was also reconstructed by means of the RF method with MC γ-samples. The RF method can also be used to construct an algorithm for estimating a continuous quantity. A MC γ-ray data set with a known simulated energy of primary γ events is filled in fine bins of a logarithmic energy E_i. For each of those bins, respectively, a classifier is trained to discern events that belong into that particular energy bin. The parameters given to the RF for training are:

- log(SIZE), DIST, WIDTH, LENGTH, log(SIZE/(LENGTH×WIDTH)), CONC, LEAKAGE, and the zenith angle.
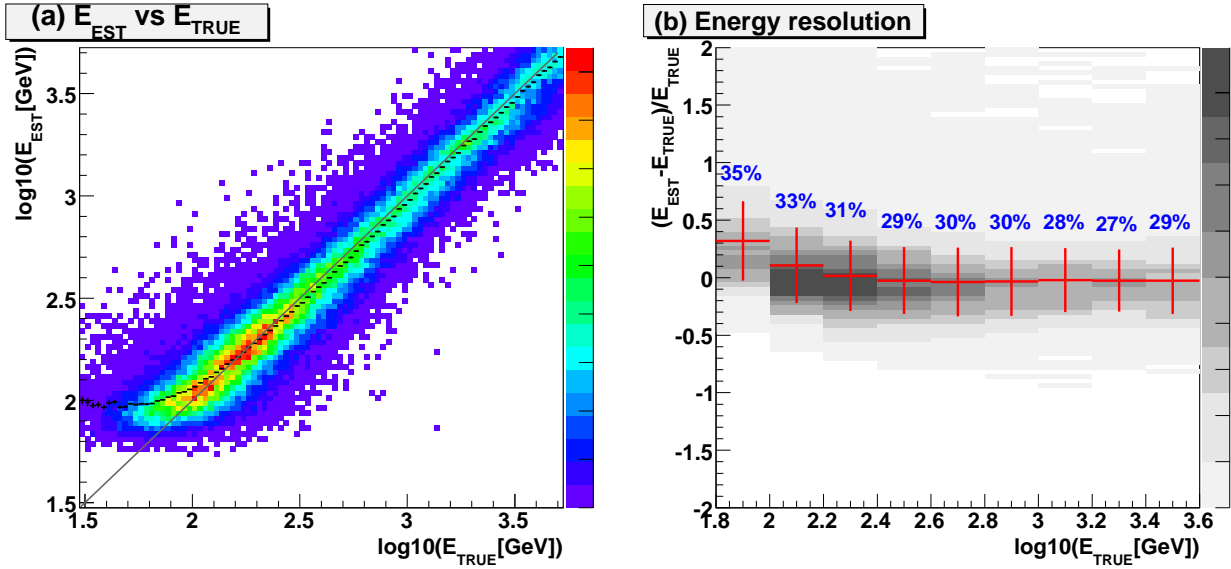
Figure 6.12: **(a)**: Relation between γ-ray energy estimated by the RF method (E_{EST}) and MC simulated γ-ray energy (E_{TRUE}). **(b)**: Energy resolution. Each number in the plot indicates the RMS of the distribution in each bin.

After training, each classifier i should recognize a specific energy range for each parameter and yield a parameter N_i.

$$E_{\text{est}} - \frac{\sum_{i=0}^{n-1} E_i N_i}{\sum_{i=0}^{n-1} N_i} \tag{6.12}$$

In this application of the RF each tree returns an estimated energy and the overall mean is calculated as the final estimated energy.

Fig. 6.12-(a) displays the distribution of the MC simulated energies (E_{TRUE}) vs. RF reconstructed energies (E_{EST}). There is a sizable bias towards higher estimated energies for a low energy range ($\lesssim 100$ GeV). This is a consequence of the trigger which, close above threshold, selects only images with fluctuations towards a higher SIZE. Fig. 6.12-(b) shows the energy resolution ($(E_{\text{EST}} - E_{\text{TRUE}})/E_{\text{TRUE}}$) for each energy bin (0.2 in $\log(E_{\text{TRUE}})$). The value indicated in the figure is the RMS of the resolution. Apart from the lowest energy bin (<100 GeV), this results shows an energy resolution with about 30% RMS.

6.9 Flux calculation

The differential energy spectrum $\mathrm{d}F/\mathrm{d}E$ of a source is defined as:

$$\frac{\mathrm{d}N_\gamma}{\mathrm{d}E \cdot \mathrm{d}A_{\text{eff}} \cdot \mathrm{d}t} \left(\equiv \frac{\mathrm{d}N}{\mathrm{d}E} \right) \tag{6.13}$$

As this formula shows, in addition to the number of γ-ray events (N_γ), (1) "A_{eff}", i.e. the effective collection area, (2) "t", i.e. the effective observation time, have to be derived for the flux calculation.

6.9.1 Effective Collection Area

The effective collection area is the area in which the MAGIC telescope can detect γ-ray shower events. The area can be described using the detection efficiency ϵ of the γ-ray shower with parameters of the primary energy of γ-ray E, the shower impact parameter b, the azimuth angle ϕ, and the zenith angle θ as follows:

$$A_{\text{eff}}(E,\theta) = \int_0^{2\pi} \int_0^{\text{inf}} \epsilon(E,\theta,\phi,b)b\,\mathrm{d}b\mathrm{d}\phi \tag{6.14}$$

In our analysis, the effective collection area for MAGIC observations can be computed using MC γ samples:

$$A_{\text{eff}}(E,\theta) = \frac{N_\gamma^{\text{survived}}(E,\phi,\theta)}{N_\gamma^{\text{simulated}}(E,\phi,\theta)} \times A_{\text{simulated}}, \tag{6.15}$$

where $N_\gamma^{\text{survived}}$ is the number of surviving γ-ray samples after all cuts and $N_\gamma^{\text{simulated}}$ is the number of γ-ray samples simulated by MC. Our MC γ samples were generated up to 300 m for the impact parameter, which is a large enough range to apply Eq. 6.15. Fig. 6.13 shows the calculated effective collection area by MC samples in the zenith angle range of 8° to 30°. One can see points in two colors, blue and red. The blue points represent the collection area just after image cleaning. The red points show the area after applying all cuts to evaluate γ-ray signals. These cuts comprise: (1) leakage cut[2] (< 0.2), (2) SIZE cut (> 100 p.e.), (3) HADRONNESS cut (85 % for γ cut efficiency) and (4) θ^2 cut (70% for γ cut efficiency). At low energies, the effective area shows a sharp drop as the energy decreases. For these lowest energies the effective area is limited by hardware trigger during the observations and the SIZE cut during the analysis. For larger energies, there is a slow variation of the effective collection area with energy. Only for the largest energies the effective area drops due to leakage of the shower pictures out of the MAGIC camera.

6.9.2 Effective Observation time

Since dead time in the hardware system is inevitable, the effective observation time is not identical to the total observation time and has to be calculated.

The distribution of cosmic ray events in time follows a Poisson distribution. Thus, in the ideal case of a detector with vanishing dead time, the distribution of time differences t between

---

[2] This cut is applied for excluding events with shower images only partly recorded on the camera ("leaked" images). Due to their incomplete image shape, image parameters can not be derived for them precisely. This usually happens if the shower image is too big with respect to the camera size. Thus, this cut mostly affects high energy events.
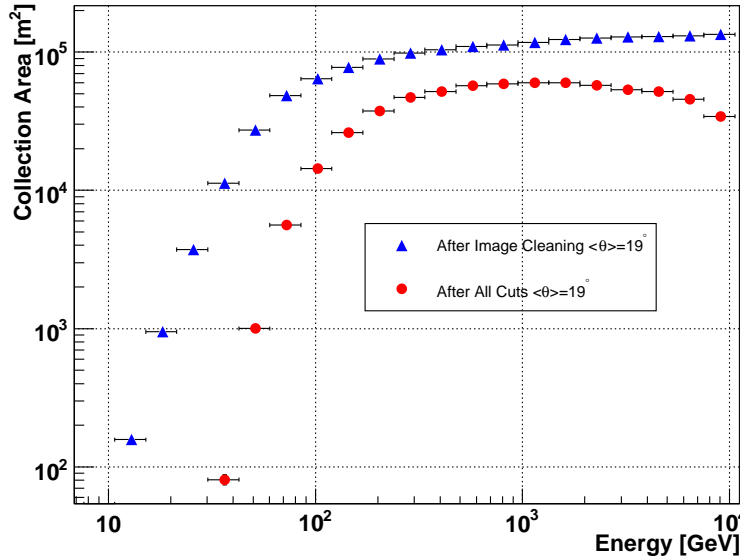
Figure 6.13: Effective collection area of γ-ray events in small zenith angles ($8°$ to $30°$. mean$\sim$ $19°$). Blue points represent the collection areas after image cleaning (no SIZE cut). Red points are the collection areas after applying all cuts for the spectrum calculation.

successive events can be described as:

$$\frac{\mathrm{d}N}{\mathrm{d}t} = N_0 \cdot \lambda \exp(-\lambda t) \tag{6.16}$$

where λ is the ideal events rate.

In the experiment the distribution $\mathrm{d}N/\mathrm{d}t$ of time differences t between successive events can be measured. The ideal event rate can be determined by fitting the experimental distribution with the expression $[B \cdot \lambda \cdot \exp(-\lambda t)]$, in the region $t > d_{max}$. d_{max} is the maximum value of the dead time in hardware and can be understood as the time difference above which $\mathrm{d}N/\mathrm{d}t$ behaves like an exponential. B and λ are free parameters to be determined in the fit. Using the total real number of recorded shower events ($N_{recorded}$), the effective observation time t_{eff} is given by:

$$t_{eff} = \frac{N_{recorded}}{\lambda} \tag{6.17}$$

Fig. 6.14 shows a typical distribution of time difference t along with a fit between 0.003 and 0.07 [s]. The effective observation time was determined to be $t_{eff} = 1819.2 \pm 4.8$ s.

The estimated energy E_{est} is not exactly identical to the true energy E_{true} of the γ-ray and shows some distortions (see Fig. 6.12) because of biases in measurements and the finite resolution of the detector. We therefore apply the **"Unfolding"** procedure in order to convert the distribution of excess events in the estimated energy into a distribution of excess events in the
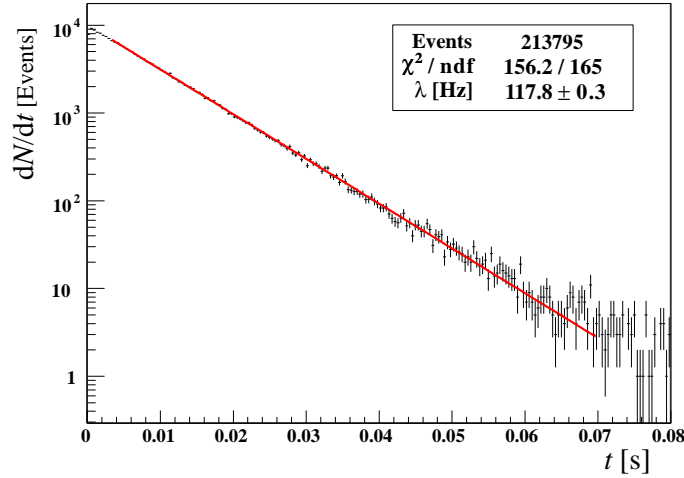
Figure 6.14: Determination of the effective observation time by a fit to the distribution of the event time difference. The resulting inverse event rate $(1/\lambda)$, when multiplied with the number of events, yields the effective observation time.

true energy for final results of the γ-ray spectrum. The unfolding can be understood as a reshuffling of events from the bins of E_{est} and into the bins of E_{true}. The effective collection areas in the new bins of E_{true} are computed again under the same conditions as the experimental distribution. A detailed discussion of the unfolding procedures for the MAGIC experiment can be found in [45]. Three methods are available for the unfolding procedure in MARS. In the analyses of this thesis, the scheme proposed by Bertero (1988) [58] was used.

Fig. 6.15 shows the final result (after unfolding) of the differential energy spectrum of the Crab Nebula observations in September 2006 (The data samples are the same as those for the θ^2 plot of Fig. 6.11). The result was fitted with (1) a simple power law and (2) a variable power law with a variable photon index.

(1) simple power law:

$$\frac{\mathrm{d}N_\gamma}{\mathrm{d}E\mathrm{d}A\mathrm{d}t} = (5.3 \pm 0.2) \times 10^{-10} \left(\frac{E}{0.3 \text{ TeV}}\right)^{-2.42\pm0.05} \frac{\gamma}{\text{TeV cm}^2 \text{ s}} \tag{6.18}$$

$\chi^2/\text{N.D.F} = 8.1/7$.

(2) variable power law with variable photon index:

$$\frac{\mathrm{d}N_\gamma}{\mathrm{d}E\mathrm{d}A\mathrm{d}t} = (5.4 \pm 0.3) \times 10^{-10} \left(\frac{E}{0.3 \text{ TeV}}\right)^{(-2.35\pm0.11)-(0.11\pm0.16)\times\log_{10}\left(\frac{E}{0.3 \text{ TeV}}\right)} \frac{\gamma}{\text{TeV cm}^2 \text{ s}} \tag{6.19}$$

$\chi^2/\text{N.D.F} = 7.6/6$.

These results agree well with previous measurements taken by HEGRA [27] (indicated by a dashed line in the figure) and MAGIC observation results in 2005 [43].
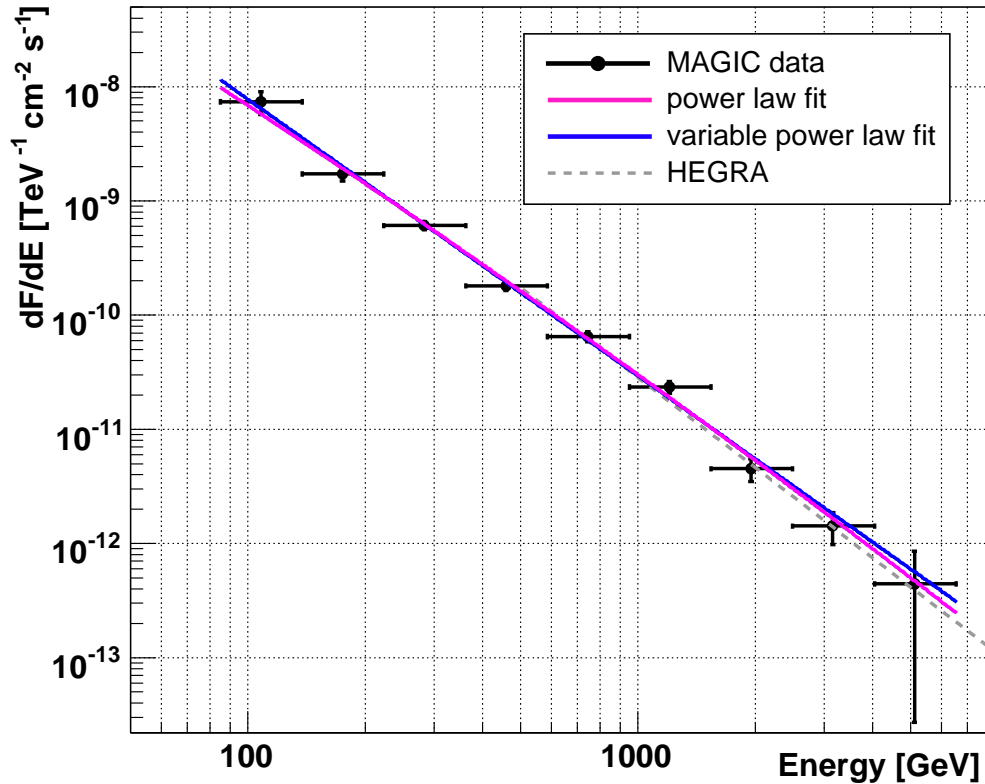
Figure 6.15: Measured differential energy spectrum of the Crab Nebula. The data were taken in September 2006 by the MAGIC telescope at a zenith angle range of $< 30°$. Black points denote data points from the MAGIC observations. Horizontal black bars represent energy ranges of bins, and vertical black bars are 1-σ error bars of data points. The results of fits of the MAGIC measured data points both with a simple power law (*blue*, Eq. 6.18) and a variable power law (*pink*, Eq. 6.19) are shown. The spectral model fit to the previous measurement by the HEGRA collaboration [27] is also shown by a gray dotted line.

6.9.3 Zenith Angle dependence

Under the observation condition of larger zenith angles, a γ-ray shower passes through a longer distance in the atmosphere, hence the intensity of the Cherenkov light from the shower at the ground is reduced more due to the absorption and scattering in the atmosphere. As a result, energy thresholds can increase with larger zenith angle observations. On the other hand, the telescope can gain a larger acceptance at a larger zenith angle due to the geometry of the atmosphere. This effect can lead to increasing the sensitivity of observations. Our MC γ samples were generated continuously in wide zenith angle ranges so that we could select appropriate samples according to the zenith angle range in each observation. In Fig. 6.16, the effective collection areas after all cuts in two different zenith angle ranges are described. One can see that with a large zenith angle condition the effective collection area at high energies is bigger, while it becomes significantly smaller as the energy decreases.

Here, we demonstrate analysis results of the Crab Nebula data taken for 0.87 hours in September 2006 with a zenith angle range from 36 to 43.5. Fig. 6.17 shows the results of a differential energy spectrum from these Crab Nebula observations. It can be fitted by a simple power law:

$$\frac{\mathrm{d}N_\gamma}{\mathrm{d}E\,\mathrm{d}A\,\mathrm{d}t} = (4.9 \pm 0.6) \times 10^{-10} \left(\frac{E}{0.3\ \mathrm{TeV}}\right)^{-2.44 \pm 0.14} \frac{\gamma}{\mathrm{TeV\ cm^2\ s}} \tag{6.20}$$

$\chi^2/\mathrm{N.D.F} = 2.6/4$.
The result is consistent with the previous measurement taken by HEGRA (a dotted line in the figure) and the result of small zenith angle observations.

This zenith angle range is equivalent to the range of 1ES1959+650 observations in chapter 9. Some parts of the observations in chapter 10 for Mkn421 are also carried out with a larger zenith angle.

6.10   Light curve

A light curve (LC) represents a variation of an integrated γ-ray flux with a specific energy range with a specific time binning. Numbers of the excess γ-ray events, the effective collection area with a proper zenith angle range, and the effective observation time are computed in each time bin.

The γ-ray flux from the Crab Nebula should be stable (cf. Chapter 1). Therefore, the LC of the Crab Nebula is well suited to show the stability of the telescope and the data analysis performance. Fig. 6.18 shows the LC of γ-ray above 200 GeV with a 15-min binning for 3 days (21st, 24th and 25th of September, 2006). A fit to the data with a constant value gave a result with $\chi^2/\mathrm{N.D.F} = 7.6/13$ as follows:

$$F(E > 200\,\mathrm{GeV}) = (2.21 \pm 0.11) \times 10^{-10}\,[\mathrm{cm^{-2}s^{-1}}] \tag{6.21}$$

This value is also consistent with the results from the MAGIC observation in 2005 [43].
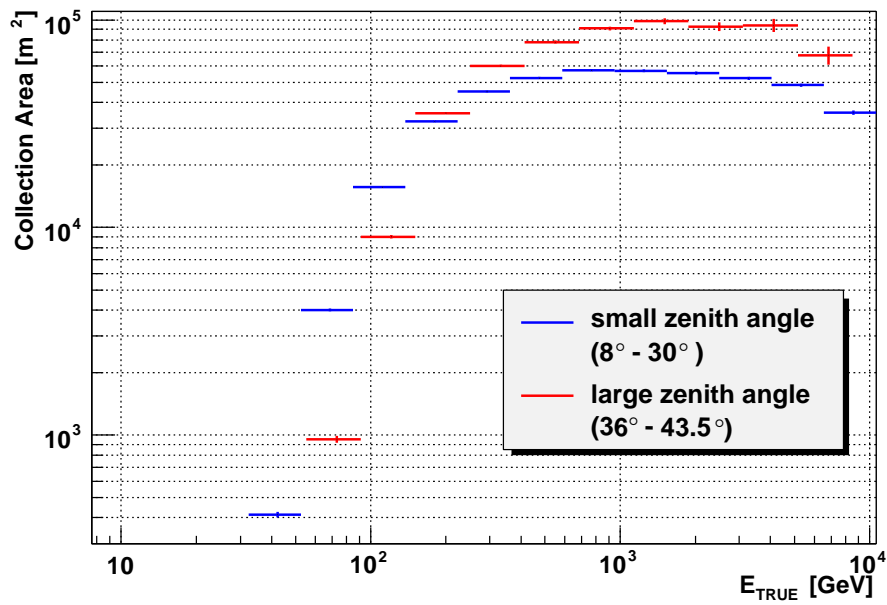
Figure 6.16: Effective Collection areas after all cuts in two different zenith angle ranges. [Blue point:] Small zenith angle (8° to 30°). [Red point:] Large zenith angle (36° to 43.5°).
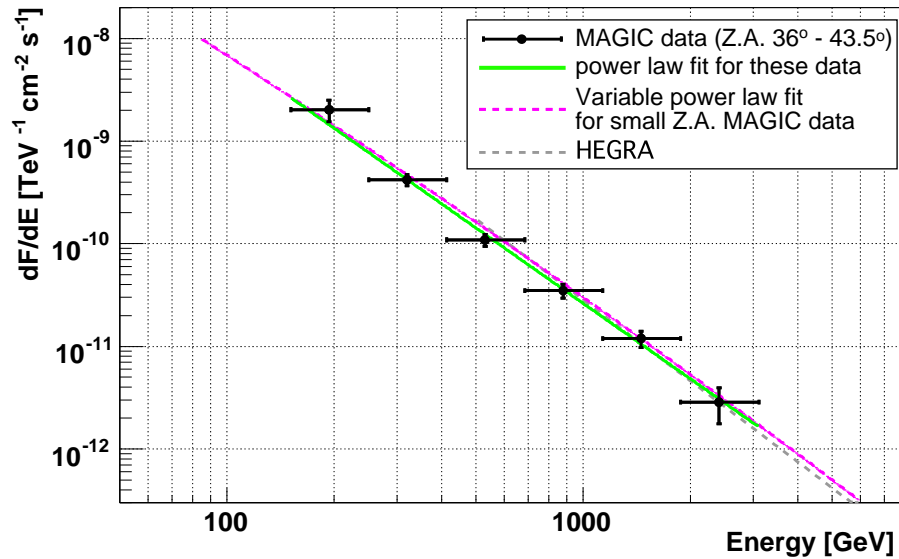
Figure 6.17: Measured differential energy spectrum of the Crab Nebula from larger zenith angle observations. The data were taken in September 2006 by the MAGIC telescope in a zenith angle range between 35° and 43.5°. Black points denote the data measured with the MAGIC telescope. Horizontal black bars represent energy ranges of bins, and vertical bars are 1-σ error bars of the data points. The fit to the larger zenith angle observation data with a power law (Eq. 6.20) is shown by a green line. For comparison, a dotted purple line denotes the fit by a variables power-law to the small zenith angle observation by MAGIC (see Eq. 6.15 and Fig. 6.19). The fit to the previous measurement by the HEGRA collaboration [27] is also shown by a gray dotted line. All spectra show good agreements within statistical errors.
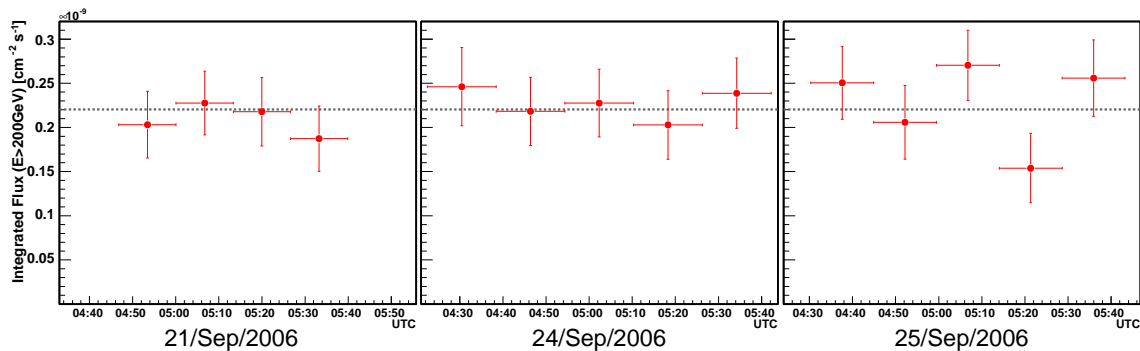
Figure 6.18: Measured light curve above 200 GeV with a 15-min binning from Crab Nebula observations by MAGIC in September 2006. A horizontal bar represents the time range (15 min) in each bin, and a vertical bar corresponds to a 1-σ error of each data point. A horizontal blue dotted line denotes the result of a fit to all data points with a constant value.

6.11 Systematic errors

In addition to statistical errors, the reconstructed γ-ray flux is also affected with systematic uncertainties, most of which are difficult to assess. The systematic effects influence both the energy reconstruction and flux calculation. In this section, the main sources of systematic effects are described. Discussion of the systematic errors of the MAGIC telescope is also found in [43].

The main sources for errors in the energy reconstruction are:

Atmospheric conditions for Cherenkov light: 15%
> The MC simulation does not take into account the microclimate conditions. The production rate of Cherenkov light in the atmosphere can vary because of density fluctuations on hourly/daily/seasonal basis. In addition, the atmospheric transmittance (e.g., Mie-scattering) is also changed depending on the weather condition (e.g., dust, moisture and cloud). These can affect the reconstructed γ-ray energy by about 15% [57].

Light losses in the telescope optical system: 10%
> The telescope optical system consists of mirrors, the camera entrance window and the Winston cone light guide. Degradation of their reflectivities may cause additional losses of the Cherenkov light. The overall light loss in the optical system is adjusted in the MC simulations to dedicated measurements and monitored by the muon calibrations (see section 6.3). However, there may be errors in the simulated light distribution on the camera (e.g. the size of the PSF and halos of the focused spot on the camera) and in improper simulation for the light guide. The systematic errors on the reconstruction energy may be 10%.

Performances of PMT: 13%
> Because of the calibration error of reference photo-diode for the QE measurement, uncertainty in the quantum efficiency is 2%. Degradation of the coating enhancing the UV-sensitivity may cause the uncertainly of 3%. The PMT has a uncertainty in the photoelectron collection efficiency of 10%. Uncertainties of F-factors used to calibrate the recorded signal is estimated to be 8% [105]. In total, the systematic errors of PMT performances lead to 13%.

The overall systematic uncertainty in the energy scale is estimated to be 22%, by assuming Gaussian error propagation. The energy is likely underestimated as most of the effects result in a loss of Cherenkov photons.

A continuous monitoring of the atmosphere with complementary instruments and methods like LIDARs, Bolometer and absolute measurements of the extinction coefficient, would reduce the uncertainties caused by atmospheric conditions to a few percent. A proper simulation/ray tracing of the light guide and PMT cathode would reduce the corresponding uncertainties to the level of one percent on the expense of a larger computational effort. The uncertainty of the F-factor method can be avoided using a different calibration methods, e.g. the blind pixel method or calibrating with a PIN-diode [105]

The second type of systematic errors is uncertainties of flux calculation caused by the determination of effective collection area.

Camera acceptance: 5%
> In the MC simulations a camera with homogeneous acceptance is simulated. Defect PMTs and trigger inefficiencies may introduce a systematic error of 5% of the flux level.

Estimation of efficiencies for γ-ray events: 10%
> The trigger efficiency and the cut efficiency in the analysis chain for γ-ray events are estimated by MC simulated γ-ray samples. Differences between the real and simulated images of γ-ray showers (partly due to difference of the real and simulated optical PSF of the telescope and the earth's magnetic filed) may introduce systematic errors. Overall uncertainty can be estimated by applying different cut values in e.g., SIZE and HADRONNESS for the data in the analysis chain. The overall efficiency is estimated to be uncertain by about $\sim 10\%$. In addition, different analysis parameters (e.g., different signal extraction methods (ALPHA or DISP), image cleaning parameters) may introduce systematic errors, although they showed only minimal changes in the results by 2%.

Those effects introduce a systematic uncertainty in the flux scale by 11%. The effects could increase in low energies ($\lesssim 150$ GeV). Camera inhomogeneities could show up on the level of up to 20% in low energies because of low SIZE values for the shower images. The effective area degreases rapidly in the low energies while it changes rather slowly in higher energies (see Fig. 6.13). Hence, the effective areas in the low energies are sensitive to differences between the real and simulated images of γ-ray showers. The uncertainty may increase up to 30% for the lower energies. Consequently, the systematic uncertainty in the flux scale below 150 GeV may increase up to 36%.

Finally, there are also effects which result in a distortion of the energy scale. They are caused by non-linearities in the PMT gain, the amplifiers, the optical transmission (transmitter/receiver) and the FADCs. The overall non-linearity is about 10% estimated from the characteristics of the VCSELs that are used in the optical transmission and contribute most to the non-linearities [190].

Based on experience with previous Cherenkov telescopes, the systematic error on the slope of the measured γ-ray spectrum is 0.2 [29].

Chapter 7

Discovery of VHE γ-ray emission from BL Lacertae

7.1 Introduction

BL Lacertae (1ES2200+420, R.A. $22^h02^m43.3^s$, decl. $+42°16'40''$ [J2000.0], $z = 0.069$ [176]) is the historical prototype of a class of powerful γ-ray emitters so-called "BL Lac objects". The mass of the supermassive black hole in the center of BL Lacertae is estimated to be $\sim 10^8 M_\odot$ [251].

BL Lacertae is classified as an low-frequency peaked BL Lac (LBL) object (see Chapter 2) with a synchrotron peak frequency of 2.2×10^{14} Hz [216], and is one of the best-studied objects in the various energy bands. No VHE γ-ray emission from any LBLs was ever confirmed before this work.
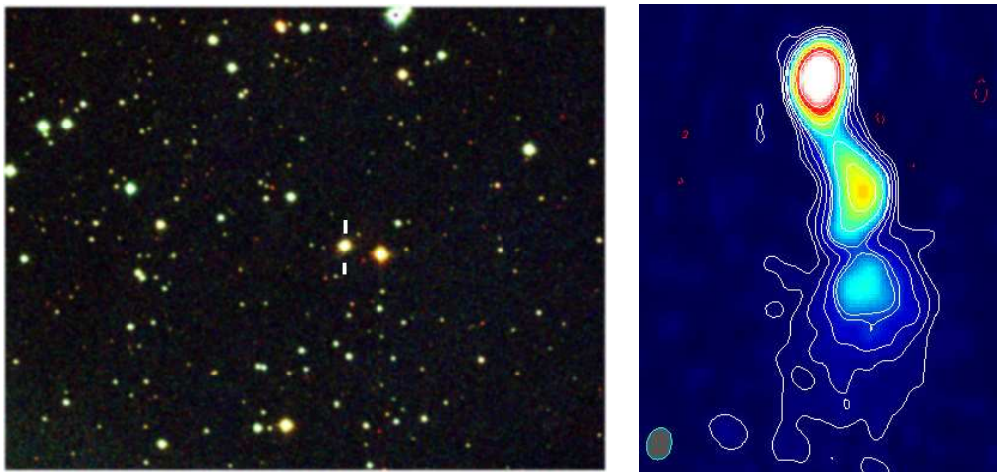
Figure 7.1: Images of BL Lacertae. **[Left]** optical sky image around BL Lacertae. Vertical lines indicate BL Lacertae. **[Right]** VLBA image of BL Lacertae, observed in 1997 with 22 GHz [211].
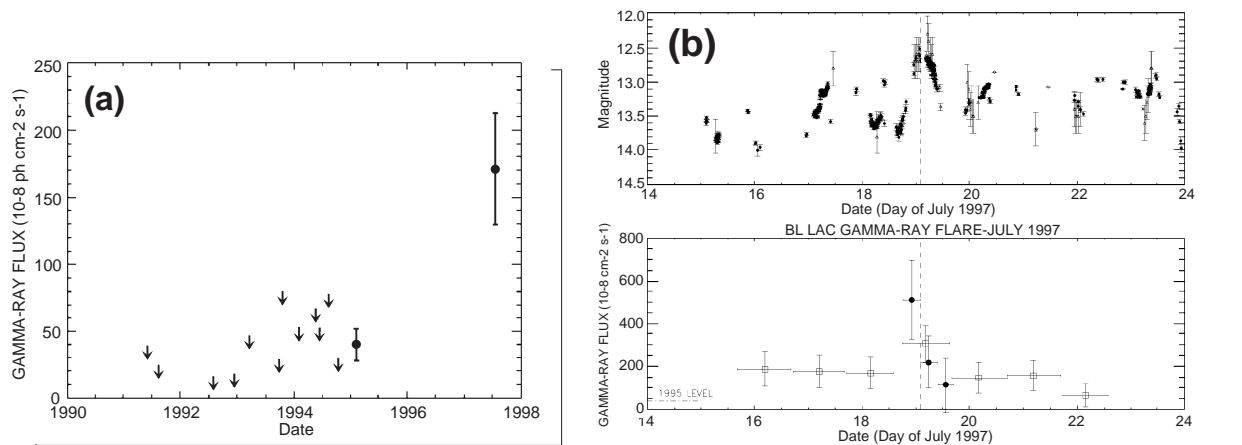
Figure 7.2: Gamma-ray (E>100MeV) light curves of BL Lacertae during the EGRET observation. **(a):** Complete time history of EGRET γ-ray observations. Until January 1995, this source had not been detected. The arrows represent 95% confidence upper limits. **(b):** Optical (*top*) and γ-ray (*bottom*) light curves for the 1997 July flare. Both plots show that there was a peak on July 19. The dashed vertical line crossing both plots shows the end of the γ-ray flare, for comparison with the optical flare. Detailed information can been found in [64]

Villata et al. (2004) [243] have presented long-term light curves in optical and radio emission over 30 years and reported cross-correlation between the optical light curve and hardness ratio with some delay in radio emission. They have claimed evidence of a $\sim$ 8 year periodicity in radio but less evidence in optical. Several authors (e.g., [122, 225]) have also reported periodic and quasi-periodic variations in the optical and radio light curves.

Gamma-ray observations by EGRET (see section 1.3) resulted only in an upper limit of 1.4 $\times$ 10^{-7} cm^{-2} s^{-1} until 1995. In 1995, EGRET observed γ-rays above 100 MeV at a flux level of $(4.0\pm1.2) \times 10^{-7}$ cm^{-2} s^{-1} with 4.4 σ significance [75]. During an optical outburst in 1997, a γ-ray flare was measured with 10 σ significance by EGRET at a flux level of (1.72 ± 0.42) $\times$ 10^{-6} cm^{-2} s^{-1}, 12 times higher than the previous upper limit [64]. The External inverse-Compton model has been suggested for the interpretation of the γ-ray emission in the 1997 flare (e.g., [167, 208]). The Light curves of EGRET measurements both complete period and 1997 flare period are shown in Fig. 7.2.

In the VHE γ-ray range, the Crimean Observatory has claimed a detection with 7.2 σ significance [182], while HEGRA, observing during the same period, obtained only a significantly lower upper limit [152] (see Fig. 7.3 and section 7.4.1). Other past observations of this target resulted in upper limits only [75, 152, 12, 136].

In this Chapter I report about the discovery of VHE γ-ray emission from BL Lacertae in 2005. Simultaneous observations in the optical band in 2005 and 2006 permitted a search for correlations between optical and VHE γ-ray activities.
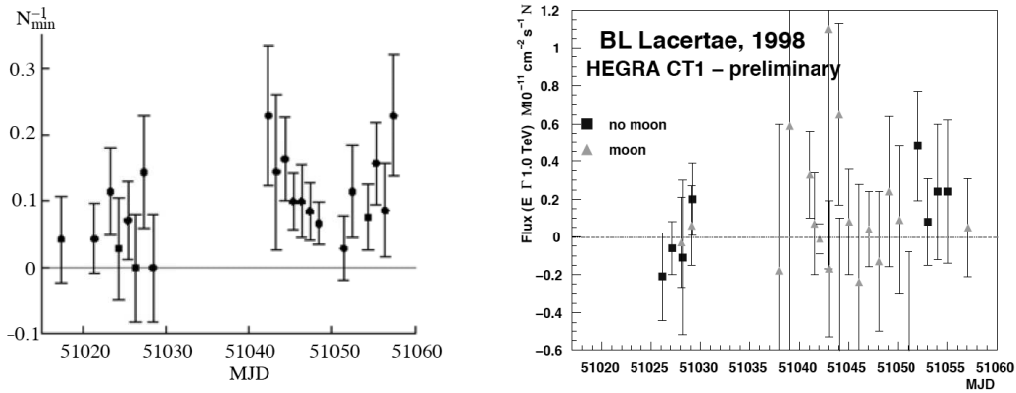
Figure 7.3: Comparison of the BL Lacertae light curve of VHE γ-ray emission ($\gtrsim 1$ TeV) in July-August 1998 as measured by the Crimean Astrophysical Observatory (left, in counts per minute) and HEGRA CT1 (right). (the figure taken from [152])

7.2 Observations and Data Analysis

BL Lacertae was observed with the MAGIC telescope in 2005 and 2006 to search for VHE γ-ray emission from this target.

Optical R-band (640 nm) observations were provided by the Tuorla Observatory Blazar Monitoring Program[1] with the 1.03 m telescope at the Tuorla Observatory, Finland, and the 35 cm KVA telescope on La Palma, Canary Islands. Radio observations were also performed in 2005 with UMRAO[2] at 4.8 GHz, 8.0 GHz and 14.5 GHz, and at 37 GHz with the Metsähovi Radio Observatory.

7.2.1 The 2005 observations

The source was observed for 21.3 hours from August until December 2005. Previous BL Lacertae observations had indicated a correlation between enhanced optical activity and high energy γ-ray emission (see Fig 7.2). Therefore, a part of VHE γ-ray observations were triggered as a Target of Opportunity (ToO) after enhanced optical activity in addition to the scheduled observation in 2005. The observations were carried out in ON/OFF observation mode. The telescope was pointing directly onto the object, recording so-called ON-data. The background was estimated from observations of regions where no γ-rays are expected, so-called OFF-data, which were taken with similar sky conditions to ON-data.

The standard analysis chain with MARS packages (details described in Chapter 6) was used for the data analysis.

---

[1] more information at http://users.utu.fi/kani/1m/

[2] http://www.astro.lsa.umich.edu/obs/radiotel/index.php

Data runs with anomalous trigger rates due to bad observation conditions and a short sample taken at large zenith angle ($> 30°$) were rejected from the further analysis. The observation log in 2005 is summarized in Table 7.1.

The remaining ON-data corresponded to 17.8 hours, while the OFF-data corresponded to 57.2 hours, both between $13°$ and $30°$ zenith angle. Shower image parameters of the raw data were calculated and compared for the ON and OFF data in order to check their consistency; excellent agreement was found in both the lower SIZE events ($150 < $ SIZE $ < 250$ photoelectrons) as shown in Fig. 7.4 and the higher SIZE events (> 350 photoelectrons) in Fig. 7.5. They show Hillas shower image parameters of LENGTH, WIDTH, DIST and SIZE separately. In addition, CONC2, log(SIZE/LENGTH $\times$ WIDTH), and the event distribution on the camera in ϕ (angle between camera X-axis and line joining camera center with Image Center of Gravity), and HADRONNESS are represented in the Figures. The selected data samples before γ/hadron separation are completely dominated by hadron events and the expected admixture of γ-ray events are below the statistical fluctuations of the data. After γ/hadron separation by the Random Forest (RF) method, ALPHA analysis method was applied for the final signal evaluation.

7.2.2   The 2006 observations

Follow-up observations were carried out from July to September 2006 for 26.0 hours, using the wobble observation mode, where the object was observed at an $0.4°$ offset from the center of the camera. The data were analyzed using MARS package. 25.0 hours of the data passed quality selection criteria for the analysis. The observation log in 2006 is summarized in Table 7.2.

The RF method was used for the γ/hadron separation. The source dependent image parameters (DIST, M3LONG) were not used as input parameters because the DISP method was used for the final signal evaluation.

7.3   Results

7.3.1   The 2005 results

In Fig. 7.6-(a), the ALPHA distribution is shown. The OFF data are normalized to the ON data in the range between $20°$ and $80°$. The number of background events was determined by a second order polynomial fit (without linear term) to the ALPHA distribution of the normalized OFF-data. An excess of 216 events over 1275.6 normalized background events yields a significance of 5.1 σ for data with SIZE above 350 photoelectrons. The corresponding peak in the energy distribution is about 200 GeV γ-ray energy (see Fig. 7.6-(b)).

Fig. 7.7 shows the local sky map for the 2005 γ-ray candidates. The map was produced from the excess events distribution smoothed with a 2-D Gaussian of $0.1°$. The black cross marks the nominal position of BL Lacertae. The small offset and the extension of the image are comparable to the telescope point spread function (PSF, $0.1°$) and the telescope pointing error ($2'$).

The 2005 VHE γ-ray above 200 GeV as well as hard X-ray (by SWIFT-BAT[3]), X-ray (by

---

[3]http://swift.gsfc.nasa.gov/docs/swift/results/transients/
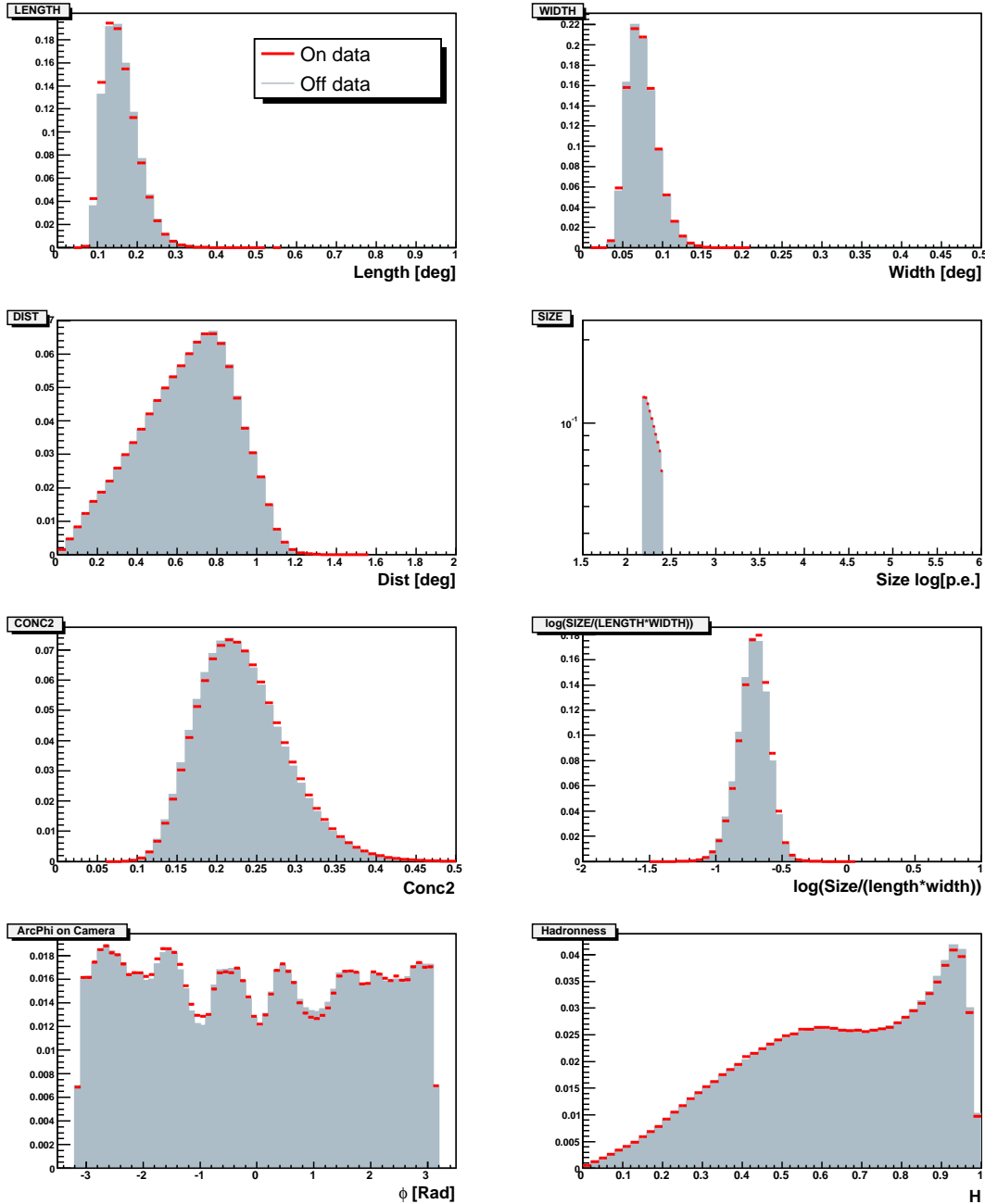
Figure 7.4: Comparison of the shower image parameters between ON and OFF data using events with the event $150 < \text{SIZE} < 250$ photoelectrons before the γ/hadron separation. The area of each distribution is normalized to 1 with respect to the total number of events. Red lines indicate the distributions in ON-data, while blue histograms represent the OFF-data. The Red lines include the errors, which can not be recognized due to small values. The parameters are LENGTH, WIDTH, DIST, SIZE, CONC2, log(SIZE/LENGTH $\times$ WIDTH), and the event distribution on the camera in ϕ (angle between camera X-axis and line joining camera center with Image Center of Gravity), and HADRONNESS

.
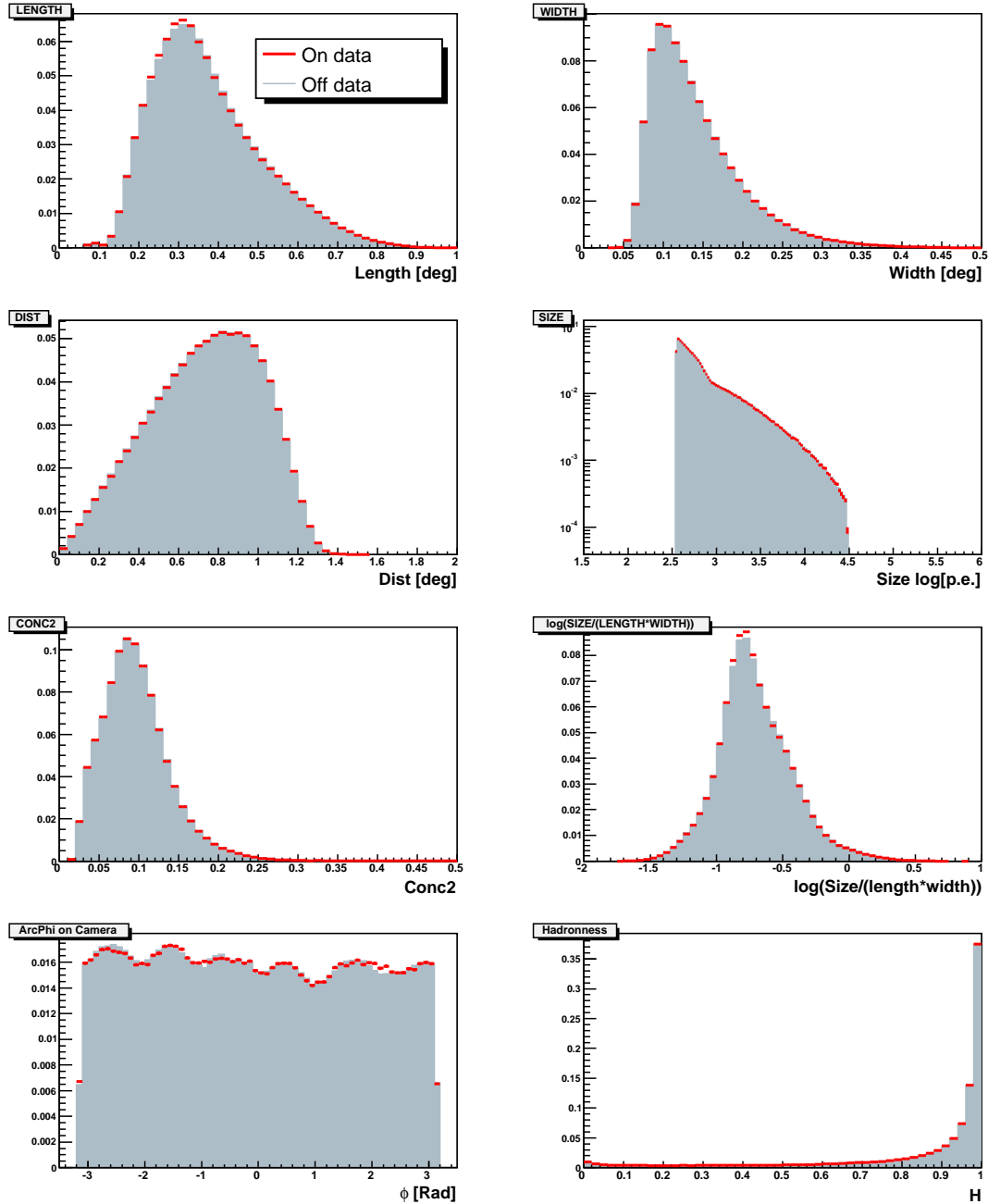
Figure 7.5: Comparison of the Hillas parameters between ON and OFF data with the event SIZE > 350 photoelectrons before the γ/hadron separation. The area of each distribution is normalized to 1 with respect to the total number of events.

Table 7.1: Summary of the MAGIC observations for BL Lacertae in 2005. Description of columns: (1) Start time of the MAGIC observation in UTC. (2) Zenith angle range during the observation. (3) Mean value of the zenith angle. (4) Total number of events in the data. (5) Observation time. (6) Data taking rate. (7) Data rate after the SIZE cut above 100 photoelectrons. (8) Effective observation time of the data used for the analysis. (9) Availability of optical data from Tuorla. The "(+/-1day)" indicates that optical data taken next/before day of the MAGIC observation (quasi-simultaneous optical data) are available.

(1) Observation start time (UTC)	(2) ZA range [deg]	(3) mean ZA [deg]	(4) # Eve. [10^6]	(5) Obs. T [h]	(6) Rate [Hz] (before)	(7) Rate [Hz] (SIZE>100)	(8) T_{eff} [h] (used)	(9) availability of optical data
02.08.2005 02:05:45	13.5–18.0	14.7	1.02	1.29	220.0	131.0	1.28	Yes (+1day)
04.08.2005 01:47:09	13.5–18.4	14.9	1.28	1.59	223.9	130.7	1.58	Yes
08.08.2005 01:28:45	13.5–16.0	14.3	0.87	1.15	210.2	119.6	1.15	Yes
10.08.2005 01:15:00	13.5–16.3	14.4	1.01	1.28	220.5	130.0	1.28	Yes
03.09.2005 00:09:39	13.5–18.6	15.4	0.38	0.92	113.6	63.5	0 (low rate)	–
04.09.2005 23:46:17	13.5–18.5	15.3	0.55	0.93	164.6	92.6	0 (low rate)	–
10.09.2005 23:37:03	13.5–14.5	13.8	0.37	0.67	153.2	86.1	0 (low rate)	–
25.09.2005 23:36:45	15.9–25.9	20.9	0.76	1.08	196.0	130.3	1.07	Yes
28.09.2005 22:35:39	13.4–27.2	17.6	1.03	1.73	164.3	118.5	1.73	Yes
05.10.2005 23:07:03	17.1–25.0	20.8	0.49	0.89	155.1	114.0	0.89	Yes
25.10.2005 21:43:30	16.5–24.1	20.0	0.66	0.87	213.4	143.1	0.87	Yes
28.10.2005 00:15:14	43.6–54.4	48.8	0.62	0.91	188.6	113.9	0 (high ZA)	–
28.10.2005 19:49:11	13.5–24.8	17.5	1.08	1.38	218.0	141.6	1.37	Yes
29.10.2005 21:05:37	14.3–22.9	18.9	0.45	0.64	196.3	127.6	0.60	No
31.10.2005 20:48:34	13.6–24.6	18.0	1.04	1.34	216.2	143.1	1.34	Yes
19.11.2005 19:40:02	14.2–18.8	16.2	0.58	0.71	228.0	148.3	0.71	No
20.11.2005 20:36:11	19.7–28.9	25.0	0.57	0.72	219.4	141.6	0.72	Yes
24.11.2005 19:40:39	15.9–28.9	22.2	0.55	1.26	122.2	97.9	1.26	No
26.11.2005 19:43:24	17.2–28.4	22.7	0.65	1.10	163.5	111.4	1.10	No
02.12.2005 19:38:20	19.7–28.8	24.1	0.61	0.88	190.6	125.2	0.89	Yes (+1day)
Total			14.58	21.34			17.85	

Table 7.2: Summary of the MAGIC observations for BL Lacertae in 2006.

(1) Observation start time (UTC)	(2) ZA range [deg]	(3) mean ZA [deg]	(4) # Eve. [10^6]	(5) Obs. T [h]	(6) Rate [Hz] (before)	(7) Rate [Hz] (SIZE>100)	(8) T_{eff} [h] (used)	(9) availability of optical data
20.07.2006 01:07:37	22.6–31.0	26.4	0.55	0.77	199.6	126.2	0.59	Yes
25.07.2006 03:32:13	14.3–19.4	17.0	0.24	0.45	151.8	88.6	0.30	Yes
26.07.2006 03:23:35	14.2–27.3	20.1	0.86	1.51	159.9	94.3	1.51	Yes
28.07.2006 04:19:11	21.9–32.0	26.8	0.54	0.78	192.2	119.7	0.52	Yes
01.08.2006 04:32:41	26.9–35.2	31.1	0.27	0.38	197.3	126.2	0.14	Yes
03.08.2006 03:18:46	16.2–29.6	23.1	0.61	0.91	186.8	113.0	0.85	Yes
04.08.2006 03:07:16	15.8–29.5	22.2	0.83	1.40	165.2	97.7	1.35	Yes
05.08.2006 03:03:43	15.9 –29.5	22.3	1.01	1.38	202.2	123.7	1.33	Yes
06.08.2006 03:02:10	16.1–20.4	17.6	0.22	0.34	186.1	117.7	0.34	Yes
20.08.2006 01:54:12	14.3–28.8	21.5	0.74	1.02	201.1	125.5	1.02	No
21.08.2006 01:44:35	14.3–30.3	20.7	0.85	1.20	197.3	124.1	1.07	No
22.08.2006 01:34:15	14.3–29.5	20.9	1.23	1.77	193.8	122.4	1.73	Yes
23.08.2006 01:00:27	13.5–29.5	19.6	1.42	2.09	189.3	121.3	2.00	Yes
24.08.2006 01:24:27	13.5–30.2	20.6	1.10	1.59	192.2	121.9	1.48	Yes
25.08.2006 00:52:22	13.5–27.1	18.2	1.24	2.03	171.9	108.9	2.03	No
27.08.2006 00:51:51	13.5–28.5	20.2	0.98	1.58	172.2	110.9	1.58	Yes (+1day)
16.09.2006 00:21:57	16.3–24.6	20.4	0.53	0.92	163.3	103.1	0.92	Yes (-1day)
16.09.2006 23:51:34	14.3–29.7	20.9	1.06	1.76	166.6	105.5	1.70	No
18.09.2006 00:06:40	15.9–27.9	20.3	0.27	0.52	142.4	89.9	0.52	No
19.09.2006 00:14:58	16.8–28.3	22.1	0.68	1.12	170.6	106.8	1.12	No
20.09.2006 00:08:33	16.1–29.6	22.4	0.79	1.35	162.0	102.8	1.30	Yes
21.09.2006 00:23:33	19.0–27.3	23.2	0.45	0.82	151.4	96.5	0.82	No
23.09.2006 00:19:57	20.2–28.0	23.6	0.49	0.75	184.3	120.0	0.75	Yes
Total			16.96	26.41			24.98	

RXTE-ASM[4]), optical and radio light curves are shown in Fig. 7.8. No significant evidence of flux variability in VHE γ-rays was found in the 2005 data. A fit for a constant flux yields a $\chi^2/\text{N.D.F} = 16.3/15$. The small excess around MJD 53669-53675, also coinciding with a significant optical excess, is below 3 sigma. The derived average integral flux is $(0.6 \pm 0.2) \times 10^{-11}$ cm^{-2} s^{-1} , which corresponds to about 3 % of the Crab Nebula flux as measured by the MAGIC telescope [245]. In the optical light curve, the contribution from the host galaxy (1.38 mJy [184]) was subtracted. The optical light curve shows a flare around the end of October 2005 (around 53670 in MJD). Also, radio light curves at 37 GHz [159] and 14.5 GHz show enhanced activity starting November 2005. No significant excess could be found in both X-ray bands.

The reconstructed differential energy spectrum (Fig. 7.9) is well described by a simple power law:

$$\frac{\mathrm{d}N_\gamma}{\mathrm{d}E\mathrm{d}A\mathrm{d}t} = (1.9 \pm 0.5) \times 10^{-11} \left(\frac{E}{0.3\,\text{TeV}}\right)^{-3.6 \pm 0.5} \frac{\gamma}{\text{TeV cm}^2\,\text{s}} \tag{7.1}$$

7.3.2 The 2006 results

Fig. 7.10 shows the θ^2 plot for 2006 data using events with SIZE above 350 photoelectrons. With the final selection of $\theta^2 < 0.03$ deg^2, only 17 excess events were obtained, which corresponds to a 0.32 σ excess significance. In Fig. 7.8-(b), the light curve of VHE γ-ray above 200 GeV is compared with light curves in X-rays and optical. The diurnal VHE γ-ray data are in good agreement with statistical fluctuations around Zero. A constant fit to the data resulted in $(0.07 \pm 0.2) \times 10^{-11}$ cm^{-2} s^{-1}. No significant excess in VHE γ-ray emission could be found in the 2006 data. The optical light curve also shows a lower intensity than in 2005.

An upper limit of the integrated VHE γ-ray flux above 200 GeV in 2006 was derived using the Rolke approach [213]. The upper limit in the number of excess, calculated with the Rolke approach, was converted into flux units using the effective collection area and the effective observation time. We obtained the upper limit of 125.9 events in the number of excess with a 95% confidence level, which corresponds to 0.46×10^{-11} cm^{-2} s^{-1} for the flux upper limit.

The observation results in 2005 and 2006 are summarized in Table 7.3.

Table 7.3: Summary of the BL Lacertae observation results in 2005 and 2006

year	On. T$_{\text{eff}}$	Obs. mode			
2005	17.8	On-Off			
2006	25.0	Wobble			
year	Excess events	Off event (Normalized)	excess significance	VHE flux ($>$200 GeV) [cm^{-2} s^{-1}]	optical flux [mJy]
2005	216 ± 43	1275.6 ± 19.7	$5.1\,\sigma$	$(0.6 \pm 0.2) \times 10^{-11}$	9.2
2006	17 ± 55	1825.6 ± 34.1	$0.32\,\sigma$	$< 0.46 \times 10^{-11}$ (95 % C.L.) *	4.2

(*) the average value derived by a fit to the light curve is $(0.07 \pm 0.2) \times 10^{-11}$
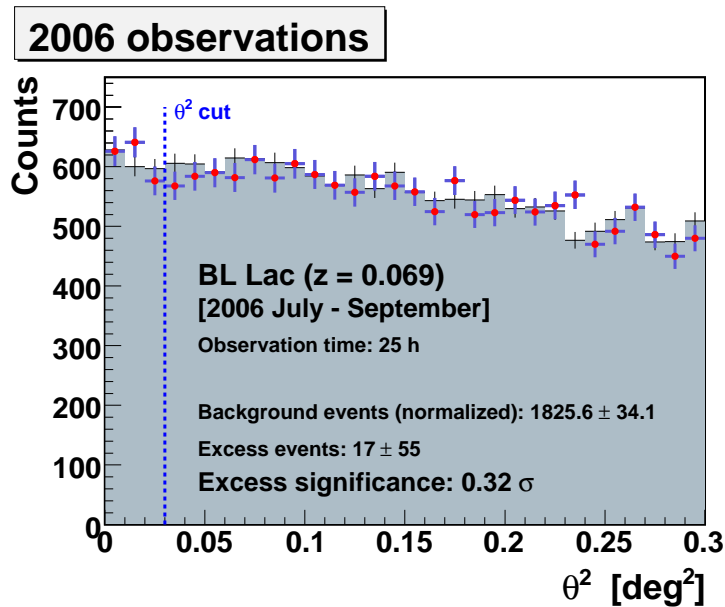
---

[4]http://xte.mit.edu/ASM_lc.html
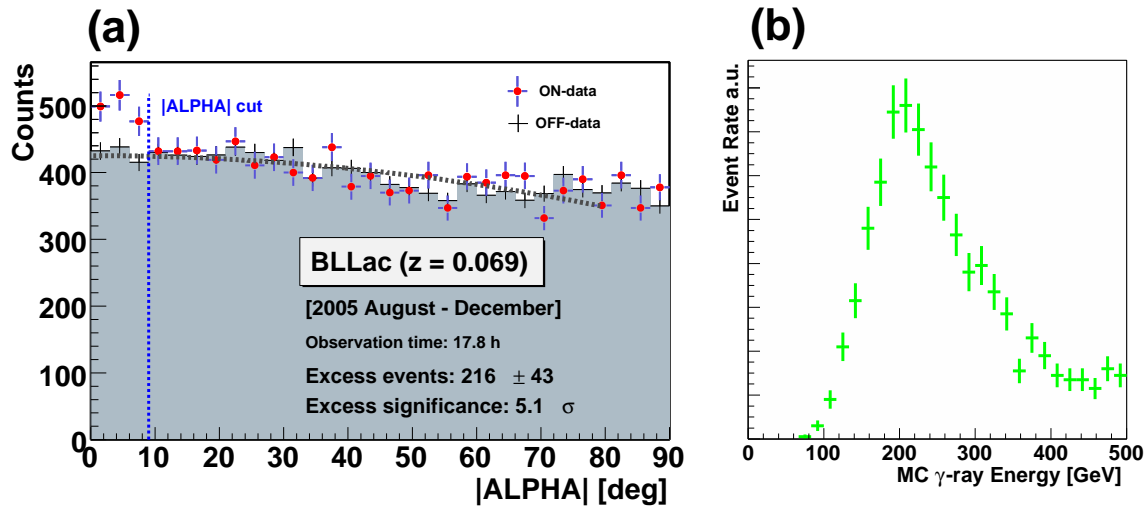
Figure 7.6: (a): ALPHA-distribution of the 2005 data from the BL Lacertae observations by MAGIC using events with SIZE above 350 photoelectrons. The filled circles represent ON-data. The light crosses correspond to normalized OFF-data. In each data point, a horizontal bar denotes a bin size and a vertical bar denotes 1σ uncertainty. The dotted curve describes a second order polynomial fit to the distribution of the OFF-data. The vertical line indicates the ALPHA selection, which yields a total excess of 216 events at a significance level of 5.1 σ. (b): Energy distribution of MC γ-rays with a spectral photon index of -3.6 using events with SIZE above 350 photoelectrons (after applying the same cuts as for the ALPHA-distribution of (a)). The corresponding peak is about 200 GeV γ-ray energy.
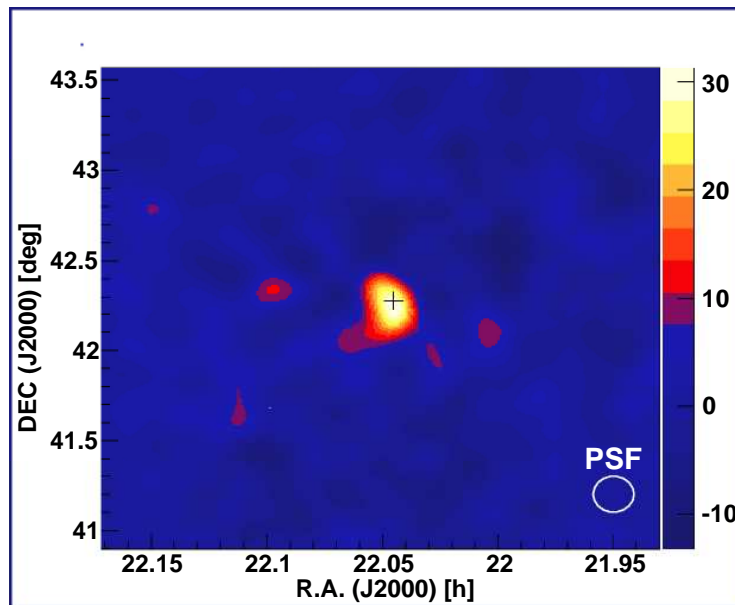
Figure 7.7: Sky map of the region around the position of BL Lacertae (black cross) for reconstructed γ events with > 350 photoelectrons from the 2005 observations.
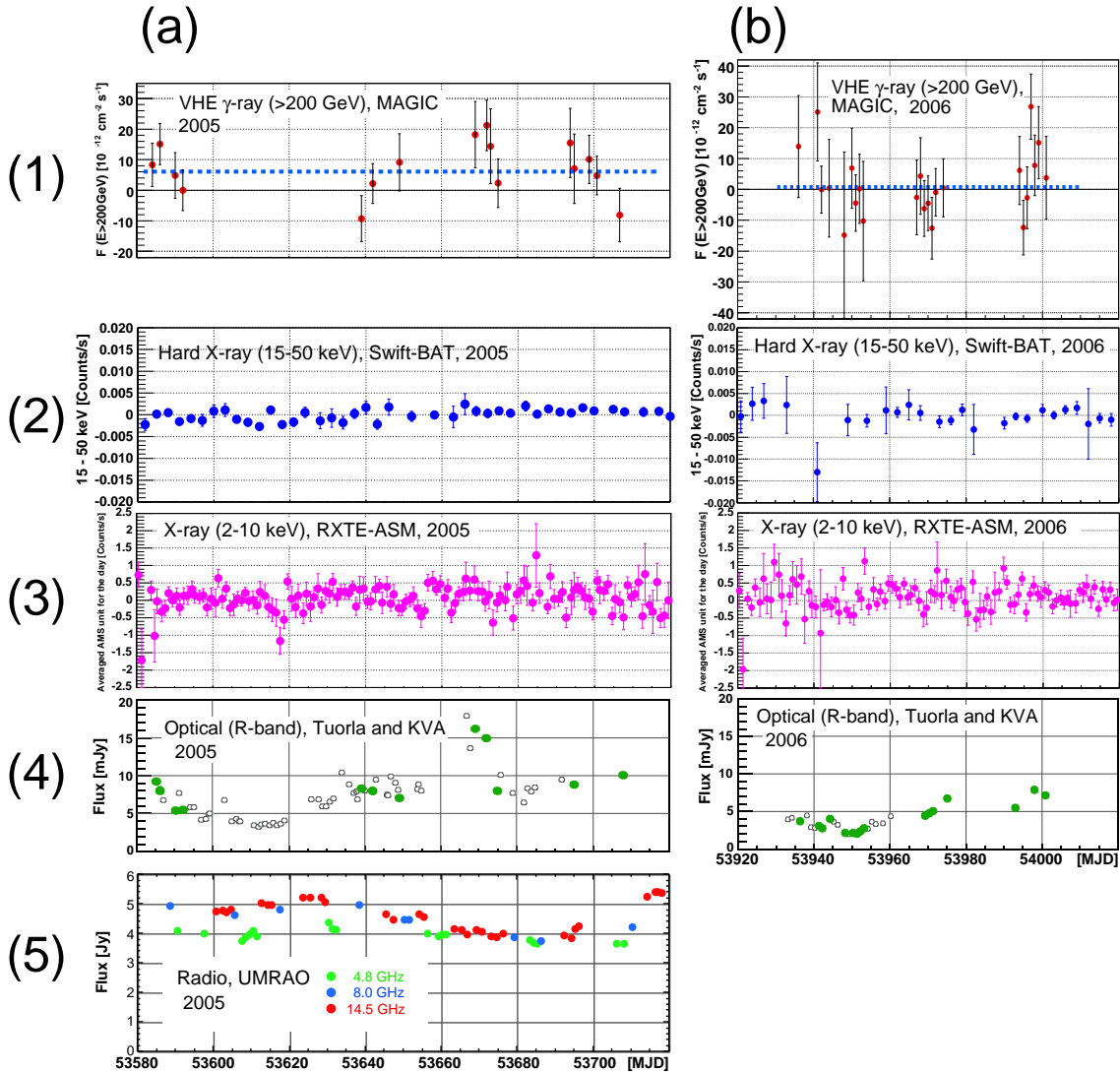
Figure 7.8: Light curves of BL Lacertae in the various energy bands in 2005 and 2006. [from Upper to Lower panels]: (1) VHE γ-ray (> 200 GeV) flux as measured with the MAGIC telescope. Dotted horizontal lines represent the average flux in each year. (2) Hard X-ray of 15-50 keV in one-day average flux by SWIFT BAT detector. (3) X-ray of 2-10 keV in one-day average flux by RXTE-ASM detector. (4) Optical (R-band) flux as measured with the 1.03 m Tuorla and the 35 cm KVA telescope. In the optical light curve, the filled points represent the optical flux at times when simultaneous MAGIC observations were carried out. The measured average flux of those points is 9.2 mJy for 2005 and 4.2 mJy for 2006. (5) Radio flux with 4.8 GHz (*green*), 8.0 GHz (*light blue*) and 14.5 GHz (*red*) measured with UMRAO. [Left panels (a)]: the 2005 data. [Right panels (b)]: the 2006 data.
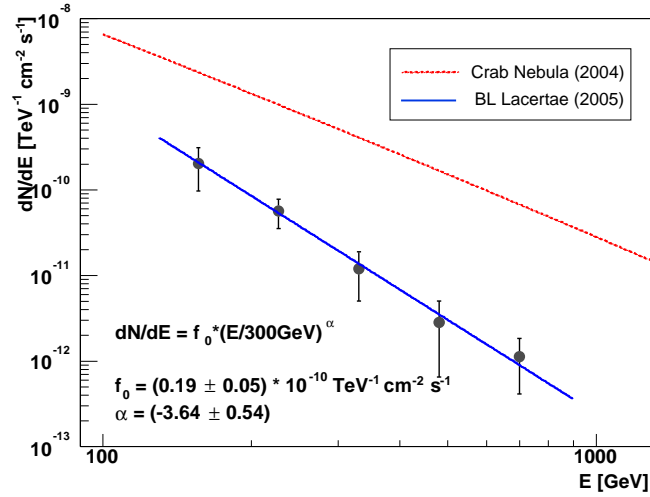
Figure 7.9: Differential energy spectrum of the 2005 BL Lacertae data in the VHE γ-ray band as measured with the MAGIC telescope. The solid line represents a power-law fit to the measured spectrum. The fit parameters are listed in the figure. For comparison, the line fitted to the measured MAGIC CRAB spectrum using a power law with a changing photon index is shown by a dashed line [245].

Figure 7.10: θ^2 distribution of the 2006 data from the BL Lacertae observations by MAGIC using events with SIZE above 350 photoelectrons. The filled circles represent the ON-data. The light crosses correspond to the normalized OFF-data. In each data point, a horizontal bar denotes a bin size and a vertical bar denotes 1σ uncertainty. The vertical blue line indicates the θ^2 selection condition, which yielded a total excess of 17 events at a significance level of 0.32 σ.

7.4 Discussions

7.4.1 Comparison to previously measured results of the VHE γ-ray bands

The Whipple 10 m telescope observed BL Lacertae for 39.1 hours in 1995 and derived a flux upper limit (99.9% C.L.) above 350 GeV at 3.8% of the Crab flux, corresponding to $F(E >$ $350\,\text{GeV}) < 0.4 \times 10^{-11}$ [cm^{-2} s^{-1}] [136]. The HEGRA stereoscopic CT system derived an upper limit (99% C.L.) above 1.1 TeV at 28% of the Crab flux, corresponding to $F(E > 1.1\,\text{TeV}) <$ 0.41×10^{-11} [cm^{-2} s^{-1}] [12]. These upper limits are consistent with our results. On the other hand, Nespher et al. (2001) [182] claim VHE γ-ray detection using the GT 48 telescopes of the Crimean Astrophysical Observatory from their observations in the summer of 1998. The reported integral γ-ray flux is $F(E > 1\,\text{TeV}) = (2.1 \pm 0.4) \times 10^{-11}$ [cm^{-2} s^{-1}], which is two orders of magnitude higher than the extrapolated value from our MAGIC result. During the same period, July to August 1998, no significant signal was found by HEGRA-CT1, and their reported flux upper limit in the same energy band is 7 times lower than the Crimean result [152] (see also Fig. 7.3). Given the locations of both telescopes, the VHE γ-ray detection reported in [182], cannot be explained without a remarkably huge and a very rapid flux variation offset by a few hours in consecutive nights from the HEGRA-CT1 observation. In case of a leptonic origin of the γ-ray emission, such a flare would possibly coincide with high activity in optical as in the outburst of July 1997, when the increase in flux was observed both in the optical and X-ray to γ-ray bands [64, 233]. However, no increased optical activity was detected during the Crimean observation period (optical magnitude: $13.5 - 14.6$, while $13.0 - 14.6$ in 2005). Throughout the EGRET observations for BL Lacertae, such a notably huge and rapid flare feature was never reported in high energy γ-ray emission, which may be considered to have the same origin as the VHE γ-ray emission.

7.4.2 Correlation between VHE γ-ray and optical fluxes

In Fig. 7.8, filled circles in the optical light curve represent simultaneous observations with the MAGIC telescope, accepting a ± 1 day offset with respect to the MAGIC observations. In 2005, there were 12 out of 16 nights with simultaneous observations (average flux: 9.2 mJy), while 16 out of 23 nights in 2006 (average flux: 4.2 mJy) have coinciding observations.

The correlations of our observed VHE γ-ray data with optical data are shown in Fig. 7.11. We fit the data of the diurnal flux with a constant and with a linear function. The results of both fits show the nearly equal and reasonable probabilities from χ^2 tests. The fit results are shown in Fig. 7.11. From the statistical tests, no significant correlation between VHE γ-ray and optical flux could be found. It should be noted that the measurement uncertainties of VHE γ-ray fluxes are relatively large, which makes it difficult to apply the correlation studies.

On the other hand, in the yearly scale, the optical flux in 2005 is 9.2 mJy on average over the 12 days which coincide the MAGIC observations. The optical average flux in 2005 shows a significantly higher value than that of 2006, which corresponds to 4.2 mJy. The absence of a significant excess of VHE γ-rays in the 2006 data indicates that the average flux of VHE γ-ray flux in 2006 was significantly lower than the average flux in 2005 (see Table 7.3).
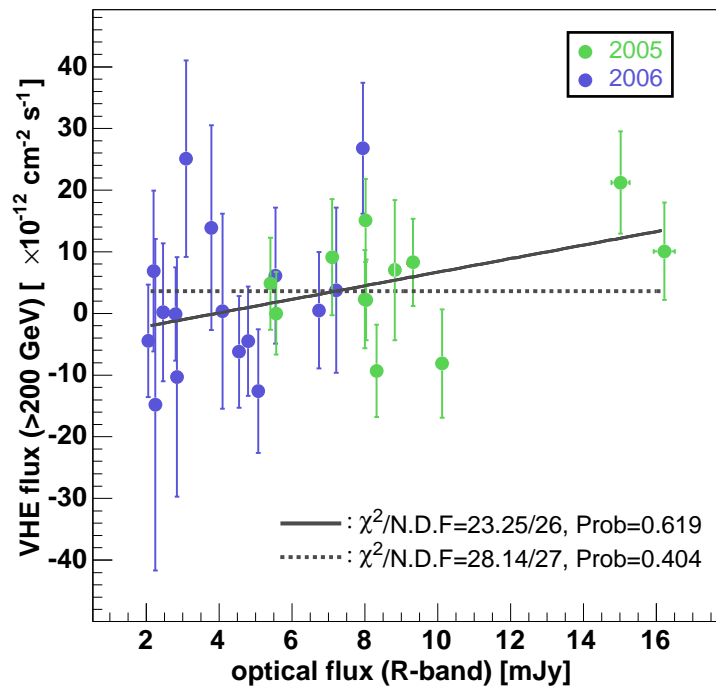
Figure 7.11: Optical (R-band) vs. VHE γ-ray flux correlation during the MAGIC observations for BL Lacertae. The fluxes in the daily scale in 2005 are denoted by the blue points, those in 2006 by the green points. The dotted line denotes a constant fit and the solid line corresponds to a linear fit (the fit probabilities are also given).

In summary, although there is no significant correlation from the statistical point of view, our results show similar tendencies both in the optical and the VHE γ-ray flux variations. Similarly, the γ-ray activity seen by the EGRET observations in 1997 showed a strong correlation with optical activity (see Fig. 7.2). Such a correlation is favorable to leptonic origin scenarios [64].

7.4.3 Spectral energy distributions

As our measurement shows results favorable to leptonic origin scenarios, we discuss here the spectral energy distribution (SED) with the leptonic model from previous studies. Fig. 7.12 shows the SED of BL Lacertae with data in 2005 and some historical data together with model calculations by Ravasio et al. (2002) [208]. The VHE γ-ray points are corrected for the extragalactic background light (EBL) absorption using the "low-IR" EBL model of Kneiske et al. (2004) [148]. Our optical and VHE γ-ray points agree well with the solid line, which was derived using a one-zone synchrotron self-Compton (SSC) model on the 1995 data, whereas some deviations can be seen from the dotted line, which describes the 1997 flare data and involves SSC as well as external Compton (EC) components [208]. In general, it is necessary to introduce the EC component to explain γ-ray emission from LBL objects [109]. However, to describe our result such an additional EC component is not necessarily required.
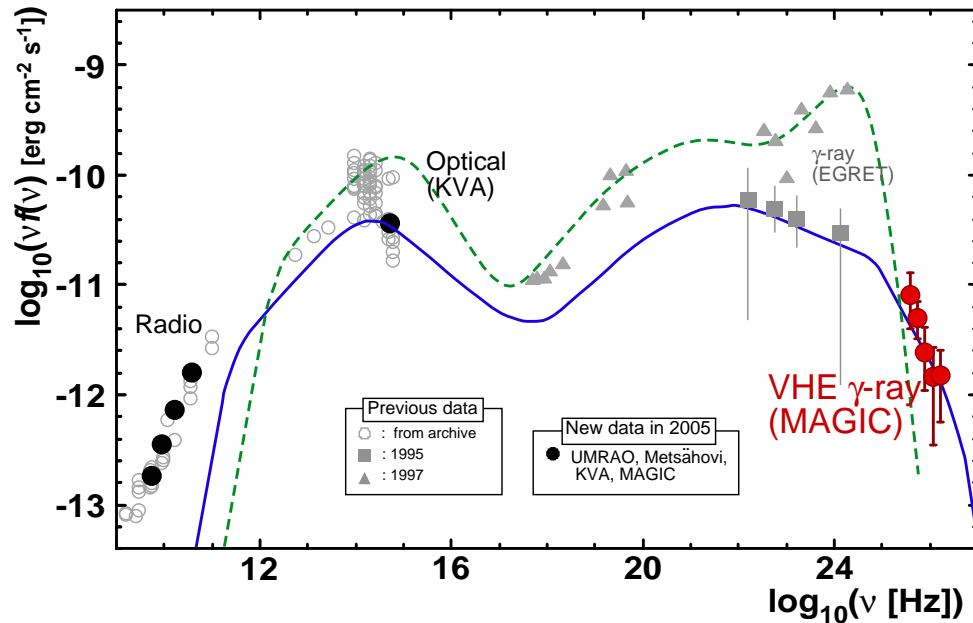
Figure 7.12: SED of BL Lacertae in 2005 and some historical data. The black filled circles represent data taken by KVA and MAGIC as well as radio data by UMRAO and Metsähovi from the year 2005. Gray points describe previous data (taken from ASDC [The ASI Science Data Center: http://www.asdc.asi.it/], see also in the inlay). The lines are taken from [208]. The solid line represents the one-zone SSC model for the 1995 data, the dotted line is produced with SSC and EC components for the 1997 flare data.

7.5   Summary

We observed BL Lacertae for 22.2 hours from August to December 2005 and for 26 hours from July to September 2006. The source is the historical prototype and eponym of a class of LBL objects.

A VHE γ-ray signal was discovered with a 5.1 σ excess in the 2005 data. Above 200 GeV, an integral flux of $(0.6 \pm 0.2) \times 10^{-11}$ cm^{-2} s^{-1} was measured, corresponding to approximately 3% of the Crab flux in this energy range. The differential spectrum between 150 and 900 GeV is rather steep with a photon index of -3.6 ± 0.5. The light curve shows no significant variability during the observations in 2005. For the first time a clear detection of VHE γ-ray emission from an LBL object was obtained with a signal below previous upper limits. The VHE γ-ray emission obtained by our observations can be described with a one-zone SSC model as described for previous studies of the γ-ray emission observed by EGRET in 1995. An additional EC component, which has to be used to explain the γ-ray flare observed by EGRET in 1997, is not necessarily required for the VHE γ-ray emission in our case. On the other hand, the 2006 data show no significant excess. This drop in flux follows the observed trend in optical activity.

The results of this thesis suggest that VHE γ-ray observations during times of higher optical states can be more efficient for this source. Future long term monitoring of VHE γ-ray emission could provide detailed information of a possible periodicity, predicted by e.g., [225], and correlations with other wavelengths. Due to the observed steep spectrum, lowering the energy threshold of IACTs (e.g., with the upcoming MAGIC-II project), would significantly increase the detection prospects for this new class of sources.

Chapter 8

Multiwavelength observations of Markarian 501

Mkn501 (R.A. $16^h53^m52.2^s$, decl. $+39°45'37.0''$ [J2000.0]) first appeared in a catalog of 1515 strong UV sources. In 1972, a radio counterpart could be identified [83], which shortly afterwards was classified as a BL Lac object and measured to have a redshift to $z = 0.034$ [239].

Mkn501 is the second established TeV blazar [205] after Mkn421. Fig. 8.1 shows the overall light curve of Mkn501 in the VHE γ-ray band since the year of discovery of the TeV γ-ray emission, 1996. In 1997, this source went into a state of surprisingly high activity, and became close to 10 times brighter than the Crab Nebula in the TeV range [7]. In 1998-1999, the mean flux dropped by an order of magnitude [8]. In 2005, rapid flux variability with a few minutes time scale in its flare activities was reported by the MAGIC collaboration [41]. Although several multiwavelength studies for this object [144, 154, 235, 107] have been reported, data taken simultaneously both in X-ray and VHE γ-ray in its low state of activity were not yet available.

8.1   Long term light curves in 2005 and 2006

Fig. 8.2 and 8.3 show diurnal light curves of the VHE γ-ray emission above 200 GeV, X-ray between 2 keV and 10 keV and optical R-band in 2005 and 2006, respectively. The VHE γ-ray data were obtained with the MAGIC telescope. Detailed results and discussions for the 2005 data including the flare activities can be found in [41]. Parts of the 2006 observations were carried out within the TeV blazar "monitoring" program [116] of the MAGIC telescope. These observations have been regularly performed for short observation times (typically 20 $\sim$ 60 min) every several days by the MAGIC telescope as long as the source was visible. Such observations can alert us to a high activity state of the source, whose occurrence cannot be predicted. This information is extremely useful for launching planned target of opportunity (ToO) multiwavelength campaigns for such a high state. In addition, these unbiased samples allow us to investigate the general features of source activities.

The X-ray data were taken by RXTE/ASM, which is the X-ray satellite for all sky monitoring
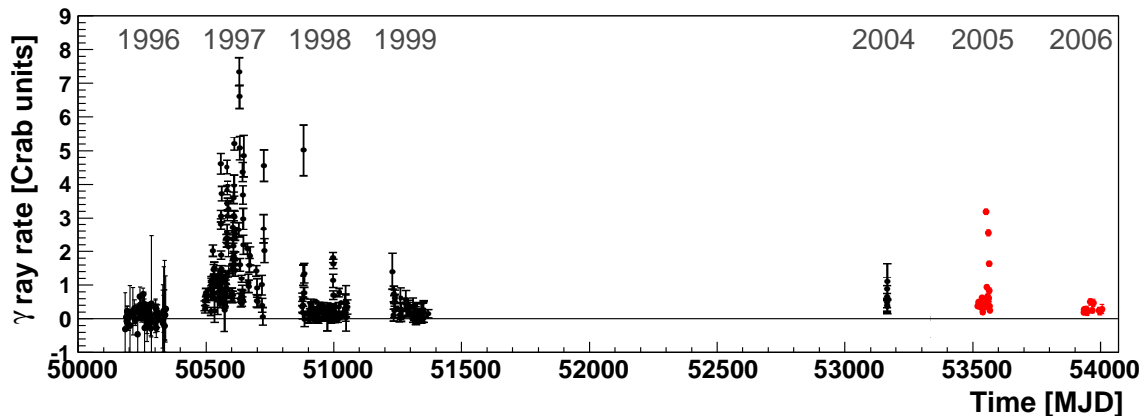
Figure 8.1: Overall light curve of Mkn501 in the VHE γ-ray emission between April 11, 1996, and September 20, 2006. 1996 data taken from [151], 1997-2004 data taken from [113], 2005 data taken from [41], and 2006 data from this work. The 2005 and 2006 data in red points were measured with the MAGIC telescope. Note that the data have different energy thresholds and are, therefore, presented in Crab Nebula units at the thresholds of each data.

observations. The data are available in the web page[1] immediately after the observations. Optical R-band observations were provided by the Tuorla Observatory Blazar Monitoring Program[2] with the 1.03 m telescope at the Tuorla Observatory, Finland, and the 35 cm KVA telescope at La Palma, Canary Islands. The magnitudes were then converted to linear fluxes using the formula $F[Jy] = 3080.0 \times 10^{-(mag/2.5)}$ in R-band (640 nm).

In 2005, two huge flare activities (June 30th and July 9th) were observed in the VHE γ-ray band with the MAGIC telescope (Fig. 8.2). Details about these flares are also discussed in [41]. On the other hand, no corresponding huge flare could be seen in the X-ray band. However, this does not indicate that no counter X-ray flare took place during these TeV flare activities, because of (1): A relatively poor sensitivity of the instrument for the X-ray monitoring (RXTE/ASM). The instrument does not have sufficient sensitivity for detecting significant signals during a low state of activity. The distinction of the flux levels between low and high states is not so clear. (2): Poor time coverage. Although the RXTE/ASM satellite is monitoring all sky, it observes each source once in every orbit ($\sim$ 90 min) for only a short time of exposure. On the other hand, the observed 2005 flares were recorded only for about one hour for each flare activity. Only a few samples of data were available as simultaneous observation results. Due to these facts, it is necessary to organize multiwavelength (MWL) observations with other dedicated X-ray satellites.

In 2006, the source generally showed a quiet and low state of activity. No flare activity was detected with the MAGIC telescope as shown in Fig. 8.3. No strong variability was found, neither in X-ray nor in optical. The flux in the optical band on average also showed a slightly lower value than that of 2005.

---

[1]http://xte.mit.edu/ASM_lc.html

[2]more information at http://users.utu.fi/kani/1m/

We organized a MWL campaign in July 2006 for this source with the Japanese X-ray Satellite "Suzaku", which has a high sensitivity in the widest energy range among current working X-ray satellites. In the VHE γ-ray light curve of 2006 the data points during this MWL campaign correspond to the first three points. This campaign was held in one of the lowest states of this source during these 2 years in the VHE γ-ray band, as one can see in the figures (Fig. 8.2 and 8.3). It provided us with simultaneous data samples in X-ray and VHE γ-ray during a low state of activity that previous MWL campaigns had not been able to supply due to the limited sensitivity of γ-ray telescopes.

In this Chapter, I present observations and results of this extensive MWL campaign and discuss the relevant multi-energy bands data.
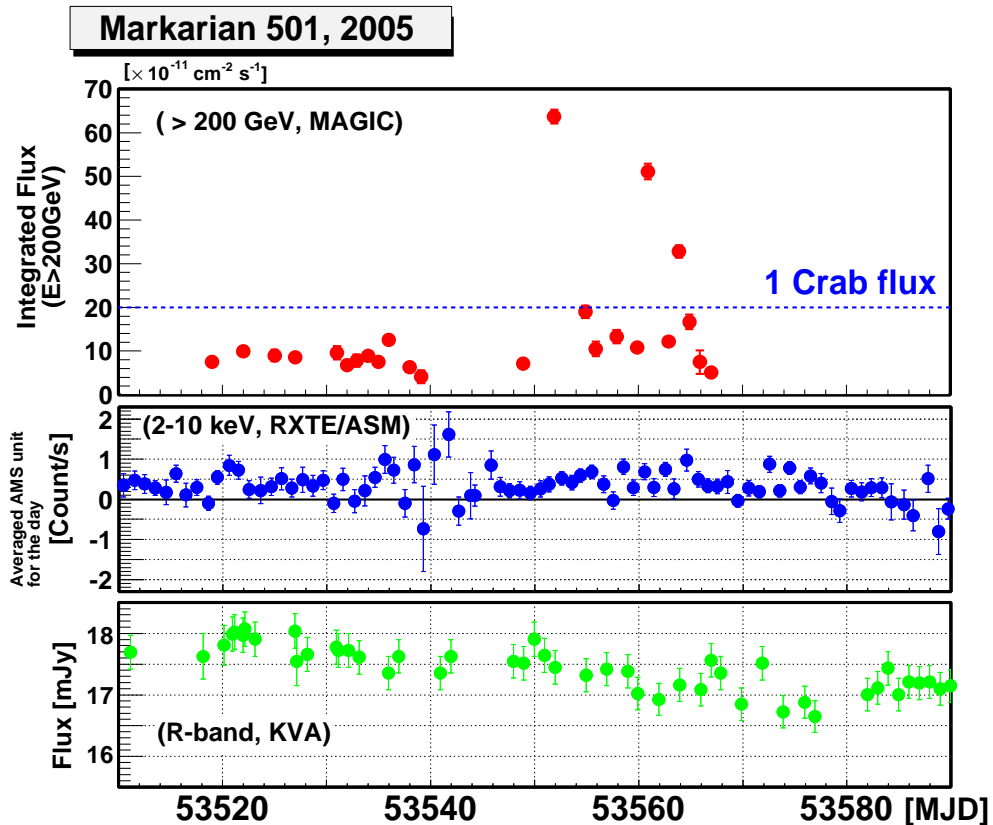
Figure 8.2: Diurnal multifrequency light curves during the MAGIC observations of Mkn501 in May-July, 2005. **[Top]**: VHE γ-ray above 200 GeV as measured by MAGIC (taken from [41]). A horizontal dotted line represents one flux level of the Crab Nebula in this energy range. **[Middle]**: X-ray by RXTE/ASM. **[Bottom]**: optical R-band by KVA.
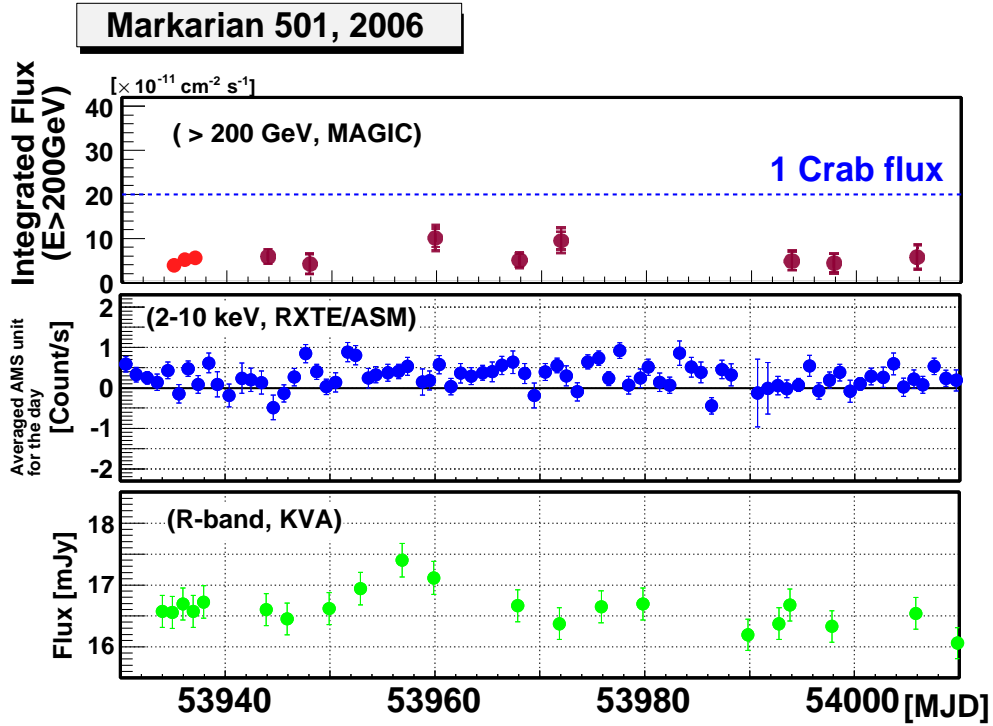
Figure 8.3: Diurnal multifrequency light curves during the MAGIC observations of Mkn501 in July-September, 2006. **[Top]**: VHE γ-ray above 200 GeV was measured by MAGIC within the scope of this thesis. Red points indicate the MWL campaign observation. Dark red points show the data taken during "monitoring observation" [116]. A horizontal dotted line represents one flux level of the Crab Nebula in this energy range. **[Middle]**: X-ray by RXTE/ASM. **[Bottom]**: optical R-band by KVA.

Table 8.1: Summary of the MAGIC observations for the MWL campaign in July 2006.

Observation day (start)	(UTC) start - end time	ZA range [deg] (mean)	Obs. T [h]	Rate [Hz][1] (after cut)	Eff. Obs. T.[2] [h] (used)
18.07.2006	21:35:35–01:05:08	11.0–36.0 (19.2)	3.49	130.3	3.18
19.07.2006	21:30:53–01:02:17	11.0–35.5 (19.1)	3.49	134.2	3.18
20.07.2006	21:30:13–01:00:42	11.0–35.9 (17.2)	3.50	117.0	2.79
Total			10.5		9.1

(1) after applying the SIZE cut of >100 p.e.
(2) effective observation time of the analyzed data

8.2 Multiwavelength campaign in July 2006

8.2.1 VHE γ-ray with the MAGIC telescope

Observations

Observations for the multiwavelength campaign were conducted in the nights of July 18th, 19th and 20th, 2006, for 10.5 hours, in wobble mode, where the object was observed at an $0.4°$ offset from the camera center. Detailed information on the observations is summarized in Table 8.1.

After rejecting the data with low trigger rates due to bad observation conditions and a high zenith angle range ($> 35°$), the remaining data of 9.1 hours were processed for analysis. The analysis was basically performed with the standard analysis software "MARS" as described in Chapter 6. In order to improve the analysis performance for the data, the arrival time information of the Cherenkov light was used for the image cleaning process as an advanced option. This option allowed us to use lower tail cut levels: 6 p.e. instead of 7 p.e. for core pixels and 4 p.e. instead of 5 p.e. for boundary pixels. Based on the DISP method, the θ parameter was used for the final cut to evaluate the γ-ray signals.

Results

The observed excess signal of 522 events over 939 normalized background events below $\theta^2 < 0.03\,\mathrm{deg}^2$ corresponding to 13.4 σ excess was observed in the total campaign data of 9.1 hours observation as shown in Fig. 8.4. Events were selected only from the data with SIZE above 350 p.e..

The upper panel in Fig. 8.6 shows the light curve with a 1-hour binning during this campaign. The average integrated flux above 200 GeV is $(4.6 \pm 0.4) \times 10^{-11}$ cm^{-2} s^{-1} (χ^2/N.D.F = 10.1/10), which corresponds to about 23% of the Crab Nebula flux as measured with the MAGIC telescope [43]. No significant variability was found. However, due to the low source flux level, we could only have seen variability of a factor of 2-3.

The spectrum in the VHE γ-ray band is well described by a simple power law from 85 GeV to 2 TeV with

$$\frac{\mathrm{d}N_\gamma}{\mathrm{d}E\mathrm{d}A\mathrm{d}t} = (1.24 \pm 0.11) \times 10^{-10} \left(E/0.3 \text{ TeV} \right)^{-2.85 \pm 0.14} \frac{\gamma}{\text{TeV cm}^2 \text{ s}}. \tag{8.1}$$

The flux level and the photon index of this measured spectrum are compatible with those in the lowest state among 2005 MAGIC observation results, which were derived by the night-by-night basis analysis ($\mathrm{d}N_\gamma/(\mathrm{d}E\mathrm{d}A\mathrm{d}t) = (1.36 \pm 0.21) \times 10^{-10} \left(E/0.3 \text{ TeV} \right)^{-2.73 \pm 0.29}$ [41]) for this object.

8.2.2 X-ray observations with the Suzaku satellite

X-ray observations by Suzaku were carried out between July 18th, 2006, 18:33:00 UTC and July 19th, 2006, 17:27:00 UTC (sequence number 071027010). The net exposure time after screening was 35 ksec in both XIS and HXD detectors. HXD/GSO data were not used in the following analysis, since the performance and background of the GSO are still under study.
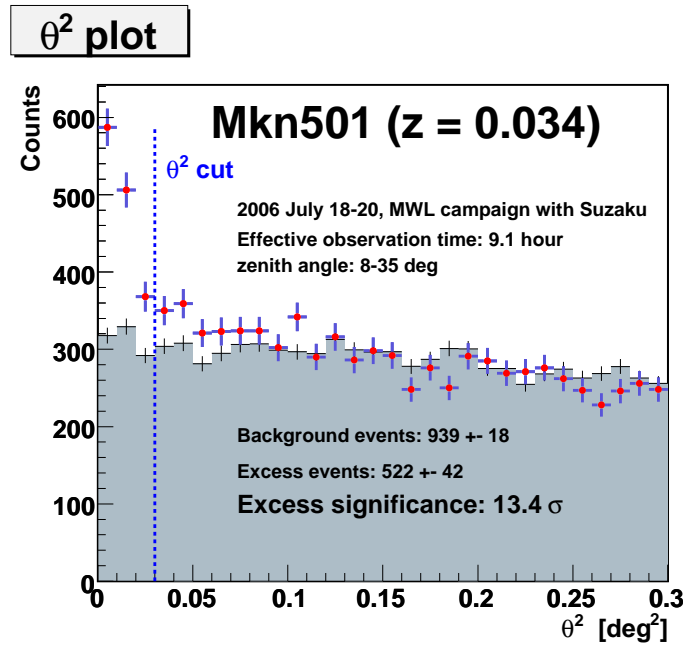
Figure 8.4: θ^2 distribution of Mkn501 from the 2006 MWL campaign observations with events above 350 photoelectrons. A cut of $\theta^2 < 0.03\,\mathrm{deg}^2$ (dashed blue line) yielded the signal of 522 events over 939 normalized background events, corresponds to a 13.4 σ excess.
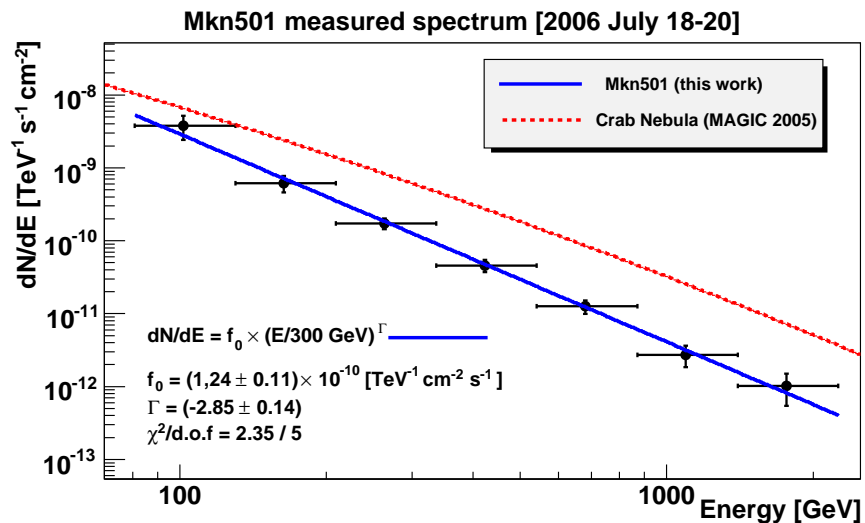
Figure 8.5: Differential energy spectrum of the VHE γ-ray emission of Mkn501 averaged over 3 days during the MWL campaign as measured with the MAGIC telescope. Blue line shows the fitting line with a simple power law. The fit parameters are listed in the figure. For comparison, the measured MAGIC Crab spectrum [43] is shown by a red dashed line.

The light curve of Mkn501 recorded with the XIS detectors (E<10 keV) is shown in the middle panel of Fig. 8.6. The flux level was gradually growing during the observation and an increase of about 50 % can be seen between the beginning and the end of the observation.

A joint XIS and HXD/PIN (0.5-50 keV energy band) fit was performed using a model with a broken power law and a fixed column density ($N_H = 1.5 \times 10^{20}\,\text{cm}^{-2}$) for the galactic absorption (using the command "wabs*bknpower" on the analysis program of "XSPEC"[3]). Best fit parameters with associated errors are: $\Gamma_1 = 2.17 \pm 0.01, \Gamma_2 = 2.33 \pm 0.01, E_{\text{break}} = 1.43^{+0.02}_{-0.04}$.
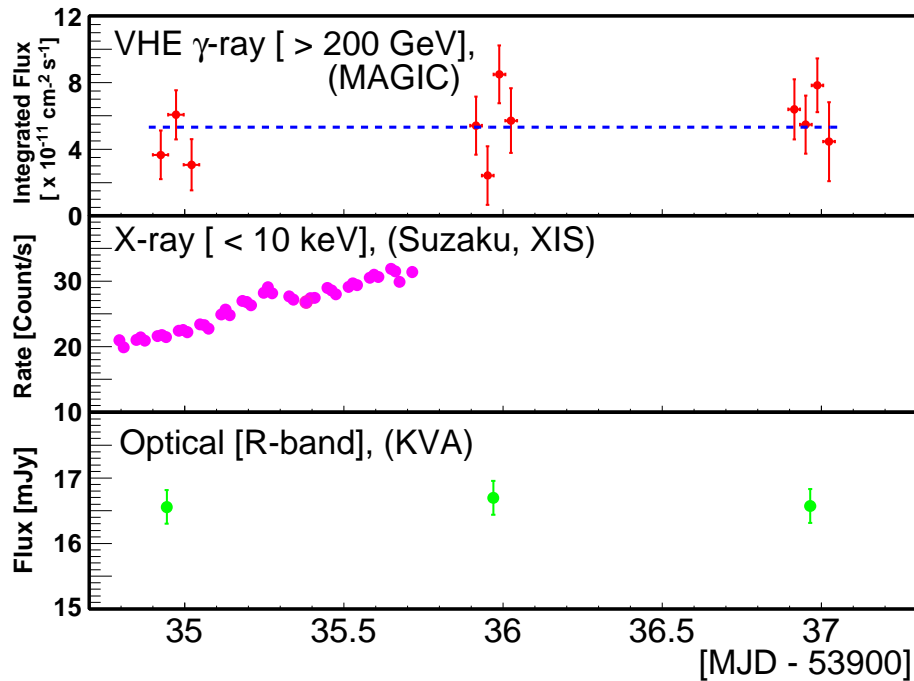
Figure 8.6: Light curves of Mkn501 in different energy bands during this MWL campaign in July 2006. **[Top]:** VHE γ-ray measured with the MAGIC telescope. A dotted horizontal line represents the average flux. **[Middle]:** X-ray net data with Suzaku XIS detectors. **[Bottom]:** Optical R-band flux measured by KVA.

8.3 Spectral energy distributions

8.3.1 Comparisons with previous measurements

Fig. 8.7 shows measured spectral energy distributions (SEDs) of Mkn501 in the VHE γ-ray band obtained during this MWL campaign as well as the spectra measured by MAGIC in 2005 [41] and by CAT on April 16th, 1997 [89]. The CAT data were taken in a previous MWL campaign with the BeppoSAX X-ray satellite when the source showed a high flux. Spectra in the MAGIC

---

[3]http://heasarc.gsfc.nasa.gov/docs/xanadu/xspec/

2005 observations were derived from the low-, medium- and high-flux data sets based on the flux levels and the flare data of June 30th. The correlation between the power law spectral index and integrated intensity above 150 GeV is shown in Fig. 8.8. In this figure, results of MAGIC 2005 observations were obtained on a night-by-night basis analysis. Two days of the flare data (June 30th and July 9th) were split into two samples for each stable and variable parts (detailed information can be found in Albert et al. (2007) [41]). Including the new result of 2006 obtained in the work of this thesis, Fig. 8.8 consists of 27 points. This figure indicates that the spectral slope is getting harder as the flux is increasing. The 2006 data for this MWL campaign represents one of the steepest photon indices and the lowest fluxes levels compared to the published data of Mkn501 in the VHE γ-ray band so far.

The spectra of Mkn501 in the VHE γ-ray band show a strong variability, but the variability shows different features depending on the energy bands. In Fig. 8.7, the difference in flux at $\sim$ 1 TeV is almost two orders of magnitude, while close to 100 GeV only a difference of a factor 2-3 in flux can be seen. These features are associated with the trend of anti-correlation between the spectral index and the intensity. The spectral peak, which may correspond to the inverse-Compton peak, can be seen only in the highest flux states (April 16th, 1997, by CAT and June 30th, 2005, by MAGIC) in this energy range (> 100 GeV).

The spectrum obtained by Suzaku on July 19th, 2006, during our MWL campaign is described in Fig. 8.9 together with historical X-ray data by the BeppoSAX satellite (taken from ASDC[4]). X-ray data also show a strong variability. The difference in flux is no more than one order of magnitude in the soft X-ray band (< 1 keV). On the other hand, the flux variability becomes stronger in the hard X-ray range (> 10 keV). In addition, the spectral peak by the synchrotron emission evolves towards higher energies as the flux increases. In particular, in the highest flux ever recorded (the data of April 16th, 1997), the synchrotron peak reached an extraordinarily high energy around 100 keV.

As one can see in the comparison of these X-ray spectra (Fig. 8.9), the Suzaku data represents a spectrum in a low X-ray state of this source as well as the MAGIC data taken for the 2006 MWL campaign represents the spectrum in a low state of the VHE γ-ray band. Finally, it is worth mentioning once more that the CAT data in Fig. 8.7 and the highest flux of the BeppoSAX data in Fig. 8.9 (data on 16th of April 1997) were taken simultaneously.

8.3.2 SSC model

Fig. 8.10 shows an overall SED of Mkn501 together with data obtained during this MWL campaign and some historical data [41, 235]. The "de-absorbed" data in blue points at the VHE γ-ray band were corrected for the extra-galactic background light (EBL) absorption using the "low-IR" model of Kneiske et al. (2004) [148]. In optical, the host galaxy contributions (12.0 ± 0.3) [mJy] [184] have already been subtracted.

Assuming a uniform injection of the electrons throughout a homogeneous emission region, we applied a one-zone SSC model for our campaign data to estimate physical parameters of the emitting region using the code developed by Tavecchio et al. [234, 235]. The details of the SSC

---

[4]http://www.asdc.asi.it/
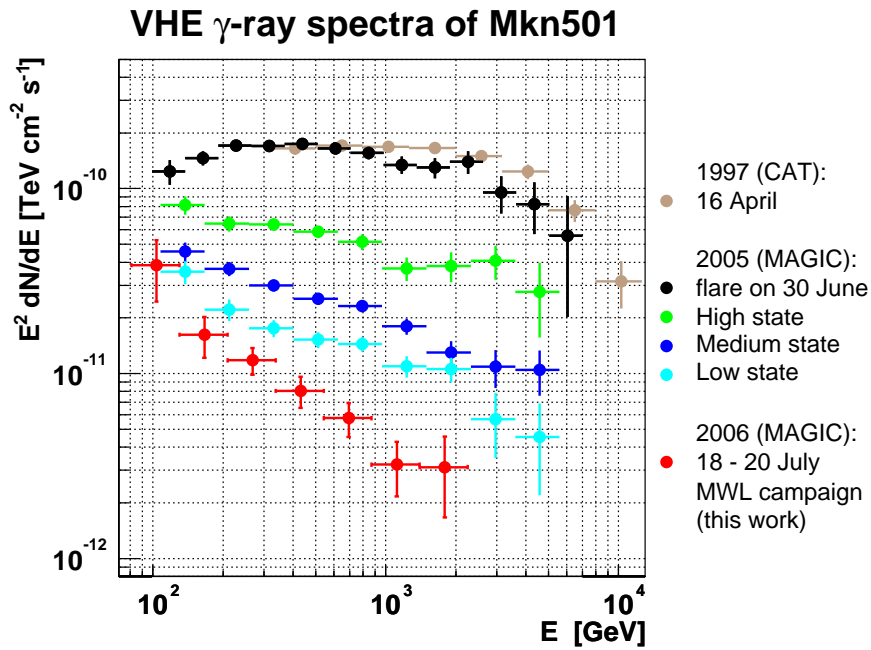
Figure 8.7: Measured VHE γ-ray spectra of Mkn501 in different activity states. The CAT data were taken from [89], the 2005 MAGIC data from [41], the 2006 data from this work. Vertical bars denote the 1 σ statistical error. Horizontal bars represent energy bins.
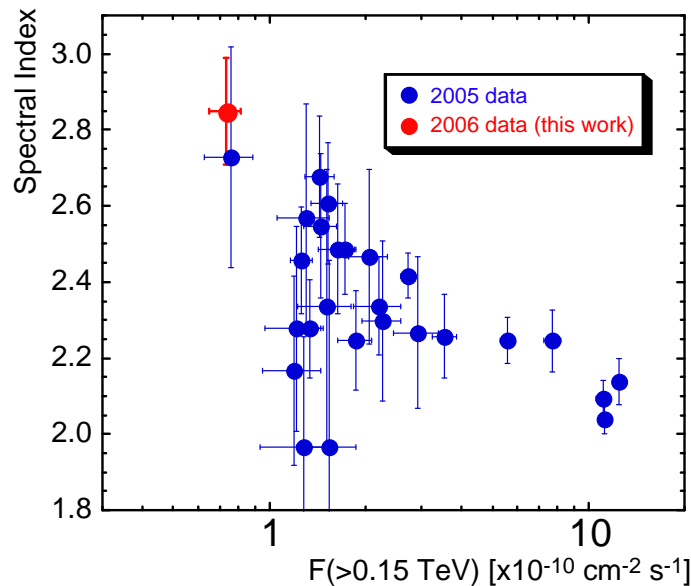
Figure 8.8: Correlation between integrated flux above 150 GeV and spectral shape. Each blue point denotes a single night of observation in 2005 taken from Fig. 11 of [41]. Red point represents the observational result in July 2006 during the MWL campaign described in this work. Vertical and horizontal bars denote 1 σ uncertainties in each value.
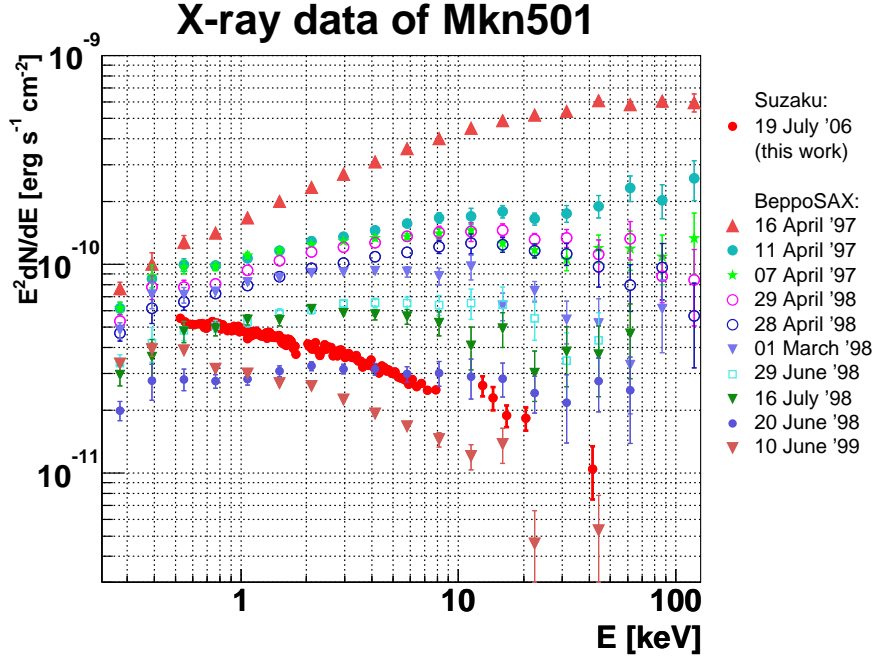
Figure 8.9: X-ray data of Mkn501 in different activity states by Suzaku (this work) and by BeppoSAX (taken from ASDC).

model are described in section 2.3.1. Briefly, a spherical shape (blob) is adopted for the emission region with a radius R, filled with a tangled magnetic field with an intensity B. An electron distribution is described by a smoothed broken power-law energy distribution with slopes n_1 from γ_{min} to the break energy γ_b and n_2 up to a limit of γ_{max} and with a normalization factor K. The relativistic effect is taken into account by the Doppler beaming factor δ.

R is selected to be 1×10^{15} cm, which had been adopted in [41] for the SED during the rapid flare observed by MAGIC in 2005. Since no cut-off in high energy ranges of spectra can be seen both in the X-ray and VHE γ-ray bands, γ_{min} and γ_{max} are fixed at 1 and 10^7, respectively. First, we applied the SSC model for the low state SED which was obtained during our MWL campaign in 2006. The one-zone SSC model can reproduce well the obtained X-ray and VHE γ-ray spectra in this low state of activity of the source. However, it is apparent that the model underestimates the optical flux. This can be explained by the assumption that the emission from radio to UV has a different origin than the high-energy emission. This interpretation has already been applied to previous SEDs of Mkn501 by [145]. We also tried to reproduce the SED obtained during the flare on June 30th, 2005, using this SSC model. Unfortunately, there was no simultaneous X-ray data other than RXTE/ASM available at that time. However, the RXTE/ASM flux point (black triangle in Fig. 8.10) shows a compatible level in the X-ray spectrum taken by BeppoSAX (cyan dots in Fig. 8.10) on April 16th, 1997. In addition, the VHE γ-ray spectrum taken by MAGIC on June 30th, 2005, was almost equivalent to the spectrum measured by CAT on April 16th, 1997, as they are shown in Fig. 8.7. Therefore, we used these BeppoSAX spectrum as a guide for the X-ray spectrum during the VHE γ-ray flare on June 30th, 2005. Finally, we could reproduce this

SED in a high state only by changing the Lorentz factor of the electron at break energy in the electron spectrum, γ_b. These SSC models for the low and high states of Mkn501 are represented by dotted lines in Fig. 8.10. The derived parameters for these SSC models are listed in Table 8.2.

In Table 8.3 we compared some results of previous SED studies based on SSC model for Mkn501. All of them were derived from applying one-zone SSC models for real observational data. Not all studies used the simultaneous X-ray and VHE γ-ray data. In fact, the data simultaneously taken were available only for high flux states, especially during the huge outbursts in 1997. Nevertheless, SSC model parameters of δ and B derived from our 2006 MWL campaign show values similar to those of previous works with different flux states, except for models of Tavecchio et al. (1998) [234] (lower δ and higher B) and Konopelko et al. (2003) [150] (higher δ and lower B) (Both of them are the models for the 1997 high states.) Note again that only our work used simultaneous X-ray and VHE γ-ray data for a low flux state.

Tavecchio et al. (2001) [235] could model different emission states of Mkn501 in 1997 and 1999 by mainly changing the break energy of electrons, slightly modifying its spectral slopes and number density, and by keeping other parameter unchanged. Pian et al. (1998) [199] also could reproduce different flux states by just changing the electron distribution with same values for others. In these frameworks, the electron spectrum was the key component representing the different activity states of Mkn501; especially, γ_{break} could play a main role there.

Table 8.2: SSC model parameters of Mkn501.

data	R	δ	$\gamma_{\min}$	γ_{br}	$\gamma_{\max}$	B	K	n_1	n_2
	cm					Gauss	particle/cm^3		
2006 (low)	1.03×10^{15}	20	1	6.7×10^4	1×10^7	0.27	1×10^5	2	4
2005 (flare)	1.03×10^{15}	20	1	1×10^6	1×10^7	0.27	1×10^5	2	4

Table 8.3: Comparison of the SSC model parameters, δ, B and R to previous studies for Mkn501.

δ	B [G]	R [cm]	flux state[1]	reference
15	0.8	5×10^{15}	H,M(1997) and typical L	Pian et al. (1998) [199]
8-20	0.1-0.5	$7 - 9 \times 10^{15}$	typical L	Tavecchio et al. (1998) [234]
7	1	2.5×10^{15}	H (1997)	Tavecchio et al. (1998) [234]
15	0.2	4.5×10^{15}	L (1996)	Kataoka et al. (1999) [144]
12-36	0.07-0.6	N/A[2]	H (1997)	Bednarek & Protheroe (1999) [54]
14	0.15	2.9×10^{15}	H (1997)	Katarzynski et al. (2001) [145]
14	0.15	4.2×10^{15}	M (1997)	Katarzynski et al. (2001) [145]
10	0.32	1.9×10^{15}	H, M (1997) and L (1999)	Tavecchio et al. (2001) [235]
11	0.2	10×10^{15}	typical low state	Kino et al. (2002) [147]
50	0.04	3.5×10^{15}	H (1997)	Knopelko et al. (2003) [150]
20	0.27	1.03×10^{15}	H (2005) L (2006)	this work

(1) H: High state, M: Medium state, L: Low state (among histical data)

(2) R was not specified, but they modeled with variability time scale of 2min to 2.5h
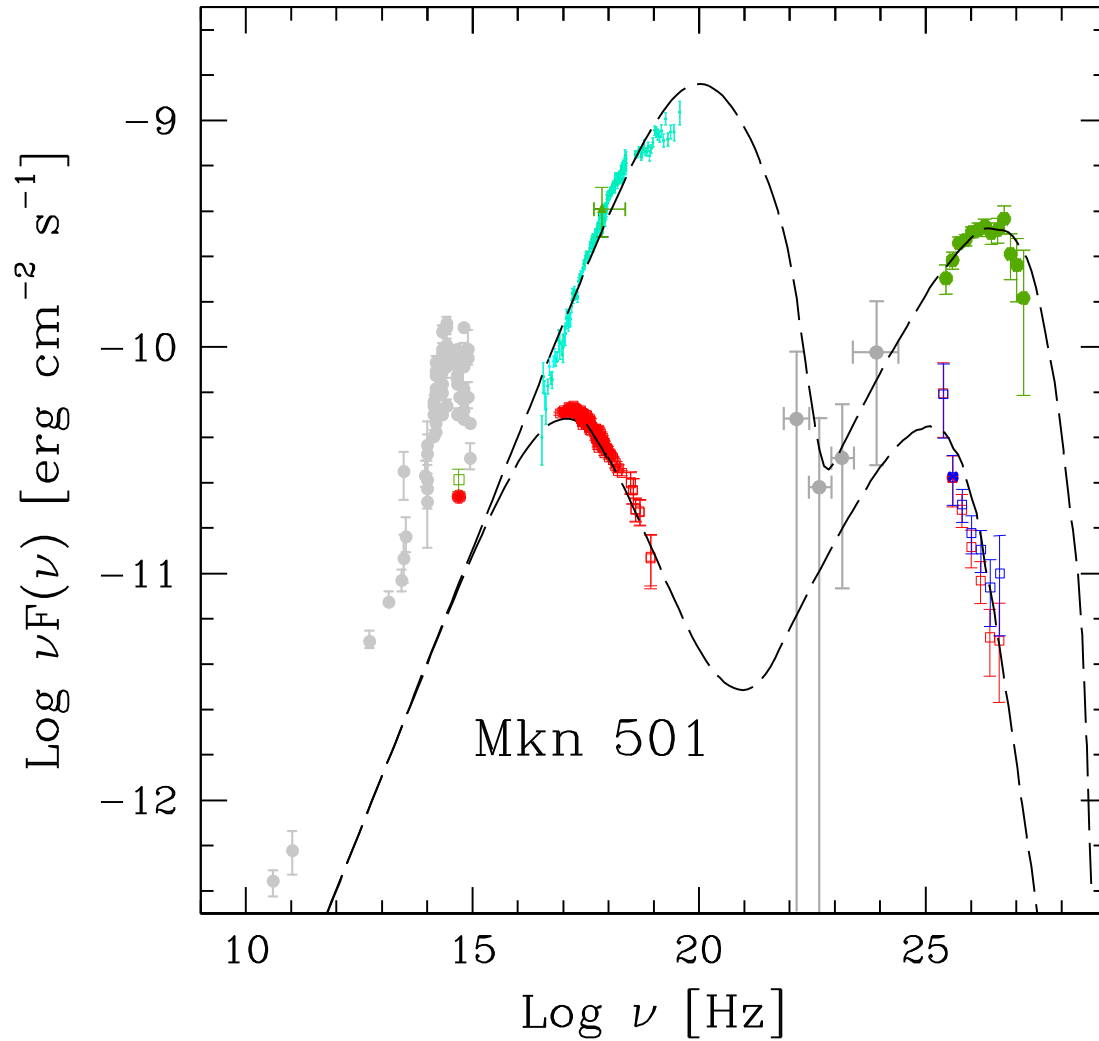
Figure 8.10: Overall SED of Mkn501 as measured in July 2006 and some historical data. Red points are measured data from this campaign with the data points by KVA (optical), Suzaku (X-ray) and MAGIC (VHE γ-ray). Blue points are corrected VHE γ-ray fluxes by the "low-IR" EBL model of Kneiske et al. (2004) [148]. Green points are data taken on 30th of July 2005 by KVA (optical), RXTE/ASM (X-ray) and MAGIC (VHE γ-ray). Cyan points denote the X-ray spectrum taken by BeppoSAX on 16th of April 1997. Grey points are historical data taken from NASA Extragalactic database (radio-optical) and from [144](γ-ray data observed by EGRET). The lines describe the SSC model developed by [234, 235] for the data. Details of the model can be seen in the text and in Table 8.2.

8.4   Summary

I present first results of an MWL campaign for TeV blazar Mkn501 during its low state of activity by MAGIC, Suzaku in July 2006. VHE γ-ray signals were clearly detected with a 6.3 σ level from 9.1 hours of data samples during the MWL campaign.

The average integrated flux above 200 GeV was $(4.6 \pm 0.4) \times 10^{-11}$ cm^{-2} s^{-1}, which corresponds to about 23% of the Crab Nebula flux as measured with the MAGIC telescope. No significant variability was found. The spectrum in the VHE γ-ray band was well described by a simple power law from 85 GeV to 2 TeV with a photon index of -2.85 ± 0.14. The flux level and the photon index of this measured spectrum were compatible with those found in the lowest state 2005 MAGIC observation results, which were derived by the night-by-night basis analysis.

The X-ray spectrum with the Suzaku Satellite was derived from sub-keV to several tens of keV in this campaign. The flux level in X-ray showed a low state of activity as well as the VHE γ-ray flux showed a low state. The small increase in flux could be seen in the X-ray band during the observation.

Compared to previous measured spectra, both energy bands showed a historically strong variability. The variability contained different features depending on the energy bands. In the VHE γ-ray band there was an almost two orders of magnitude difference in flux at ~ 1 TeV, while close to 100 GeV a difference of only a factor 2-3 in flux could be seen. Similar features could be found in the X-ray bands. The difference in flux was less than one order of magnitude in the soft X-ray (~ 1 keV) band, but it became more significant at higher energies and reached about two orders of magnitude around 100 GeV. These results indicate a trend of anti-correlation between the spectral index and the intensity both in X-ray and VHE γ-ray bands. The spectral slope is getting harder as the flux is increasing.

The overall SED in the low state taken during our MWL campaign was well represented by a homogeneous one-zone SSC model. Based on the parameters for this low state, the high state SED in 2005 could be reproduced only by changing the Lorentz factor of the electron at break energy in the electron spectrum. Others showed similar values to the ones derived in previous studies. This might suggest that the electron energy at the spectral break could be the key parameter to represent the different activity states of Mkn501.

Chapter 9

Observations of 1ES1959+650

9.1 1ES1959+650

1ES1959+650 (R.A. $19^h59^m59.95^s$, decl. $+65°08'54''$ [J2000.0], $z = 0.047$) was discovered in the radio band as a part of a 4.85 GHz survey performed with the 91 m NRAO Green Bank telescope [119, 51]. In the optical band it is highly variable and shows a complex structure composed by an elliptical galaxy plus a disc and an absorption dust lane [127]. The mass of the central black hole has been estimated to be in the range of $1.3 - 4.4 \times 10^8 M_\odot$ as derived either from stellar velocity dispersion or from bulge luminosity [95]. The first X-ray measurement was performed by *Einstein*-IPC during Slew Survey [93]. Subsequently, the source was observed by ROSAT, BeppoSAX. RXTE, XMM-Newton. In the two BeppoSAX pointings, for instance, the synchrotron spectra peaked in the range of 0.1-0.7 keV were observed up to 45 keV. The peak was moving to higher energy as with the flux increases [229].

9.2 Previous observations in the VHE γ-ray band

The first VHE γ-ray signal from 1ES1959+650 was reported in 1998 by the Seven-Telescopes Array in Utah, with a 3.9 σ significance [187]. Observing the source in 2000, 2001 and early 2002, the HEGRA collaboration reported only a marginal signal [137]. In May 2002, the X-ray flux of the source had significantly increased. Both the Whipple [134] and HEGRA [10] collaborations subsequently confirmed a higher VHE γ-ray flux as well. Further high γ-ray activity periods were found in the same year, with some flares exceeding the Crab Nebula flux by a factor of 2-3. An interesting aspect of the source activity in 2002 was the discovery of a so-called "orphan" flare (viz., a flare of VHE γ-rays not accompanied by correlated increased activity at other wavelengths), recorded on July 4th by Whipple [156]. This orphan flare, observed in the absence of high activity in X-rays, is not expected from conventional one-zone SSC models. On the other hand, SEDs of other HBLs including the X-ray band and the VHE γ-ray band can successfully be explained using models based on the SSC mechanism. Further observations of 1ES1959+650 are, therefore of special importance.

In September and October 2004, the MAGIC telescope observed VHE γ-rays from this

source with a $\sim 8\,\sigma$ significance of the excess in a relatively short observation time (6.5 hours) even during a state of low activity ($\sim 20\%$ of Crab Nebula flux). The details of the results have been reported in the paper of Albert et al. (2006) [36]. We continued observations for 1ES1959+650 in the 2005 and 2006 seasons as well. Especially, at the end of May 2006, we organized simultaneous multiwavelength (MWL) observations together with the X-ray satellite Suzaku in order to observe both the broad band X-ray continuum and wide range VHE γ-ray emission with the aim of simultaneously obtaining the synchrotron and IC components. In addition, another X-ray satellite, Swift, performed several observations with short exposure times around this period. The source was also observed in the optical R-band from ground optical telescopes.

In this cheaper, I report the results of the MAGIC observations for 1ES1959+650 in 2005 and 2006 and focus on the extensive MWL campaign for this source in May 2006.

9.3   VHE γ-ray with the MAGIC telescope

9.3.1   The 2005 observations

In 2005, observations of 1ES1959+650 with the MAGIC telescope were carried out between May and July. They were performed in the On/Off mode, and total observation time for ON data was 22.3 hours. The zenith angles ranged from $36.4°$ (which corresponds to the lowest value at the culmination point of the source) to $46.5°$. After the standard quality selections and the zenith angle cut ($< 43.5°$) for the data taking, 19.6 hours of ON data samples in total were processed for further analysis. The zenith angle cut was applied to keep the zenith angle range in the data samples at a moderate level, because at high zenith angles air shower properties change rapidly. The ON observations are summarized in Table 9.1. The OFF data samples were taken between May and October independently from the ON observations, but with similar conditions (same zenith angle range and light of night sky) at a sky region where no γ-ray emission was expected. In total, 20 hours of the OFF data samples were used for background estimation.

The data were analyzed with MARS, the standard analysis software for MAGIC observations as described in detail in chapter 6. 7 photoelectrons for core pixels and 5 photoelectrons for boundary pixels were chosen as the tail cut levels for image cleaning. Comparisons of the distributions for each Hillas shower image parameter demonstrate good agreement between ON and OFF data samples.

The final cut for the γ-ray signal evaluation was executed under ALPHA analysis. Fig. 9.1-(a) shows the ALPHA distribution between ON and OFF data after the γ/hadron separation cut based on the RF method. Only data with SIZE above 350 photoelectrons were selected for the plot and the OFF data were normalized with respect to the ON data in the range between $20°$ and $80°$. With the cut of ALPHA $< 9°$, an excess of 275 events over 959 normalized background events corresponds to a significance of $6.3\,\sigma$

Table 9.1: Summary of the MAGIC observations for 1ES1959+650 in 2005

Observation day (start)	(UTC) start - end time	ZA range [deg] (mean)	Obs. T [h]	Rate [Hz][1] (after cut)	Eff. Obs. T.[2] [h] (used)
09.05.2005	04:24:02-05:00:22	37.7–39.4 (38.7)	1.02	126.0	0.63
11.05.2005	03:11:47-05:00:11	37.4–44.4 (40.4)	1.80	116.9	1.41
14.05.2005	02:36:14-05:11:35	36.7–46.5 (40.6)	2.59	116.5	1.73
15.05.2005	02:40:14-03:31:57	41.5–45.8 (43.4)	0.86	99.1	0.22
21.05.2005	04:39:25-05:03:18	36.4–36.8 (36.6)	0.40	135.1	0.40
01.06.2005	03:02:22-04:30:54	36.4–39.0 (37.3)	1.48	117.4	1.43
02.06.2005	03:37:52-04:27:26	36.4–37.3 (36.7)	0.83	114.4	0.79
05.06.2005	03:57:22-04:47:59	36.4–36.7 (36.5)	0.84	132.2	0.81
06.06.2005	03:59:07-04:46:17	36.4–37.1 (36.5)	0.79	128.9	0.77
09.06.2005	03:41:31-04:47:06	36.4–37.1 (36.6)	1.06	117.5	1.06
11.06.2005	03:36:37-04:45:09	36.4–37.3 (36.8)	1.13	128.5	1.12
15.06.2005	03:08:19-04:50:41	36.4–38.2 (36.8)	1.71	128.7	1.65
02.07.2005	01:34:28-02:45:33	36.4–37.5 (36.7)	1.18	123.4	1.14
04.07.2005	01:28:37-03:16:28	36.4–37.3 (36.7)	0.95	120.6	0.91
06.07.2005	01:10:18-02:54:16	36.4–37.9 (36.8)	1.79	116.2	1.74
10.07.2005	00:43:34-02:36:59	36.4–38.1 (36.9)	1.94	120.6	1.92
12.07.2005	00:40:19-02:38:10	36.4–38.0 (36.8)	1.96	119.6	1.84
Total			22.3		19.6

(1) after applying the SIZE cut of >100 p.e..
(2) effective observation time of the analyzed data.

Table 9.2: Summary of the MAGIC observations for the 1ES1959+650 multi-wavelength campaign in 2006

Observation day (start)	(UTC) start - end time	ZA range [deg] (mean)	Obs. T [h]	Rate [Hz] (after)	Eff. Obs. T. [h] (used)
21.05.2006	02:36:38-04:46:53	36.6–43.8 (39.6)	2.17	98.2	2.05
22.05.2006	03:17:04-05:06:56	36.4–40.9 (37.9)	1.83	99.8	1.78
23.05.2006	02:03:08-05:05:52	36.4–46.7 (39.9)	3.04	107.3	2.07
24.05.2006	02:18:23-05:02:19	36.4–44.3 (39.5)	2.74	112.6	2.11
25.05.2006	02:31:45-05:01:29	36.4–43.5 (38.8)	2.50	115.8	2.19
26.05.2006	02:20:07-04:50:54	36.4–43.5 (39.1)	2.51	114.3	2.33
27.05.2006	02:16:43-04:51:52	36.4–44.1 (38.4)	2.59	111.5	1.75
Total			17.4		14.3
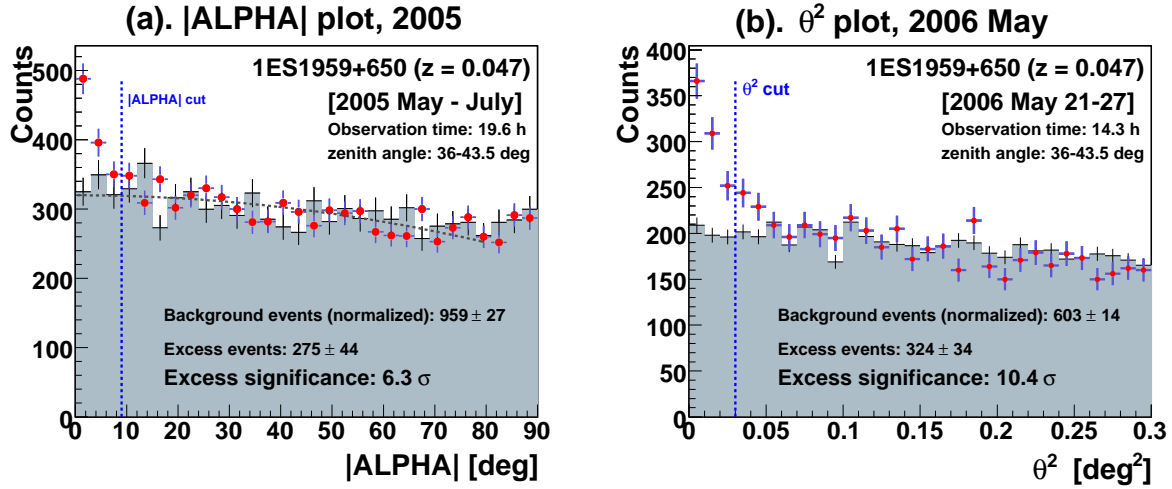
Figure 9.1: **[Left] (a)**: ALPHA distribution of 1ES1959+650 above 350 photoelectrons in 2005 observations. The filled circles represent ON-data. The black crosses correspond to normalized OFF-data and the dotted curve describes a second order polynomial fit to the distribution of the OFF-data. The vertical line indicates the ALPHA selection condition, which yields a total excess of 275 events at a significance level of 6.3 σ. **[Right] (b)**: θ^2 distribution of 1ES1959+650 above 350 photoelectrons in May 2006 observations. A cut of $\theta^2 < 0.03\,\mathrm{deg}^2$ (dashed blue line) yields a signal of 324 events over 603 normalized background events, corresponding to a 10.4 σ excess.

9.3.2 The 2006 observations

1ES1959+650 was observed with the MAGIC telescope on 7 nights from 21st to 27th of May, 2006, for 17.4 hours. These observations were performed within the MWL campaign (see details in section 9.4 in this chapter). The zenith angles during these observations ranged from $36.4°$ to $47°$. Observations were performed in wobble mode, where the object was observed at a $0.4°$ offset from the camera center. After the quality and zenith angle cut ($< 43.5°$) for the data the total effective observation time of the analyzed data was 14.3 hours. The MAGIC observations for the MWL campaign are summarized in Table 9.2. In addition to the observations for the MWL campaign in May 2006, this source was monitored with the MAGIC telescope for 40 to 60 minutes in each observation at intervals of several days. The analysis was performed using the standard MAGIC analysis software MARS. The γ-ray excess was derived from the θ^2 distribution based on the DISP method.

Fig. 9.1-(b) shows the θ^2 distribution of events with SIZE above 350 photoelectrons after a γ/hadron separation cut based on the Random Forest method from the data taken for the MWL campaign. A cut of $\theta^2 < 0.03\,\mathrm{deg}^2$ resulted in an excess of 324 events over 603 normalized background events corresponding to a 10.4 σ excess.
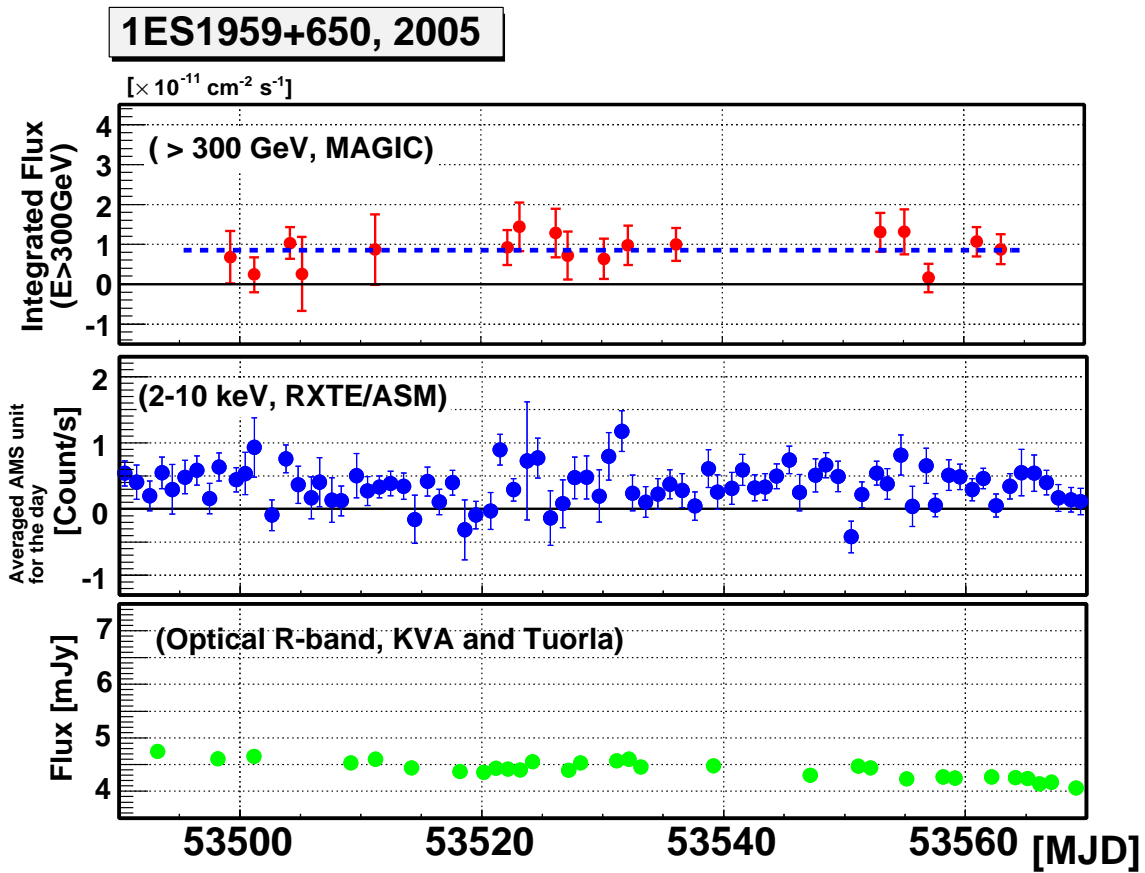
Figure 9.2: Diurnal light curves of 1ES1959+650 in 2005. **[Top]**: VHE γ-rays above 300 GeV as measured by MAGIC. The horizontal blue line represents the average flux. **[Middle]**: X-ray by RXTE/ASM. **[Bottom]**: optical R-band by KVA.
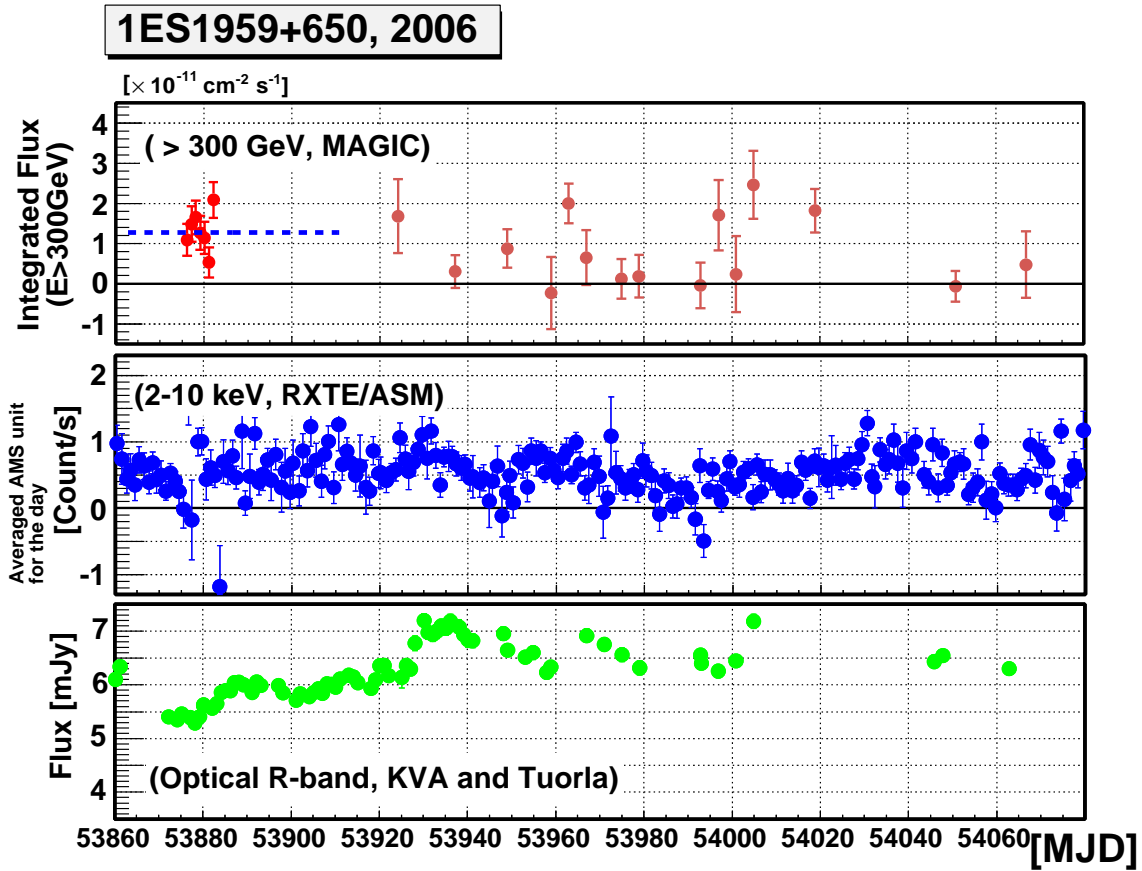
Figure 9.3: Diurnal light curves of 1ES1959+650 in 2006. **[Top]**: VHE γ-rays above 300 GeV as measured by MAGIC. Red points indicate the MWL campaign observation for this work. Dark red points show the data taken during "monitoring observation" [116]. The horizontal blue line represents the average flux during the MWL campaign observations. **[Middle]**: X-ray by RXTE/ASM. **[Bottom]**: optical R-band by KVA.

9.3.3 Light curves

Diurnal light curves of the VHE γ-ray band (above 300 GeV) by MAGIC, the X-ray band by RXTE/ASM and the Optical R-band by KVA and Tuorla are shown for the 2005 season in Fig. 9.2 and for the 2006 season in Fig. 9.3. In 2005, the average integrated flux of the VHE γ-ray band was $(0.85 \pm 0.12) \times 10^{-11}$cm^{-2}s^{-1} ($\chi^2$/N.D.F = 10.2/16), which corresponds to about 7% of the Crab Nebula flux at this energy range [43]. In 2006, the constant fit to 7 nights of the May data for the MWL campaign yielded $(1.27 \pm 0.16) \times 10^{-11}$cm^{-2}s^{-1} ($\chi^2$/N.D.F = 8.5/6), which corresponds to about 10% of the Crab Nebula flux. The fit results were consistent with constant flux levels in both years. No flare activity could be found in the VHE γ-ray emission during these 2-year observations with the MAGIC telescope. On the other hand, the average value over the May 2006 observations showed a significantly higher (factor of 1.5) flux than that derived from the entire 2005 observations. In fact, different analysis methods were applied in the final γ-ray signal extraction for the 2005 data (by ALPHA analysis) and the 2006 data (by θ^2 analysis). The systematic error caused by this difference of analysis methods was estimated much smaller ($\approx 2\%$) than the statistical error of the average flux in each year.

Optical R-band emission in 2006 also showed a clearly higher flux than in 2005. In addition, a strong variability in the 2006 results could be found by about 2 mJy between low and high state even though the VHE γ-ray emission did not show any significant variability.

In the X-ray bands, the instrument's (RXTE/ASM) sensitivity was not high enough to allow a discussion of the difference in fluxes between these 2 years.

9.3.4 Spectra

Average spectra as measured with the MAGIC telescope were separately derived from the 2005 observations and the 2006 May observations, which can be seen in Fig. 9.4. Both derived spectra are well described by a simple power law from 150 GeV to 3 TeV:
the 2005 result (χ^2/N.D.F = 2.20/4)

$$\frac{\mathrm{d}N_\gamma}{\mathrm{d}E\mathrm{d}A\mathrm{d}t} = (1.6 \pm 0.3) \times 10^{-12} \left(\frac{E}{1\,\mathrm{TeV}}\right)^{-2.62\pm0.25} \quad [\mathrm{TeV}^{-1}\ \mathrm{cm}^{-2}\ \mathrm{s}^{-1}]. \tag{9.1}$$

the 2006 May result (χ^2/N.D.F = 2.91/4)

$$\frac{\mathrm{d}N_\gamma}{\mathrm{d}E\mathrm{d}A\mathrm{d}t} = (2.7 \pm 0.3) \times 10^{-12} \left(\frac{E}{1\,\mathrm{TeV}}\right)^{-2.58\pm0.18} \quad [\mathrm{TeV}^{-1}\ \mathrm{cm}^{-2}\ \mathrm{s}^{-1}]. \tag{9.2}$$

In Fig. 9.5, the average spectrum energy distributions (SEDs) in different years between 2004 and 2006 are represented. The SEDs of the 2005 and 2006 observations were derived from this work and the 2004 SED was taken from the paper of our MAGIC collaboration [36]. In the normalized flux at 1 TeV, the 2006 SED shows $\sim$60% of the 2004 value and the 2005 result is even lower, i.e. about 40% of the 2004 value, while the photon indices are compatible among the SEDs in these three years. However, it is too early to conclude that 1ES1959+650 has a different feature in SED from Mkn501, in which we can see a correlation between the flux level

and the photon index (see Chapter 8), because the 1ES1959+650 results show only a factor of 2-3 difference in flux, while we can recognize more than one order of magnitude of difference in the flux of Mkn501. The data samples obtained during flare states in the VHE γ-ray band of 1ES1959+650 are highly desired and interesting for further SED studies of this source in the VHE γ-ray band.
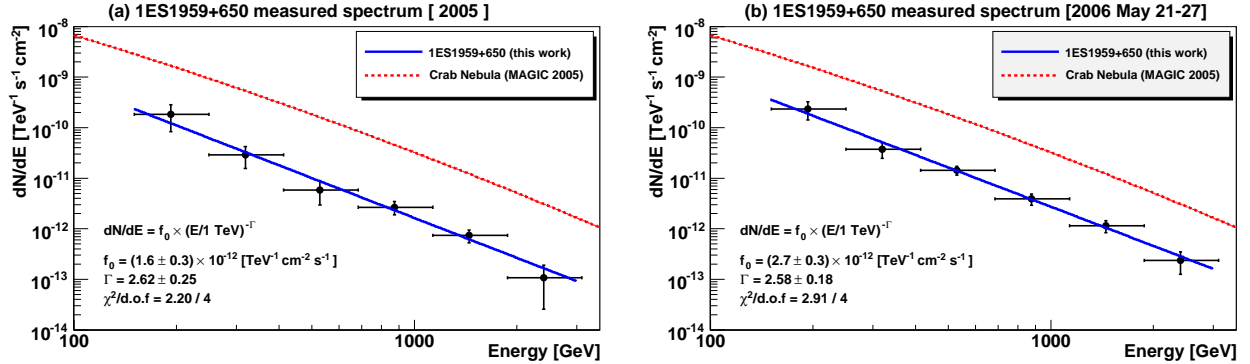
Figure 9.4: Differential energy spectra of 1ES1959+650. The blue solid line represents a power-law fit to the measured spectrum. The fit parameters are listed in the figure. For comparison, the measured MAGIC Crab spectrum [43] is denoted by a red dashed line. **[Left]**: average spectrum over the 2005 observations. **[Right]**: average spectrum over the May 2006 observations for the MWL campaign.

9.4 Multiwavelength campaign in May 2006

9.4.1 X-ray observations with Suzaku

The Suzaku satellite was pointing to 1ES1959+650 between 01:13:23 of May 23rd and 04:07:24 of May 25th, 2006 (UTC). The total on-source time was 160 ksec. The HXD/PIN light curve showed a rapid increase of the noise after about 100 ksec (possibly due to the unexpected in-orbit radiation[1]) and the data after this event could not be used for analysis. HXD/GSO data were not used in the following analysis, since performance and background of the GSO are still being studied. After screening, the total net exposure times for XIS and HXD were 99.3 ksec and 40.2 ksec, respectively. Detailed information about the analysis procedure used can be found in [236, 230].

For the spectral analysis the XIS data were used in the range of 0.7-10 keV. Below 0.7 keV there were still unsolved calibration problems. The XIS spectra were extracted for $t < 10^5$ sec in order to perform a joint XIS and HXD/PIN (0.7-50 keV energy band) fit. Fitted with a broken power law, the HXD/PIN points lay below the model, requiring a steeper spectrum. A good fit

---

[1]see http://www.astro.isas.ac.jp/suzaku/log/hxd/
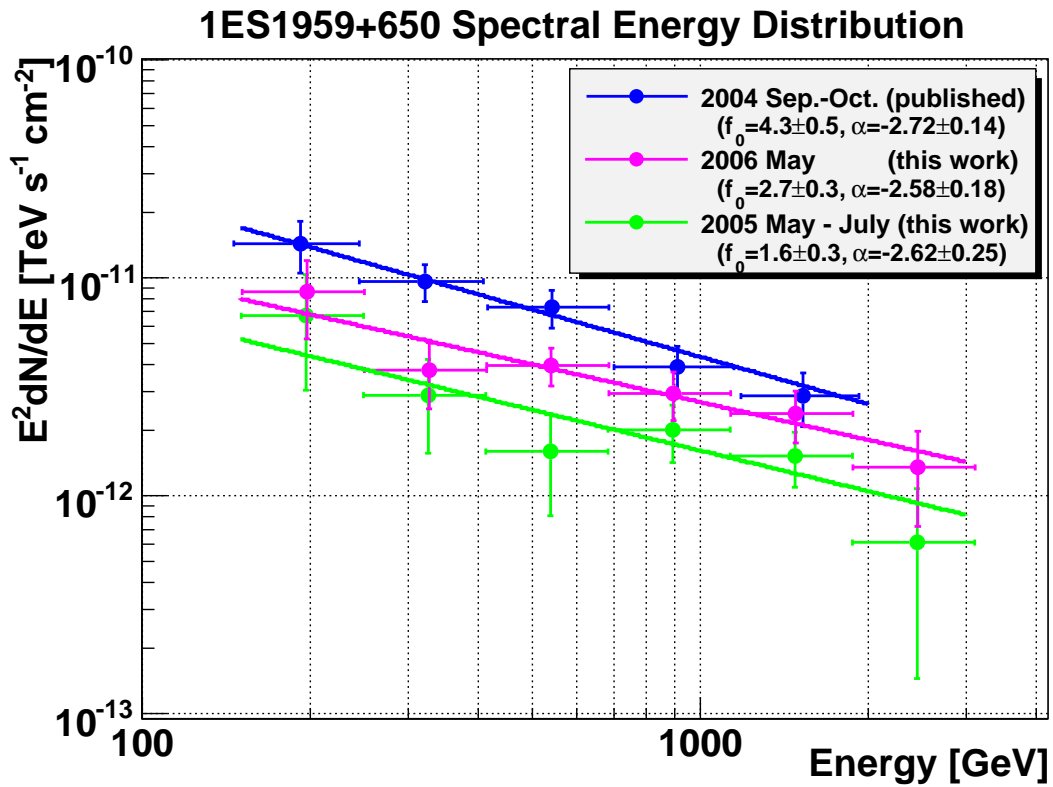
Figure 9.5: Spectrum energy distributions in the VHE γ-ray band of 1ES1959+650 in 2004 (*blue*), 2005 (*green*), and 2006 (*pink*). Each line represents a fit by a simple power law for each spectrum. The fit parameters are listed in the inset (f_0: normalized flux at 1 TeV $[\times 10^{-12}\,\text{TeV}^{-1}\,\text{cm}^{-2}\,\text{s}^{-1}]$, α: spectral index.). The 2005 and 2006 spectra were from this work, and the 2004 spectrum was taken from the published MAGIC results [36].

was obtained using a model with three power-laws (using a command of `"wabs*bknpower"` on the analysis program of `"XSPEC"`[2]). The best fit parameters with associated errors are: $\Gamma_1 = 1.94 \pm 0.01$, $\Gamma_2 = 2.195 \pm 0.002$, $\Gamma_3 = 2.7 \pm 0.03$, $E_{br,1} = 1.83 \pm 0.03$ [keV], $E_{br,2} = 16 \pm 3$ [keV].

9.4.2   Swift Observations

The Swift satellite [106], with its easy and flexible scheduling, is excellently suited for the observation of bright blazars. It carries three instruments: The Burst Alert Telescope (BAT) is optimized for 15-150 keV, while the X-Ray Telescope (XRT) is sensitive in the 0.3 -10 keV band. In addition, a UV/optical telescope can provide data in the 170-600 nm band. 1ES1959+650 was also observed with Swift around the Suzaku and MAGIC MWL campaign on 19th, 21st and from 23rd to 29th of May, 2006, in target of opportunity observations. In this thesis, only the optical-UV data were used.

9.4.3   Light curves

The light curves of 1ES1959+650 in VHE γ-rays and X-rays as measured by MAGIC and Suzaku during the campaign are shown in Fig. 9.6.

   The X-ray light curves consist of soft (0.2-2 keV) and hard (2-10 keV) X-rays, and the hardness ratio (2-10 keV/0.2-2 keV) as recorded with the XIS1 detector. The data track a flare of small amplitude ($\sim 10\%$) with a rising time of $t_r \sim 20 - 30$ ksec. The variability is faster in the 2-10 keV band than in the 0.2-2 keV band, which becomes evident also in the hardness ratio. In the light curves, particularly, the sudden drop is visible at $\sim 1.5 \times 10^5$ sec.

   For the VHE γ-ray emission, the diurnal integrated flux above 300 GeV is represented. The average flux during these 7 nights corresponds to $\sim 10\%$ of the Crab Nebula flux as already discussed in the previous section. This flux corresponds to one of the lowest levels so far observed in the VHE γ-ray band, about a factor of two lower than the lowest flux detected previously both with HEGRA in the years 2000-2001 [10] and MAGIC in 2004 [36], and well below the highest level detected in May 2002 [156]. No significant strong variability can be seen in the light curve of the VHE γ-ray band. However, due to the low source flux level, we could only see variability of a factor of 2-3.

9.4.4   Spectral Energy Distributions

The overall spectral energy distribution (SED) of 1ES1959+650 as measured at the end of May 2006 is shown in Fig. 9.7, together with other historical data (see the figure caption for the detailed information). During our multiwavelength campaign we simultaneously observed the SED from optical to UV, soft and hard X-rays and VHE γ-ray bands, monitoring both the synchrotron and inverse-Compton components. The "low-IR" model of Kneiske et al. (2004) [148] was used for the correction of the absorption of the VHE γ-ray emission by the extra-galactic background

---

[2]http://heasarc.gsfc.nasa.gov/docs/xanadu/xspec/
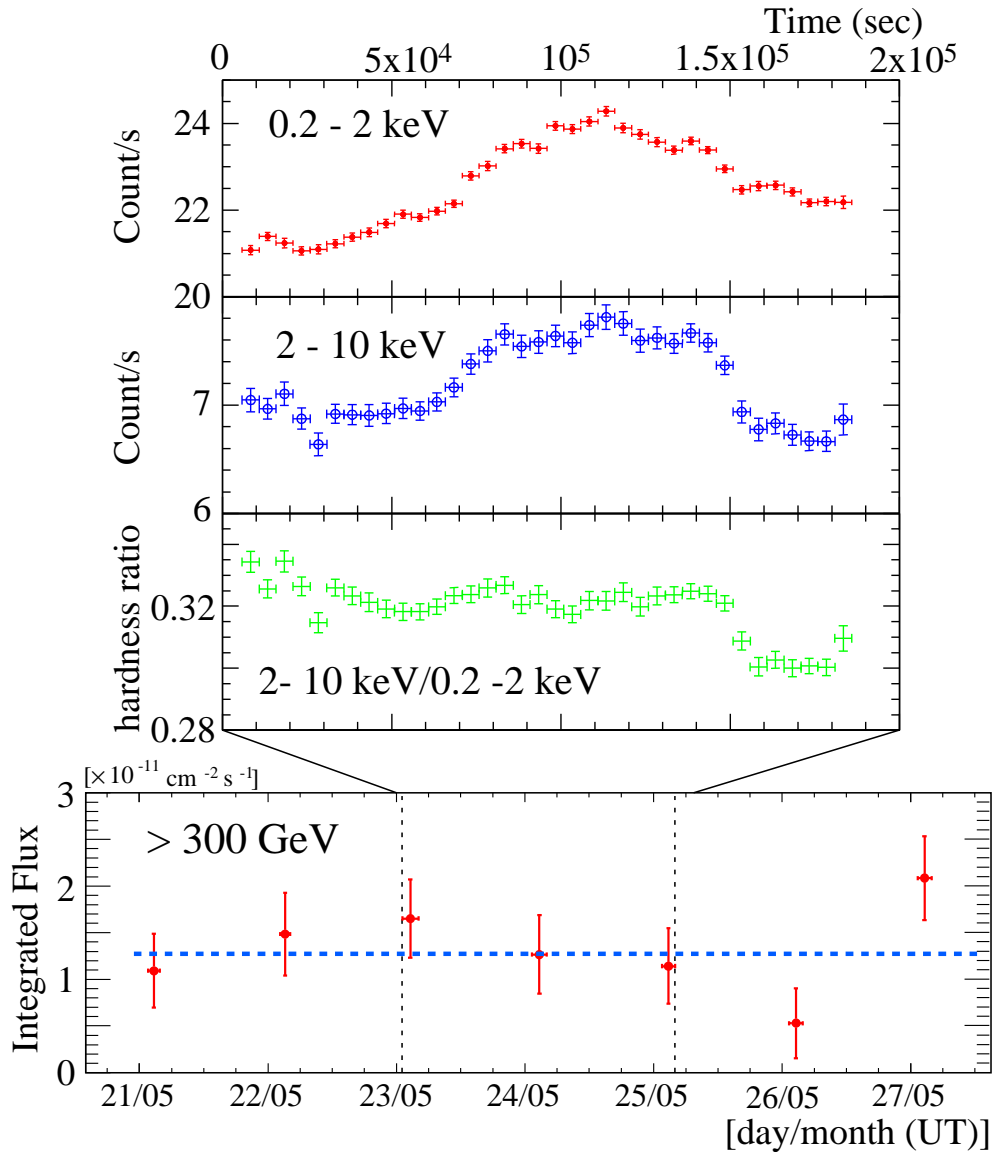
Figure 9.6: Light curves of 1ES1959+650 during the MWL campaign in May 2006. **[Upper]:** X-ray light curves obtained by the Suzaku XIS1 detector. Time= 0 is 1:13:23 on 23rd of May 2006 (UTC). *Top to bottom:* Count rates in the 0.2-2 keV band, in the 2-10 keV band and the hardness ratio (2-10 keV/0.2-1 keV). **[Lower]:** Diurnal light curve of VHE γ-ray (> 300 GeV) measured by the MAGIC telescope. In each data point, a horizontal bar represents the observation window and a vertical bar denotes 1-σ error bar. The dotted horizontal line represents the average flux. The dotted vertical lines show the observation window of the Suzaku pointing.

light (EBL). In the optical R-band provided by ground telescopes, the correction due to the galactic absorption (0.473 mag [218]) and the subtraction of the host galaxy contribution (1.7 mJy in R-band [184]) were already applied. The same procedures were adopted for the Swift-UVOT data, although the galaxy contribution was subtracted only for the UBV filter (for the galaxy contribution in these filters the "standard" colors for an elliptical galaxy was used [102]). The historical data in this figure show very strong changes in the X-ray band, while in the optical this is much more attenuated.

During our MWL campaign the source was found to be in a high state with respect to the historical behavior both in X-ray and optical (e.g., [229]), although not at the highest state as observed in X-ray (e.g., [134]). In the VHE γ-ray band, instead, the source was at one of the lowest states recorded so far. The VHE γ-ray band historically also showed strong variability, in particular if one considers that, in this band, fewer observations have been carried out than in the optical and X-ray ones. However, from our data we did not see strong (i.e. a factor of 2-3) variability in the VHE γ-ray band. Our MAGIC data have probably recorded the part of the SED slightly above the peak of the inverse-Compton component. Therefore, one would expect to see a high level of variability. The lack of variability in the MAGIC data and the low flux level recorded both indicate that the source was not very active in this band at that time. All in all one can say that during our campaign the source was quite stable (i.e. did not change by more than a factor of 2) from the optical to the VHE γ-ray band.

We modeled the observed SED with optical-UV (Swift), X-ray (Suzaku) and VHE γ-ray γ-ray (MAGIC) bands by using a one-zone SSC model developed by [234, 235]. In old studies for low flux states (e.g., SED in 2001 [229]), an assumed value for the inverse-Compton component by a non-simultaneous VHE γ-ray spectrum was necessary for deriving the SSC physical parameters. In this case, however, simultaneous observations in optical, X-ray and VHE γ-ray bands were carried out. The X-ray spectrum as observed by Suzaku was about a factor of 2 higher than the one measured with BeppoSAX in 2001 and the synchrotron peak located a slightly higher energy than in 2001. The optical fluxes were similar to the one reported for the SED in 2001.

In the one-zone SSC model, the source is a sphere with a radius R moving with a bulk Lorentz factor Γ and is seen at an angle θ by the observer, resulting in a Doppler beaming factor δ. The magnetic field is tangled and uniform while the injected relativistic particles are assumed to have a (smooth) broken power law spectrum with a normalization K, extending from γ_{min} to γ_{max} and with indices n_1 and n_2 below and above the break at γ_b. Based on this model, the SED of May 2006 could be well described using the parameters in Table 9.3. Comparing these values with those derived from the SED in 2001, the parameters turned out to be very similar. Apart from a lower value of the magnetic field ($0.8 \rightarrow 0.25$ G), other parameters were consistent or had only minor differences which did not lead to significant changes of the SSC curve. (e.g., $R : 9 \times 10^{15} \rightarrow 7.3 \times 10^{15}$ [cm], $\gamma_b : 5.0 \times 10^4 \rightarrow 5.7 \times 10^4$, $\delta : 17.8 \rightarrow 18$). Compared to other HBLs, for instance, our result of Mkn501 (in the last chapter), γ_{max} showed a lower value due to the presence of the energy cut-off in the hard X-ray range (at several tens keV). A larger value was selected for R because, unlike in Mkn501, rapid variability was not found in 1ES1959+650. Consequently, smaller electron normalization value was achieved. Nevertheless, most parameters show similar values in general, which might suggest that they are typical values for HBL objects.

Table 9.3: SSC model parameters of 1ES1959+650.

data	R	δ	γ_{min}	γ_{br}	γ_{max}	B	K	n1	n2
	cm					Gauss	particle/cm^3		
2006 (this thesis)	7.3×10^{15}	18	1	5.7×10^4	6×10^5	0.25	2.2×10^3	2	3.4

9.5 Summary

I present results of the observations with the MAGIC telescope for the TeV blazar 1ES 1959+650 in 2005 and 2006. VHE γ-ray emission was clearly detected both in 2005 and 2006. In 2005, we obtained a signal excess with a 6.3 σ level from 19.6 hours of data samples and, in 2006, a 10.4 σ excess was achieved from 14.3 hours of data samples. Each spectrum between 150 GeV and 3 TeV could be derived from the data taken in each year.

Diurnal light curves of integrated flux above 300 GeV showed no flare activity during these two years. The average integrated flux was $(0.85 \pm 0.12) \times 10^{-11} \mathrm{cm}^{-2}\mathrm{s}^{-1}$ in 2005, and $(1.27 \pm 0.16) \times 10^{-11} \mathrm{cm}^{-2}\mathrm{s}^{-1}$ in 2006. The 2005 data showed a significantly lower flux than the 2006 data. Compared to the result of previous MAGIC observations in 2004, the flux in 2005 (F_{2005}) is about 40% that of 2004 (F_{2004}) and the flux in 2006 (F_{2006}) is about 60% that of 2004 (F_{2004} : F_{2005} : F_{2006} = 1 : 0.4 : 0.6). On the other hand, the photon indices are compatible in these three years.

The 2006 observations with the MAGIC telescope were carried out within the scope of a MWL campaign together with X-ray satellites, Suzaku and Swift, and ground optical telescopes. Data from the optical, UV, soft- and hard-X-ray and VHE γ-ray bands were obtained in this campaign.

The X-ray light curve measured by Suzaku showed a small flare with an amplitude of $\sim$10%, while no significant variability could be seen in the light curve of the VHE γ-ray band measured by MAGIC. However, due to the low source flux level, we could have confirmed the variability only in the case that the flux showed more than a factor of 2-3 variation in the VHE γ-ray band.

The source SED during this MWL campaign showed the usual double-hump shape. With respect to historical values, during our campaign the source exhibited a relatively high state in X-rays and optical, while in the VHE γ-ray band it was at one of the lowest levels so far recorded. The overall SED was well represented by an homogeneous one-zone SSC model. The derived physical parameters could suppose to be typical values of HBL objects.
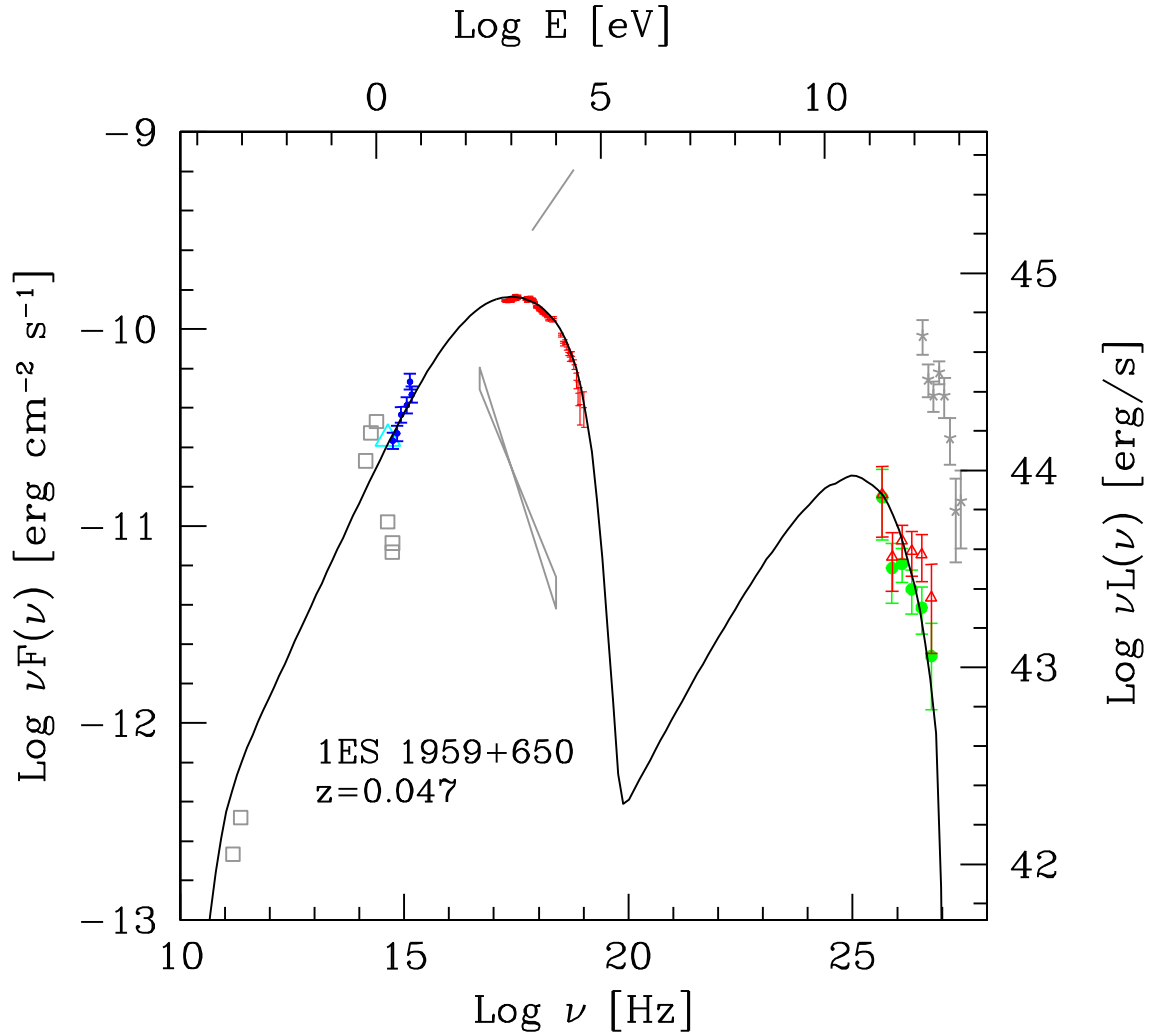
Figure 9.7: Overall SED of 1ES1959+650 as measured at the end of May 2006, together with other historical data. Optical-UV data are from on-ground (cyan triangle) and UVOT/Swift (blue triangles). The average Suzaku spectrum (red) and the Swift spectra (blue) taken on May 24 [higher] and May 29 [lower] are reported. Green points (filled circles) show the observed MAGIC spectrum, while the red points (empty triangles) have been corrected for the extragalactic light absorption using the "low-IR" model of Kneiske et al. (2004) [148]. Historical data are taken from [229] (radio-optical), [52] (X-ray, low), [156] (X-rays, high), and [10] (VHE γ-ray, high). The line refers to the one-zone SSC model for the campaign data in May 2006 using the code developed by [234, 235]. See text for the fit parameters. The historical spectra for the X-ray and VHE γ-ray bands correspond to the highest and lowest flux so far recorded for this source in these bands.

Chapter 10

Monitoring of Markarian 421

10.1   Markarian 421

Mkn421 (R.A. $11^h04^m27.2^s$, decl. $+38°12'32.0''$ [J2000.0], $z = 0.031$) is the brightest HBL object in the X-ray and UV sky and the first extragalactic source detected at TeV energies [204]. It is the closest known and the best studied TeV blazar in all accessible wavelengths from radio waves to VHE γ-rays. In the VHE γ-ray band, it is the most active and brightest TeV blazar, thus being one of the few blazars that can be detected nearly all the time with Cherenkov telescopes. It has frequently shown flare states and strong flux variability, larger than one order of magnitude in flux amplitude, and occasional flux doubling times as short as 15 minutes [26, 103]. Variations in the hardness of the TeV γ-ray spectrum during flares were reported by several groups (e.g., [28, 157]). Simultaneous observations in the X-ray and GeV-TeV bands show a strong evidence of flux correlation (e.g., [63, 155]).

First observations with the MAGIC telescope were performed between November 2004 and April 2005, just after the telescope started its scientific operation [46]. Clear signals with $\sim 50\,\sigma$ excess were detected in the observations for about 15 hours. A differential spectrum was derived between 100 GeV and 3 TeV, suggesting the inverse-Compton (IC) peak to be at around 100 GeV. The results of the MAGIC observations supported the results of the spectral variation and the correlation between the X-ray and GeV-TeV bands reported in several previous studies.

10.2   Monitoring program

Mkn421 was observed with the MAGIC telescope under the "monitoring" program [116]. The observation strategy of this program is to evenly distribute short observations over the total observable period throughout the year. Usually, they are allocated at intervals of 3-4 days, but during the presence of bright moon and bad weather conditions, inevitably some gaps occur. In order to get a wide coverage, some observations can be scheduled during partial moon or modest twilight. The source can be available with a zenith angle of 12° at its culmination point. However, depending on the source visibility, some observations are performed with higher zenith angle conditions ($> 30°$), which lead to higher energy thresholds than with low zenith angle

conditions. This strategy allows for an extended observation time coverage throughout the year.

For this program the wobble observation mode was selected. Since the data samples can have a wide variety of observational conditions due to the strategies mentioned above, the wobble observation mode can provide proper background samples for each condition.

Each of these sampling observations should be long enough to detect a given minimum flux level taking into account the sensitivity of the telescope. Typically, 40 to 60 minutes are allocated to each observation. A 40-minutes' observation with the MAGIC telescope corresponds to a signal detection sensitivity of about 20% Crab flux level with a 5 σ significance. In fact, the source had shown a flux higher than this level in most previous observations (e.g., [63, 46]).

When a source is detected to be in a high state of activity, follow-up observations are planned to be carried out every day during the following days and for a reasonably longer time than usual (2-3 hours) as far as the observation conditions are fulfilled. In this chapter, I report the results of the monitoring program for Mkn421 in the "cycle-II" of the MAGIC scheduling term corresponding to the period from April 2006 to January 2007.

10.3   Observations in cycle-II

The monitoring program began in April 2006. However, due to hardware upgrade works at the beginning of the cycle[1], some technical problems occurred which affected the data. As a result, the data quality was poor until 20th of May, 2006. Here, those data are used for informative purposes only and are excluded from further discussion.

Table 10.1 summarizes the monitoring observations for Mkn421 until January 2007. Not only the data taken during the commissioning phase (until 20th of May, 2006) mentioned above, but also those recorded during some additional observation days were removed because of the poor observation conditions. Finally, 13 days were available as acceptable quality data. Among these 13-day observations, only the data of 11th of January 2007 were taken under moderate-moon condition, while other data were taken in normal dark nights. However, it is not necessary to apply any special treatment to the data of January 11th, 2007, because this observation was carried out within the acceptable conditions for applying normal analysis procedure (with respect to the discriminator threshold for the trigger and the DC current of the PMT) based on the MAGIC technical paper for observations under moon condition [47]. All data were processed with the standard MAGIC analysis tools and normal procedures were applied for data with dark night conditions. The zenith angle was ranging wider than in other observations, i.e. from $16°$ to $47°$. The analysis was performed using proper MC γ samples with the same zenith angle range. Upon the availability of MC, a zenith angle cut at $45°$ was applied, which, however, discarded only a negligible amount of the data. Finally, a θ parameter based on the "DISP" method was used for the final cut to evaluate the γ-ray signal.

---

[1]Ultra-fast FADCs (2GSamples/s) had been installed in April 2006. However, data were taken with the (old) 300 GSamples/s FADCs until February 2007 when the Ultra-fast FADCs began to be officially used in normal observations.

Table 10.1: Summary of the MAGIC observations for Mkn421 in cycle-II

Observation start time (UTC)	ZA range [deg] (mean)	Obs. T [min]	Rate[Hz][1] (before)	Rate[Hz][2] (after)	T_{eff}[min][3] (used)	flux[4] state
21.05.2006 21:23:14	16.0–20.3 (18.2)	20.3	197.0	122.8	17.6	H
23.05.2006 21:43:16	20.5–24.8 (22.7)	18.6	181.9	114.8	18.1	M
25.05.2006 21:24:41	19.0–27.7 (25.2)	42.2	198.9	122.0	18.0	H
23.11.2006 05:38:36	24.1–32.7 (28.4)	48.6	170.4	107.3	46.8	L
27.11.2006 05:35:23	23.1–29.5 (26.1)	40.0	179.4	115.0	33.9	n/a
16.12.2006 02:59:11	31.4–46.3 (38.8)	71.8	164.3	102.5	49.5	L
20.12.2006 03:36:44	28.3–36.7 (32.6)	43.3	126.2	74.9	39.2	L
24.12.2006 02:33:32	36.5–45.0 (40.7)	39.0	152.3	94.2	37.7	L
28.12.2006 02:18:24	37.7–44.6 (41.8)	39.0	114.2	73.2	37.7	L
11.01.2007 01:13:35	35.3–47.0 (41.2)	59.3	132.2	87.8	34.1	n/a
15.01.2007 01:38:19	30.6–39.0 (34.7)	39.1	149.6	91.5	38.0	L
23.01.2007 00:31:49	33.4–44.2 (39.4)	59.6	137.0	85.7	39.1	M
24.01.2007 00:40:35	31.7–43.4 (37.4)	59.6	135.4	83.3	48.2	L

(1) Data taking rate after image cleaning only.
(2) Data rate of event with SIZE > 100 p.e..
(3) Effective time of the data used for the analysis.
(4) H:High state, M:Medium state, L:Low state, n/a:not applicable

10.4   Results and discussions

10.4.1   Light curves

Fig. 10.1 shows the light curve (LC) of the VHE γ-ray emission above 300 GeV as measured with the MAGIC telescope between April 2006 and January 2007. The results from the data taken on the days listed in table 10.1 are represented by red points in Fig. 10.1. The error bars of these points include statistical errors only as in normal plots. The results from the data taken during the hardware upgrading work in April 2006 are also written in the plot in grey color. Due to the low quality of those data, an additional error of 30% was added into the statistical error in quadrature for each point and each error bar was extended according to that value over the short horizontal lines, which indicate the range of the statistical error. There is one green point in the LC. The quality of the corresponding data was as bad as the data quality for other grey points, but simultaneous X-ray data taken by the Suzaku satellite at that day are available[2].

As the LC of Fig. 10.1 shows, a clear excess of VHE γ-ray signals was obtained in each observation and strong variability could be found in the measured flux of Mkn421. Especially, in May 2006, the source showed a high state of activity and the fluxes both on 21st and 25th of May reached about 3×10^{-10} cm^{-2} s^{-1}, which corresponds to more than 2 Crab flux at this energy range. Between those two days, the flux on 23rd of May was still high but only almost half of

---

[2]This information is used for the discussion in the next chapter.

the highest fluxes of those days. Although there are not enough data samples available for the period around those days, the LC suggests the flux varied by a factor of two in the time scale of a day at most.

Mkn421 showed a relativity low state of activity between November 2006 and January 2007. In particular, the fluxes on 23rd of November, 20th, 24th and 28th of December 2006 were only $3 \sim 4 \times 10^{-11}\,\mathrm{cm}^{-2}\,\mathrm{s}^{-1}$, corresponding to almost an order of magnitude less than the highest flux in this LC. The flux on 23rd of January 2007 showed the highest value in these 3 months and reached $(13.6 \pm 1.3) \times 10^{-11}\,\mathrm{cm}^{-2}\,\mathrm{s}^{-1}$, corresponding to about 1 Crab flux. However, the next day, i.e. on 24th of January 2007, the flux dropped to less than half the value of the previous day. Despite the flux levels being lower than those in May, fast variability with a time scale of less than a day could be seen as well.
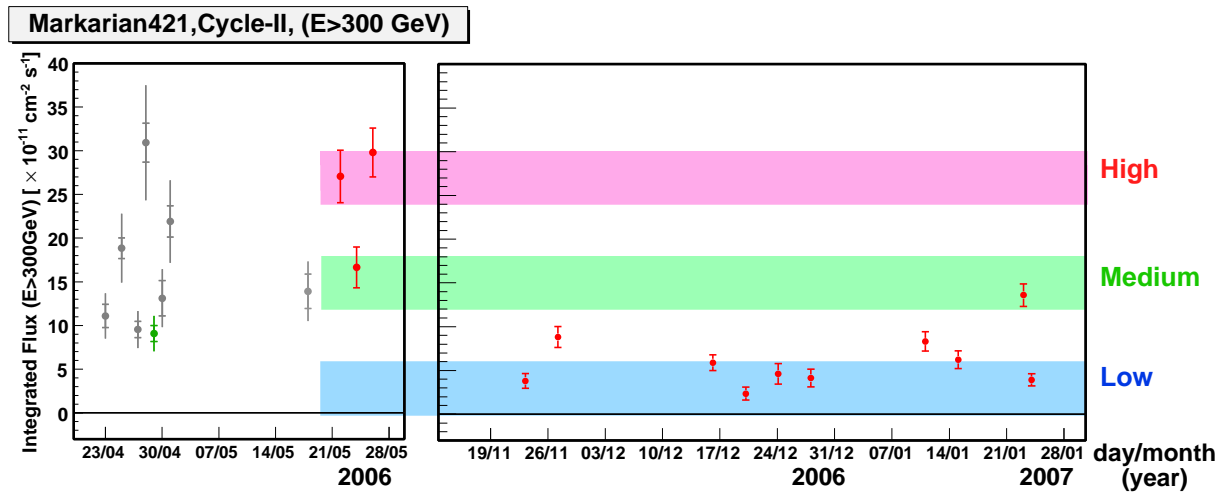
Figure 10.1: Diurnal light curve of VHE γ-rays above 300 GeV of Mkn421 in 2006 as measured by MAGIC. Red points that were taken after 21st of May are used for discussions in this thesis. The defined ranges of each high-, medium- and low-state for the spectral analysis are represented by the color bands in red, green and blue, respectively. Gray points in the first sector of the plot are the results that were taken during the hardware upgrading. Due to the worse telescope performance during that time, the quality of those data was poor. An additional error of 30% was added into the statistical error in quadrature for each point and each error bar was extended according to that value over the short horizontal lines, which indicate the $1\,\sigma$ of the statistical error. For the day denoted by the green point, simultaneous X-ray data taken by the Suzaku satellite are available.

10.4.2 Spectra

In order to investigate the spectra at different flux levels, the diurnal data were combined into three groups, according to the integral flux above 300 GeV ($F_{>300\text{GeV}}$ in $\text{cm}^{-2}\,\text{s}^{-1}$ scale) as shown in Fig. 10.1. The groups were defined as the low state for $F_{>300\text{GeV}} < 6 \times 10^{-11}$ (< 0.5 Crab flux), as the medium state for $12 \times 10^{-11} < F_{>300\text{GeV}} < 18 \times 10^{-11}$ (1-1.5 Crab flux), and as the high state for $24 \times 10^{-11} < F_{>300\text{GeV}} < 30 \times 10^{-11}$ (2-2.5 Crab flux). The range of each group was defined with a gap between the states, as one can see in Fig. 10.1 with color bands in order to highlight the divergence among the groups. Consequently, the data on 27th of November and 11th of January were not used for the spectral reconstructions.

Based on this definition, the high flux data sets contain data of 21st and 25th of May, 2006 (2 days), the medium flux date sets include those of 23rd of May 2006 and 23rd January 2007 (2 days), and the low flux data sets consist of the data taken on 23rd of November, 16th, 20th, 24th and 28th of December 2006 and 15th and 24th January 2007 (7 days).

The differential energy spectra for all three flux regions together with the fit results by a power law (PL) are shown in Fig. 10.2; the fit parameters are also listed in Table 10.2. For fair comparisons, the fits were applied in the same range from 170 GeV to 1.7 TeV for all flux states. Fig. 10.2 shows the differential energy spectra multiplied by E^2 in all flux states.

At 300 GeV, the difference in flux is about a factor 2 both between low and medium, and between medium and high. At 1 TeV, the difference between the flux states becomes more significant, corresponding to about one order of magnitude between low and high state. Although the photon indices between low and medium states are still consistent within an error, the spectrum tends to harden as the flux increases, which can be seen also in the Mkn501 results (see Chapter 8). Such a correlation was also reported in a previous study on Mkn421 [46], in which the photon indices were derived by the fits to the spectra between 700 GeV and 4 TeV.

It is interesting that the highest energy points of our spectra at the 2 TeV range represent the comparable flux levels regardless of the flux states even though the error bars are large in each state of the spectra. This may suggest the presence of a global energy cut-off around 2 TeV in this source, but further investigations are, of course, necessary.

To see the intrinsic spectral features of the source, we applied the correction for the absorption due to extra-galactic background light (EBL). Fig. 10.4 shows the de-absorbed spectral energy distributions (SEDs), in which the "low-IR" model of Kneiske et al. (2004) [148] was selected as the EBL model for correction. Since Mkn421 is the closest TeV blazar ever detected, the absorption effect is tiny at our observed energy range. Consequently, the spectral shapes do not change so much from the original ones.

If we assume leptonic origin scenarios for emission models, the flat shape up to 1 TeV in the high state SED may suggest that the IC peak could be situated in the observed energy range. The spectrum's trend to soften as the flux decreases may suggest that the IC peak position is shifting towards a lower energy, just below 100 GeV along with medium- and low-flux states. A discussion of the SED using a one-zone SSC model is presented in the next chapter.
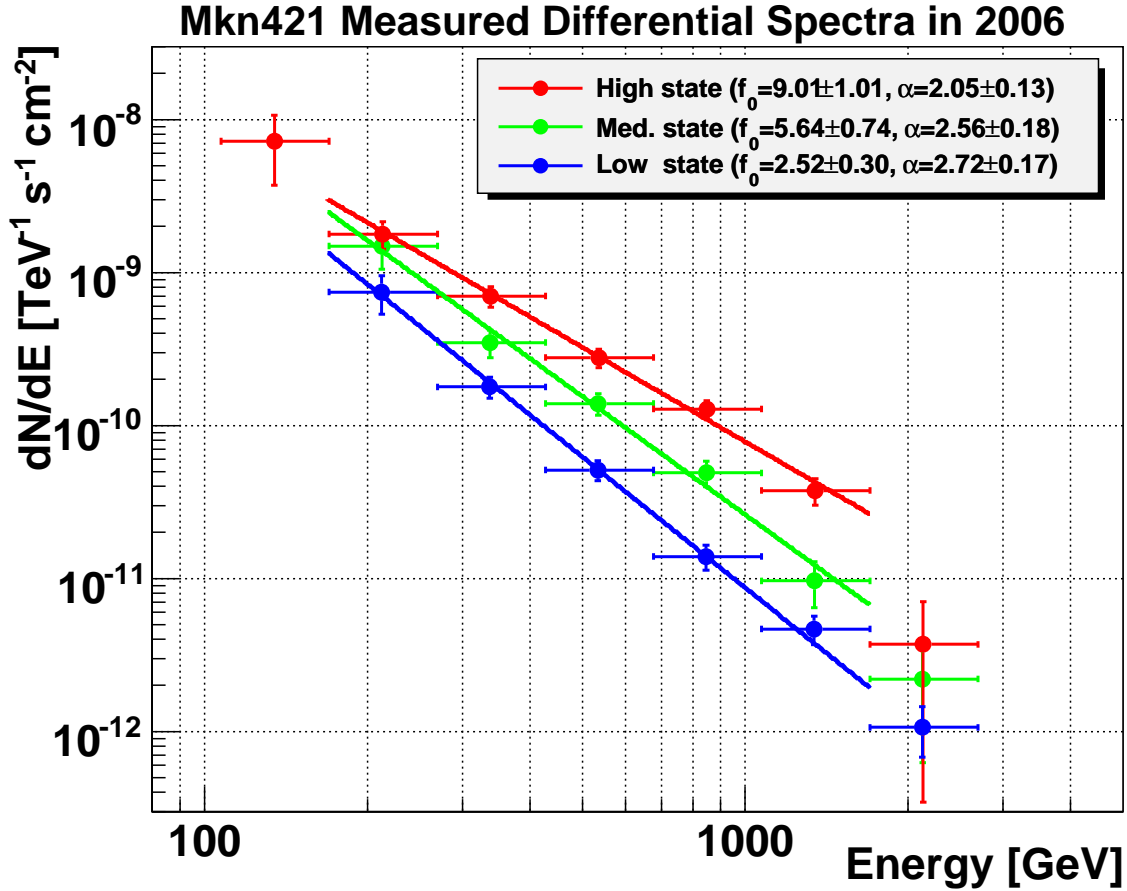
Figure 10.2: Differential energy spectra of Mkn421 in 2006 for three different $> 300\,\text{GeV}$ flux levels as measured by MAGIC: high (red), medium (green) and low (blue). Vertical bars denote 1σ uncertainties; horizontal bars denote energy bins. Lines show PL best fits in the range from 170 GeV to 1.7 TeV. The fit parameters are listed in the inset (f_0: normalized flux at 300 GeV $[\times 10^{-10}\,\text{TeV}^{-1}\,\text{cm}^{-2}\,\text{s}^{-1}]$, α: spectral index.). See also Table 10.2 for detailed information.

Table 10.2: Mean spectral parameter of Mkn421.

state	Eff. On time [h]	Excess[a] σ	f_0^b (at 300 GeV)	α: photon index (PL)[c] (170-1700 GeV)	χ^2 for PL fit
Higher	0.63	10.0	9.01 ± 0.94	2.05 ± 0.13	2.3/3
Middle	0.95	10.1	5.64 ± 0.74	2.56 ± 0.18	2.8/3
Lower	5.25	10.4	2.52 ± 0.30	2.72 ± 0.17	0.72/3

(a) significance of detected signal for flux calculations (SIZE > 100 p.e.).
(b) scale is $[\times 10^{-10}\,\text{TeV}^{-1}\,\text{cm}^{-2}\,\text{s}^{-1}]$
(c) the PL is defined as $f_0 \left(\frac{E}{300\text{GeV}}\right)^{-\alpha}$
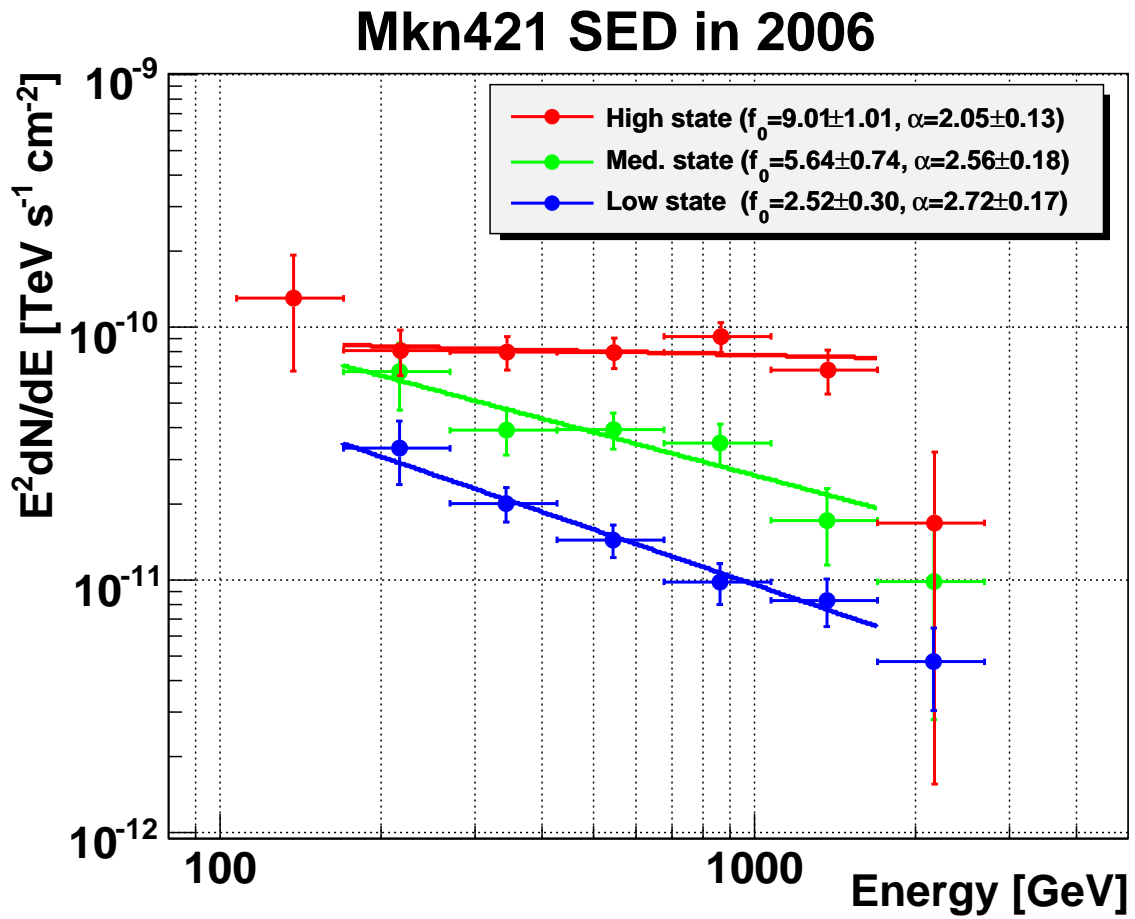
Figure 10.3: Measured spectral energy distributions of Mkn421 for three different flux states in 2006. See details in the caption of the previous figure.
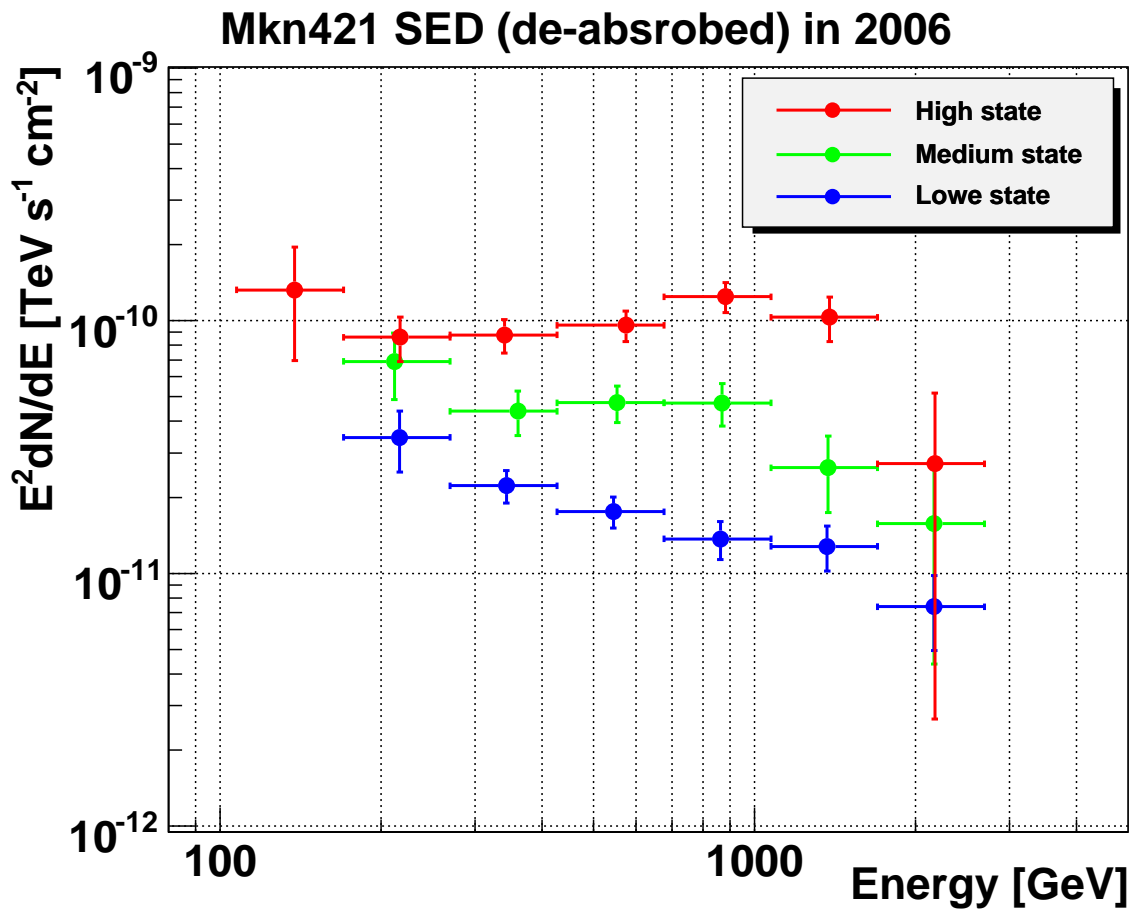
Figure 10.4: De-absorbed spectral energy distributions of Mkn421 for three different flux states in 2006. "low-IR" model of Kneiske et al. (2004) [148] was used for the correction of EBL absorption.

10.5   Summary

We carried out monitoring observations of Mkn421 between May 2006 and January 2007 with the MAGIC telescope. Each data sample was taken for a span of about 40 to 60 minutes and showed clear signals of VHE γ-ray emission. In the measured light curve above 300 GeV, a strong variability with one order of magnitude difference in amplitude (up to more than 2 Crab flux at maximum) and a time scale of less than a day could be found.

Spectral studies were performed between 170 GeV to 2.5 TeV using three different flux groups, into which the data were combined according to the integral flux above 300 GeV. The spectrum was found to harden with the photon index changing from -2.72 ± 0.17 to -2.05 ± 0.13 as the flux increased. In the leptonic origin scenario this spectral behavior may suggest that the IC peak could be situated around $\sim$100GeV and be shifting toward a lower energy as the flux decreases.

The monitoring observation of Mkn421 is still going on; we have observed this source on a regular basis in order to accumulate data. These data are expected to comprise various flux states. Further investigations e.g., based on the different flux states including the lowest state, will provide us with excellent knowledge about the activity of the jet. In addition, MWL observations with X-ray with various flux states are also important for the SED study.

Chapter 11

Discussions

In this chapter, additional details of the observed spectral energy distributions (SEDs) for the four TeV blazars, Mkn501, 1ES1959, Mkn421 and BL Lacertae, are presented.

11.1 Synchrotron Self-Compton model for four TeV blazars

SSC model "grid scanning" for Mkn501

In individual chapters, the observed SEDs were discussed using the SSC model (see details about the model in section 2.3.1) to derive the physical parameters in the jets. Especially, for Mkn501 (in Chapter 8), we could reproduce the SEDs of Mkn501 in different flux states (i.e. "high" and "low" states) only by changing the electron Lorentz factor at peak energy γ_b. However, due to incomplete information about the SED shape (i.e., peak positions of SEDs could not be determined directly from the observed ones), we could not conclude that the changing γ_b was a unique solution to describe different flux states of the SEDs. In order to study the contributions of other parameters in the SSC model for describing the Mkn501 SEDs in different flux states, we produced a large number of samples of photon spectra using the SSC model by changing each parameter in a certain range with a fixed interval. Then we compared those spectra to observed SEDs. Here, this procedure is called "grid scanning". The SSC model was developed with the same codes as those used in Chapters 8 and 9 [234].

The data samples of the Mkn501 SEDs in "High" and "Low" states were selected following the discussions in Chapter 8 (see also Fig. 11.3-(a)).

The procedure of the "grid scanning" is described as follows:

1. Based on the discussion in Chapter 8, several parameters were fixed in advance: $n_1 = 2$, $n_2 = 4$, $\gamma_{\min} = 1$, $\gamma_{\max} = 1 \times 10^7$.

2. The size of the emission region (R) was selected (1×10^{15} [cm] or 2×10^{15} [cm]).

3. Photon spectra were simulated using the SSC model (hereafter, these spectra are called "SSC spectra") by changing each of the parameters, γ_b, B, K and δ, individually. The

intervals were almost constant in the log scale for γ_b, B and K, and in the linear scale for δ. The scan range and the number of steps of each parameter are summarized in Table 11.1.

4. Every simulated SSC spectrum was applied for the observed SED of Mkn501, and a reduced chi-square $\chi^2_{red}(= \chi^2/\text{N.D.F})$ was evaluated in each comparison between a SSC spectrum and the observed SED.

5. For each parameter (γ_b, B, K, δ), their distributions weighted by $1/\chi^2_{red}$ were plotted. For example, when a SSC spectrum which was derived with "$\gamma_b = 1 \times 10^5$" provided "10" for χ^2_{red}, a value of "0.1 (=1/10)" was added to the bin of "1×10^5" in γ_b (="5" in $\log \gamma_b$).

As discussed in Chapter 8 (see also [41]), the size of emission region R was constrained to be 1×10^{15} [cm] by the fast variability observed during the high state. On the other hand, such a fast variability was not found during the low state. Assuming that the size of emission region can vary, here, $R = 2 \times 10^{15}$ [cm] was also considered for the low state.

The "grid scanning" was performed for each observed SED. For the low state, it was also performed for each R-value separately. Therefore, three attempts of the "grid scanning" procedure were performed in total. (i.e., (1) for the high state SED with $R = 1 \times 10^{15}$, (2) for the low state SED with $R = 1 \times 10^{15}$, (3) for the low state SED with $R = 2 \times 10^{15}$).

The parameter distributions were compared between the high state with $R = 1 \times 10^{15}$ and the low state with $R = 1 \times 10^{15}$ in Fig. 11.1, and between the high state with $R = 1 \times 10^{15}$ and the low state with $R = 2 \times 10^{15}$ in Fig. 11.2.

As one can see in Fig. 11.1, the distribution of γ_b shows the most significant difference between the high and the low states among four parameter distributions. The other parameters do not show pronounced distinctions in their distributions. In Fig. 11.2, the differences in the other parameters become more obvious than in Fig. 11.1. However, γ_b still clearly shows different distributions between the high and the low states. From these facts, we would conclude the parameter of γ_b could play an important role in the one-zone SSC model representing the physical conditions in the jet linking between the high and the low states of activity.

SSC model parameters

Here, applications of the SSC model for the observed SEDs of Mkn421 and BL Lacertae are discussed in order to derive the physical parameters of their jets (SSC model parameters). The SSC model parameters for Mkn501 and 1ES1959+650, for which we have simultaneous X-ray and VHE γ-ray data, were already derived in each dedicated chapter (see Chapters 8 and 9). At the end of the section, the derived SSC model parameters for all four TeV blazars are summarized.

Mkn421:   The SSC model was applied for the observed SEDs of Mkn421 which we discussed in Chapter 10. There are no corresponding X-ray data taken simultaneously with our VHE γ-ray data. Alternatively, an X-ray spectrum measured by Suzaku on April 28th, 2006, was available. It was observed when the source showed a flux state comparable to the "medium" state of our

Table 11.1: Summary of the SSC model parameters used in the "grid scanning". In total, 38912×2 SSC spectra ($\times 2$ means two values of R) were produced.

parameter	range of value	condition
γ_{min}	1	fixed
γ_{max}	10^7	fixed
n_1	2	fixed
n_2	4	fixed
γ_b	$(7 \times 10^3 - 7 \times 10^6)$	19 steps (in log)
B [G]	$(0.05 - -0.7)$	8 steps (in log)
K [cm^{-3}]	$(500 - 1.5 \times 10^5)$	16 steps (in log)
δ	$(10 - 55)$	16 steps (every 3)
R [cm]	1×10^{15}	for the high state SED
R [cm]	$1 \times 10^{15}, 2 \times 10^{15}$	for the low state SED
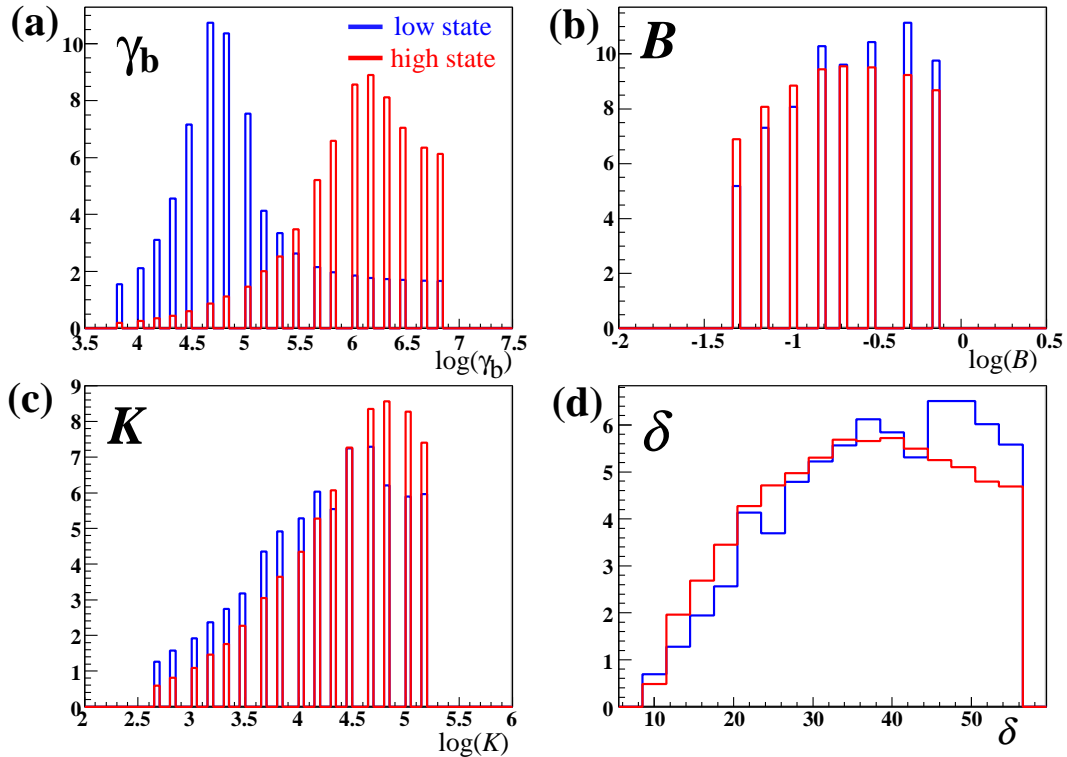
Figure 11.1: Distributions of the SSC model parameters weighted by $1/\chi^2_{red}$. $R = 1 \times 10^{15}$ [cm] were considered for both the high (*red*) and the low (*blue*) states. (a): γ_b in log scale, (b): B in log scale, (c): K in log scale, (d): δ in linear scale
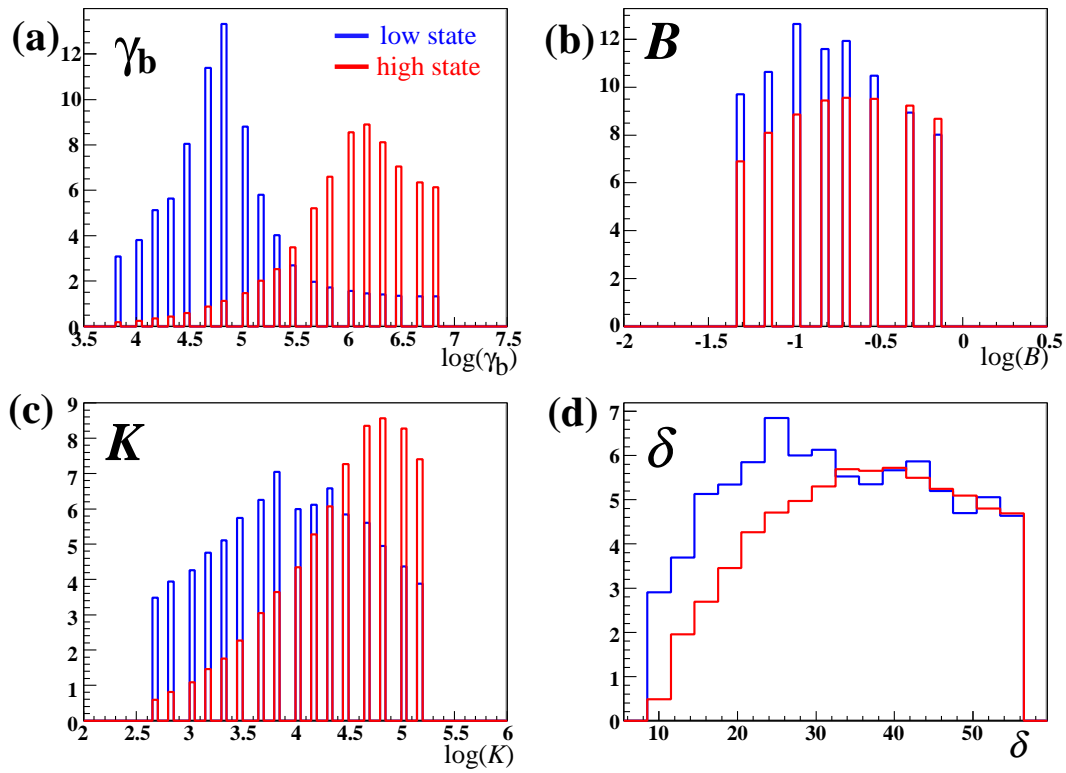
Figure 11.2: Distributions of the SSC model parameters weighted by $1/\chi^2_{\rm red}$. $R = 1 \times 10^{15}$ [cm] for the high state (*red*) and $R = 2 \times 10^{15}$ [cm] for the low state (*blue*) were considered.

definition in the VHE γ-ray band (see Fig. 10.1 in Chapter 10). Therefore, we decided to use this X-ray spectrum for describing the "medium" state SED of Mkn421.

Based on the fast variability with a time scale of less than 1 hour ever observed in Mkn421 [103], a nominal value of the emission region size $R = 2 \times 10^{15}$ [cm] [166] was adapted. The γ_{min} and n_1 were pre-assigned to be 1 and 2, respectively, as well as in the other blazars. As a result, the SED of the "medium" state with the VHE γ-ray and the X-ray bands could be reproduced by the SSC model with parameters listed in Table 11.2. The result is shown in Fig. 11.3-(c).

Since Mkn421 showed a trend of spectral hardening with an increase of flux like in Mkn501 (see Chapter 10), the framework discussed in the last section (i.e., changing γ_b for describing different states of SEDs) was also applied for the SEDs of Mkn421. The VHE γ-ray spectrum in the low state could be reproduced by just changing γ_b from the value in the medium state: $4 \times 10^4 \rightarrow 2.5 \times 10^4$ (medium→low). On the other hand, the high state VHE γ-ray spectrum could not be described within that framework. Even additional small changes of the other parameter values did not succeed in describing the VHE γ-ray spectrum in the high state. No strong conclusion can be drawn here because the high state SED comprises only the VHE γ-ray band (no data in other energy bands). Nevertheless, it might suggest that emission in the high state would originate from much different conditions of the jet than those in the medium/low flux states.

BL Lacertae: In Chapter 7, we only compared our observed data to a SSC spectrum which was derived by a previous study [208], not produced in this thesis. Therefore, we applied our SSC model for the observed SEDs in this section.

No simultaneous X-ray data were available for this source in 2005. However, for LBLs like BL Lacertae (see section 2.2 about the sub-class of blazars), the flux information in the optical band is useful for one-zone SSC models, because in LBLs the optical band is located around the peak of synchrotron components in their SEDs. In addition, the optical emission shows rapid ($\lesssim$ 1 day) and strong (more than one order of magnitude in amplitude) variability, as one can see in the high energy emission. It suggests that the optical and the high energy emissions originate from the same emission region[1].

Parameters of the SSC model were based on the previous study [208] which was cited in Chapter 7 for comparison to our observed SED in 2005. The same value for the size of emission region was used, $R = 7 \times 10^{15}$ [cm], because no information about the time scale of variability for this source was available in our data samples taken in 2005. Finally, the following small changes from the original values were applied for the other parameters: $\delta(20 \rightarrow 17)$, $\gamma_b(3.5 \times 10^3 \rightarrow 5 \times 10^3)$, $\gamma_{max}(5 \times 10^5 \rightarrow 2.5 \times 10^5)$, $B(0.2 \rightarrow 0.15)$, $n_2(3.8 \rightarrow 3.6)$. The derived SSC spectrum could reproduce the observed SED with the optical and the VHE γ-ray bands in 2005 as shown in Fig. 11.3-(d).

---

[1]As we discussed in Chapter 8 on Mkn501, in HBLs optical emission could be generated from a much larger region than the emission region for X-ray and VHE γ-ray. This assumption was supported by the fact that optical emission is rather stable and only shows slower variability than X-ray and VHE γ-ray emission in HBLs

Table 11.2 summarizes the physical parameters derived for 6 different SEDs; (1) Mkn501-high (high flux state), (2) Mkn501-low (low flux state), (3) 1ES1959+650 (for the MWL campaign in 2006), (4) Mkn421-medium (medium flux state), (5) Mkn421-low (low flux state), (6) BL Lacertae. Compared to these SSC parameters derived of 6 SEDs (four TeV blazars), the magnetic field strength, B, and the jet beaming factor, δ, show similar values among all SEDs ($B : 0.15 - 0.27$[G], $\delta : 17 - 28$). On the other hand, $\gamma_{\rm b}$, $\gamma_{\rm max}$ and K, which represent the electron spectrum, show differences among the SEDs of more than one order of magnitude. This might suggest that the electron spectrum of the source would be responsible for the observed SED rather than the magnetic field strength or the jet beaming factor.

Table 11.2: Summary of the SSC model parameters of four TeV blazars. (1)-(3) were derived using simultaneous VHE γ-ray and X-ray data.

	data	R	δ	$\gamma_{\rm br}$	$\gamma_{\rm max}$	B	K	n1	n2
		cm				Gauss	particle/cm^3		
(1)	Mkn501 (low)	1.03×10^{15}	20	6.7×10^4	1×10^7	0.27	1×10^5	2	4
(2)	Mkn501 (high)	1.03×10^{15}	20	1×10^6	1×10^7	0.27	1×10^5	2	4
(3)	1ES1959+650	7.3×10^{15}	18	5.7×10^4	6×10^5	0.25	2.2×10^3	2	3.4
(4)	Mkn421 (medium)	2×10^{15}	28	4×10^4	5×10^5	0.26	3×10^4	2	3.5
(5)	Mkn421 (low)	2×10^{15}	28	2.5×10^4	5×10^5	0.26	3×10^4	2	3.5
(6)	BL Lacertae	7×10^{15}	17	5×10^3	2.5×10^5	0.15	8.9×10^4	2	3.6

$\gamma_{\rm min} = 1$ for all cases

11.2   Photon and Electron spectra for four TeV blazars

In this section, photon spectra of the four TeV blazars (6 spectra) and their electron spectra of the sources derived by the SSC model (see parameters in Table 11.2) are summarized.

Photon spectra

In Fig. 11.4, all photon spectra of four TeV blazars in the VHE γ-ray band are directly compared.

Fig. 11.4-(a) shows 6 measured photon SEDs. Following the framework in [88], Fig. 11.4-(b) shows power spectra (bolometric luminosity) for the four TeV blazars. The differential power spectra were normalized by multiplying the "de-absorbed" photon SEDs by $4\pi d_L^2$, where d_L^2 is the luminosity distance. The "de-absorbed" SEDs were corrected for the γ-ray absorption by extragalactic background light (EBL) using the "low-IR" EBL model of Kneiske et al. (2004) [148].

Measured photon SEDs (Fig. 11.4-(a)) show differences in amplitude as they were observed. The integral fluxes above 200 GeV were observed with about two orders of magnitude difference between the highest spectrum (Mkn501-high: ~ 4 Crab flux) and the lowest spectrum (BL Lacertae: ~ 0.03 Crab flux). On the other hand, in the photon power spectra (Fig. 11.4-(b)), the difference in amplitude among the spectra becomes smaller than that in measured SEDs. The
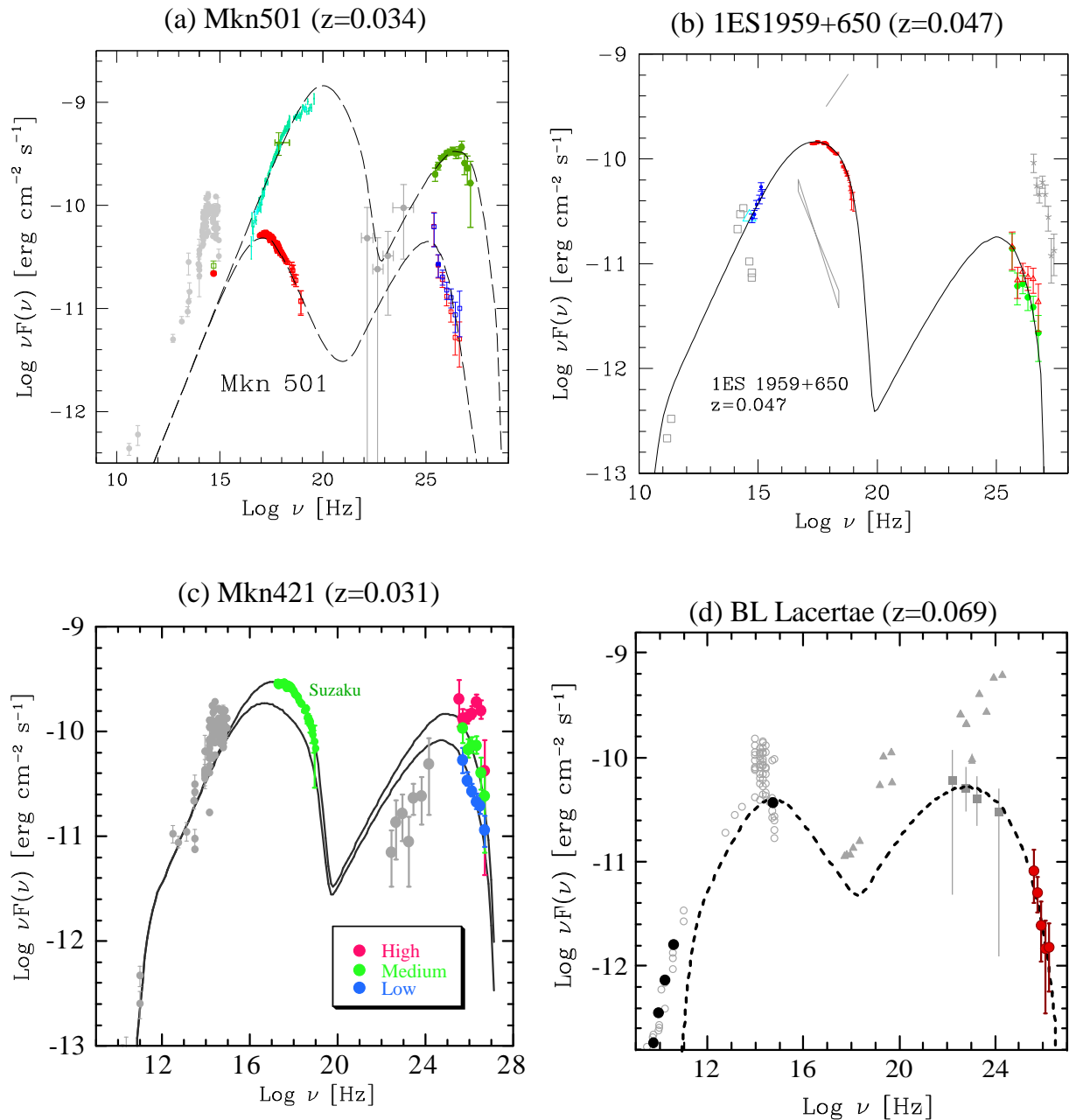
Figure 11.3: Overall SEDs of four TeV blazars. (a) Mkn501, (b) 1ES1959+650, (c) Mkn421 and (d) BL Lacertae. Curves in plots represent derived SSC spectra for observed SEDs. References of the data points are given in Fig. 8.10 for (a), in Fig. 9.7 for (b), Fig. 10.4 for (c), Fig. 7.12 for (d). Gray points denote historical data.

spectrum of Mkn501-high still shows a much higher power than any other spectra, and the spectrum of Mkn421-medium shows a slightly higher power than the others. The other four spectra show similar power levels. It is interesting that all spectra would appear to reach almost the same power level (2-3×10^{44} [erg/s]) around slightly less than 100 GeV if the spectra were extended to lower energies.

Electron spectra

For describing the electron spectra of the sources, a smoothed broken power law has been adapted in the SSC model, which is given by

$$N(\gamma) = K\gamma^{-n_1} \left(1 + \frac{\gamma}{\gamma_b}\right)^{n_1 - n_2} \exp\left(\frac{-\gamma}{\gamma_{max}}\right). \tag{11.1}$$

The derived electron number density spectra using Eq. 11.1 from the 6 SEDs (four TeV blazars) are shown in Fig. 11.5-(a).

Using the total energy density of relativistic electrons u_e, the total kinetic power of relativistic electrons $L_{e,kin}$ is given by [147]

$$L_{e,kin} = \frac{4}{3}\pi R^2 c u_e \delta^2$$

$$u_e = \int_{\gamma_{min}}^{\gamma_{max}} \gamma m_e c^2 N(\gamma) d\gamma \tag{11.2}$$

Fig. 11.5-(b) shows differential kinetic power spectra of electrons per logarithmic electron energy interval (i.e., per $\log\gamma$).

The electron kinetic power spectrum of Mkn501-high shows the highest power in the high energy range ($\log\gamma \gtrsim 4.5$). In fact, Mkn501-high shows the highest flux in the photon spectra among our data sets as well. The others show a similar electron kinetic power in this range of the electron energy as they show similar levels in the photon power spectra in the VHE γ-ray range in Fig. 11.4-(b). Therefore, the high energy part of the electron kinetic power could represent the output bolometric power of photons in the VHE γ-ray range. The source activity may be attributed to how much the electron kinetic power is extending to high energies.

In lower electron energies ($\log\gamma \lesssim 3.5$), the kinetic power spectra show constant levels with no difference between different states of the sources. It is interesting that Mkn501 and 1ES1959+650 show almost identical electron kinetic power levels although these spectra were derived independently from different data samples. Mkn421 shows a slightly higher power than Mkn501 and 1ES1959+650. Note that the spectra of Mkn501 and 1ES1959+650 were derived by the data which were taken simultaneously with the VHE γ-rays and the X-rays, while the spectrum of Mkn421 was derived with non-simultaneous X-ray data with the VHE γ-rays. On the other hand, BL Lacertae, which belongs to the LBLs, shows a significantly higher electron kinetic power than the other HBLs. These arguments can also be applied for the total kinetic power of relativistic electrons. The values derived by Eq. 11.2 for 6 spectra are summarized in Table 11.3. The HBL objects, Mkn501, 1ES1959+650 and Mkn421 show similar values of the

total electron kinetic power, irrespective of their flux states. The LBL BL Lacertae has a significantly higher total electron kinetic power than the other HBLs. These facts may suggest that the total kinetic power of relativistic electrons would be responsible for the sub-classes of blazars. This hypothesis may support a scenario proposed by [69] for explaining the physical origin of the sub-classes of blazars (see also section 2.2), i.e., accretion power to super massive black holes at the core in LBLs is higher than that in HBLs, and then electrons can extract more power from the accretion power.

In summary, we would conclude that

- photon spectra could be attributed to the electron population in the jet.
  Especially,

  - The kinetic power of high energy electrons ($\log \gamma \gtrsim 4.5$) could be responsible for the source activity of blazars.

  - The total kinetic power of relativistic electrons could be responsible for the sub-classes of blazars.

Table 11.3: Total kinetic power of relativistic electrons for 6 spectra of four TeV blazars

	Spectrum	$L_{\mathrm{e,kin}}$ [erg/s]
(1)	Mkn501 (low)	2.8×10^{43}
(2)	Mkn501 (high)	2.3×10^{43}
(3)	1ES1959+650	2.1×10^{43}
(4)	Mkn421 (medium)	5.1×10^{43}
(5)	Mkn421 (low)	4.9×10^{43}
(6)	BL Lacertae	5.6×10^{44}
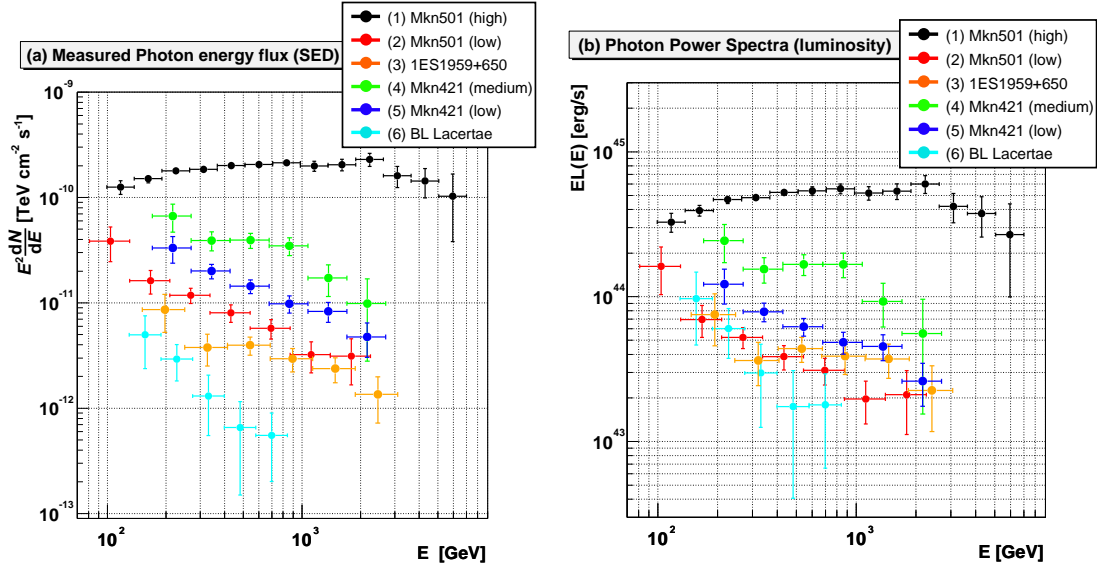
Figure 11.4: Photon spectra of four TeV blazars, Mkn501, 1ES1959+650, Mkn421, BL Lacertae. References for the data are given in the text. **[Left] (a):** Measured photon spectrum energy distributions. **[Right] (b):** Power spectra assuming isotropic emission. Here we plot the luminosity per natural logarithmic energy interval: $EL(E) = 4\pi d_L^2 E^2 (\mathrm{d}N/\mathrm{d}E)_{\text{de-abs}}$, where $(\mathrm{d}N/\mathrm{d}E)_{\text{de-abs}}$ is the "de-absorbed" flux corrected for EBL absorption using "low-IR" model in [148] and d_L is the luminosity distance.
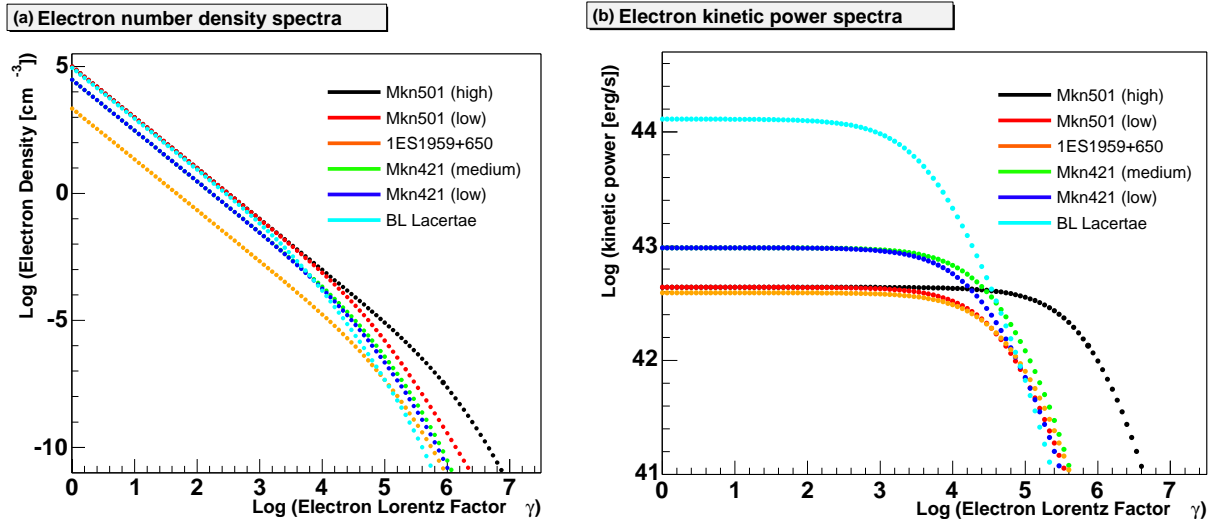
Figure 11.5: Derived electron spectra of four TeV blazars, Mkn501 (high and low state), 1ES1959+650, Mkn421 (medium and low state) and BL Lacertae. **[Left] (a):** Electron number density spectra. **[Right] (b):** Electron kinetic power spectra per logarithmic electron energy interval: $\frac{4}{3}\pi R^2 c \delta^2 \gamma^2 m_e c^2 N(\gamma)$ is plotted.

Chapter 12

Concluding remarks

A new Imaging Atmospheric Cherenkov Telescope (IACT), the MAGIC telescope, began its scientific operation in the fall 2004 and opened a new energy window in very high energy (VHE) γ-ray astronomy. This thesis presented observations with the MAGIC telescope in the new window of VHE γ-ray bands for four TeV blazars, including the discovery of a VHE γ-ray source. Simultaneous multiwavelength (MWL) observations in the new VHE γ-ray and the X-ray bands provided wide-range spectral energy distributions (SEDs) of the blazars. The synchrotron self-Comptom (SSC) model, which is the currently favored model for explaining the origin of VHE γ-ray emission in blazars, was used for discussing these SEDs. In this section, my contributions in this thesis are summarized together with outlooks for these topics.

A new type of photosensor, the hybrid photodetector (HPD) with an 18-mm diameter GaAsP photocathode, was developed together with Hamamatsu Photonics as one of the key tasks within the MAGIC-II project in order to further lower the energy threshold. We successfully achieved the target value in quantum efficiency (QE), which is the most important parameter in the development of this new type of photosensor. The QE spectrum on average reached over 50% at 500 nm. An 18-mm effective area in the diameter of the photocathode was confirmed with a 15% fluctuation at peak to peak value. Compared to the PMTs currently used in MAGIC-I, the overall Cherenkov photon conversion efficiency would be improved by a factor of 2 with the new photosensor. This can be seen as equivalent to increasing the mirror diameter from 17 m to 24 m. Other performance values also fulfilled the requirements to be met by photosensors in IACTs. Durability against background light in the field for use in the MAGIC camera was also verified by measurements and simulation studies. The results indicate that the MAGIC camera equipped with HPDs can maintain its quality over 10 years with only a small number of replacements of dead tubes damaged by the intense light from bright stars.

The new photosensors, i.e. the HPDs with an 18 mm GaAsP photocathode, are ready to be used in IACTs with low threshold settings. After my contribution, design studies of HPD pixel arrays including their electric circuits for output signals were carried out by colleagues at MPI. Based on these studies, the production of HPD pixel arrays will start for field tests in the camera of the second MAGIC telescope. After the field tests (planned in 2008), we intend to upgrade the camera of the second MAGIC telescope from PMTs to HPDs.

Searching for new TeV blazars, we proposed observations of BL Lacertae ($z = 0.069$) in 2005 and 2006. A VHE γ-ray signals was discovered with a 5.1 σ excess in the 2005 data. Above 200 GeV, an integral flux of $(0.6 \pm 0.2) \times 10^{-11}$ cm^{-2} s^{-1} was measured, corresponding to approximately 3% of the Crab flux. The differential spectrum between 150 and 900 GeV was rather steep with a photon index of -3.6 ± 0.5. The light curve showed no significant variability during the observations in 2005. The VHE γ-ray emission obtained in our observations could be described with a one-zone SSC model. Additional external seed photons for inverse Compton scattering (EC component) were not necessarily required for the VHE γ-ray emission in our case. On the other hand, the 2006 data showed no significant signal. This drop in flux followed the observed trend in the optical activity. The results of this thesis indicate that VHE γ-ray observations during times of higher optical states can be more efficient for this source.

Including this new source, BL Lacertae, the number of TeV blazars increased from 7 (in 2004) to 19 (in 2007) in these years. Moreover, we also established the BL Lacertae as a new class of TeV blazars, "LBLs". Currently, BL Lacertae is the first and only LBL among the 19 TeV blazars. Recently (in 2007), a VHE γ-ray signal was also discovered from 3C279, an "FSRQ". Now, VHE γ-ray emission was confirmed in all sub-classes of blazars.

In order to achieve wide-range SEDs with simultaneously taken data, we performed MWL campaigns with the MAGIC telescope and the X-ray Satellite Suzaku for Mkn501 in July 2006 and for 1ES1959+650 in May 2006. In both campaigns, VHE γ-ray signals from about 100 GeV to a few TeV were clearly detected together with X-ray spectra from sub-keV to several tens of keV. They were the first MWL campaigns for these sources in which VHE γ-ray spectra below 300 GeV were obtained.

The MWL campaign of Mkn501 was performed during one of the lowest states of source activity in both the VHE γ-ray and the X-ray bands. We could obtain the first data samples in a low state which were simultaneously taken in the VHE γ-ray and the X-ray bands for Mkn501. The flux level (about 20% of the Crab flux) and the photon index (-2.85 ± 0.14) of the measured spectrum were compatible with those observed in the lowest state during these two years (2005 and 2006). During the MWL campaign of 1ES1959+650, the source exhibited a relatively high state in X-rays and optical, while the VHE γ-ray flux was at one of the lowest levels so far recorded, corresponding to about 10% of the Crab Nebula flux. Nevertheless, the first data samples taken simultaneously in which the VHE γ-ray band showed its low flux state were successfully obtained. In both campaigns, no significant variability could be seen in the light curve of the VHE γ-ray band measured by MAGIC.

Monitoring observations were performed for the three bright TeV blazars, Mkn501, 1ES1959+650, and Mkn421. Their diurnal light curves during 1-3 year periods of observations were discussed. Apart from some huge flaring activities in July 2005, Mkn501 mostly stayed in a quiescent state for two years (2005 and 2006). No flaring activity of 1ES1959+650 was found during three years (2004 - 2006). On the other hand, the measured light curve of Mkn421 in 2006 showed a strong variability with one order of magnitude difference in the flux (up to about a factor of 2 of the Crab flux) and with a time scale of less than a day. These facts indicate that Mkn421 is the most active source among TeV blazars in the VHE γ-ray bands.

Compared to previously measured spectra, both VHE γ-ray and X-ray bands of the blazars showed a historically strong variability. The spectral peak in the VHE γ-ray band could be seen only in the highest state of Mkn501. In most cases, the peak positions seem to be located $\lesssim 80$ GeV, lower than our spectral analysis threshold. The results of Mkn501 indicate a trend of anti-correlation between the spectral index and the intensity both in the VHE γ-ray and the X-ray bands. The measured spectra of Mkn421 in the VHE γ-ray band suggested a similar behavior, i.e., the spectrum tends to harden as the flux increases. On the other hand, the spectra of 1ES1959+650 derived on a yearly basis between 2004 and 2006 showed that their photon indices were compatible during the three years. However, the difference in flux between those spectra was only a factor of 2, while the other two sources (Mkn501, Mkn421) showed a difference of about one order of magnitude. Therefore, we could not conclude that 1ES1959+650 had different features than the other sources. The data samples of 1ES1959+650 obtained during its flaring states in the VHE γ-ray bands are interesting in this context.

The measured SEDs of the four TeV blazars in this thesis could be well represented by a homogeneous one-zone SSC model. Concerning the derived physical parameters of the jets, the strength of the magnetic fields (B) and the Doppler beaming factor (δ) showed similar values for all SEDs (B:0.15-0.27 [G], δ:17-28). They might indicate typical values of the jets for TeV blazars. On the other hand, the derived electron spectra showed large variations. This might suggest that the electron population in the jet could be responsible for the SED of a blazar. In particular, flaring activity could be caused by increasing the Lorentz factor of the electrons at the break energy in the electron spectrum. Sub-classes of blazars between LBL and HBL objects could be characterized by the total kinetic power of the relativistic electrons. BL Lacertae, an LBL object, showed higher total kinetic power than other sources.

Despite the progress in understanding blazars based on the new observation results presented in this thesis, we still need to invest major efforts to find the answer to the fundamental question of AGNs, namely how the energy is extracted from the black bole. In particular, the following topics are still open.

- Are there any AGNs in which high energy photons are mainly of hadronic origin? If yes, what conditions make the difference between "lepton accelerators" and "hadron accelerators"?

- How do jets become active (flaring)? Which are the mechanisms?

- How is the jet formed?

To find answers to these questions with the current instruments is rather problematic. For example, there is a huge gap of 6 decades in the measured SEDs, between about 100 keV and about 100 GeV, with the currently available instruments. In most observations, the peak energy and total luminosity of the second (high energy) bump in SEDs could not be directly determined from the observations due to that energy gap. As a result, we need additional assumptions for the emission models. In this thesis, I focused on leptonic origin models, especially the SSC model, because this model was favorable for most of the previous observations of TeV blazars.

In fact, it is still difficult to discriminate between hadronic origin (i.e. π^0 decay) and leptonic origin (i.e. inverse Compton scattering) with the currently available SEDs.

Continuous observations are also important to determine the SEDs in different flux states because source activity states cannot be predicted in advance. Current monitoring instruments for high energy photons (above X-ray) do not have sufficient sensitivity to detect signals except for huge flaring states. Coordinated simultaneous observations can provide wide-range SEDs as this thesis shows, but the time overlap covered in such observations is too short ($\sim$ several days) to obtain spectra in various flux states, in particular, to catch the flaring states.

Applying emission models for complete SEDs in different activity states will give us precise physical parameters in the jet. Variation of these parameters could be associated with the dynamical evolution of jet environments. Variability and correlation between different energy bands can also constrain the emission models. For instance, short time variability would favor leptonic origin scenarios and be associated with the emission from regions very close to the central black hole. The variability time scales are attributed to structures of the jet, which may be related to shock creation mechanisms in the jet. The measurement of time delays between variations in different energy bands in the light curves can tell us about the physics condition of the jets because the cooling process of relativistic particles may be energy dependent.

So far, discussions of emission models were performed for only a few bright TeV blazars (mostly for Mkn421, Mkn501, 1ES1959+650 and PKS2155-304) because wide-range SEDs were taken only for those blazars. It is necessary to extend the discussion to other blazars in order to understand the fundamental physics of blazars.

The following future observations will contribute to answering these open issues:

- GLAST [200], a new γ-ray satellite is planned to be launched in May, 2008. This satellite will observe the energy range from 30 MeV to 300 GeV. This energy range is complimentary to the IACTs' range. In addition, IACT projects will be upgraded (e.g., MAGIC-II, H.E.S.S.-II). For instance, the MAGIC-II project is expected to improve the sensitivity of the current MAGIC-I by a factor 2-3 by means of a stereoscopic observation mode with an analysis threshold down to about 40 GeV.

  Combining both instruments, GLAST and new IACTs, can provide complete spectra from MeV to TeV with simultaneously taken data. This energy range covers most of the second (high energy) bump in the SEDs of blazars. Therefore, we can expect to obtain direct information about the peak energy and total luminosity of the second bump. This range can distinguish between hadronic origin emission and leptonic origin emission because, in the former case, the spectrum may have a characteristic bump around 100 MeV and a power law for the higher energy range from the decay of $\pi^0 \rightarrow \gamma\gamma$.

  If hadronic origin sources are identified, it will be the first clear evidence of extra-galactic sites of cosmic-ray accelerators. In addition, neutrinos should be accompanied by γ-ray emission in the case of hadronic origin. Such sources can be interesting targets for the "ICE CUBE" project, which is searching for high energy cosmic neutrinos. Discovery of hadronic origin sources can provide an important guideline for a new astronomy, the "high-energy neutrino astronomy".

- The GLAST satellite will cover the whole sky region in 3 hours thanks to its large field of view (about 2 steradian). Hence, it will continuously observe sources in the γ-ray range. In the X-ray band, a Japanese group is planning to install "MAXI" [94] on the International Space Station in 2009. This is a new all-sky survey instrument which will have a sensitivity which is one order of magnitudes higher than the current all-sky survey instrument (RXTE/ASM). The monitoring observation for bright TeV blazars in the MAGIC project is also ongoing; we have observed the sources on a regular basis in order to accumulate data. These observations will provide us with spectra and long term light curves with various flux states.

  In addition, the long term light curves will allow us to conduct periodic studies of the emissions. Discovery of periodicities in the light curves may give us new insight into the jet and black-hole system (e.g., precession of the jet, binary black-hole system, etc.).

- Finally, the new projects will certainly increase the number of γ-ray blazars. For example, new IACTs, like MAGIC-II and H.E.S.S.-II, are expected to discover about 100 sources among the HBL objects. The GLAST satellite is expected to detect several 1000 blazars, mainly in LBLs and FSRQs. Such a number of samples may allow us to perform systematic studies to find the answer for the fundamental physics of blazars.

List of Acronyms and Abbreviations

1ES	First Einstein Survey
AC	Alternating Current
AD	Avalanche Diode
ADC	Analog to Digital Converter
AGASA	Akeno Giant Air Shower Array
AGN	Active Galactic Nucleus
ASDC	ASI Science Data Center
ASM	All-Sky Monitor [detector on board of RXTE]
a.s.l.	above sea level
Az	Azimuth
BH	Black Hole
BeppoSAX	Satellite per Astronomia a raggi X (Satellite for X-ray astronomy)
CANGAROO	Collaboration of Australia and Nippon for a GAmma-Ray Observatory in the Outback
CAT	Cherenkov Array at Themis
CGRO	Compton Gamma-Ray Observatory
C.L.	Confidence Level
CMB	Cosmic Microwave Background
COG	Center-Of-Gravity
CORSIKA	COsmic Ray SImulations for KAscade
CR	Cosmic Ray
CTA	Cherenkov Telescope Array
DAQ	Data Acquisition
DC	Direct Current
decl.	Declination
EAS	Extensive Air Shower
EBL	Extragalactic Background Light
EGRET	Energetic Gamma-Ray Experiment Telescope
EC	External inverse Compton
FADC	Flash Analog to Digital Converter
FIFO	First In, First Out
FOV	Field-Of-View
FSRQ	Flat Spectrum Radio Quasar

FWHM	Full Width at Half Maximum
GLAST	Gamma-ray Large Area Space Telescope
GPIB	General Purpose Interface Bus
GRB	Gamma-Ray Burst
GRH	Gamma-Ray Horizon
GZK	Greisen-Zatsepin-Kuzmin
H.E.S.S.	High Energy Stereoscopic System
HBL	High-frequency peaked BL Lac
HE	High Energy
HEGRA	High Energy Gamma-Ray Astronomy
HPD	Hybrid PhotoDetector
HV	High Voltage
HXD	Hard X-ray Detector [on board of Suzaku]
IAC	Instituto de Astrof'isica de Canarias
IACT	Imaging Atmospheric Cherenkov Telescope
IC	Inverse Compton
IR	InfraRed
KASCADE	KArlsruhe Shower Core and Array DEtector
KVA	Kungliga Vetenskapsakademien [telescope]
LBL	Low-frequency peaked BL Lac
LED	Light Emitting Diode
LIDAR	LIght Detecting And Ranging
LONS	Light Of the Night Sky
$M_\odot$	Solar Mass
MAGIC	Major Atmospheric Gamma-ray Imaging Cherenkov
MARS	MAGIC Analysis and Reconstruction Software
MC	Monte Carlo [simulations]
MHD	MagnetoHydroDynamic
MJD	Modified Julian Day
MWL	MultiWaveLength
Mkn	Markarian
N.D.F	Number of Degrees of Freedom
NEA	Negative Electron Affinity
NED	NASA Extragalactic Database
NKG	Nishimura-Kamata-Greisen
NRAO	U.S. National Radio Astronomy Observatory
NSB	Night Sky Background
ORM	Observatorio del Roque de los Muchachos
PG	Palomar-Green catalog of UV-excess stellar objects
pc	parsec, parallax of one arc second
p.e.	Photoelectrons
PhC	PhotoCathode
PIN	P-type, Intrinsic, N-type [diode]

PKS	Parkes catalogue of radio sources
PL	Power Law
PMT	PhotoMultiplier tube
PSF	Point Spread Function
PWN	Pulsar wind nebula
QE	Quantum Efficiency
R.A.	Right Ascension
RASS	ROSAT All-Sky Survey
RF	Random Forest
RMS	Root Mean Square
ROSAT	Röntgen Satellite
RXTE	Rossi X-ray Timing Explorer
SED	Spectral Energy Distribution
SMBH	SuperMassive Black Hole
SNR	SuperNova Remnant
SSC	Synchrotron Self-Compton
ToO	Target of Opportunity
UHE	Ultra High Energy
UMRAO	the University of Michigan RAdio Observatory
UTC	Coordinated Universal Time
UV	Ultra Violet
UVOT	UV/Optical Telescope [on board of Swift]
VCSEL	Vertical Cavity Surface Emitting Laser
VERITAS	Very Energetic Radiation Imaging Telescope Array System
VHE	Very High Energy
VLA	Very Large Array
VLBA	Very Long Baseline Array
WLS	WaveLength Shifter
XIS	X-ray Imaging Spectrometer [on board of Suzaku]
XRT	X-Ray Telescope [on board of Swift]
ZA	Zenith Angle

List of Figures

List of Tables

Bibliography

[1] R. U. Abbasi et al. *Phys. Rev. Lett.*, 92:151101, 2004.

[2] J. Abraham et al. *Nucl. Instrum. Methods Phys. Res. A*, 523:50, 2004.

[3] J. Abraham et al. *Science*, 5852:938, 2007.

[4] T. Abu-Zayyad et al. *Nucl. Instrum. Methods Phys. Res. A*, 450:253, 2000.

[5] M. Aguilar et al. *Physics Reports*, 336:331, 2002.

[6] F. Aharonian, A. M. Atoyan, and T. Kifune. *MNRAS*, 291:162, 1997.

[7] F. Aharonian et al. *A&A*, 342:69, 1999.

[8] F. Aharonian et al. *ApJ*, 546:898, 2001.

[9] F. Aharonian et al. *A&A*, 393:L37, 2002.

[10] F. Aharonian et al. *A&A*, 406:L9, 2003.

[11] F. Aharonian et al. *A&A*, 421:529, 2004.

[12] F. Aharonian et al. *A&A*, 421:529, 2004.

[13] F. Aharonian et al. *A&A*, 436:L17, 2005.

[14] F. Aharonian et al. *Science*, 307:1938, 2005.

[15] F. Aharonian et al. *A&A*, 442:895, 2005.

[16] F. Aharonian et al. *A&A*, 436:L17, 2005.

[17] F. Aharonian et al. *A&A*, 448:L19, 2006.

[18] F. Aharonian et al. *Nature*, 440:1018, 2006.

[19] F. Aharonian et al. *A&A*, 460:365, 2006.

[20] F. Aharonian et al. *Nature*, 439:695, 2006.

[21] F. Aharonian et al. *A&A*, 475:L9, 2007.

[22] F. Aharonian et al. *A&A*, 473:L25, 2007.

[23] F. Aharonian et al. *A&A*, 477:353, 2007.

[24] F. A. Aharonian. *Very High Energy Cosmic Gamma Radiation: A Crucial Window on the Extreme Universe*. World Scientific, 2004.

[25] F. A. Aharonian and A. M. Atoyan. *Astr. Space Sci.*, 79:321, 1981.

[26] F. A. Aharonian et al. *A&A*, 393:89, 2002.

[27] F. A. Aharonian et al. *A&A*, 614:897, 2004.

[28] F. A. Aharonian et al. *A&A*, 437:95, 2005.

[29] F. A. Aharonian et al. *ApJ*, 636:777, 2006.

[30] F. A. Aharonian et al. *ApJ*, 664:L71, 2007.

[31] H. Ahn et al. *Proc. 30th Int. Cosmic Ray Conf. (Mérida)*, 2007.

[32] J. Albert et al. *ApJ*, 648:L105, 2006.

[33] J. Albert et al. *ApJ*, 642:L119, 2006.

[34] J. Albert et al. *Science*, 312:1771, 2006.

[35] J. Albert et al. *ApJ*, 654:L119, 2006.

[36] J. Albert et al. *ApJ*, 639:761, 2006.

[37] J. Albert et al. *ApJ*, 666:L17, 2007.

[38] J. Albert et al. *ApJ*, 654:L119, 2007.

[39] J. Albert et al. *ApJ*, 667:L21, 2007.

[40] J. Albert et al. *ApJ*, 667:358, 2007.

[41] J. Albert et al. *ApJ*, 669:862, 2007.

[42] J. Albert et al. *Nucl. Instrum. Methods Phys. Res. A*, 2007. submitted (astro-ph/0612385).

[43] J. Albert et al. *ApJ*, 2007. submitted (astro-ph/arXiv:0705.3244).

[44] J. Albert et al. *Nucl. Instrum. Methods Phys. Res. A*, 2007. submitted (astro-ph/arXiv:0709.3719).

[45] J. Albert et al. *Nucl. Instrum. Methods Phys. Res. A*, 583:494, 2007.

[46] J. Albert et al. *ApJ*, 663:125, 2007.

[47] J. Albert et al. *AstroPart. Phys.*, 2007. submitted (astro-ph/arXiv:0702475).

[48] A. Amenomori et al. *Phys.Lett.*, B632:58, 2006.

[49] A. Barrau et al. *Nucl. Instrum. Methods Phys. Res. A*, 416:278, 1998.

[50] J. A. Barrio et al. The magic telescope. unpublished (MPI-PhE 98-05), March 1998.

[51] R. H. Becker, R. L. White, and A. L. Edwards. *ApJS*, 75:1, 1991.

[52] V.. Beckmann et al. *A&A*, 383:410, 2002.

[53] W. Bednarek. *ApJ*, 402:L29, 1993.

[54] W. Bednarek and R. J. Protheroe. *MNRAS*, 310:577, 1999.

[55] A. R. Bell. *MNRAS*, 182:443, 1978.

[56] C. Benn and S. Ellison. *New Astronomy Reviews*, 42:503, 1998.

[57] K. Bernlöhr. *AstroPart. Phys.*, 12:255, 2000.

[58] M. Bertero. *Electronics and Electron Physics*, 75, 1989.

[59] P. L. Biermann et al. *Proceedings of the 7eme Colloquium Cosmologie, 'High Energy Astrophysics from and for Space'*, 2003. (astro-ph/0211503).

[60] R. D. Blandford. *in Compton Gamma-Ray Observatory, AIP Conf. Proc.*, 280, 1993.

[61] R. D. Blandford and J. P. Ostriker. *ApJ*, 221:L29, 1978.

[62] R. D. Blandford and R. L. Znajek. *MNRAS*, 179:433, 1977.

[63] M. Błażejowski et al. *ApJ*, 630:130, 2005.

[64] S. D. Bloom et al. *ApJ*, 490:L145, 1997.

[65] G. R. Blumenthal and R. J. Gould. *Rev. Mod Phys.*, 42:237, 1970.

[66] R. Bock et al. *Nucl. Instrum. Methods Phys. Res. A*, 516:511, 2004.

[67] C.F. Bohren and D. Huffman. *Absorption and scattering of light by small particles*. John Wiley, New York, 1983.

[68] M. Böttcher. *Zeitabhängiger Strahlungstransport in Jets van aktiven galaktischen Kernen.* Ph.D, Thesis, Universität Bonn, 1997.

[69] M. Böttcher and C. D. Dermer. *ApJ*, 564:86, 2002.

[70] S. M. Bradbury et al. *Nucl. Instrum. Methods Phys. Res. A*, 387:45, 1997.

[71] L. Breiman et al. *Machine Learning*, 45:5, 2001.

[72] T. Bretz et al. *Proc. 28th Int. Cosmic Ray Conf. (Tsukuba)*, 1:2943, 2003.

[73] J. N. Capdevielle and J. Gawin. *J. Phys. G: Nucl. Part. Phys.*, 8:1317, 2002.

[74] E. Carmona et al. *Proc. 30th Int. Cosmic Ray Conf. (Mérida)*, 2007.

[75] M. Catanese et al. *ApJ*, 480:562, 1997.

[76] M. Catanese et al. *ApJ*, 501:616, 1998.

[77] A. Cavaliere and V. D'Elia. *ApJ*, 571:226, 2002.

[78] A. Celotti and G. Ghisellini. *MNRAS*. in press (astro-ph/arXiv:0711.4112).

[79] P. M. Chadwick et al. *ApJ*, 513:161, 1999.

[80] K. S. Cheng, C. Ho, and M. Ruderman. *ApJ*, 300:500, 1986.

[81] P. A. Cherenkov. *Dokl. Akad. Nauk, SSSR*, 2:451, 1934.

[82] N. Chiba et al. *Nucl. Instrum. Methods Phys. Res. A*, 331:338, 1992.

[83] G. Colla et al. *A&AS*, 7:1, 1972.

[84] P. S. Coppi and R. D. Blandford. *MNRAS*, 245:453, 1990.

[85] L. Costamante and G. Ghisellini. *A&A*, 384:56, 2002.

[86] A. Dar and A. Laor. *ApJ*, 478:L5, 1997.

[87] O. C. de Jager and A. K. Harding. *ApJ*, 396:161, 1992.

[88] C. D. Dermer and N. Gehrels. *ApJ*, 447:103, 1995.

[89] A. Djannati-Atai et al. *A&A*, 350:17, 1999.

[90] E. Domingo-Santamaria et al. *Proc. 29th Int. Cosmic Ray Conf. (Pune)*, 5:363, 2005.

[91] D. Donato et al. *A&A*, 375:739, 2001.

[92] L. Elterman et al. *Appl. Opt.*, 3:6, 1964.

[93] M. Elvis, D. Plummer, J. Schachter, and G. Fabbiano. *ApJS*, 80:257, 1992.

[94] MAXI experiment. http://www-maxi.tksc.nasda.go.jp/indexe.html.

[95] R. Falomo, J. K. Kotilainen, and A. Treves. *ApJ*, 566:738, 2002.

[96] E. Fermi. *Phys. Rev.*, 75:1169, 1949.

[97] R. C. Fernow. *Introduction to Experimental Particle Physics*. Cambridge University Press, 1986.

[98] H. Fesefeldt. PITHA-85/02, 1985.

[99] V. P. Fomin et al. *AstroPart. Phys.*, 2:137, 1994.

[100] G. Fossati et al. *MNRAS*, 299:433, 1998.

[101] I. Frank, I. Tamm, and C. R. Acad. *Sci. URSS*, 14:109, 1937.

[102] M. Fukugita, K. Shimasaku, and T. Ichikawa. *PASJ*, 107:945, 1995.

[103] J. Gaidos et al. *Nature*, 383:319, 1996.

[104] T. K. Gaisser. *Cosmic Rays and Particle Physics*. Cambridge University Press, 1990.

[105] M. Gaug. *Calibration of the MAGIC Telescope and Observation of Gamma Ray Bursts*. Ph.D. thesis, Universitat Autonoma de Barcelona, March 2006.

[106] N. Gehrels et al. *ApJ*, 611:1005, 2004.

[107] G. Ghisellini, A. Celotti, G. Fossati, and L. Costamante. *A&A*, 386:833, 2002.

[108] G. Ghisellini et al. *ApJ*, 407:65, 1993.

[109] G. Ghisellini et al. *MNRAS*, 301:451, 1998.

[110] G. Ghisellini and L. Maraschi. *ApJ*, 340:181, 1989.

[111] G. Ghisellini, F. Tavecchio, and M. Chiaberge. *A&A*, 432:401, 2005.

[112] V. L. Ginzburg and S. L. Syrovatskii. *Origin of Cosmic Rays*. Macmillan, New York, 1964.

[113] M. Gliozzi et al. *ApJ*, 646:61, 2006.

[114] S.V. Godambe et al. *Proc. 30th Int. Cosmic Ray Conf. (Mérida)*, 2007.

[115] F. Goebel et al. *Proc. 29th Int. Cosmic Ray Conf. (Pune)*, 5:375, 2005.

[116] F. Goebel et al. *Proc. 30th Int. Cosmic Ray Conf. (Mérida)*, 2007. (astro-ph/arXiv:0709.2023).

[117] P. Goldreich and W. H. Julian. *ApJ*, 157:869, 1969.

[118] R.J. Gould and Schréder G. P. *Phys. Rev.*, 155:5, 1967.

[119] P. C. Gregory and J. J. Condon. *ApJS*, 75:1011, 1991.

[120] K. Greisen. *Annual Review of Nuclear Science*, 10:63, 1960.

[121] K. Greisen. *Phys. Rev. Lett.*, 16:748, 1966.

[122] V. A. Hagen-Thorn et al. *Astronomy Report*, 41:154, 1997.

[123] R. C. Hartman et al. *ApJ*, 385:L1, 1992.

[124] R. C. Hartman et al. *ApJS*, 123:79, 1999.

[125] M. Hayashida, R. Mirzoyan, and M. Teshima. *Nucl. Instrum. Methods Phys. Res. A*, 567:180, 2006.

[126] D. Heck et al. Corsika: A monte carlo code to simulate extensice air showers. 1998. http://www-ik.fzk.de/corsika/.

[127] J. Heidt et al. *A&A*, 341:683, 1999.

[128] W. Heitler. *The Quantum Theory of Radiation*. Clarendon Press, 1954.

[129] A. M. Hillas. *AstroPart. Phys.*, 22:425, 1984.

[130] A. M. Hillas. *Proc. 29th Int. Cosmic Ray Conf. (La Jolla)*, 3:445, 1985.

[131] M. Hillas. *Proceeding of "Cosmology, Galaxy Formation and Astroparticle Physics on the pathway to the SKA", Oxford*, April 2006. (astro-ph/0607109).

[132] J. Hinton. Rapporteur talk (OG 2.1 - 2.4) in Int. Cosmic Ray Conf. (Merida) (astro-ph/arXiv:0712.3352), 2007.

[133] J. A. Hinton et al. *New Astron. Rev.*, 48:331, 2004.

[134] J. Holder et al. *ApJ*, 583:L9, 2003.

[135] D. Horan et al. *ApJ*, 571:753, 2002.

[136] D. Horan et al. *ApJ*, 603:51, 2004.

[137] D. Horns et al. *in The Universe Viewd in Gamma-Rays*, 2002. (Tokyo: Universal Academy).

[138] C. C. Hsu et al. *Proc. 30th Int. Cosmic Ray Conf. (Mérida)*, 2007.

[139] P. Huentemeyer et al. *Proc. 30th Int. Cosmic Ray Conf. (Mérida)*, 2007.

[140] S. Inoue and F. Takahara. *ApJ*, 463:555, 1996.

[141] P. Jakobsson et al. *A&A*, 447:897, 2006.

[142] F. C. Jones. *Phys. Rev.*, 167:1159, 1968.

[143] A. Kashlinsky. *Phys. Reports*, 409:361, 2005.

[144] J. Kataoka et al. *ApJ*, 514:138, 1999.

[145] K. Katarzynski et al. *A&A*, 367:809, 2001.

[146] A. K. Kembhavi and J. A. Narlikar. *Quasars and Active Galactic Nuclei*. Cambridge University Press, 1999.

[147] M. Kino, F. Takahara, and M. Kusunose. *ApJ*, 564:97, 2002.

[148] T. M. Kneiske et al. *A&A*, 413:807, 2004.

[149] F. X. Kneizys et al. *The MODTRAN 2/3 Report and LOWTRAN 7 Model*. Phillips Laboratory, Hanscom AFB, MA 01731, USA, 1996.

[150] A. Konopelko et al. *ApJ*, 597:851, 2003.

[151] D. Kranich. private communication.

[152] D. Kranich. *ASP Conf. Proc.*, 299:3, 2003.

[153] H. Krawczynski, P. S. Coppi, and F. Aharonian. *MNRAS*, 336:721, 2002.

[154] H. Krawczynski et al. *A&A*, 353:97, 2000.

[155] H. Krawczynski et al. *ApJ*, 559:187, 2001.

[156] H. Krawczynski et al. *ApJ*, 601:151, 2004.

[157] F. Krennrich et al. *ApJ*, 575:L9, 2002.

[158] G. Lagache, J.-L. Puget, and H. Dole. *ARA&A*, 43:727, 2005.

[159] A. Lähteemäki. private communication.

[160] L. D. Landau and E. M. Lifshitz. *The Universe in Gamma Rays*. Springer, 2001.

[161] T.-P. Li and Y.-Q. Ma. *ApJ*, 272:317, 1983.

[162] G. Lombardi et al. *Publications of the Astronomical Society of the Pacific*, 118:1198, 2006.

[163] M. S. Longair. *High energy astrophysics*. Cambridge University Press, Cambridge, 1992.

[164] E. Lorenz et al. *Nucl. Instrum. Methods Phys. Res. A*, 504:280, 2003.

[165] M. Lynden-Bell. *Nature*, 223:690, 1969.

[166] D. J. Macomb et al. *ApJ*, 449:L99, 1995.

[167] G. M. Madejski et al. *ApJ*, 521:145, 1999.

[168] G. Maier et al. *Proc. 30th Int. Cosmic Ray Conf. (Mérida)*, 2007.

[169] K. Mannheim. *A&A*, 269:76, 1993.

[170] K. Mannheim and P. L. Biermann. *A&A*, 253:L21, 1992.

[171] L. Maraschi et al. *ApJ*, 397:L5, 1999.

[172] S. Martinez et al. *Nucl. Instrum. Methods Phys. Res. A*, 357:567, 1995.

[173] A. Mastichiadis and J. G. Kirk. *A&A*, 320:19, 1997.

[174] D. Mazin and M. Raue. *A&A*, 471:439, 2007.

[175] B. McInnes and M.F. Walker. *Publications of the Astronomical Society of the Pacific*, 86:529, 1974.

[176] J. S. Miller et al. *ApJ*, 219:L85, 1978.

[177] R. Mirzoyan et al. *Nucl. Instrum. Methods Phys. Res. A*, 442:140, 2000.

[178] R. Mirzoyan and E. Lorenz. *Proc. 25th Int. Cosmic Ray Conf.*, 7:265, 1997.

[179] K. Mitsuda et al. *PASJ*, 59:1, 2007.

[180] M. Mori et al. *Proc. 30th Int. Cosmic Ray Conf. (Mérida)*, 2007.

[181] A. Mücke and R. J. Protheroe. *AsrtoPart. Phys.*, 15:121, 2001.

[182] Y. I. Neshpor et al. *Astron. Rep.*, 45:249, 2001.

[183] E. Nieppola et al. *A&A*, 445:441, 2006.

[184] K. Nilsson et al. *A&A*, 475:199, 2007.

[185] J. Nishimura. *Handbuch der Physik*, volume XLVI/2. 1967.

[186] J. Nishimura and K. Kamata. *Progress in Theoretical Physics*, 7:185, 1952.

[187] T. Nishiyama et al. *Proc. 26th Int. Cosmic Ray Conf. (Salt Lake City)*, 3:370, 1999.

[188] J. B. Oke and R. E. Schild. *ApJ*, 161:1015, 1970.

[189] R. A. Ong. *Physics Reports*, 305:93, 1998.

[190] A. N. Otte. *Observation of VHE γ-Rays from the Vicinity of magnetized Neutron Stars and Development of new Photon-Detectors for Future Ground based γ-Ray Detectors*. Ph.D. thesis, Technische Universität München, Octorber 2007.

[191] P. Padovani. *Ap&SS*, 309:63, 2007.

[192] P. Padovani et al. *ApJ*, 588:128, 2003.

[193] P. Padovani et al. *ApJ*, 662:182, 2007.

[194] P. Padovani and P. Giommi. *ApJ*, 444:567, 1995.

[195] D. Paneque. *The MAGIC Telescope: Development of new technologies and first observation*. Ph.D. thesis, Technische Universität München, August 2004.

[196] D. Paneque et al. *Nucl. Instrum. Methods Phys. Res. A*, 504:109, 2003.

[197] E. S. Perlman et al. *ApJS*, 104:251, 1996.

[198] D. Petry. Ph.D. thesis, Technische Universität München, September 1997.

[199] E. Pian et al. *ApJ*, 492:L17, 1998.

[200] GLAST project. http://www-glast.stanford.edu/.

[201] ICE CUBE project. http://icecube.wisc.edu/.

[202] R. J. Protheroe and P. L. Biermann. *AstroPart. Phys.*, 6:293, 1997.

[203] G. Pühlhofer et al. *AstroPart. Phys.*, 20:267, 2003.

[204] M. Punch et al. *Nature*, 358:477, 1992.

[205] J. Quinn et al. *ApJ*, 456:L83, 1996.

[206] P. Raffaelo et al. *Nucl. Instrum. Methods Phys. Res. A*, 567:218, 2006.

[207] J. Ranft. *Phys. Rev.*, D51:64, 1995.

[208] M. Ravasio et al. *A&A*, 383:763, 2002.

[209] M. J. Ree. *Nature*, 211:468, 1966.

[210] M. J. Ree and P. Meszaros. *MNRAS*, 258:41, 1992.

[211] C. Reynolds. Ph.D. thesis (www.jive.nl/~reynolds/), 2002.

[212] B. Riegel et al. *Proc. 29th Int. Cosmic Ray Conf. (Pune)*, 5:219, 2005.

[213] W. Rolke, A. Lopez, and J. Conrad. *Nucl. Instrum. Methods Phys. Res. A*, 551:493, 2005.

[214] B. Rossi and K Greisen. *Reviews of Modern Physics*, 13:240, 1941.

[215] T. Y. Saito et al. *Proc. 30th Int. Cosmic Ray Conf. (Mérida)*, 2007. (astro-ph/arXiv:0709.2052).

[216] R. M. Sambruna et al. *ApJ*, 515:140, 1999.

[217] D. B. Sanders et al. *ApJ*, 325:74, 1988.

[218] D. J. Schlegel, D. P. Finkbeiner, and M Davis. *ApJ*, 500:525, 1998.

[219] V. Schönfelder. *Fluid Mechanics*. Pergamon Press, Oxford, 1982.

[220] M. Sikora, M. C. Begelman, and M. J. Ree. *ApJ*, 421:153, 1994.

[221] T. Stanev. *ApJ*, 479:290, 1997.

[222] F. W. Stecker and O. C. de Jager. *Space Sience Reviews*, 75:401, 1996.

[223] F. W. Stecker, M. A. Malkan, and S. T. Scully. *ApJ*, 648:774, 2006.

[224] M. Stickel et al. *ApJ*, 374:431, 1991.

[225] A. M. Stirling et al. *MNRAS*, 341:405, 2003.

[226] P.A. Sturrock. *ApJ*, 164:529, 1971.

[227] G. Superina et al. *Proc. 30th Int. Cosmic Ray Conf. (Mérida)*, 2007. (astro-ph/arXiv:0710.4057).

[228] A. Szabo and R. Protheroe. *Astropart. Phys.*, 2:375, 1994.

[229] G. Tagliaferri et al. *A&A*, 412:711, 2003.

[230] G. Tagliaferri et al. *ApJ*, 2008. in press (astro-ph/arXiv:0801.4029).

[231] T. Takahashi et al. *ApJ*, 470:89, 1996.

[232] M. Takeda et al. *Astropart. Phys.*, 19:447, 2003.

[233] C. Tanihata et al. *ApJ*, 543:124, 2000.

[234] F. Tavecchio et al. *ApJ*, 509:608, 1998.

[235] F. Tavecchio et al. *ApJ*, 554:725, 2001.

[236] F. Tavecchio et al. *ApJ*, 665:980, 2007.

[237] M. Teshima. *Proc. 30th Int. Cosmic Ray Conf. (Mérida)*, 2007. Rapporteur talk (HE 1).

[238] M. Teshima et al. *Proc. 30th Int. Cosmic Ray Conf. (Mérida)*, 2007. (astro-ph/arXiv:0709.1475).

[239] M. Ulrich et al. *ApJ*, 198:261, 1975.

[240] C. M. Urry and P. Padovani. *PASP*, 107:803, 1995.

[241] V. V. Vassiliev. *AstroPart. Phys.*, 12:217, 2000.

[242] R. Vermeulen and M. Cohen. *ApJ*, 430:467, 1994.

[243] M. Villata et al. *A&A*, 424:497, 2004.

[244] H. Völk, E. Brezhko, and L. Ksenofontov. *A&A*, 433:229, 2005.

[245] R. M. Wagner et al. *Proc. 29th Int. Cosmic Ray Conf. (Pune)*, 4:163, 2005.

[246] J. V Wall and J. A. Peacock. *MNRAS*, 216:173, 1985.

[247] A. Watson. *Proc. 30th Int. Cosmic Ray Conf. (Mérida)*, 2007. [Highlight talk].

[248] T.C. Weekes. *Space Sci. Rev.*, 75:1, 1996.

[249] T. C. Weeks et al. *ApJ*, 160:1, 1989.

[250] K. W. Weiler and R. A. Sramek. *Ann. Rev. Astron. Astrophys.*, 26:295, 1988.

[251] X. B. Wu, F. K. Liu, and T. Z. Zhang. *A&A*, 389:742, 2002.

[252] T. Yamamoto et al. *Proc. 30th Int. Cosmic Ray Conf. (Mérida)*, 2007. (astro-ph/arXiv:0707.2638).

[253] W. M. Yao et al. *J.Phys.*, G33:1, 2006.

[254] G. B. Yodh et al. *Phys. Rev.D*, 27:1183, 1983.

[255] G. T. Zatzepin and V. A. Kuzmin. *JETO Lett.*, 4:78, 1966.

Acknowledgments